Towards Mild, Microporous Oxidation and Solid Acid Heterogeneous Catalysts

by Vinton Carter

Submitted in part fulfilment of the requirements for the

Degree of PhD

on 30th October, 1998.

(i) I, Vinton Carter, hereby certify that this thesis, which is approximately 50000 words in length, has been written by me, that it is the record of workl carried out by me and that it has not been submitted in any previous application for a higher degree.

date 30/10/98 signature of candidate... ...

(ii) I was admitted as a research student in 10, 1995 and as a candidate for the degree of PhD in 10, 96; the higher study for which this is a record was carried out in the University of St Andrews between 1995 and 1998.

date 30/10/98 signature of candidate.... ....

(iii) I hereby certify that the candidate has fulfilled the conditions of the Resolution and Regulations appropriate for the degree of PhD in the University of St Andrews and that the candidate is qualified to submit this thesis in application for that degree.

date 30/10/98 signature of supervisor.... ..

In submitting this thesis to the University of St Andrews I understand that I am giving permission for it to be made available for use in accordance with the regulations of the University Library for the time being I force, subject to any copyright vested in the work not being affected thereby. I also understand that the title and abstract will be published, and that a copy of the work may be made and supplied to any *bona fide* library or research worker.

date 30/10/98 signature of candidate...

Ackowledgments

I am very grateful to many people for all their assistance during this work. I owe special thanks to my supervisor, Paul Wright, who has been a constant source of inspiration and enthusiasm. Also, I am indebted to the people with whom I share a lab, particularly to Dave Woodcock who has solved almost every problem I have taken to him. Thanks also to all the staff in the Purdie Building for their support.

Abstract

Exploratory syntheses were made in the area of aluminium methylphosphonates, following on the synthesis of microporous polymorphs by Maeda, by varying the Al:P ratio, duration of heating, temperature and the presence of an organic mineraliser. Three new phases were prepared phase pure in this way. The structures of two of these were solved by *ab initio* XRD techniques. AlMePO-1 of unit cell composition $[Al(OH)PO_3CH3.H_2O]_4$ crystallised in space group $P2_1/a$, with unit cell parameters, a =9.474 Å, b =7.07Å,c =7.865Å and β = 106.6°. AlMePO-2 of formula $Al_3[(CH)_3PO_3]_2(OH)_3 \cdot 0.75H_2O$, crystallised in space groups *Pmnb*, a=19.733 Å, b = 10.154 Å, c = 5.148 Å. The third new material whose structure was not solved, was believed to have a triclinic unit cell with parameters, a = 9.644 Å, b = 12.374 Å, c = 5.063 Å, α = 91.14°, β = 90.36°, γ = 92.13°. Multiple quantum MASNMR was developed for use on materials of the above types and several structures were analysed in this way. MQMASNMR was found to increase enormously the available resolution for quadrupolar nuclei, e.g. Al. Attempts were made to incorporate transition metals into the frameworks of the microporous methylphosphonates, with some success, but products dominated by leaching effects in catalysis experiments. Phosphonate substitution with PH, PCH_2CO_2H and phosphate was attempted with limited success. A rare solid-state transformation was discovered between the alpha and beta polymorphic materials, for which a mechanism was proposed based upon XRD, MASNMR and TG-MS data, amongst others. A low temperature, high resolution neutron diffraction study of AlMePO-β was performed, allowing the accurate placement of the methyl groups on the internal channel wall for the first time. It was discovered that a significant part of the wall was free from obstruction by methyl groups.

List of publications arising from this work

L.-J. Sawers, V. J. Carter, A. R. Armstrong, P. G. Bruce, P. A. Wright and B. E. Gore, *Journal Chemical Society, Dalton Transactions,* 1996, 3159-3161.

V. J. Carter, J. D. Gale, R. E. Morris, E. Sastre, J. Perez-Pariente, *Journal of Materials Chemistry*, 1997, 7(11), 2287-2292.

G. B. Hix, V. J. Carter, D. S. Wragg, R. E. Morris, P. A. Wright, *Journal of Materials Chemistry*, 1999, **9**, 179-185.

V. J. Carter, J. P. Kujanpää, J. F. C. Turner, C. R. A. Catlow, K. Knight, P. A. Wright, in preparation.

D. Tunstall, V. J. Carter, P. A. Wright, in preparation.

Table Of Contents

Chapter 1

Introduction to heterogeneous catalysis, microporous materials and the current state of the field

The importance of catalysts and the products that they bring within our reach cannot be overemphasised. In recent years, the industrial trend has been away from traditional, stoichiometric reagents in favour of catalytic routes. The reasons for this are simple and compelling. Modern legislature forces manufacturers of chemicals to be ever more careful about how they go about producing their products both in terms of pollution and in rising costs of overheads such as labour. Rather than use a 1:1 ratio of a metal dichromate to oxidise hydrocarbon feedstocks, whence comes an enormous amount of waste (there is often far more waste than product produced),[1] it is in the manufacturers interest to use a catalyst in combination with a cheap, clean co-oxidant such as H_2O_2, which gives H_2O as waste. In addition to the savings made through there being less clean up work, catalytic reactions usually give more energy efficient processes.[2]

One of the requirements that a manufacturer has when searching for a catalyst is that it be heterogeneous to his reaction system. It is quite frequently the case that catalysts are very expensive substances. In order for them to be cost efficient, the owner must be able to recover it and reuse it, as many times as possible. Heterogeneous catalysts are favoured in industry because of the greater ease and lower cost of engineering them into a plant and of recycling them. Indeed, so great are the difficulties and or costs of using homogeneous systems that many processes remain uncatalysed industrially despite the existence of effective liquid phase catalysts.[3] Hence, heterogeneous catalysts are a sought after commodity. Of all the processes for which there is a demand for catalysts, oxidation of feedstocks and / or for the production of fine chemicals is one of the largest and, potentially, most lucrative.[3]

In order to be a good heterogeneous catalyst, that is, to be cost effective, and of benefit to the manufacturer, it has to be specific, active, reasonably cheap to produce (although this is offset by the useful lifetime of the material – the longer it can be used, the more expensive it can be to produce) and mechanically, chemically and thermally stable under the conditions in which it will be used. Unfortunately, while there are many materials that are active and specific, or long lasting and cheap to produce, rarely are all

these qualities found in the same material. For example, clays, particularly if pillared, are durable, cheap, active and stable. However, rarely are they specific in their catalytic action although there are exceptions.[4]

However, one group of materials that quite often offers these qualities in effective combinations, is that loosely termed as microporous materials or molecular sieves, e.g. zeolites and other such solids (known as zeotypes). These materials are crystalline solids which have structures incorporating channels or pores of similar dimensions to those of small molecules, i.e. ~5-10 Å. The naturally occurring microporous materials, zeolites, are aluminosilicates. Zeolites have negatively charged frameworks due to the lower valency of aluminium compared to silicon. Every aluminium in the structure gives rise to a negative charge. As a result of this cations reside in the channels and can be substituted for protons. Protonated forms of zeolites behave as solid acids, catalysing bond rearrangement and formation reactions of molecules small enough to enter the pores.

More recently, artificial analogues of these materials have been produced. Purely siliceous zeolites and aluminium phosphates have been produced, both of which have neutral frameworks. Isomorphous replacement of atoms within the rather inert structures thus produced can introduce a range of activity. For example, transition metals active in redox processes can be introduced to create catalysts for oxidation processes. Alternatively, heteroatoms of a valency different to that of the replacement atom can be used to reintroduce acidity to the structures. Some replacement atoms fulfil both these roles, e.g. Ti^{IV} substituting for phosphorus (V) in an AlPO.

Microporous frameworks allow a degree of control over the size and shape of reactants, possible transition states and products of the reaction that is not easily replicated either in the liquid phase or in porous materials that are not crystalline. The crystalline nature of these materials leads to very well defined and virtually identical active sites further increasing the selectivity of the catalytic action. One of the most effective microporous oxidation catalysts to date has been titanium silicalite-1 (TS-1), a material isostructural with ZSM-5 in which some of the silicon has been replaced titanium. This compound is known to catalyse the mild oxidation of numerous alkanes,[5] alkenes[6] and alcohols[7] to epoxides and carbonyl materials.

The wide variety of possible structures and replacement elements available for aluminium phosphates made them very attractive as potential catalysts.[5-10] Indeed, the original aim of this project was to use these materials to form the basis of mild oxidation catalysts that is the ultimate goal of the work. However, very recently (1996), there has been doubt as to the true mechanism of the catalytic action of AlPOs. Sheldon *et al*,[11] after many years of working on substituted AlPOs found evidence that the majority of the effect is due to metal species in solution, which have leached from the molecular sieve. Since the primary reason to use these materials as catalysts was to take advantage of their heterogeneity, the existence of active homogeneous species make them redundant as catalysts.

However, two microporous materials have been synthesised recently, the first in a new group of materials, the aluminium methylphosphonates (AlMePOs). The two polymorphs discovered have been termed AlMePO-β[12,13] and AlMePO-α.[14] These solids, which form a logical progression of the work on aluminium phosphates, bear a strong resemblance to AlPOs except that one of the P-O bonds present in the phosphate is replaced with a P-CH_3 bond in the AlMePOs. Both polymorphs have unidimensional channels partly lined with methyl groups, a structure that makes them very hydrophobic. Hydrophobicity could be considered essential in a successful oxidation catalyst given that such a process usually involves reacting hydrophobic starting materials in order to produce hydrophilic products.[11] Since, in order to work, the catalyst must adsorb the reagents and actively desorb the products hydrophobicity would seem to be required.

Not only do the aluminium methylphosphonates have the desirable quality of hydrophobicity, they also offer many other potential advantages as a result of the organic groups. The internal character of the channels is solely a result of the groups that make up the wall. Since most of the wall is covered with organic groups, it should be possible to modify the qualities of the sieve by adjusting the type of organic group attached to the phosphorus. One can imagine being able to produce material with a range of hydrophobicities, with various types of 'extra' functionality built into the wall.

This work began with exploratory syntheses using conditions modified from the literature. During the course of this preliminary work, several new phases came to light.

It became apparent that there was a requirement for effective methods of structural analysis applicable to microcrystalline powders (the only form in which the new materials could be formed), if the aim of producing new catalysts were to be at all possible. Thus came about an involvement in the development of new methods of characterisation such as *ab initio* structure solution from laboratory powder diffraction data and multiple quantum magic angle spinning nuclear magnetic resonance (MQMASNMR) for the investigation of materials containing quadrupolar nuclei. Reports concerning these two areas of work are concentrated in Chapters 2 and 3.

The goal of new catalysts was sought by attempting the modification of the aluminium methylphosphonate microporous frameworks, AlMePO-β and AlMePO-α, in two main ways. Firstly, transition metal incorporation (as well as some other metals, e.g. Mg) has been attempted, both to create framework charges and, hence, Brønsted acid sites for solid acid catalytic activity, and to form materials containing highly dispersed redox metal centres for oxidation catalysis. Secondly, several investigations were carried out into methods of modifying the phosphonate groups which were incorporated into the framework, or layered material, so that the internal environment of the material could be controlled. The approach taken was to use various ratios of two phosphonic acids in the synthesis gel in the hope that this would be reflected in the composition of the crystallised solid. Chapters 6 and 7 deal with this work.

Of the new phases that were mentioned above, three materials were isolated from the pure aluminium methylphosphonate system which were suitable for attempted structure characterisation. Obviously, this work was connected with *ab initio* studies reported in Chapter 3. Another serendipitous discovery was the thermally initiated transformation of AlMePO-β into AlMePO-α, in the presence of water vapour. The subsequent work on investigating as thoroughly as possible the mechanism and parameters of what is a rare, interesting and, ultimately, useful route to AlMePO-α has been placed in Chapter 4. Another temperature dependent piece of work, reported in Chapter 5, is the high resolution neutron diffraction study of AlMePO-β at 4.6 K designed to investigate the exact position and orientation of the methyl groups partially covering the surface of the channels to determine the sort of access potential substrates have to oxygen and metal atoms of the framework.

References

1 R. Sheldon, *Catalytic Oxidation in the Manufacture of Fine Chemicals, in New Developments in Selective Oxidation*, G. Centi, F. Trifiro (Editors), 1990, Elsevier Science Pub., Amsterdam

2 J. Chen, J. Dakka, E. Neeleman, R. Sheldon, *Journal of the Chemical Society, Chemical Communications*, 1993, 1379.

3 R. Sheldon, Jihad Dakka, *Catalysis Today*, 1994, **19**, 215

4 S. Selvaraj, B. V. Mohan, K. N. Krishna and B. S. J. Prakash, *Studies in Surface Science and Catalysis,* 1998, **113**, 573-578.

5 Ulf Schudardt, Heloise Pastore, Estevam Spinacé, *Studies in Surface Science and Catalysis,* 1994, **84**, 1877.

6 C. Cativiela, J. García, J. Mayoral, *Journal of Molecular Catalysis. A: Chemical*, 1996, **112**, 259-267.

7 P. Kumar, R. Kumar, B. Pandey, *Synlett*, 1995, 289.

8 T. Sato, J. Dakka, R. Sheldon, *Studies in Surface Science and Catalysis*, 1994, **84**, 1853.

9 J. Chen, M. Haanepen, J. van Hooff, R. Sheldon, *Studies in Surface Science and Catalysis*, 1994, **84**, 973.

10 G. Hutchings, D. Lee, *Journal of the Chemical Society, Chemical Communications*, 1994, 1095.

11 R. A. Sheldon and H E. B. Lempers, *The stability of chromium in chromium molecular sieves under the conditions of liquid phase oxidations with* tert-*butyl hydroperoxide, 6th International Symposium on the Activation of Dioxygen and Homogeneous Catalytic Oxidation,* April, 1996, Noordigkerhout, The Netherlands.

12 K. Maeda, Y. Kiyozumi, F. Mizukami, *Angewandte Chemie, International Edition English*, 1994, **33**(22), 2335

13 K. Maeda, J. Akimoto, Y. Kiyozumi, F. Mizukami, *Journal of the Chemical Society, Chemical Communications*, 1995, 1033

14 K. Maeda, J. Akimoto, Y. Kiyozumi, F. Mizukami, *Angewandte Chemie, International Edition English*, 1995, **34**(11), 1199

Chapter 2 Multiquantum Magic Angle Spinning NMR (MQMASNMR)

Introduction

Nuclear magnetic resonance (NMR) plays a vital role in materials science as it does in other areas of chemistry in elucidating many aspects of the structure and dynamics of the compounds under study. Solid-state NMR is an area that has received much attention as those fields of research most in need of its insights have matured. In particular the line broadening that results from several causes including the static nature of atomic orientations in solids and various types of internuclear interaction has been a problem. One of the most enduring limitations has been due to the line broadening associated with quadrupolar nuclei such as ^{27}Al, which is common in materials with applications in many areas including sorbents, heterogeneous catalysts[1] and low thermal-expansion materials.[2]

This chapter is concerned with a new technique in NMR, that of multiple quantum magic angle spinning nuclear magnetic resonance (MQMASNMR). Although, MQMASNMR is becoming an important tool in the investigation of solids containing quadrupolar nuclei, it is a young methodology and, as such, the available data on relevant systems is in short supply. In using this technique to study the materials in this thesis, the aim is both to expand the small database of MQMASNMR results on such compounds and to enhance the technique itself through determination of optimal experimental conditions for this area.

This introduction presents some background to the technique of NMR, particularly in the solid-state, outlines problems that need to be overcome in order to make the fullest use of it, and examines and compares the various solutions available, including MQMASNMR, dynamic angle spinning (DAS) and double rotation (DOR). No attempt is made to be exhaustive in a description of the physical basis of these techniques; lengthier descriptions of the methodologies mentioned are referenced in the text.

Nuclear Magnetic Resonance (NMR) – Background

NMR is the study of the interaction of nuclear magnetic moments with magnetic fields. Only nuclei with a nuclear spin quantum number, $I \neq 0$, have a magnetic moment. The nuclear spin quantum number, I, which is characteristic of a particular isotope of an element, can take positive integer or half-integer values. For many common nuclei, e.g. ^{12}C and ^{16}O, the nuclear spin is zero and, therefore, so is the nuclear magnetic moment, with the consequence that these nuclei are NMR inactive.[3]

In an externally applied magnetic field, B_0, the magnetic moment may take up 2I+1 different orientations, each of which is characterised by a quantum number m_I, where

$$m_I = I, I-1, \ldots, -I$$

For spin ½ nuclei such as ^{1}H, the moment is aligned either parallel (α) or antiparallel (β) to the direction of B_0 (in fact, the vector describing the magnetic moment is considered to be precessing around B_0 but the component of the moment aligned either parallel or antiparallel to it is constant).[4] The component of the magnetic moment, μ, aligned with the z axis (parallel to the direction of the magnetic field) is

$$\mu_Z = \gamma \hbar m_I$$

where γ is the magnetogyric ratio.

The potential energies of the two states, parallel and anti-parallel alignment, are different by an amount dependent on the magnitude of B_0, the α state being lower in energy in most cases (Figure 1). At thermal equilibrium, the separation in energy states results in a Boltzmann distribution of populations with more α spins than β (in the likely case of α being the lower in energy). This difference, although small, causes a net macroscopic magnetization aligned with the direction of B_0. Such a splitting of the energy levels due to the interaction with a large external magnetic field is known as the Zeeman interaction and the difference in the potential energies, ΔV, is given by

$$\Delta V = \hbar \gamma B = h \nu_0$$

where ν_0 is known as the Larmor precession frequency and is the frequency of radiation required to cause transitions between the two states, α and β.[5]

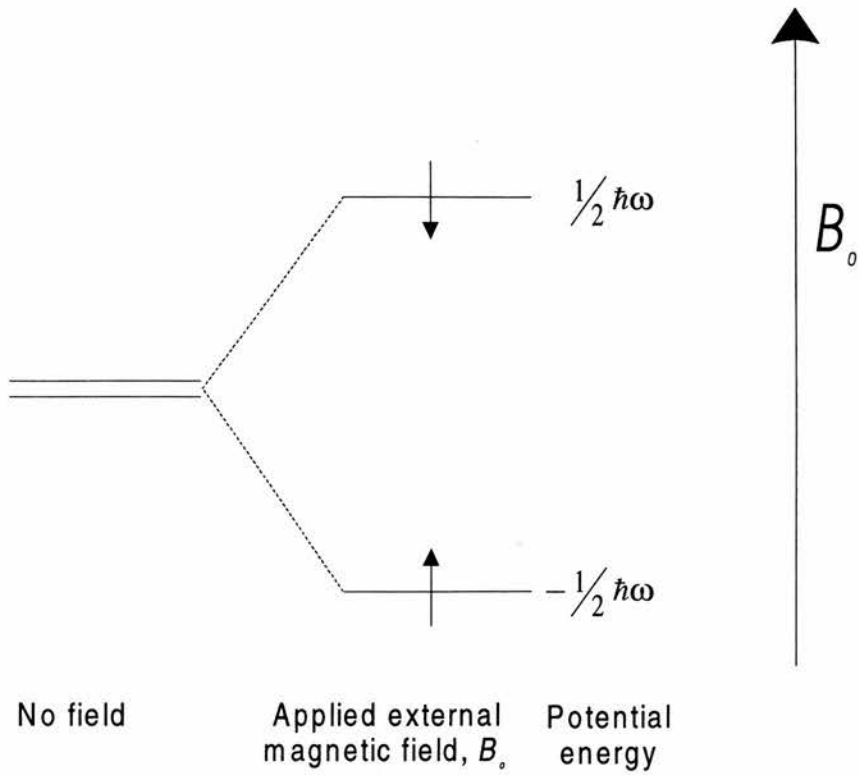

Figure 1 Energy level diagram showing orientation of nuclear magnetic moments in a magnetic field for a spin ½ nucleus.

The Rotating-Frame and Radiofrequency Fields

If an oscillating magnetic field, B_1, in the radio frequency range is applied to the system above in the static field, the magnetization undergoes a very complex motion. However, a description of the motion is made much simpler if, instead of the normal Cartesian coordinate system, another is introduced in which the x and y axes rotate around the z axis which is defined coincident with the direction of B_0. This coordinate system is known as the 'rotating-frame' and is held to rotate at the Larmor frequency, i.e. at the frequency at which the magnetization vector precesses around B_0. Thus, in the rotating-frame description, in the presence of the static field only, the magnetization vector is motionless.[5]

The B_1 field is generally applied in the form of linearly polarised electromagnetic radiation in the radiofrequency range. The direction of the radiation is coincident with the z axis, along the direction of B_0. Thus, the direction of oscillation of the magnetic field lies in the xy plane (Figure 2). However, one can consider the linearly vibrating field, $B_1(t)$, as the combination of two vectors each rotating about the z axis with equal but opposite angular velocities (Figure 3).

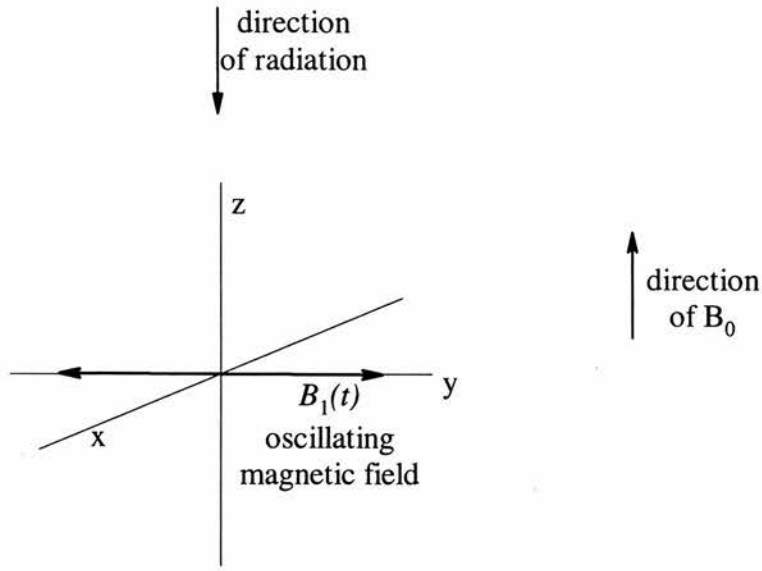

Figure 2 Representation of the orientation of the direction of the radiation and the oscillating magnetic field with respect to the *z* axis.

Thus, $B_1(t)$ becomes[4]

$$B_1(t) = B_1^0 \cos\omega_0 t$$
$$= \tfrac{1}{2} B_1^0(\cos\omega_0 t + \sin\omega_0 t) + \tfrac{1}{2} B_1^0(\cos\omega_0 t - \sin\omega_0 t)$$

where ω_0 is the angular frequency (radians sec^{-1}), t is time and B_1^0 is the amplitude of the wave.

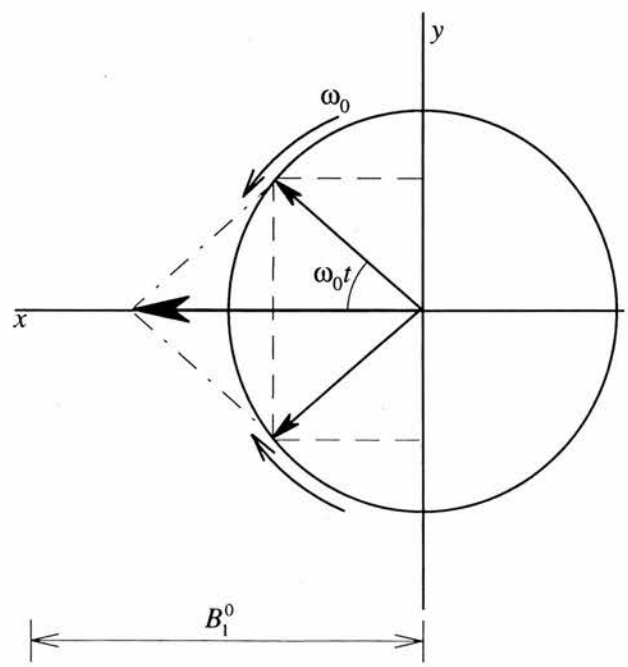

Figure 3 diagram showing the resolution of the linear magnetic field vector into two vectors rotating with equal and opposite angular frequency

The component of B_1, that rotates in the opposite direction to that in which the nuclear magnetic moments precess, has negligible interaction with them and need not be considered further. Thus, since the radiation behaves as a circularly polarised magnetic field at the resonant frequency, it is, therefore, stationary in the rotating-frame (which rotates with the same frequency as the precessing moments). This situation is equivalent to there being no B_0 within the rotating frame. However, there is the B_1 field and, so, the magnetization precesses around it.[4] The duration and strength of B_1 determine how much the magnetization vector moves away from the z axis. It is often this result of the pulse of radiation (the cause of B_1) that is used to characterise it. For example, if the pulse causes the magnetization to move all the way into the xy plane it is termed a 90° pulse.

The orientation of B_1 within the xy plane is termed the *phase*. It is defined as the angle of the magnetic vector from the x axis. As, by convention, the coordinate system is chosen so that the direction of B_1 is coincident with the x axis (the phase is zero), the precession takes place in the yz plane. However, occasions arise when it is advantageous to change the phase in repetitive patterns (phase cycles – see below). In many cases, the phases used are coincident with the x and y axes and sometimes, in this case, the phases are termed simply x and y.[5]

Chemical shift

The case described above, of a spin system in a magnetic field, is an oversimplification. One of the most important omissions is that nuclei in a real material do not experience exactly the same magnetic field as a result of B_0. This is due to the fact that the electrons orbiting the nucleus generate their own magnetic field which combines with B_0 to create an effective field (B_{eff}). Thus, each nucleus is in a slightly different field and, therefore, even homonuclear magnetic spins precess at, and absorb radiation of, different frequencies. This effect is known as *chemical* shift since it arises as a result of the electrons within the system whose state determines (or is determined by) the chemistry of the material.

Relaxation Processes

When the macroscopic magnetization, M_z, is perturbed away from its equilibrium state (aligned with the static, B_0 field) several processes work to bring it back to that state.[5] Such processes are termed relaxation. Generally speaking, they are grouped according to their effect on the magnetization vector as longitudinal relaxation, T_1 and transverse relaxation, T_2. Considering a system after the application of a $\pi/2$ pulse such that B_1 lies along the x axis of the rotating frame, causing the magnetization to lie along the y axis. With time, the magnetization relaxes back from the xy plane towards the z axis

which is taken as parallel with B_0. This process involves the transfer of energy from the spin system to the lattice and therefore is known as spin-lattice relaxation.

However, transverse relaxation also occurs during this time, causing the nuclear magnetic moments to spread out from their positions along the y axis, thus decreasing the magnitude of M_y. The dispersion of the spin vectors occurs because each experiences a slightly different effective field due to their varying chemical shifts, inhomogeneities in the spectrometer's field and local fluctuations in the field from neighbouring nuclei and electrons. T_2 refers most explicitly to the relaxation that occurs as a result of field fluctuations from neighbouring parts of the lattice, rather than from long term field inhomogeneities. Thus transverse relaxation is separated into homogeneous relaxation (due to local, short-lived and effectively random fluctuations in field due to the lattice) and inhomogeneous relaxation (due to long term gradients in the spectrometer's field). The spread of precession frequencies that causes the homogeneous and inhomogeneous relaxation manifests in the NMR frequency spectrum as a broadened peak, the width of which is proportional to T_2. Hence, these mechanisms are known also as homogeneous and inhomogeneous broadening.

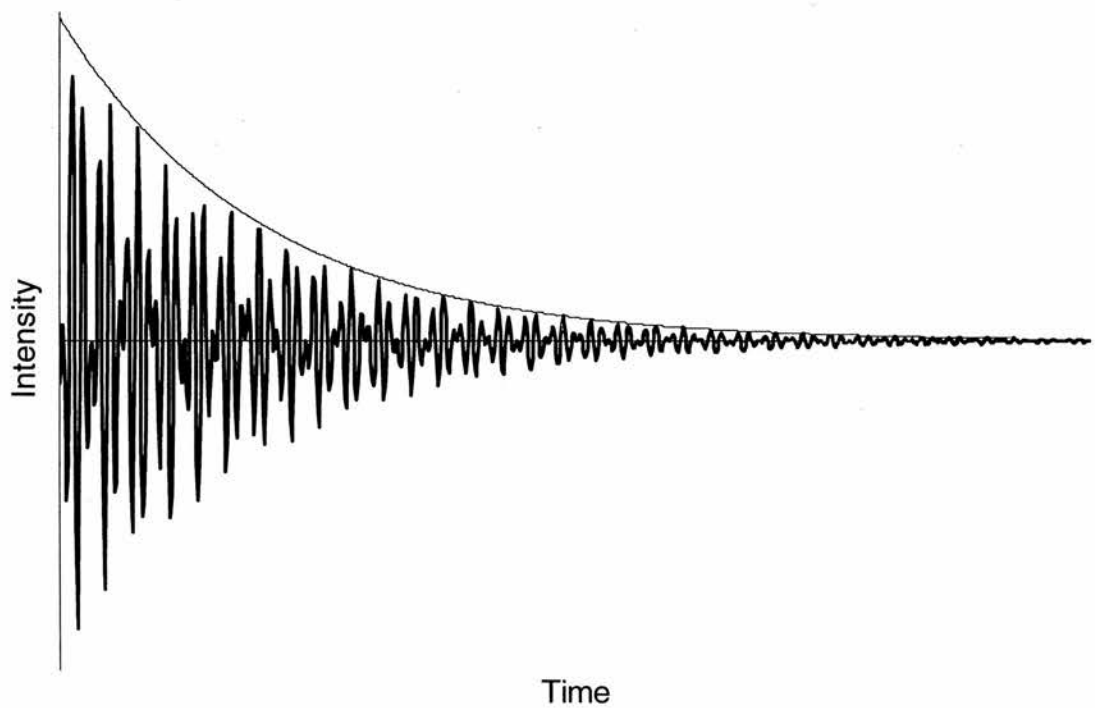

Figure 4 Free induction decay (FID) – signal composed of two frequencies.

Both relaxation mechanisms cause a reduction of M_{xy} which is responsible for inducing the signal in the detector. Hence, on the application of a 90° pulse to a spin system, an oscillating signal is observed which starts at a maximum and decays to zero, usually with an approximately exponential envelope (Figure 4). Such a decaying signal is known as a free induction decay (FID).

Spin Echo

If the homogeneous broadening is dominated by inhomogeneous effects it is possible to perform an experiment known as the spin echo effect.[5] Firstly, a $\pi / 2$ pulse is applied

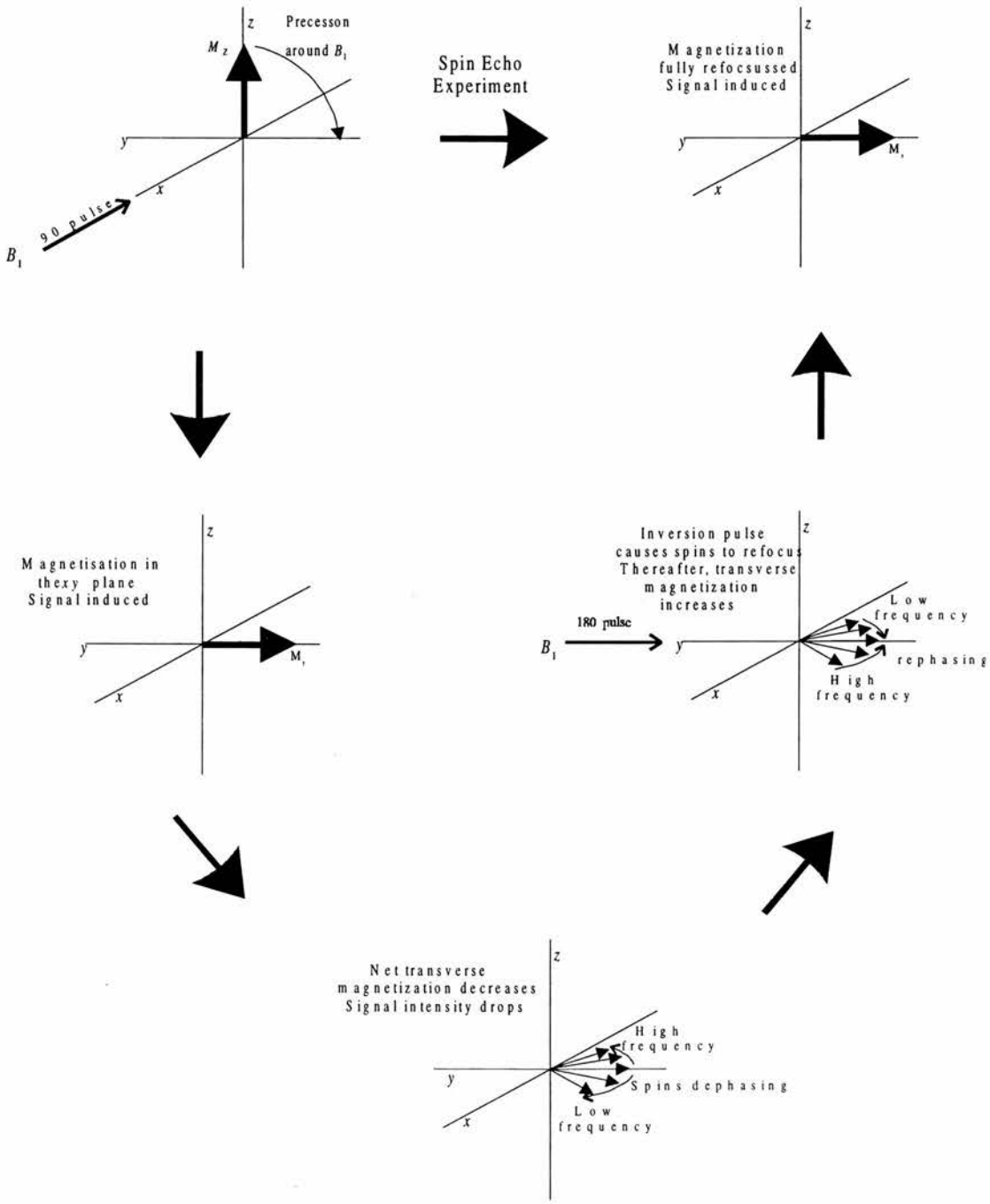

Figure 5 Spin behaviour during transverse relaxation and spin echo

causing a signal which decays to zero (FID) as relaxation takes place. A large part of the relaxation is caused by transverse spin dephasing through the varying local field strength from the inhomogeneous spectrometer magnet. If one applies a π pulse so that the spin system is inverted, the spins refocus as the inhomogeneities are effective in the opposite direction, i. e. the spins precessing faster than the others, that were ahead in the rotating frame have been switched so that they are 'behind' the slower spins and

catching up (Figure 5). As the transverse macroscopic magnetization increases, so does the intensity of the signal induced in the detector coil. The spin echo effect is used extensively in NMR, as shall be seen later.

Coherence

The concept of a *coherence* is important in NMR spectroscopy, particularly in a discussion of pulse sequences. (The definition given here is summarised from Ref 4). In contrast to populations which refer to the occupation of energy levels, coherences refer to the transitions between them. In a set of energy levels characterised by quantum number m_I, the coherences are described by a number, Δm_I, which is the magnitude of the transition and is called the coherence order, p.

Solid-State NMR and Magic Angle Spinning (MAS)

In liquids, the molecules have random orientations and are tumbling rapidly with respect to the timescale of the NMR experiment. The result is that the molecules behave as though they were at one average orientation to the field and the spectrum shows narrow peaks separated by their average chemical shifts.

In contrast, the atoms in solids are held in rigid positions with set orientations to the magnetic field. In a single crystal of material, the orientation will be defined clearly by the positions of atoms within the unit cell and by the packing arrangements of the cells. However, in a powder sample, made up of many crystallites, all orientations of the crystallographic axes and the nuclei will exist. Each orientation has a different component of the nuclear magnetic moment aligned with B_0 and thus, as with chemical shift, the resonant frequency is different. This phenomenon, known as chemical shift anisotropy (CSA), causes a broadening and loss of definition of the resonance peak. Such broadening can render the NMR spectrum very difficult to interpret due to overlapping peaks. In the worst cases, the spectrum appears as a meaningless broad hump with no easily discernible peaks and provides no information.

However, as has been stated, in liquids the geometric factor is averaged to zero due to the rapid tumbling motion of the particles. It is possible to arrange the experimental setup for solid-state NMR experiments to create an equivalent effect. It so happens5 that the Hamiltonian describing the CSA line broadening in solids is dependent on the term $\left(3\cos^2\theta - 1\right)$. If the sample is rotated about an axis at an angle β to the direction of B_0 (Figure 6), it can be shown[6] that the average value of $\left(3\cos^2\theta - 1\right)$ is

$$\left\langle 3\cos^2\theta - 1 \right\rangle = \tfrac{1}{2}\left(3\cos^2\beta - 1\right)\left(3\cos^2\chi - 1\right)$$

In a powder sample, χ takes all possible values yet β is under the direct control of the experimenter and can be varied to scale the broadening effect (Figure 6). At β = 54.7° the $(3\cos^2\theta - 1)$ term becomes zero causing the broadening due to CSA to disappear. Indeed, part of the broadening due to dipolar effects (the change in the local magnetic field as a result of magnetic dipoles on neighbouring nuclei) also has a $(3\cos^2\theta - 1)$ dependency and is reduced by spinning in this way.[5] The narrowing effect is so dramatic that the technique is known as Magic Angle Spinning (MAS), the 'magic angle' being 54.7°.

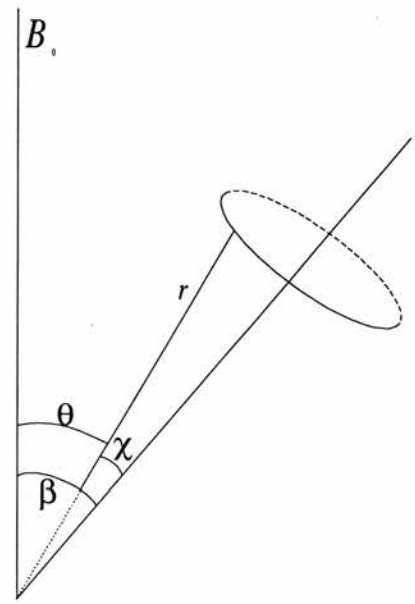

Figure 6 showing the axis for the MAS experiment around which the sample is spun

Quadrupolar Nuclei

It has been assumed so far that the electronic interactions of the nucleus can be ignored when considering its magnetic characteristics. This is true if the nucleus has a spherically symmetric charge. However, many nuclei, some of which are very important in materials science, e.g. ^{27}Al and ^{23}Na, are not spherically symmetric. These nuclei are termed quadrupolar. That such a characteristic should be important to the energies of magnetic reorientations of the nucleus is clear in the example below (Figure 7). However, it should be noted that in such a situation of cylindrical symmetry, turning the orientation by 180° does not change the energy.[7] Therefore, the energies of spin ½ nuclei are not split by quadrupolar interactions.

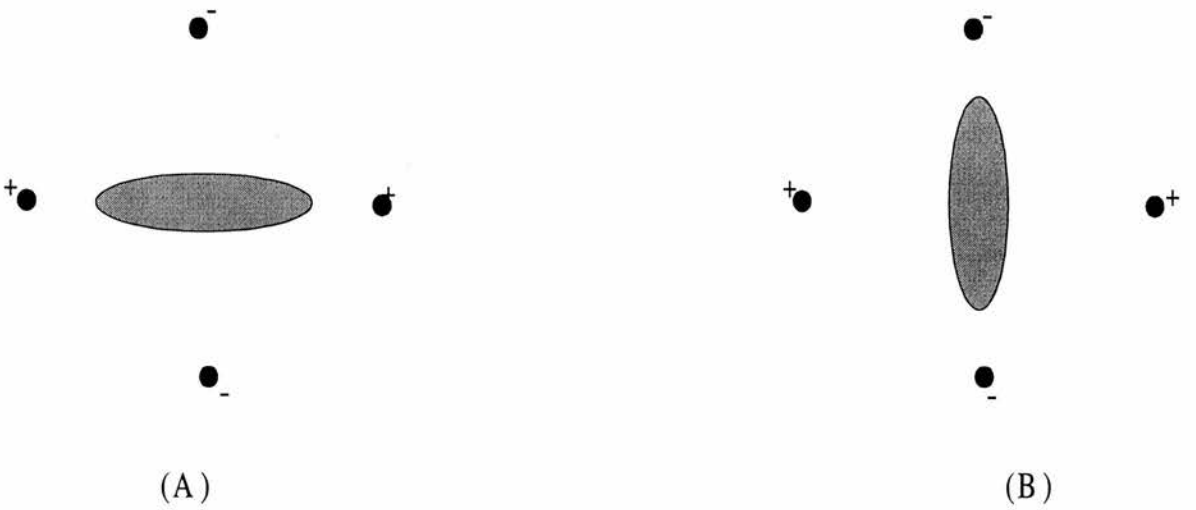

Figure 7 Different orientations of a non-spherical nucleus with neighbouring charges have different energies[7]

In the case of a Zeeman interaction that is much greater (i.e. in a large field) than the quadrupolar effect, the Hamiltonian describing the effect is,[8]

$\mathbf{H} = \mathbf{H}_Z + \mathbf{H}_Q$, with

$\mathbf{H}_Z = -\nu_L m_I$

where ν_L is the Larmor frequency, perturbed by the quadrupolar Hamiltonian and

$$\mathbf{H}_Q = -\nu_Q(\theta,\varphi)\left[2m_I^2 - m_I(m_I+1)\right]$$

where ν_Q is the quadrupolar frequency and is given by[8]

$$\nu_Q(\theta,\varphi) = \frac{e^2qQ}{h}\frac{1}{2S(S-1)}\frac{\left(3\cos^2\theta - 1 + \eta\sin^2\theta\cos 2\varphi\right)}{2}$$

and θ, φ are the angles that map the principal axes of the quadrupolar interaction into the laboratory coordinate system, η is the asymmetry parameter[a] and e^2qQ/h is the quadrupolar coupling constant of the particular nuclear environment in question.

---

[a] The asymmetry parameter is a measure of the degree to which the nuclear electronic field interaction with it's surroundings is non-axially symmetric. It can be defined from a slightly different expression of the quadrupole Hamiltonian, in terms of potentials, as[7]

$$\eta = \frac{V_{xx} - V_{yy}}{V_{zz}}$$

where $V_{\alpha\alpha}$ are the potential tensors in the principal axis system of the quadrupolar interaction. Also, defined in this way is the quadrupolar coupling constant $eq = V_{zz}$

First-order effects of the quadrupolar perturbation leave the magnitude (equivalent to the absorption frequency) of the central Zeeman transition ($+\frac{1}{2} \leftrightarrow -\frac{1}{2}$) unaffected.[9] However, second-order quadrupolar coupling effects must be taken into account also. These interactions can cause broadening of the solid-state NMR lineshape of several kHz making resolution of chemically inequivalent sites very hard or impossible.[7,10] As with other broadening effects such as dipole-dipole interactions and chemical shift anisotropy (CSA), the second-order quadrupolar broadening can be reduced by spinning the sample at an angle β to the field B_0. In such circumstances, the time-averaged NMR frequency is given by[10]

$$\nu_{-\frac{1}{2}\leftrightarrow+\frac{1}{2}} = \frac{\omega_Q^{\,2}}{\nu_L}\left[S(S+1)-\frac{3}{4}\right]\left[A_0 + 8A_2(\theta,\varphi)P_2(\cos\beta) + 8A_4(\theta,\varphi)P_4(\cos\beta)\right]$$

where S is the spin angular momentum quantum number, $\hbar\omega_Q$ is the quadrupole coupling constant, ν_L is the Larmor frequency, A_0 is a constant proportional to the isotropic chemical shift, $A_2(\theta,\varphi)$, $A_4(\theta,\varphi)$ are orientation-dependent functions (again, θ and φ are angles mapping the principle axis system of the quadrupolar interaction onto the laboratory frame – of course, in a powder, θ and φ sample take all possible values), and the scaling factors P_2, P_4 are the second- and fourth-order Legèndre polynomials. The expanded polynomials are[11,12]

$$P_2(\cos\theta) = \frac{1}{2}\left(3\cos^2\theta - 1\right)$$

and

$$P_4(\cos\theta) = \frac{1}{8}\left(35\cos^4\theta - 30\cos^2\theta + 3\right)$$

Inspection of the above expression (Figure 8) shows that there is no angle which simultaneously satisfies

$$3\cos^2\theta - 1 = 0$$

$$P_2(\cos\theta) = 0$$

$$P_4(\cos\theta) = 0$$

Thus it is impossible to remove completely the second-order quadrupolar coupling and anisotropic broadening from chemical shift and dipolar interactions by spinning the sample at one angle. MAS does partially average the broadening peaks with a residual peak width proportional to ν_q^2/ν_L, where ν_q^2 is the quadrupolar frequency and ν_L is the Larmor frequency.[13] Thus increasing the field strength also acts to narrow the line shape and MAS serves to reduce the quadrupolar broadening by a factor of 3-4.

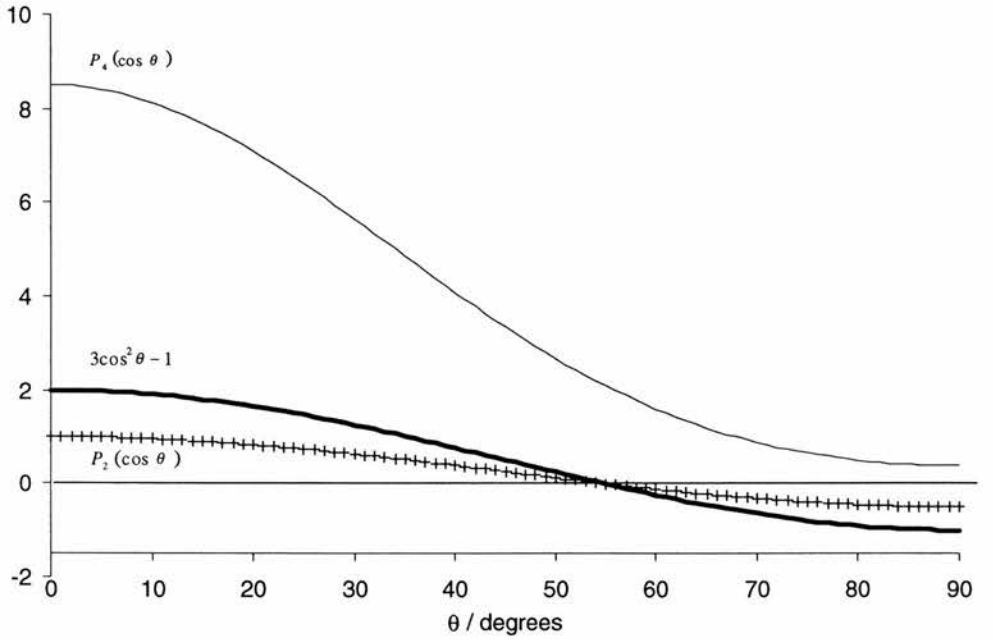

Figure 8 Plot of the angular dependencies of various parts the Hamiltonian for quadrupolar nuclei.

Although the quadrupolar broadening cannot be removed completely through normal magic angle spinning, two techniques do achieve this by taking further advantage of the angular dependence of the quadrupolar interaction. The first, double rotation (DOR), involves spinning the sample using two rotors. The inner rotor spins the sample on one axis with respect to the outer which spins on another axis. The angles of the rotation axes must satisfy the relationships[13]

$$P_2(\cos\beta_1) = 0 \quad (\beta_1 = 54.7°)$$
$$P_4(\cos\beta_2) = 0 \quad (\beta_2 = 33.6° \text{ or } 70.2°)$$

Unfortunately, there are several problems with this approach, mostly in the technical aspects of its application. It is difficult to create a rotor setup that allows fast rotation of the inner rotor within an object that is itself revolving. Even if this has been achieved, the outer rotor usually suffers from slow spinning speeds due to the angular momentum of the inner rotor which tends to work against the outer's motion, rather like a gyroscope.[13] Another disadvantage of this technique is that it removes the broadening from the central transition peak but, in the process, loses all the information available from the quadrupolar interactions.

The second technique is that of dynamic angle spinning (DAS) during which the sample is spun consecutively at two different angles, β_1 and β_2, for durations t_1 and t_2 respectively, such that the sum

$$[P_2(\cos\beta_1)t_1, P_4(\cos\beta_1)t_1] + [P_2(\cos\beta_2)t_2, P_4(\cos\beta_2)t_2] = [0,0]$$

is satisfied.[10] This technique is generally superior to DOR since it is two-dimensional in nature such that, broadly speaking, the isotropic information on one axis is separated from the quadrupolar information on the other, but not lost. Also, since only one rotation axis is used at any one time, it is much simpler to achieve fast rotation speeds allowing its applicability to a wider range of materials.[13] However, although it has been used successfully to study quadrupolar nuclei in materials such as NaC_2O_4, Na_2SO_4 (Mueller et al[14]) and the naturally occurring zeolite, stilbite[15] it does suffer from technical difficulties caused by the necessity to flick the rotor axis from one angle to another. Such a manipulation must be performed thousands of times per experiment with great accuracy and on extremely short timescales (since the spin-lattice relaxation-time must be slow compared to the flipping time for satisfactory FIDs to be collected, the interval for the change from β_1 to β_2 must be of the order of 40 ms[13]).

The Multiple-Quantum Technique

Recently Frydman and Harwood *et al*[10] proposed a new method for separating the isotropic and anisotropic information in the spectra of half-integer spin nuclei with quadrupolar broadening. It was their idea to observe other transitions than the central ½↔-½. As the quadratic form of the quadrupolar Hamiltonian predicts that $-I \leftrightarrow +I$ transitions are all free of first-order quadrupolar broadening, the information from coherences of magnitude > ±1 will not be significantly worse than that from unitary processes. In addition, the experimenter can choose from the range of coherences available thus gaining another degree of freedom with which to refocus the anisotropic effects of the quadrupolar interaction. A generalised expression for the time-averaged frequencies involving the spin quantum number is[10]

$$\nu_{-\frac{1}{2}\leftrightarrow+\frac{1}{2}} = \frac{\omega_Q^{\,2}}{\nu_L}\left[S(S+1) - \tfrac{3}{4}\right]\left[A_0 C_0^S(I) + 8A_2(\theta,\varphi)C_2^S(I)P_2(\cos\beta) + 8A_4(\theta,\varphi)C_4^S(I)P_4(\cos\beta)\right]$$

where most of the parameters are the same as above (in the expression for DAS). The $C_n^S(I)$ coefficients however, depend on the transition and the spin of the nucleus under consideration. The foundation of the multiple-quantum technique, as Frydman and Harwood *et al*[8,10] realised, is that the $C_n^S(I)$ coefficients (Table 1) are different for differing coherence orders (the particular $-I \leftrightarrow +I$ transition). Thus, the expression, analogous to the DAS situation, that needs to be satisfied for the MQ experiment is

$$[C_2^S(I_1)P_2(\cos\beta)t_1, C_4^S(I_1)P_4(\cos\beta)t_1] + [C_2^S(I_2)P_2(\cos\beta)t_2, C_4^S(I_2)P_4(\cos\beta)t_2] = [0,0]$$

where t_1 and t_2 are now evolution times of the two coherences associated with $C_n^S(I_1)$ and $C_n^S(I_2)$ respectively (where n = 2,4), rather than the dwell time at each rotation angle, as in DAS. The most advantageous solution to this equation chooses β to be the 'magic-angle' (54.7°) as this not only removes CSA and dipolar broadening but also zeroes the P_2 term so that only 4th rank broadening need be considered. The important quantity then becomes the ratio $C_4^S(I_1)/C_4^S(I_2)$ (termed the MQMAS ratio by Brown and Wimperis[9])

Table 1 The coefficients (zero-, second- and fourth- rank) of the quadrupolar evolution for various transitions in spin $^3/_2$ and $^5/_2$ nuclei (taken from Ref 10).

Spin (S)	I [transition ($-I \leftrightarrow +I$)]	C_0	C_2	C_4
$^3/_2$	$^1/_2$	3	24	54
$^3/_2$	$^3/_2$	-9	0	-42
$^5/_2$	$^1/_2$	8	64	144
$^5/_2$	$^3/_2$	6	120	228
$^5/_2$	$^5/_2$	-50	-40	-300

Hence, to perform such an experiment, one uses a pulse-sequence as shown in Figure 9. It is important that the pulse lengths are optimised for the excitation step and for the other parts of the various different experiments (see page 23 for modified experiments). Free induction decays (FIDs) are collected during t_2 for all the 6 phases needed to select the required coherence pathway and summed. This procedure is repeated for values of t_1 incremented over a suitable range. The data set is an array of spectra in t_2, one for each value of t_1. A 2-dimensional Fourier transform is applied giving a 2-dimensional frequency plot. As a result of the residual anisotropic broadening, particular well defined chemical and quadrupolar environments give a peak spread along a ridge whose slope is the MQMAS ratio. The projection of the 2-D plot onto an axis perpendicular to the ridges gives the isotropic spectrum, the orthogonal axis being the quadrupolar frequencies. Often, to make this process easier, a shearing transformation is applied such that the isotropic axes are parallel to f_1 and f_2. However, although the isotropic projections remain unaffected by shearing, it can have a detrimental effect on the 2-dimensional line shape such that the extraction of accurate η and e^2qQ/h values by line shape fitting becomes difficult.[9]

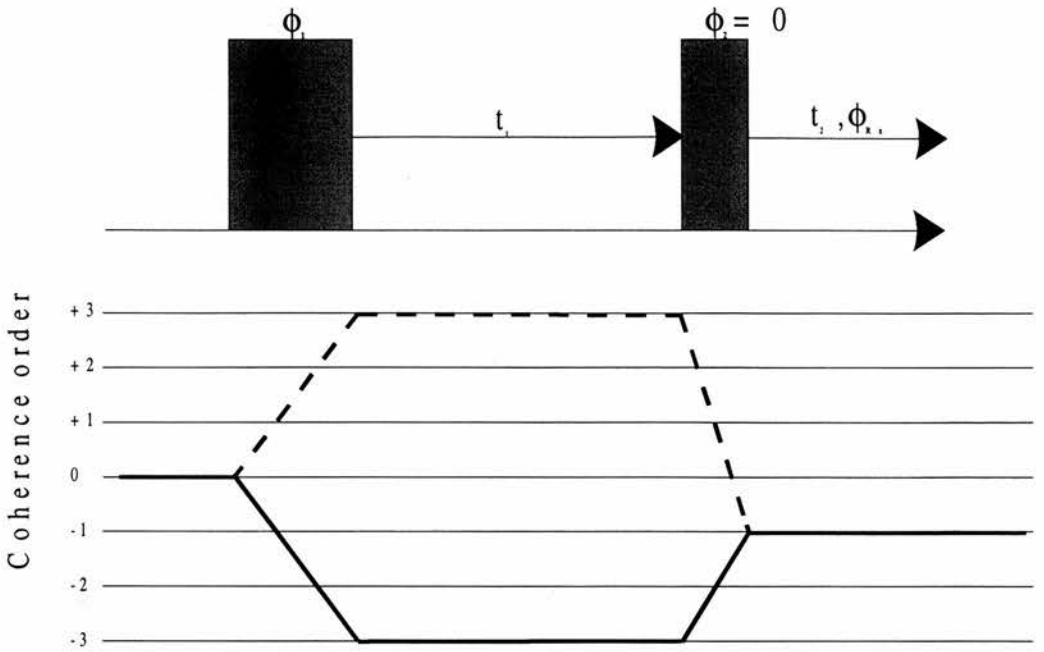

Figure 9 Diagram showing coherence pathway and two-pulse sequence for Frydman's original 3Q experiment.[8] The dotted line indicates the antiecho pathway. The evolution of the multiple quantum coherence in t_1 is refocused in t_2.The phase cycles for the first pulse and the receiver are

ϕ_1 = **0°, 60°, 120°, 180°, 240°, 300°** ϕ_{Rx} = **0°, 180°, 0°, 180°, 0°, 180°**

MQMASNMR Pulse sequences

As with other applications of NMR, the pulse sequence depends upon the exact method that one wants to use in performing the experiment. As the technique matures, further refinements to the basic methodology are made, increasing the choice of pulse sequences. In their original experiment, Frydman *et al*[8] recorded triple-quantum spectra of ^{23}Na in various salts, by using a single pulse excitation and a single pulse triple- to single-quantum conversion pulse (Figure 9).[a] This sequence was adopted after comparison with a two pulse excitation sequence demonstrated the greater efficiency of a single pulse in producing triple-quantum coherence (TQC). Another conclusion of the investigation into the excitation step was the importance of using the greatest possible rf power during ϕ_1. The efficiency of coherence transfer depends on the quadrupolar coupling constant of the nucleus. Increasing the power of the irradiation extends the range of quadrupolar environments that can be excited into multiple quantum coherence (MQC).

---

[a] Since each pulse is likely to cause a range of coherences, standard phase cycling[4] was used to select that pathway required in order to satisfy the zero sum mentioned in the previous section.

More recent work by Frydman and co-workers[16] has shown, through extensive numerical modelling and experimental verification, that the most efficient option for generating triple quantum coherence (TQC) and quintuple quantum coherence (QQC) is the use of a two-pulse excitation sequence with the interval between the pulses, set to zero. Such a mixed phase pulse had a calculated efficiency over 30% greater than that obtained previously and only a few percent short of the theoretical maximum efficiency.

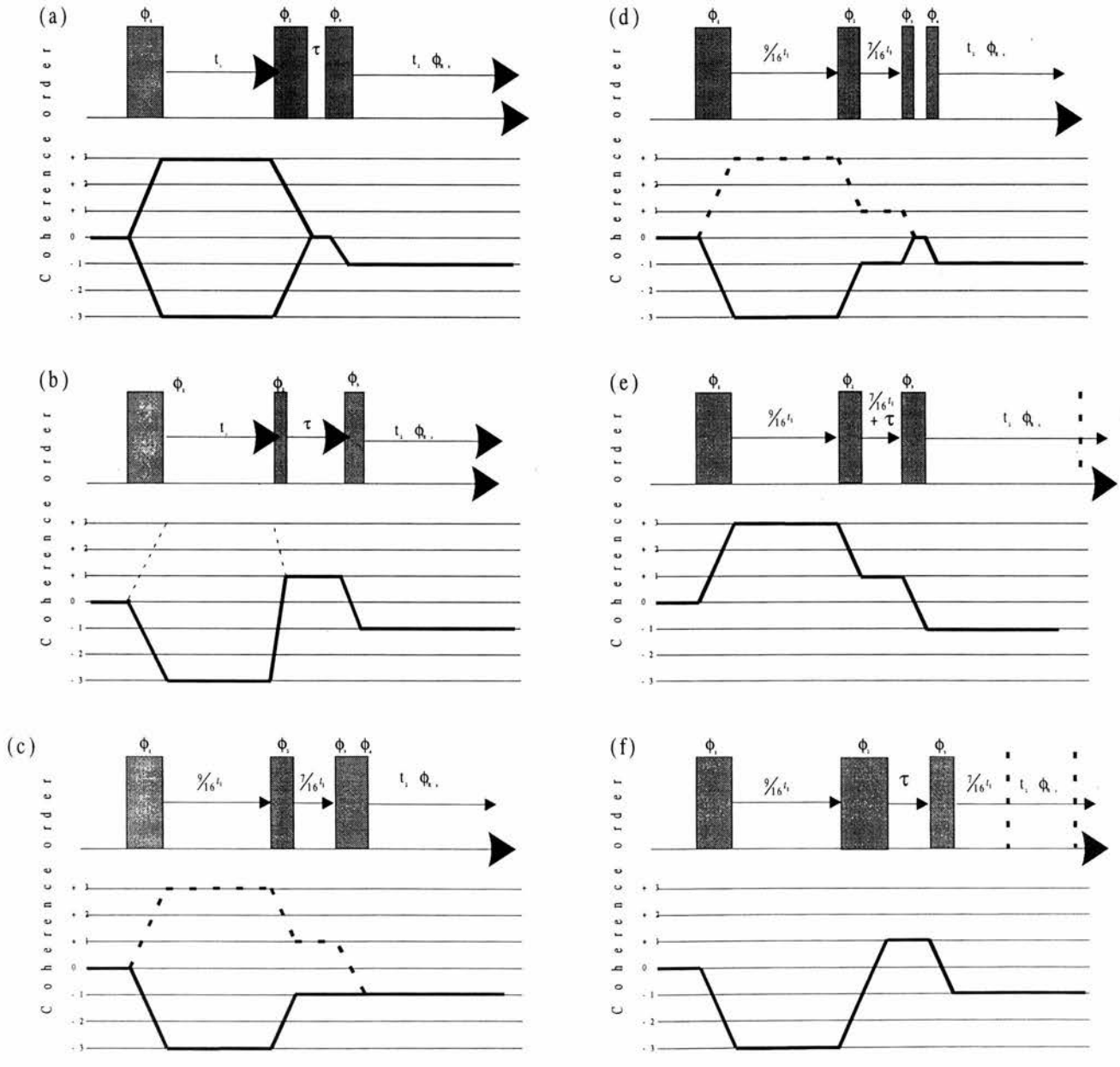

Figure 10 Pulse sequences and coherence pathways for various MQMASNMR experiments

(a) Simple amplitude-modulated with z filter
(b) Whole-echo amplitude-modulated with z filter
(c) Amplitude-modulated, split t_1 with no z filter
(d) Amplitude-modulated, split t_1 with z filter
(e) Phase-modulated, split t_1 one pathway
(f) Phase-modulated, split t_1 other pathway

Brown and Wimperis[9] described several modifications to the original 'simple phase-modulated' experiment of Frydman *et al.*[8] The problem with the simple phase-modulated technique is that it produces 2-dimensional lineshapes that are 'phase-twisted' that is, they are a mixture of absorption and dispersion peaks. As the aim of the MQMAS experiments is to obtain highly resolved, isotropic spectra free of ambiguities resulting from anisotropic quadrupolar interactions, phase-twisted peaks are undesirable. Also, the presence of the residual anisotropic broadening term (the second rank term having disappeared under the influence of MAS) causes the peaks to be stretched along a ridge whose gradient is equal to the MQMAS ratio. The modifications to the simple phase-modulated technique described by Brown *et al*[9] aim for greater ease of interpretation of results through the production of spectra containing only pure absorption-mode peaks. Also, they have found that it is possible to refocus the anisotropic quadrupolar interactions remaining such that the broadening no longer takes place along a ridge with a gradient of the MQMAS ratio but parallel to the f_2 axis.

The various modified pulse-sequences are simple amplitude-modulated, whole-echo phase-modulated, whole-echo amplitude-modulated, split t_1 amplitude-modulated and split t_1 phase-modulated. Examples of the pulse sequences and coherence transfer pathways are shown in Figure 10. The ideas and methods of the modifications are summarised below (all the information below on the various modifications to the pulse sequence is taken from ref 9 unless stated otherwise).

Echoes and half-echoes

The MQMAS technique works by refocusing the 4th rank anisotropic broadening (the 2nd rank broadening is zeroed by MAS) using the MQMAS ratio, as explained above. In the original experiment and in all those below, except split-t_1, the refocusing occurs during t_2. Since the longer the anisotropic broadening is allowed to evolve, the longer it takes to refocus, this results in there being an echo effect such that the time at which the signal appears in t_2 depends upon t_1. Therefore the echo moves to greater t_2 as t_1 is increased. However, the anti-echo (the coherence pathway whose combination of broadening coefficients = – [MQMAS ratio]) moves in the opposite direction with increasing t_1. Both the echo and anti-echo are centred on $t_2 = 0$ when $t_1 = 0$, such that only half of each echo is observed (from the maximum intensity of the FID envelope to zero). As t_1 is increased the echoes move away from each other, the anti-echo appearing at negative t_2 values.

Simple amplitude-modulated experiment : pure absorption mode lineshapes are obtained if the echo and anti-echo are combined with equal amplitude. As the amplitude of different jumps in coherence order differ for a particular pulse, the simplest way to arrange that each pathway has the same amplitude is to use a z filter in which the

symmetry of the pathway ensures identical intensities.[17] In order to restore the sign discrimination between the echo and antiecho pathways, it is necessary to use TPPI.[a]

Whole-echo experiments : this technique uses an inversion pulse to create a spin echo that moves the effective origin of t_2 to a later time. The echo itself appears at a time $\tau + C_M t_1$ and the antiecho at $\tau - C_M t_1$ where τ is the delay of the spin echo (see Figure 10) and C_M is the MQMAS ratio (in the case of coherence order, p = ±3, for spin $3/2$ nuclei, MQMAS ratio = $7/9$). The phase-modulated experiment involves collection of the echo or antiecho alone. However, since the antiecho moves backwards in t_2 with increasing t_1, the latter experiment requires a much greater delay time, τ, than for the echo experiment to ensure that the whole antiecho is within the time window for all values of t_1. An amplitude modulated experiment is possible but also suffers from the longer delays. Such an increase in collection time causes greater signal loss due to relaxation processes, giving a smaller signal to noise ratio (S/N).

The technique is possible because of a property of hypercomplex 2-dimensional Fourier transforms. If a signal's real part is symmetric and the imaginary anti-symmetric, the resulting spectrum has a real, purely absorptive part and an imaginary part that is zero. However, this relies on the assumption that the homogeneous broadening is dominated by the inhomogeneous broadening (due to long term defects in the magnetic field and, therefore subject to refocusing), otherwise the symmetry of the signal is lost and mixed phase frequency domain peaks are obtained. Another advantage of the hypercomplex 2-dimensional Fourier transform is that even unequal combination of the echo and anti-

---

[a] TPPI – time proportional phase incremention[18] – is a procedure by which the sign of the coherence order may be detected by applying a frequency shift to the f_1 dimension. This is done by incrementing the phase of the first pulse (or preparative pulse) in a sequence proportional to t_1. The procedure has the effect of shifting signals from coherence orders of different signs in opposite directions within the f1 dimension. The frequency shift is $p\omega^{(TPPI)}$ where p is the coherence order (hence the sign dependent frequency shift) and

$$\omega^{(TPPI)} = \frac{\pi}{2N\Delta t_1}$$

where N is the fractional frequency shift (the number of steps to take in changing the phase by 2π) and Δt_1 is the incremental jump in t_1, the difference in between sampling points.[18] The phase change should not be confused with the phase cycles used for selecting coherence pathways. The increment of phase changed is applied to the phase cycle as a whole.

echo in the amplitude-modulated experiment results in pure absorption-mode line shapes. This avoids the time-consuming and difficult process of equalising the intensity of the two opposite pathways or of using a *z* filter.

The advantage of this technique is that it not only gives pure absorption mode lineshapes, but also causes the anisotropic broadening ridges to be parallel to f_1 and f_2, making a shearing transformation unnecessary. The disadvantage of this technique is that a t_1 dependent phase correction must be applied to the signal. Unfortunately, suitable software to do this is not available on our instrument making this technique impossible.

Split t_1 experiment : this technique splits t_1 into two periods, in the MQMAS ratio, during which MQ coherence followed by SQ are allowed to evolve. Thus the refocusing of the anisotropic broadening that normally occurs during t_2 takes place at the end of t_1. This has the result that the echo always occurs at the same time in t_2 and this allows smaller collection times and better S/N.

This technique also can be implemented as phase- or amplitude –modulated (Figure 10). The amplitude-modulated experiment is best performed using a *z* filter as the simplest way to ensure equal intensity in the combination of the echo and antiecho. Also, TPPI is needed to restore sign discrimination. The phase-modulated arrangement has two possible coherence pathways and one may judge the most advantageous on the basis of which has the most efficient coherence transfer steps (generally the smallest steps are most efficient). Both modes of implementation give peaks unbroadened by anisotropic effects and, therefore, the isotropic axes are coincident with f_1 and f_2.

MQMAS Structural Studies on Aluminium Containing Phosphates and Phosphonates

Of all the various pulse sequences outlined above, the particular method chosen for this work was the simple amplitude-modulated experiment with *z*-filter. Although the more sophisticated experiments might have given superior results, they require more sophisticated data processing techniques than were available on our spectrometer. The simple amplitude-modulated *z*-filtered experiment (Figure 10) gives pure absorption mode peaks although the anisotropic broadening does have a slope equal to the MQMAS ratio. It is necessary to optimise the conversion pulses for the maximum sensitivity, although in material with a range of aluminium environments it is impossible to excite all species at their optimum level.

The purpose of this work has been to utilise the MQMASNMR technique for ^{27}Al in order to further characterise both new materials and particular aspects of known materials. Identifying the number of unique chemical sites in a material is one manner in which NMR is useful during *ab initio* structural studies and the elucidation of subtle aspects of solids' behaviour (see the Solid-state Transformation of AlMePO-β, Chapter 4). Also, SQMASNMR can give information concerning the local environments of the species concerned, in terms of their coordination and symmetry. However, through the access it gives to the isotropic quadrupolar information, MQMASNMR has the potential to provide much more detailed local information than traditional solid-state methods. Unfortunately, there is little, if any, information in the literature concerning the interpretation of quantities such as the asymmetry parameter, η, and the quadrupolar coupling constant, e^2qQ/h, in terms of chemical structure. Therefore, it is also the purpose of this work to contribute towards the development of a database of information from which conclusions about such interpretation might be drawn, either through mathematical analysis or, perhaps, empirically.

This chapter details the ^{27}Al MQMAS results from several materials of layered and 3-dimensional structures. The results are discussed in light of the known structures of these materials, when possible, and information from other characterisation techniques, such as X-ray diffraction (XRD), thermal gravimetric analysis (TGA) and TGA with mass-spectrometry (TG-MS). The following materials have been studied :

(1) Aluminium methylphosphonate-β (AlMePO-β)
(2) Al[33H]MePO - A mixed methylphosphonate and phosphite phase where [33H] corresponds to 33% of phosphite in the synthesis gel (see Chapter 6 for further details)
(3) Aluminium acetophosphonate (AlAcPO) a layered material[19] in which the organic

group attached to the phosphorus is an acetate group rather than a methyl group (see Chapter 6 for further details)

(4) Aluminium methylphosphonate-1 (AlMePO-1)[20]

(5) Aluminium methylphosphonate-2 (AlMePO-2) – novel double layered material (see Wright *et al*[21] and Chapter 3 for details of incomplete structure characterisation)

(6) Aluminium methylphosphonate-3 (AlMePO-3) – novel material likely to have 3-D structure (see Wright *et al*[21] and Chapter 3 for details of incomplete structure characterisation)

(7) Recently synthesised magnesium aluminium phosphate (MAPO) called STA-1 (see Noble *et al*[22] for details)

(8) Novel MAPO known as STA-2 (see Noble *et al*[23] for details)

(9) Aluminium phosphate (AlPO-31) of structure type ATO in its calcined form

In general, the materials were used as-prepared (see Experimental for details) but the STA-2 and AlPO-31 samples were studied after dehydration and calcination also. It was found that both the XRD patterns and the NMR spectra underwent considerable changes on these treatments and attempts are made to elucidate the processes occurring.

Experimental

Synthesis and sample preparation

General

Reagents were obtained from Aldrich and used without further purification unless stated otherwise. The general procedure was followed in all cases except for AlPO-31, STA-1 and STA-2 (see below). The starting materials, consisting of sources of aluminium, phosphate or phosphonate, and a structure directing agent, were mixed with water in the given proportions (Table 2) and stirred until the gel was homogeneous. The gel was sealed inside a PTFE lined stainless steel autoclave and heated at the given temperature for the reported time. Products were filtered, washed with 40-60 cm^3 distilled water and dried in air at 60°C. Product identity and purity were confirmed by X-ray powder diffraction. See also Table 3 for further synthesis notes and original references.

AlPO-31

This material was prepared according to the procedure of Zubowa *et al*[24] from pseudo-boehmite (75 wt% Al_2O_3, 25 wt% H_2O), 85 wt% H_3PO_4 and H_2O in the presence of $HN(CH_2CH_2CH_3)_2$ as the structure directing agent. The amounts of reagents used were 4.075 g pseudo-boehmite (30 mmol), 5.75 g H_3PO_4 (50 mmol), 7.65 g dipropylamine (76 mmol) and 1.1 mol water, giving a ratio of Al:P:H_2O:R in the synthesis gel 1:0.83:18.3:1.25 where R is the amine. To prepare the gel the phosphoric acid was mixed with 10.65 cm^3 H_2O to which the pseudo-boehmite was added and stirred for 2 hours. The remaining water, 7.15 cm^3 was added and stirred until homogeneous followed by the amine and a further 2 hour period of mixing (pH 8-9). The gel was left for 43 hours without stirring after which it was put into a Teflon lined stainless steel autoclave (50 cm^3) and heated at 200 °C for 24 hours. The product was filtered, washed with distilled water (~ 60 cm^3) and dried in air at 60 °C. 2.6 g of material were recovered from this procedure (~ 43 % maximum possible yield).

STA-1 and STA-2

These materials were synthesised by Graham Noble according to his procedures published in refs 22 and 23. The structure directing agents were dicationic alkylammonium hydroxides prepared in this laboratory by Graham Noble.

Table 2 Synthesis conditions for the various samples

Material	Mg source	Al source	P source	R	ratio [Mg]Al:P:R:H_2O	Gel pH	Temp / °C	t / hr
AlMePO-β	-	$Al(OH)_3$	$CH_3P(O)(OH)_2$	1,4-dioxane	1:1.5:0.5:40	3-4	160	48
AlAcPO	-	$Al(OH)_3$	$HO_2CCH_2P(O)(OH)_2$					
AlMePO-1	-	$Al(OH)_3$	$CH_3P(O)(OH)_2$	-	1:1:40	4	160	50
AlMePO-2	-	$Al(OH)_3$	$CH_3P(O)(OH)_2$	-	1.5:1:52	4	220	48
AlMePO-3	-	$Al(OH)_3$	$CH_3P(O)(OH)_2$	-	1:1.5:40	3-4	220	72
Al[33H]MePO	-	$Al(OH)_3$	$CH_3P(O)(OH)_2$ $HP(O)(OH)_2$	1,4-dioxane	1:1.5(1:0.5):40	2.5	160	120
AlPO-31	-	pseudo-boehmite	H_3PO_4					
STA-1	magnesium acetate	$Al(OH)_3$	H_3PO_4	see text	[0.1]:0.9:1:0.4:40	7	190	48
STA-2	magnesium acetate	$Al(OH)_3$	H_3PO_4	see text	[0.1]:0.9:1:0.4:40	7	190	48

Table 3 Notes on sample preparation

Sample	Note
AlMePO-β	prepared according to the procedure of Maeda *et al*[25]
AlMePO-1	prepared according to published procedure;[1] See Chapter 3 for further details
AlMePO-2	prepared according to published procedure;[21] See Chapter 3 for further details
AlMePO-3	prepared according to published procedure; [21] See Chapter 3 for further details
Al[33H]MePO	see ref [26] and Chapter 6 for further details
AlPO-31	prepared according to published procedure[24]
STA-1	synthesised by G. W. Noble[22] at St Andrews, University
STA-2	synthesised by G. W. Noble[23] at St Andrews, University

Heat Treatments

Spectra were run on samples as-prepared, dehydrated and calcined, termed, for example in the case of AlPO-31, as-prepared AlPO-31(A), dehydrated AlPO-31(D) and calcined AlPO-31(C) respectively. The heat treatments used were; dehydration : 8 hrs at 200 °C in dry N_2; calcination 8 hrs at 400 °C in dry N_2 followed by 8 hrs at 550 °C in O_2 and allowed to cool at the natural rate.

Instrumentation

Most of the NMR experimental work was performed by, or with the aid of, Dr Tunstall, University of St Andrews. MASNMR and MQMASNMR experiments were run on a Bruker MSL500, at 11.75 T with rf field of approximately 0.01 T (for the maximum power pulses). The pulse sequence used was the simple amplitude-modulated experiment, as described by Brown and Wimperis[9] (summarised above), with a *z* filter[17] to ensure that the echo and antiecho were combined with equal amplitude (Figure 10). The pulse lengths were optimised giving typical values of 4, 1.5 and 14 μs for the three pulses respectively. The last pulse has a lower power (~10%) than the first two. A typical range for the 2nd dimension (t_1) was 256 steps of 5 μs each. ^{1}H decoupling was not used in most cases as there was usually no benefit to be gained from it. Explicit mention of any exceptions to this will be made when necessary.

Table 4 Phase cycles for the pulses and receiver in the simple amplitude-modulated experiment with *z* filter.

Pulse 1 K0 +	0	36	72	108	144	180	216	252	288	324
Pulse 3 10% power	0	0	0	0	0	0	0	0	0	0
	90	90	90	90	90	90	90	90	90	90
	180	180	180	180	180	180	180	180	180	180
	270	270	270	270	270	270	270	270	270	270
Receiver phases	+X	-X	+X	-X	+X	-X	+X	-X	+X	-X
	+Y	-Y	+Y	-Y	+Y	-Y	+Y	-Y	+Y	-Y
	-X	+X	-X	+X	-X	+X	-X	+X	-X	+X
	-Y	+Y	-Y	+Y	-Y	+Y	-Y	+Y	-Y	+Y

Powder X-ray diffraction was performed on a STOE diffractometer with a linear position sensitive detector covering 6° in 2θ and employing Ge monochromated Cu-Kα$_1$ radiation (λ=1.54056 Å). Samples were prepared by mounting in a glass capillary or between two sheets of Mylar as rotating discs in the X-ray beam.

Heat treatments were performed in a silica glass tube in a tube furnace. Samples were heated at a rate of 10°C min^{-1} in all cases. The temperature in the furnace was measured at the sample using a K-type thermocouple and found to between 3 - 4°C higher than the setpoint temperatures over the range used. Thermal gravimetric analysis (TGA) was performed on a TA Instruments SDT 2960 Simultaneous DTA-TGA. Heating rates were 10 °C min^{-1} and inert atmospheres were used in all cases.

Results and Discussion

Single quantum ^{31}P and ^{27}Al, and 5Q MASNMR ^{27}Al spectra were run on the samples listed above (^{31}P data were not collected for all materials, see below). Isotropic chemical shift and the second-order quadrupolar coupling effect (SOQUE) may be calculated[27] from the unsheared plots as follows

$$\delta_{iso} = \tfrac{4}{9}\delta_1 + \tfrac{5}{9}\delta_2$$

$$\text{SOQUE (MHz)} = \left[\frac{e^2qQ}{h}\right]\left[1+\left(\frac{\eta^2}{3}\right)\right]^{1/2} = \left[-\frac{(\delta_1-\delta_{iso})}{6000}\nu_0{}^2\right]^{1/2}$$

where δ_1 and δ_2 are the centres of gravity of the peak in the f_1 and f_2 dimensions respectfully. A summary of the data is provided in Table 5.

Note : since our spectrometer does not have the software to use the MQ results to model lineshapes of the SQ spectrum to extract e^2qQ/h] and η we have in many cases estimated these. The SQ lineshape can often be recognised as coming from a single site with quadrupolar splitting, and a particular SQ shape is only consistent with a range of e^2qQ/h and η values;[a] this range can often be taken with the second-order quadrupolar interaction (SOQUE) value to quantify e^2qQ/h and η.

In assessing and discussing the use of MQMASNMR in the field of aluminium phosphates and phosphonates, the important question is to gauge the extra information that can be gained from this technique as compared to traditional MASNMR. We have run spectra of several materials which we have chosen to range from a simple aluminium phosphate with one aluminium position, through compounds with more

---

[a] The splitting of a ^{27}Al SQ peak (Hz) due to the quadrupolar interaction is related to the quadrupolar coupling constant, e^2qQ/h and asymmetry parameter, η, as follows

$$\Delta\nu = \frac{1}{24\nu_0}\left(\frac{e^2qQ}{h}\right)^2\left\{3-2\eta-\eta^2\right\}$$

where ν_0 is the Larmor frequency and $\Delta\nu$ is the splitting in the powder spectrum, i.e. without sample spinning, which may be estimated from the MAS spectrum splitting by multiplying by 4.

crystallographic sites and hence to the more novel field of phosphonates with a variety of structures.

It should be noted that aluminium chemical shifts fall into three general categories in the type of material studied here; ~40 ± 7 ppm, ~10± 10 ppm and ~ -10 ± 10 ppm which correspond to tetrahedrally coordinated, penta- or hexa- coordinated and octahedrally coordinated respectively.[29] The central region is one in which there is particular ambiguity in assigning the type of aluminium and this usually involves consideration of the chemical context and peak shape.

Aluminium Phosphates

AlPO-31

The structure of calcined AlPO-31 has been well known for some time.[24] It contains one unique aluminium and one phosphorus position, both of which, in common with all microporous AlPOs, are solely tetrahedrally coordinated by oxygen. We have recorded the ^{31}P and ^{27}Al SQ and ^{27}Al 5QMASNMR spectra for three forms of AlPO-31, as-prepared, dehydrated and calcined, known henceforth as AlPO-31(A), AlPO-31(D) and AlPO-31(C).

The SQ ^{27}Al spectrum of AlPO-31(C) shows one peak at 35.4 ppm with FWHH of ~3 ppm. The ^{31}P spectrum shows a similar result having one peak with 29.8 ppm chemical shift. The 5QMASNMR spectrum (Figure 11) simply confirms the assessment of one main aluminium site with isotropic chemical shift of 37.3 ppm. The small peak, S2, is not predicted by the crystal structure and is likely to be due to some decomposition of the material during the calcination. In the absence of the extra resolution of the 5Q technique, this site would not have been detected. Disregarding the very small S2 peak, these observations are exactly as one would expect from the crystal structure of the material. The matching of the number of aluminium and phosphorus environments seems to be a general characteristic of materials containing only tetrahedrally coordinated framework atoms. As such, the phosphorus spectrum provides a useful confirmation to the interpretation of the aluminium spectrum. In this case, the multiple quantum technique is somewhat superfluous in that it provides no new information. The situation for the dehydrated material is the same except that the Al peak has shifted

Table 5 Summary of the 5Q ^{27}Al data. Numbers refer to δ_{iso}:SOQUE(MHz):Rel Pk Height (%). The peak height figure is intended solely as an indication of the relative size of the peaks and should be interpreted quantitatively in any way.

Material	1	2	3	4	5	6	7
AlMePO-β	45.3:2.4:25	43.5:1.9:25	42.7:1.8:25	-17.2:?:25			
AlAcPO	-25.6:7.05:50	-30.5:6.33:50					
AlMePO-1	0.1:6.0:100						
AlMePO-2	10.8:3.1:40	3.1:2.7:40	8.3:1.2:20				
AlMePO-3	44.9:2.5:70	15.5.:1.9:15					
Al[33H]MePO	44.6:2.3:20	43.4:1.9:20	43.0:2.3:20	-14.1:2.3:30	-16.9:1.5:10		
STA-1	49.1:2.8:20	43.5:3.6:40	39.3:2.9:30	8.5:1.5:10			
STA-2(A)	45.6:3.0:30	38.3:1.8:70					
STA-2(D)	45.9:2.9:25	38.6:2.2:70	9.4:1.8:5				
STA-2(C)	43.1:3.1:30	36.2:1.8:70					
AlPO-31(A)	42.5:1.3:17	40.7:0.9:6	37.0:2.4:20	35.5:2.5:17	39.5:2.8:16	15.1:3.2:7	41.8:3.5:17
AlPO-31(D)	38.8:3.8:100						
AlPO-31(C)	37.3:2.6:90	36.8:0.5:10					

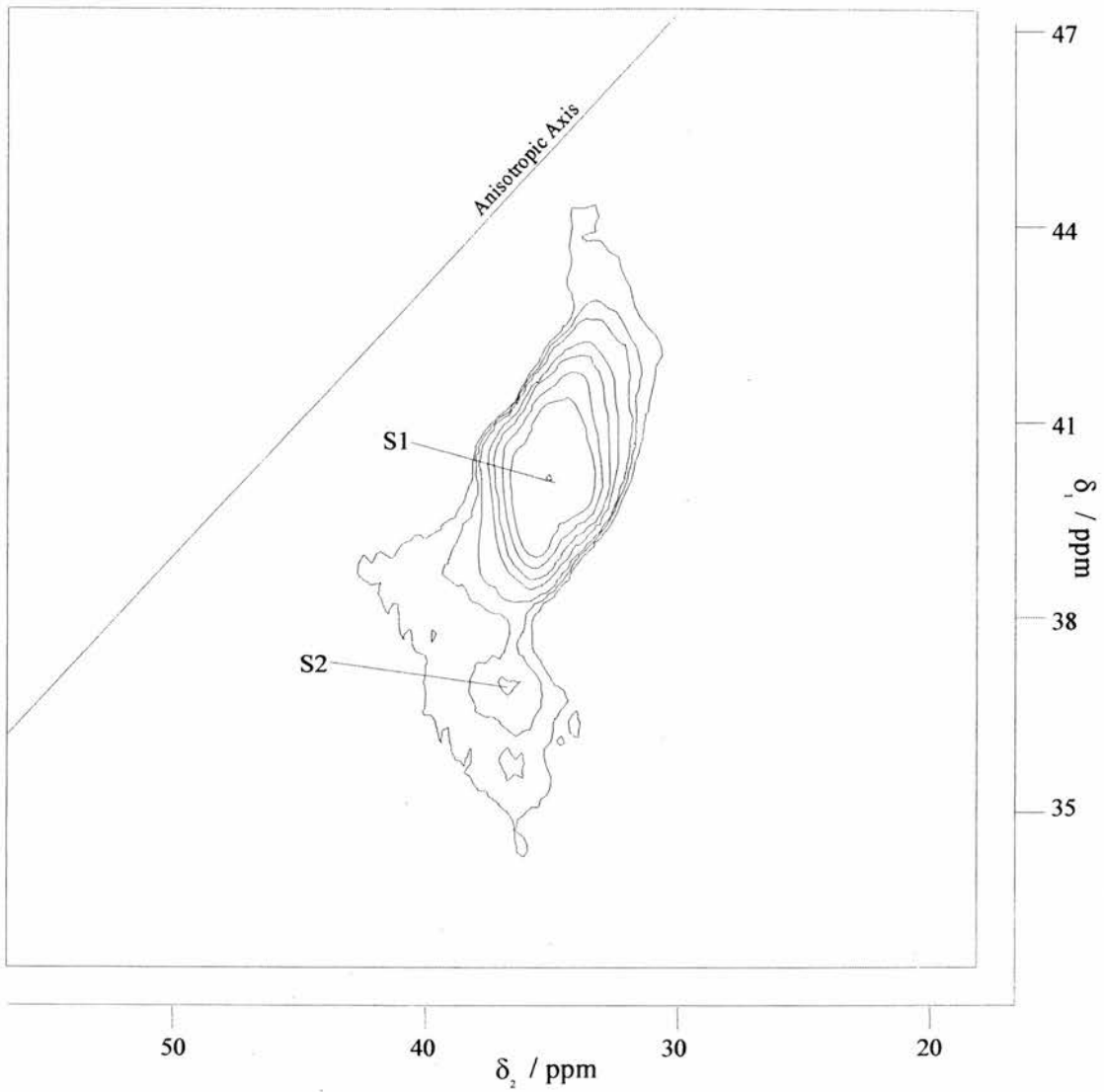

Figure 11 5Q MASNMR spectrum of AlPO-31(C). The stretched appearance of the peak is indicative of a substantial quadrupolar interaction which is confirmed by the δ_1 and δ_2 values.

slightly so that one SQ aluminium resonance appears at 37.4 ppm and one phosphorus at 29.8 ppm (Figure 12). Again the 5Q data (Figure 13) mirrors this with a resonance the isotropic chemical shift of which is 38.8 ppm. The other peaks are a result of spinning side bands or artefacts of a less clear origin (they are identifiable by being stretched along a ridge of the wrong gradient). The multiple quantum data is not needed to assess the presence of one type of site. (Note that the presence of only site at this point, i.e. before the harsh calcination treatment, supports the conclusion that the S2 site in Figure 11 is a result of some decomposition.)

However, the sample of the as-prepared material before any drying or calcination procedure is much more complex. The AlPO-31(A) SQ aluminium spectrums (Figure 14) shows two resolved narrow lines (±2 ppm) at ~ 40 ppm, a broader (8 ppm) composite response around 35 ppm and a weak response at 14 ppm. The resonances centered on 35 ppm and above fall into the tetrahedral region of chemical shift while the

other response, the weakest, is within the ambiguous range often assigned as five coordinate aluminium. The phosphorus spectrum is not well resolved either but can be divided into four responses at –23.0, –24.0 , –27.9 and –31.2 ppm. The peaks that make up the spectrum are considerably overlapped and it is impossible to assess the number of separate environments.

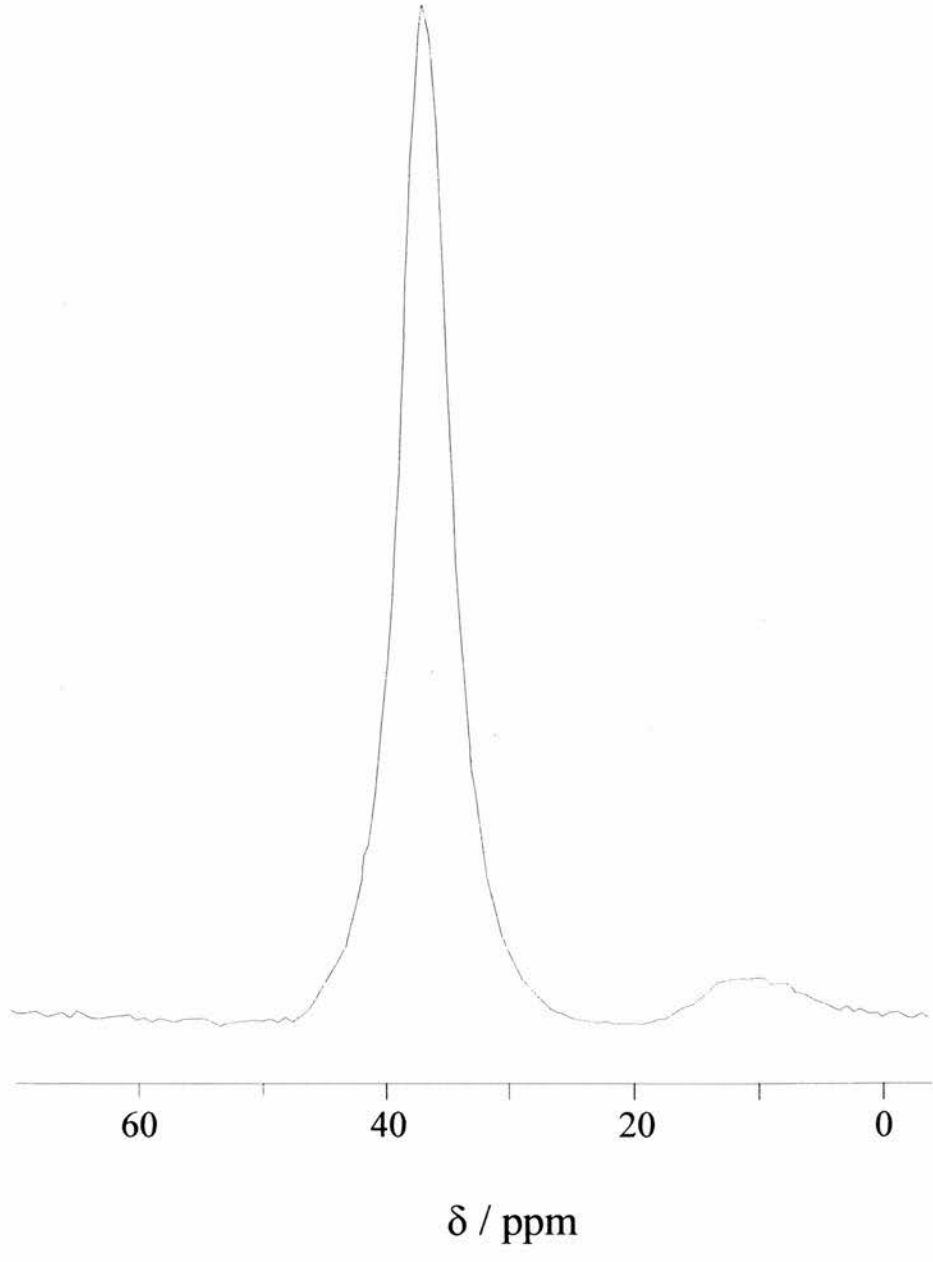

Figure 12 Single quantum ^{27}Al spectrum of AlPO-31(D).

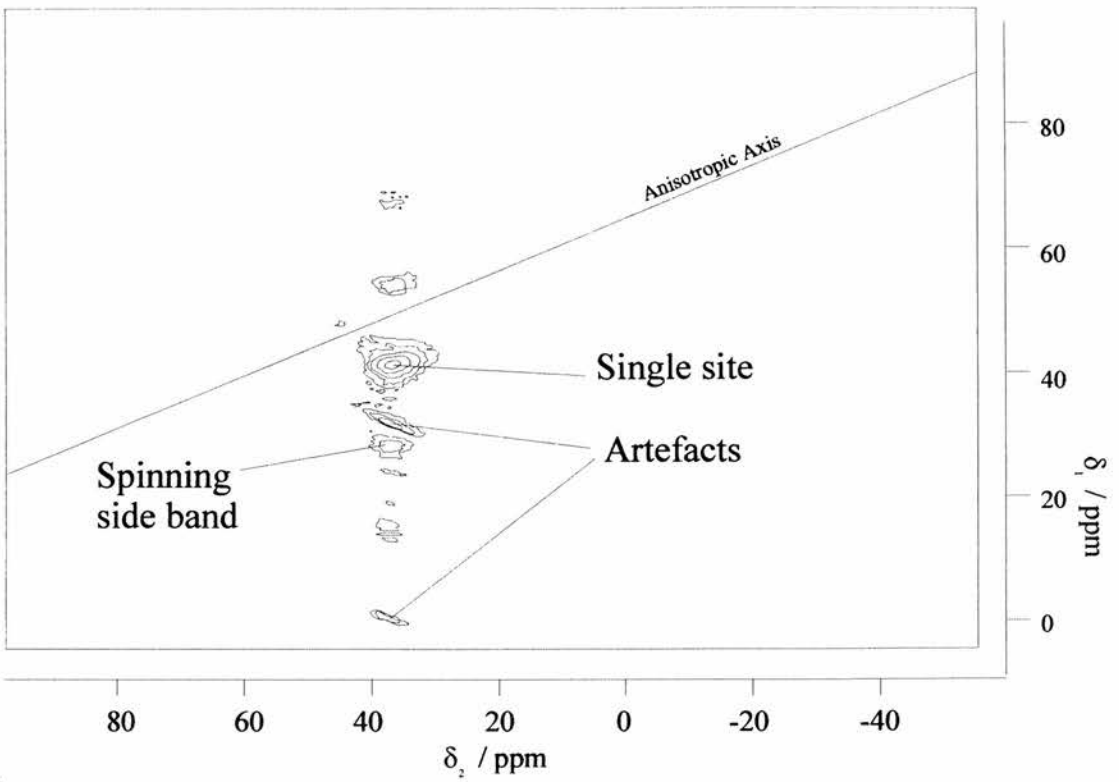

Figure 13 5Q MASNMR spectrum of AlPO-31(D) with one site. The other relatively strong peaks are artefacts whose origin is not clear within the literature. The easiest way to identify such artefacts is that they have a slope of the opposite gradient to the MQMAS ratio along which true MQ resonances are stretched.

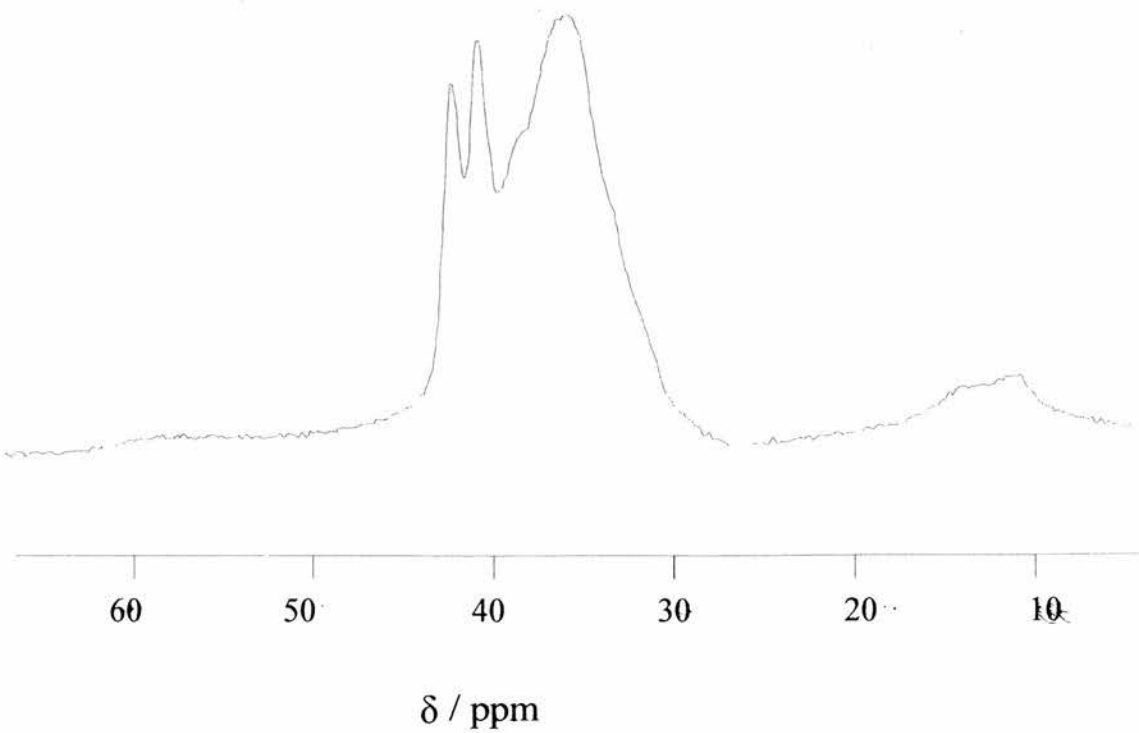

Figure 14 ^{27}Al spectrum of AlPO-31(A)

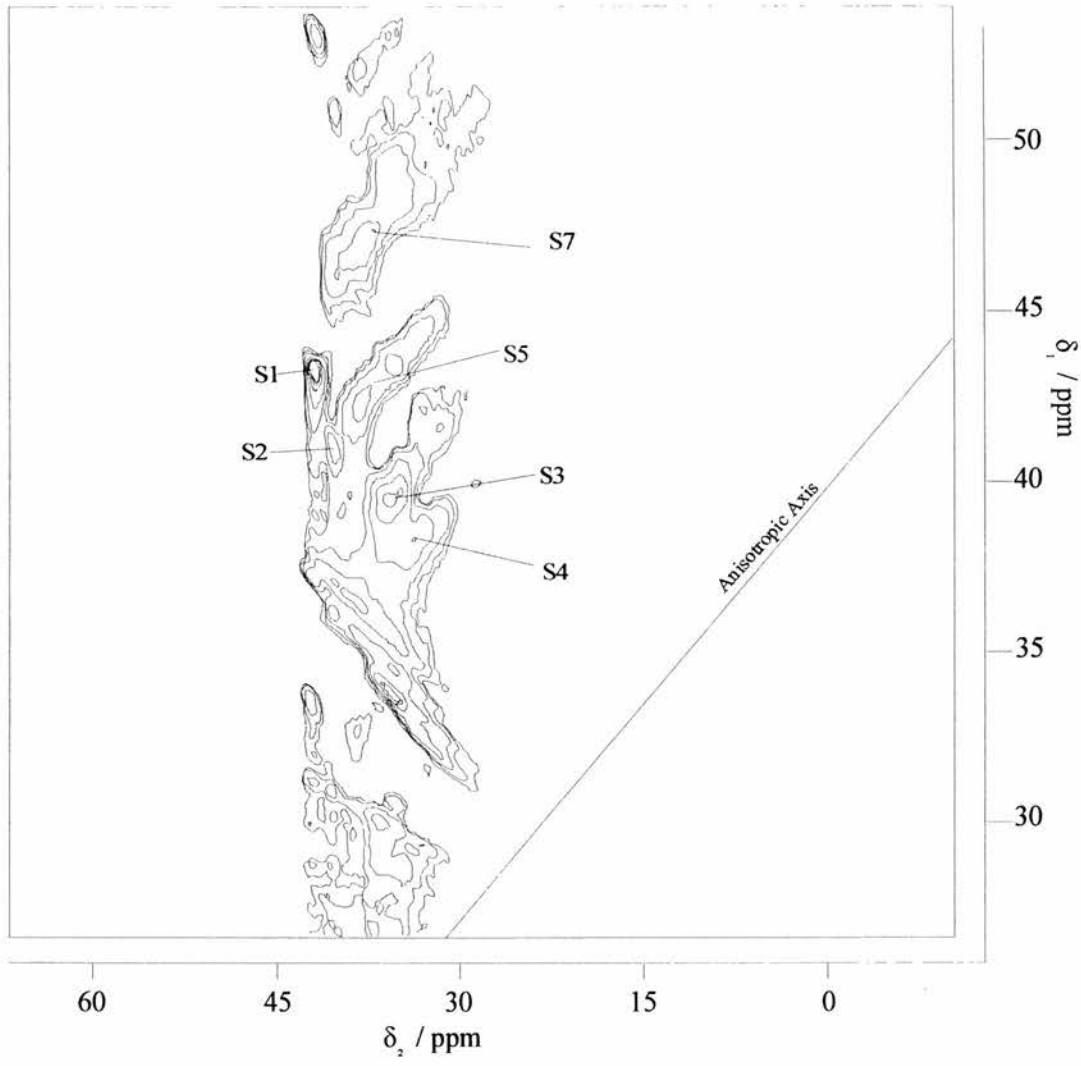

Figure 15 5Q MASNMR spectrum of AlPO-31(A)

The 5Q spectrum (Figure 15) is able to give much greater information than possible from the single quantum techniques. In total, seven resonances are resolved in the tetrahedral region between 30 – 40 ppm (see Table 5 for values), the greatest number in any of the samples run during this series of experiments. The great change in the number of environments present in the NMR spectrum is mirrored in the powder XRD (Figure 16).

The complex structure observed in AlPO-31(A) completely collapses to one analogous to the much simpler calcined material simply on dehydrating by heating in nitrogen at 200 °C. Although it has not been possible to determine fully what has occurred in this material some analysis is possible. It seems likely that the action of the absorbed water is to distort the lattice by coordination to tetrahedral aluminium. The distortion is not identical throughout the sample, some particles remaining essentially unchanged whilst

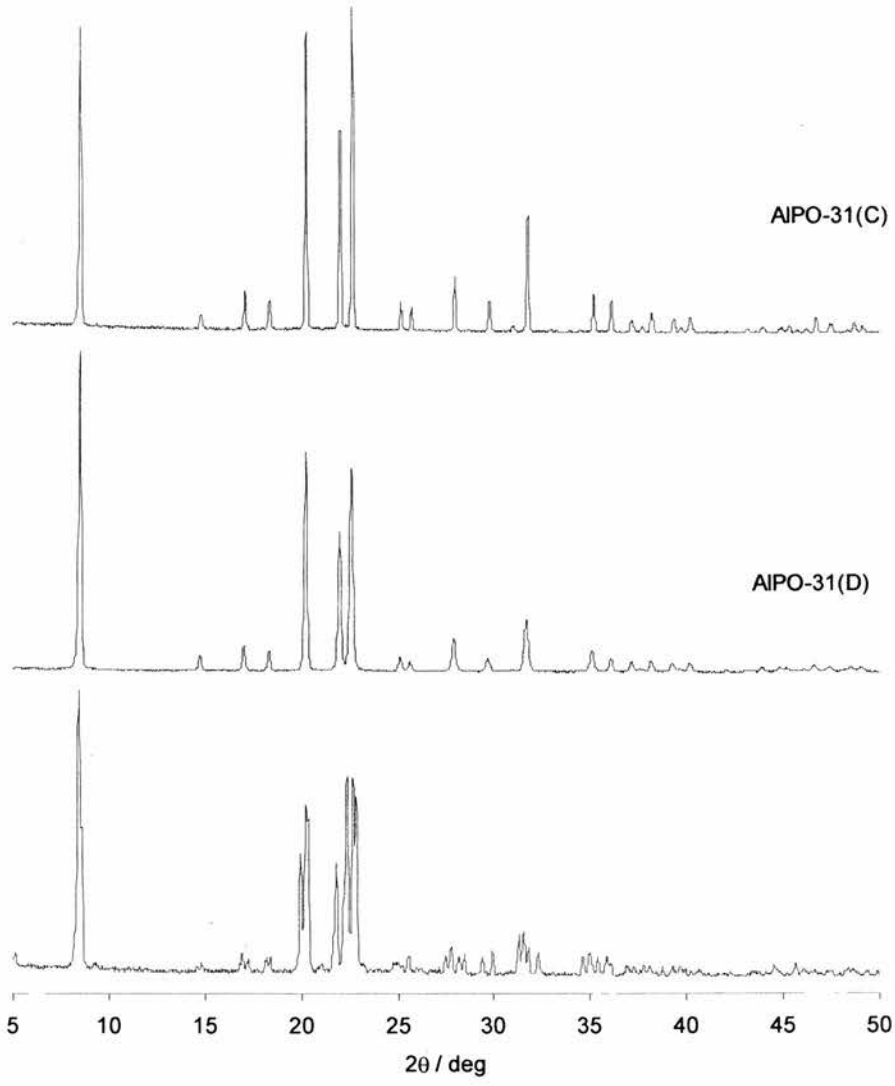

Figure 16 Comparison of the powder X-ray diffractograms of AlPO-31(A), AlPO-31(D) and AlPO-31(C) showing the 'splitting' effect of hydration on the pattern

others have different lattice parameters and / or symmetry. A two phase refinement (both materials having the same space group as the published structure) may be fitted with some success to the AlPO-31(A) XRD pattern if the lattice parameters are allowed to vary from those for the calcined material. It is found that a component of the pattern fits the calcined lattice parameters while other parts have changed. Thus, it seems likely that a range of phases exists in the hydrated sample, some of which are unchanged, some having expanded their structures, and others having distorted enough to change their symmetry. It is certain that some symmetry change has resulted from some aspects of the distortion as a low 2θ peak occurs in the hydrated sample that is absent after the removal of water.

It is obvious in the case of AlPO-31(A) that the 5Q technique provides much greater information than could be obtained otherwise. Although it has been possible to use the

phosphorus spectrum to complement the aluminium SQ data in cases of one or two crystallographically inequivalent sites, this principle clearly has severe limits in more complex cases. The advantage of 5Q in this case is the very good resolution possible from the separation of peaks having a very similar chemical shift, due to differing quadrupolar interactions.

STA-1 and STA-2

The greater resolution of 5Q compared to SQ spectra was a distinct advantage in the case of AlPO-31(A) in overcoming the limits of the information available by comparison of the phosphorus and aluminium spectra. Another circumstance, other than a large number of sites, in which it becomes impossible to gain insight from such a comparison is in the case of MAPOs, that is magnesium doped aluminium phosphates. In these materials, magnesium atoms isomorphously replace some of the aluminiums. This creates a structure with a significant number of acidic, charge balancing sites required as a result of replacing trivalent with divalent cations. Usually there is very little ordering in the position of the magnesium in the AlPO structure so that phosphate groups may be attached to a number of magnesium tetrahedra varying from none to four. This disorder broadens the peaks in the ^{31}P spectrum since each phosphorus position has a range of chemical shifts according to the number of its magnesium neighbours. STA-1 and STA-2 were chosen as an example of MAPOs upon which to test the MQ technique. These materials are microporous frameworks recently synthesised in St Andrews by Graham Noble.

STA-1 is a framework solid with a two-dimensional, intersecting channel system with an internal radius of ~7 Å. The asymmetric unit contains 4 aluminium and 4 phosphorus environments. From the crystal structure we expect the material to contain solely tetrahedrally coordinated framework atoms. The ^{27}Al SQ spectrum (Figure 17) is dominated by a very broad (~11 ppm), complex peak at 41 ppm with another, much smaller but also very broad (~12 ppm) line at ~10 ppm. The phosphorus spectrum is poorly resolved showing three large peaks at –19.0, -23.3 and 25.5 ppm superimposed on a less intense but broader line centered at 25 ppm. The phosphorus spectrum does not resolve fully the four independent crystallographic environments predicted by the crystal structure. Although four lines are present one would not assign the broadest peak to one of the predicted environments on the strength of the SQ spectrum alone.

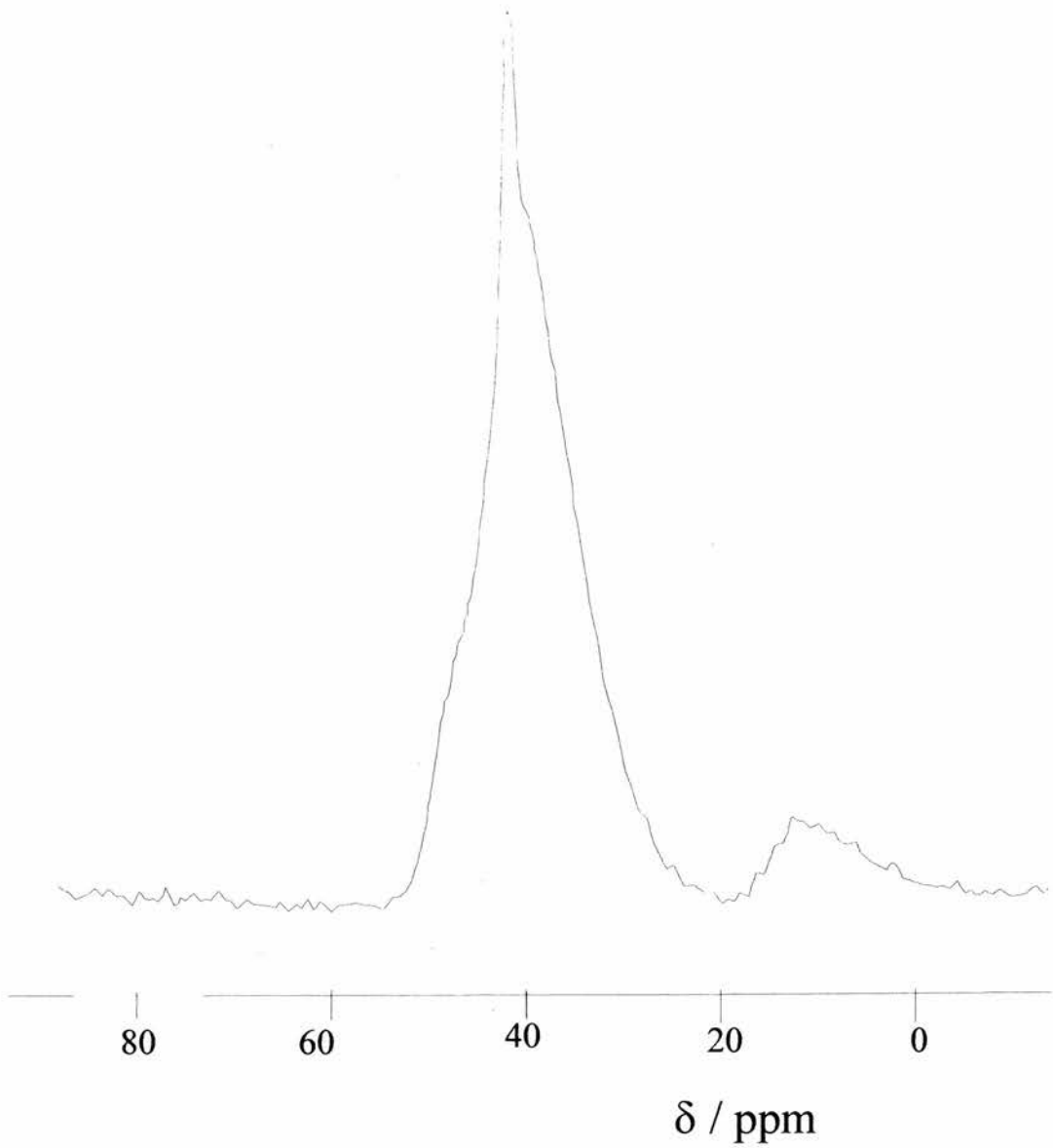

Figure 17 ^{27}Al spectrum of STA-1

The 5Q spectrum (Figure 18) distinguishes three resonances of approximately equal intensity (over the range 50 – 40 ppm - S1, S2 and S3 respectively) in the main line, and one other peak at 8.5 ppm (S4). Consideration of the line shape of the SQ spectrum allows some estimate of the asymmetry parameter to be made. A value of $\eta = 0$ would cause peak splitting of each resonance of 4-7 ppm, and the composite line shape would not correspond to the observed SQ spectrum. Thus $\eta \rightarrow 1$ values must be ascribed to some or all of the peaks.

S4 does not correspond to any of the four predicted aluminium atoms in the crystal structure, all of which are in very similar 'tetrahedral' environments. The region in which S4 falls is hard to ascribe to a particular type of aluminium environment. However, it is certain that a chemical shift of that type represents an increase in the coordination of the aluminium from tetrahedral to penta- or hexa-coordinate.

Aluminium phosphates are very hydrophilic and one expects significant adsorption of water to take place. One can speculate that the action of adsorbed water, perhaps

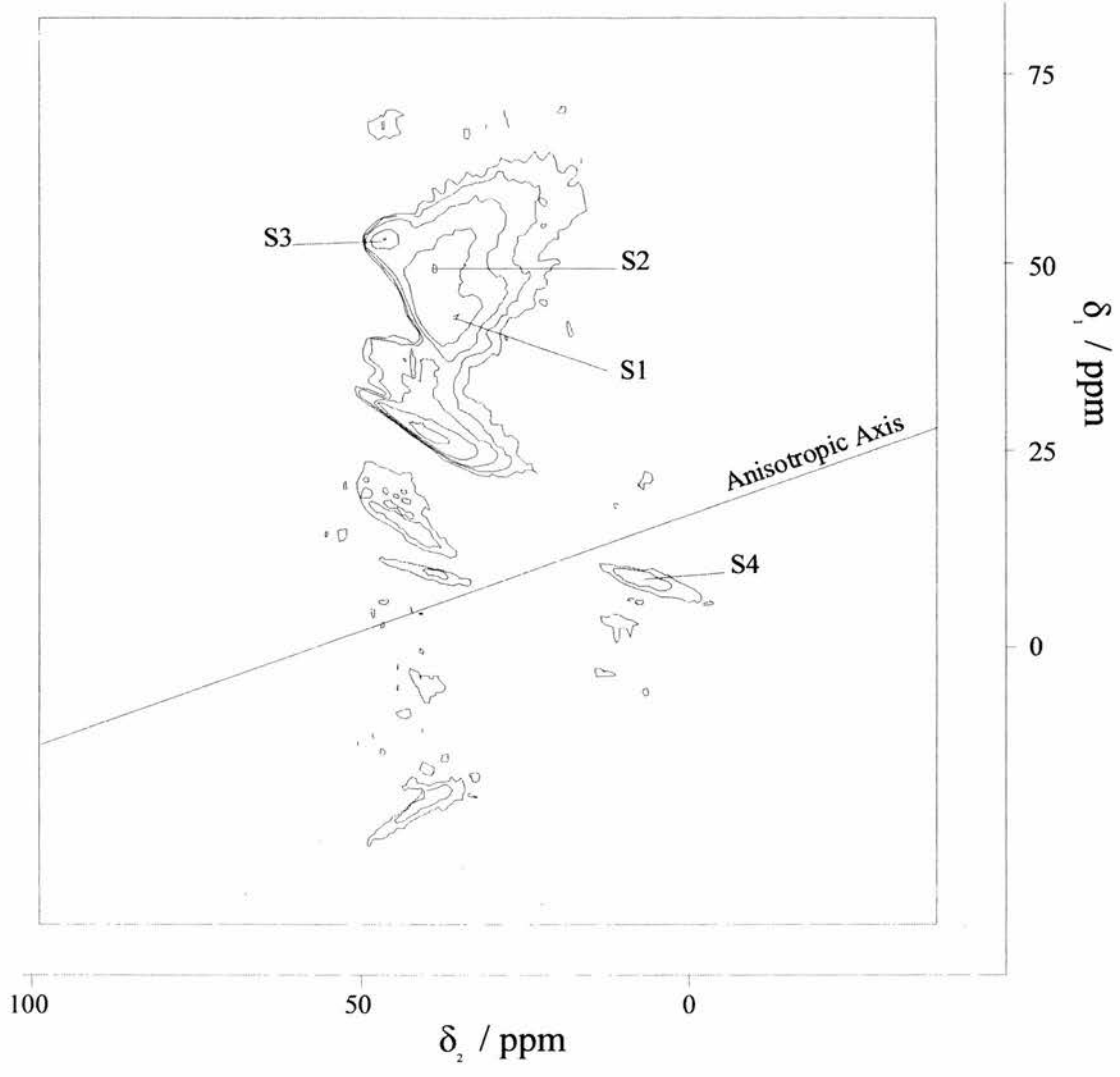

Figure 18 5Q MASNMR spectrum of STA-1

combined with the presence of the template (removal of the template causes the collapse of the structure), is the cause of the different Al environment. Rapid coordination and elimination of water molecules to a framework aluminium atom could cause a stable enough penta-coordinate aluminium species to give rise to a resonance such as S4.

However, aluminium participating in such water exchange reactions should be in a tetrahedral environment for a portion of the time. Thus, even if only one of the Al sites was involved in the hypothetical exchange reaction, one would expect to observe all four predicted Al sites, perhaps with the intensity of one lessened slightly. This is not the case in the 5Q spectrum in which we see only 3 sharp peaks. However, the SQ spectrum does contain the very broad peak underlying the other three lines. Perhaps broadening of this line could result from participation in coordination reactions and a species with such an ill defined chemical environment and quadrupolar interaction

would suffer inefficient 5Q excitation. (In general, it is found that broad SQ peaks often give almost no visible peak in the MQ spectrum through a combination of poor excitation and the signal intensity loss of broadening in two dimensions rather than one.) Thus one could assign the 'tetrahedral' exchange species to the broad line in the SQ spectrum that underlies the others. However, the quadrupolar interaction of the S4 site is very low compared to the tetrahedral sites (1.5 MHz compared to ~3 MHz). This would indicate that the site is well defined with closer to axial and / or cubic symmetry than the tetrahedral positions, a fact that is inconsistent with the above speculation.

STA-2 is also a framework solid with cages, of diameter ~7 Å, linked in one dimension through 4 Å windows and in the other two by a zigzag arrangement of intersections similar to that in ZSM-5. The asymmetric unit of the crystal structure of the as-prepared material contains two aluminium and two phosphorus atoms, all on general positions.

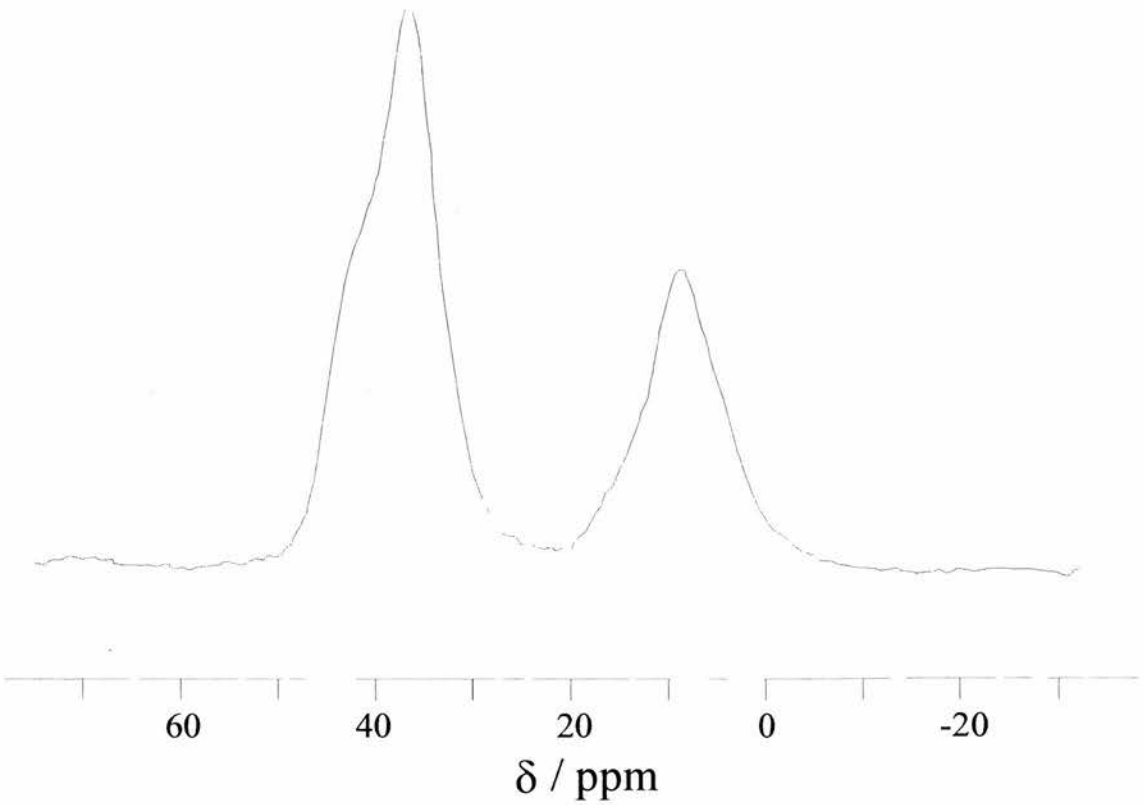

Figure 19 Single quantum ^{27}Al spectrum of STA-2(A)

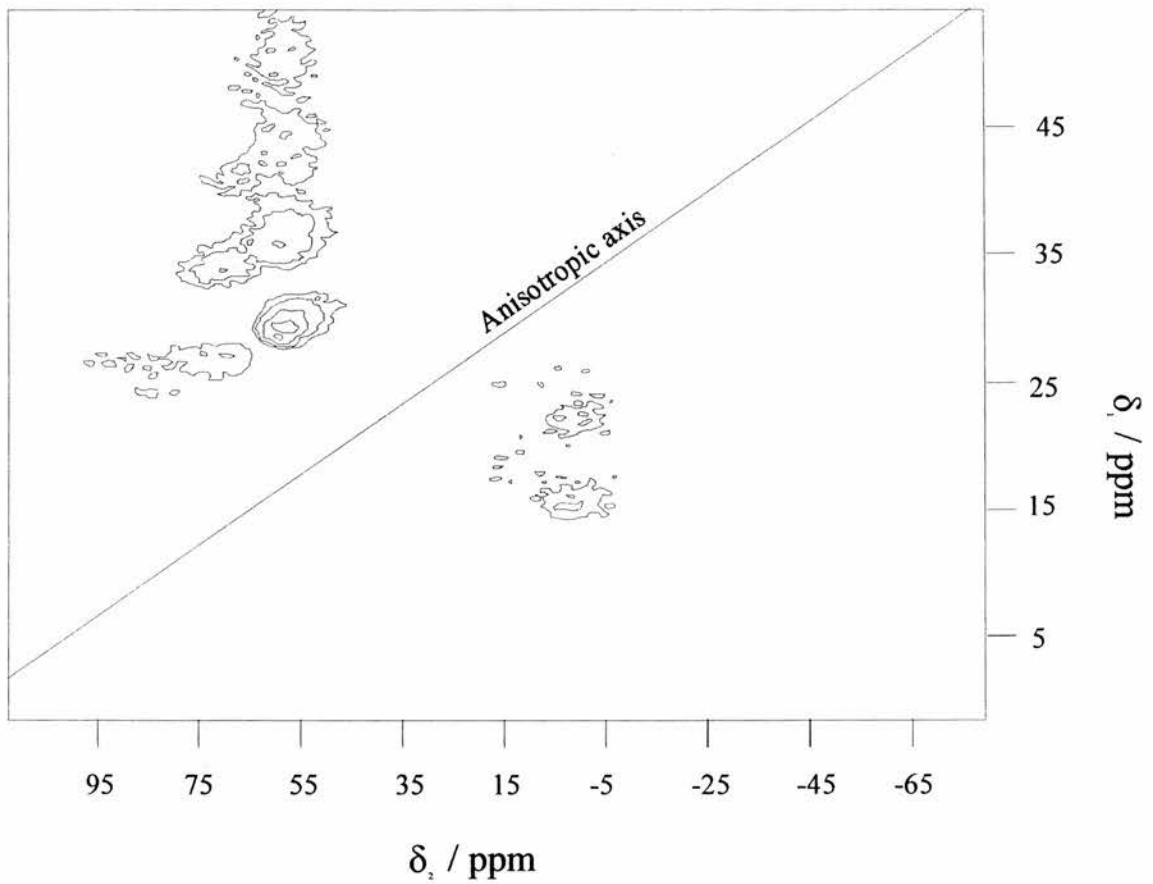

Figure 20 5QMASNMR spectrum of STA-2(A)

STA-2(A) has two broad (~10 ppm) lines in the ^{27}Al SQ spectrum (Figure 19) of approximate integrated ratio 70:30, one (37 ppm) of a complex shape and the other (9 ppm) of an approximately Gaussian envelope. The latter, weaker peak gives rise to almost no signal intensity in the 5Q spectrum (Figure 20). The stronger SQ peak is resolved into two responses, one with δ_{iso} = 45.9 ppm and the dominant at δ_{iso} = 38.3 ppm. The lack of intensity for the 9 ppm peak may be partly the result of the poor S/N for this spectrum due to the low number of acquisitions. However, such a loss of SQ signal intensity in the 5Q experiment can occur due to a difference in the MQ coherence transfer efficiency of various sites, particularly if the site is disordered with a range of quadrupolar coupling constants.

The dehydrated sample, STA-2(D), shows an unchanged tetrahedral region in both the SQ and the 5Q spectra (Figure 21 and Figure 22). The only difference between the (A) and (D) samples is a small narrowing of the 9 ppm line on proton decoupling in STA-2(A) that does not occur in the dehydrated sample. This indicates that the only hydroxyl groups and water present in the as-prepared sample are closer to the aluminium causing the 9 ppm resonance.

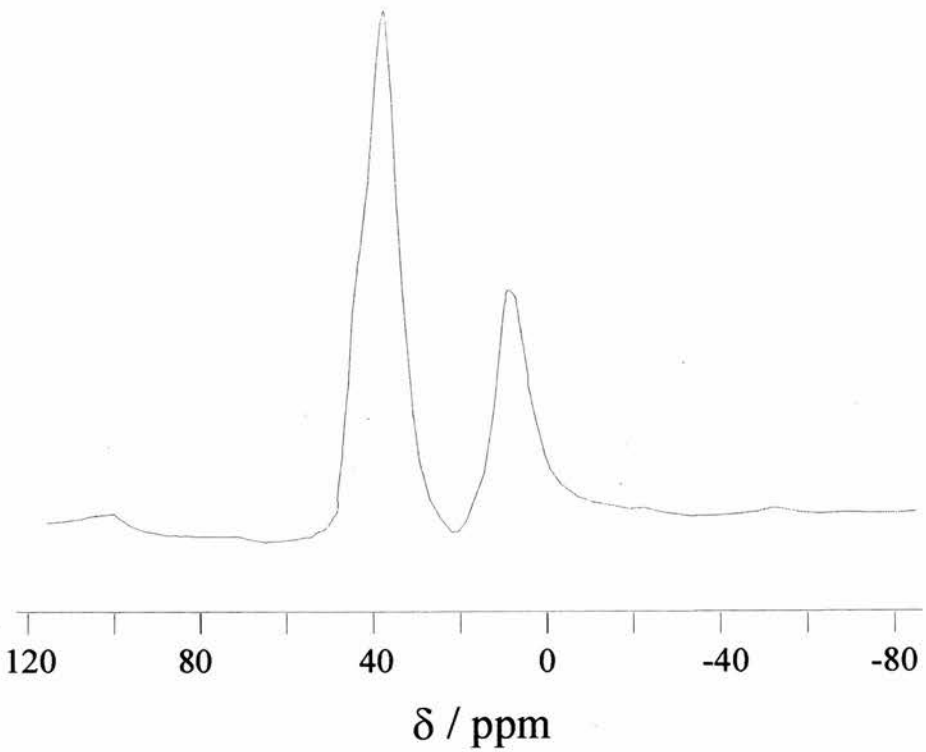

Figure 21 Single quantum ^{27}Al spectrum of STA-2(D)

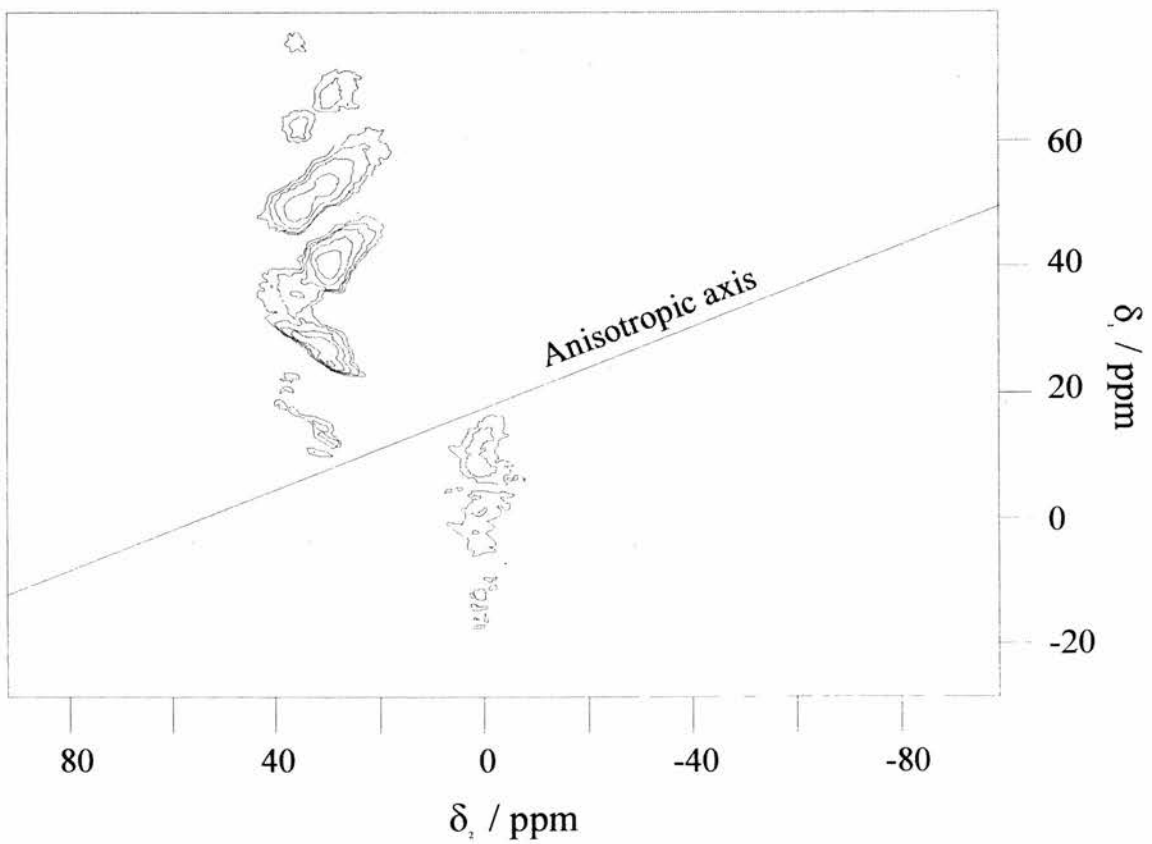

Figure 22 5Q MASNMR spectrum of STA-2(D)

The calcined sample shows a marked difference to the previous two, most notably in the disappearance from the SQ spectrum (Figure 23) of the 9 ppm peak but also in a shift of

the tetrahedral peak from 37 ppm to 35.4 ppm. This latter change is more marked in the 5Q spectrum (Figure 24); the 45.6 ppm peak → 43.1 ppm and 38.3 ppm → 36.2 ppm. The decrease in the difference between these peaks through the greater shift of the high frequency resonance also manifests as a narrower and less complex SQ lineshape.

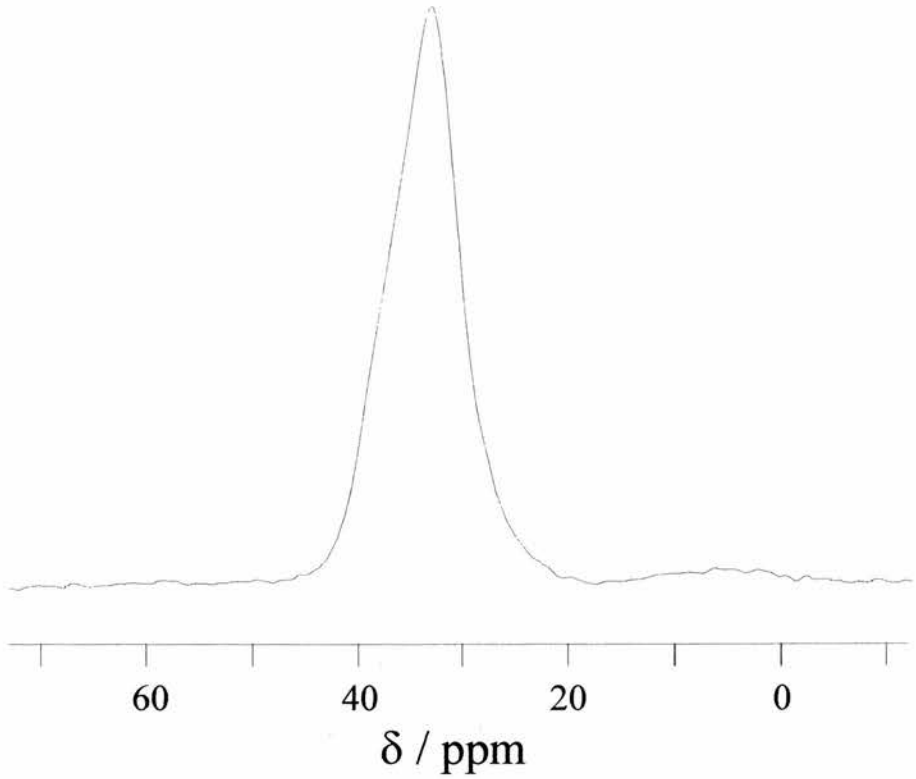

Figure 23 Single quantum ^{27}Al spectrum of STA-2(C)

Since the 9 ppm peak disappears on calcination it is possible that it is in some way connected with the template. However, rather than an aluminium – template interaction within the microporous material, the most likely explanation is that the 9 ppm peak is caused by some Al in the structure being bound to extra water causing it to be 6 coordinate, a phenomenon not observed by XRD (Figure 25). Such species would be removed upon calcination.

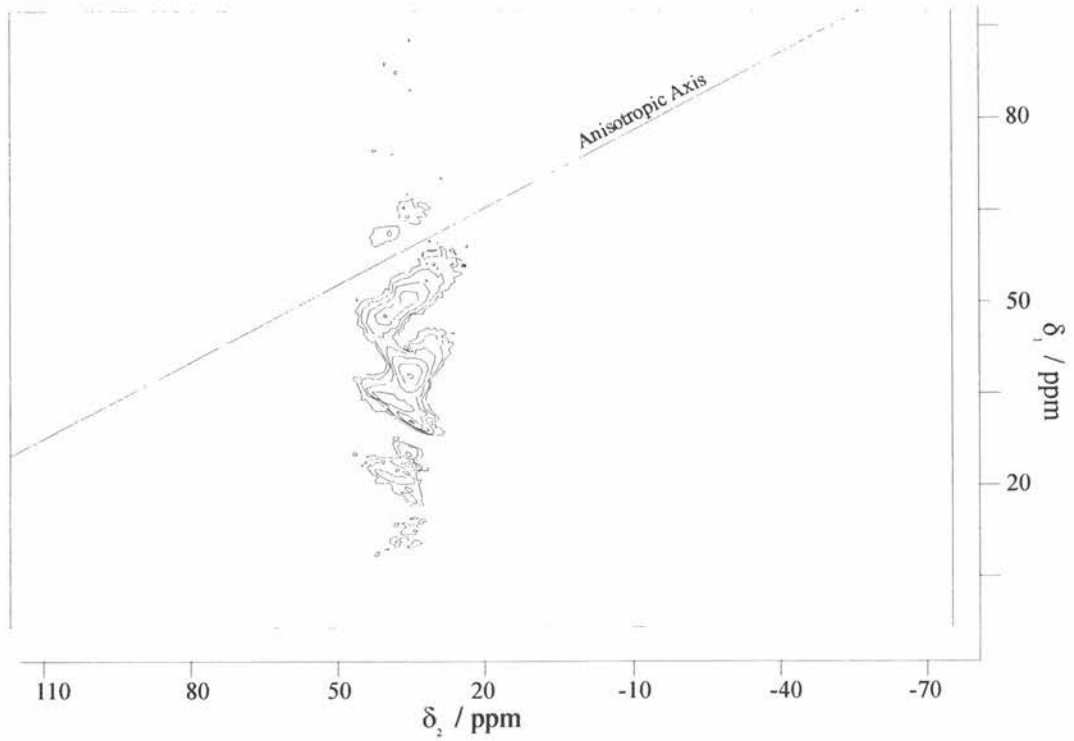

Figure 24 5Q MASNMR spectrum of STA-2(C)

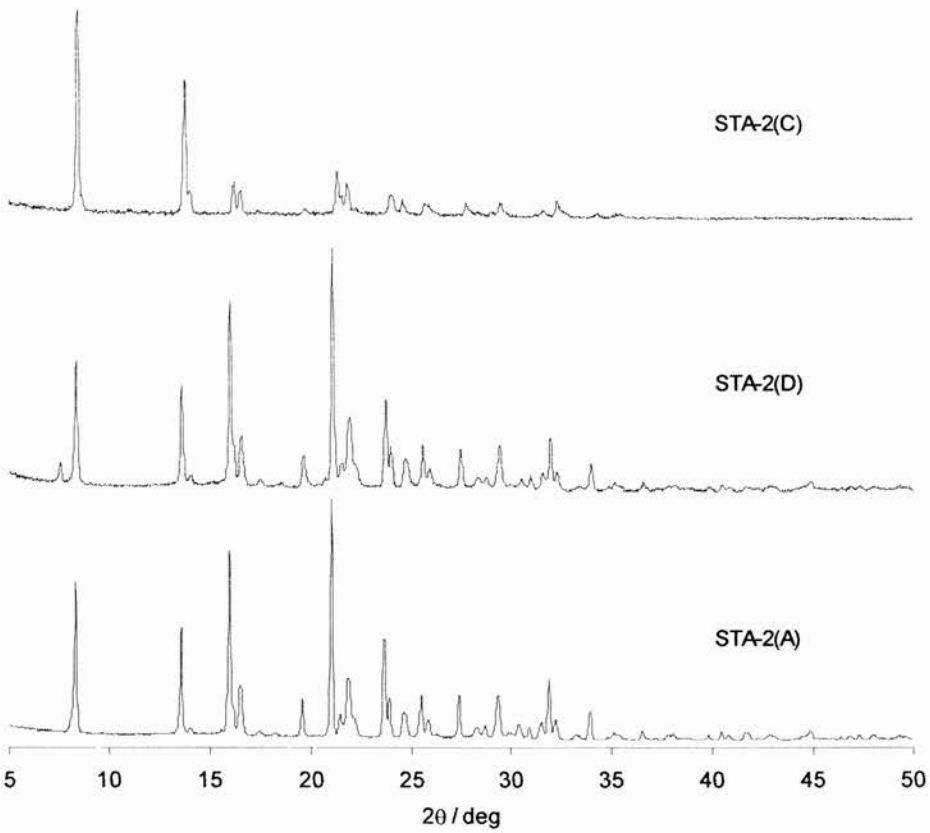

Figure 25 Powder XRDs for the three STA-2 samples showing the slight change of the pattern on calcination.

Aluminium Phosphonates

AlMePO-β

Our studies of this compound (Figure 26 and Figure 27) did not include recording the 5Q spectrum of the octahedral region since our aim was to test the agreement of our results with previous measurements in the literature.[27] Such studies show a single octahedral environment (-17.2 ppm) in the SQ and 5Q spectra. Of more interest for the purpose of testing our instrument is the tetrahedral region in which Rocha *et al*[27] were able to distinguish in the three aluminium sites predicted from the crystal structure the 5Q spectrum. Our results show very good agreement with the literature values (see Table 6) showing that our results are of comparable quality to those of Rocha *et al.*[27]

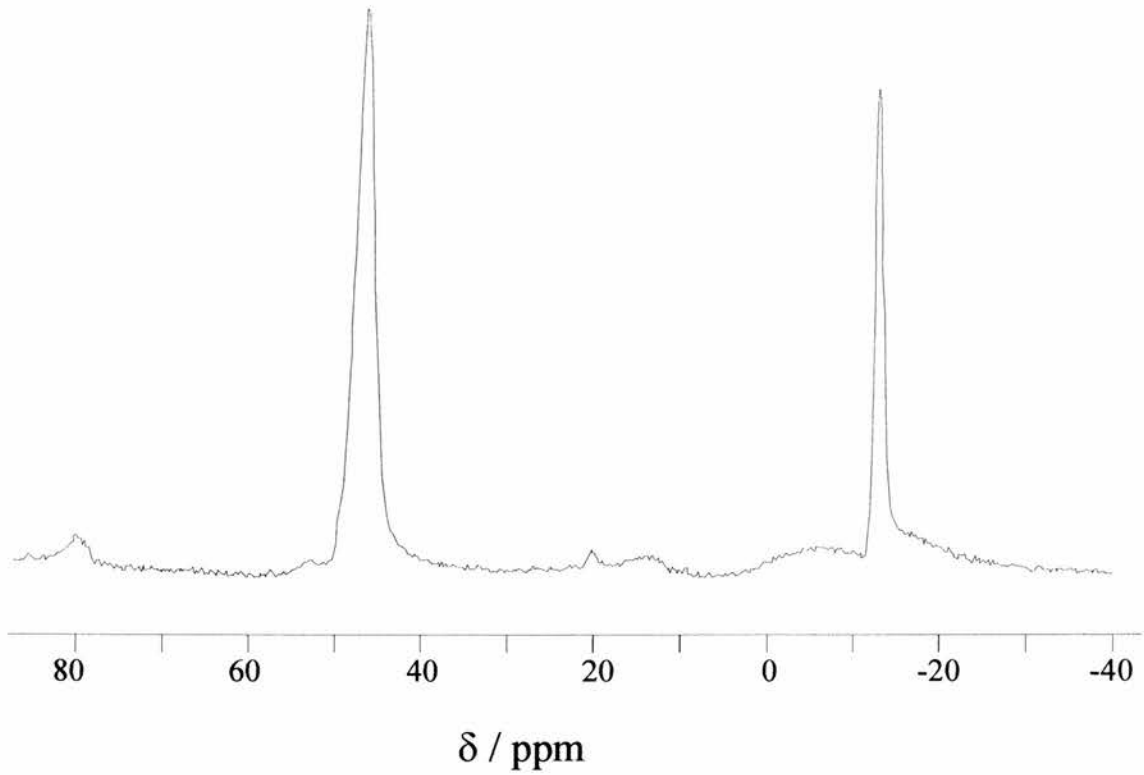

Figure 26 Single quantum ^{27}Al spectrum of AlMePO-β

Also of note are the peak shapes of the tetrahedral sites which show none of the characteristic splitting of sites having $\eta = 0$. It is interesting to consider that the tetrahedral sites are sufficiently distorted from axial symmetry to give rise to asymmetry parameter values $\rightarrow 0$ (see the section Al-27 Chemical Shift, Quadrupolar Parameters And Site Symmetry, below, for further comment).

Table 6 Comparison of the published data for AlMePO-β with our own measurements

	δ_{iso}			SOQUE / MHz		
Rocha *et al*[27]	45.0	42.8	42.3	2.5	2.0	1.9
Our results	45.3	43.5	42.7	2.4	1.9	1.8

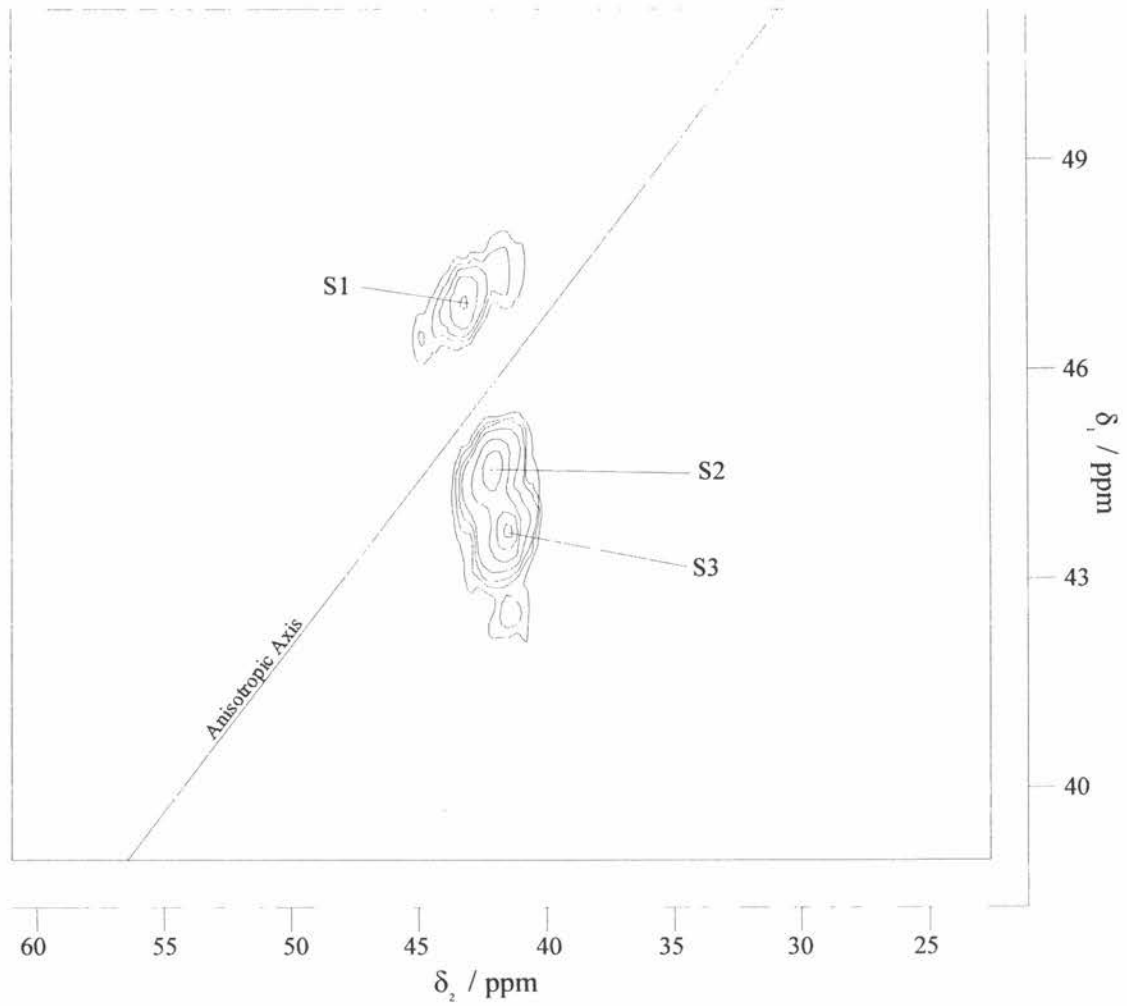

Figure 27 5Q MASNMR spectrum of AlMePO-β.

AlMePO-1

This layered material contains a single, well defined 6 coordinate aluminium environment. The SQ spectrum (Figure 26) shows a characteristic line shape and chemical shift for a single octahedral site with $\eta \rightarrow 1$ and a large quadrupolar interaction. This conclusion is borne out by the 5Q spectrum (Figure 27) in which a single ridge is observed, greatly broadened along the anisotropic axis.

It is possible to observe a splitting in the SQ spectrum of ~1.5 ppm (200 Hz) which is related to the unspun splitting by multiplying by a factor of four[7] (800 Hz). Analysis of this and the SOQUE value from 5Q (see above) identifies $\eta = 0.97$ and $e^2qQ/h = 6.0$ MHz. Thus, alone neither the SQ nor MQ provide a great deal of extra information but from the comparison between them it is possible to obtain estimates of the quadrupolar

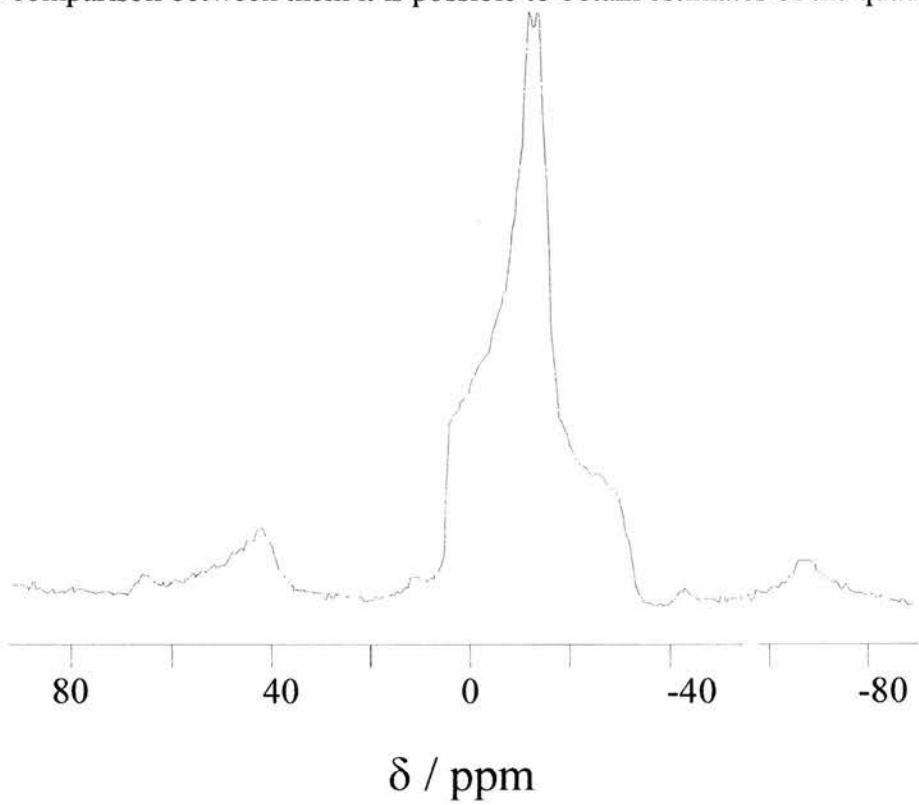

Figure 28 Single quantum ^{27}Al spectrum of AlMePO-1

parameters without sophisticated fitting of the single quantum lineshape. Also, in this case, the phosphorus spectrum contains a single, narrow (~2 ppm) peak at 13.6 ppm. This is valuable in characterising the material since the phosphonates can exist in a range of Al:P ratios and the identification of the number of Al environments does not allow inference to the phosphorus sites.

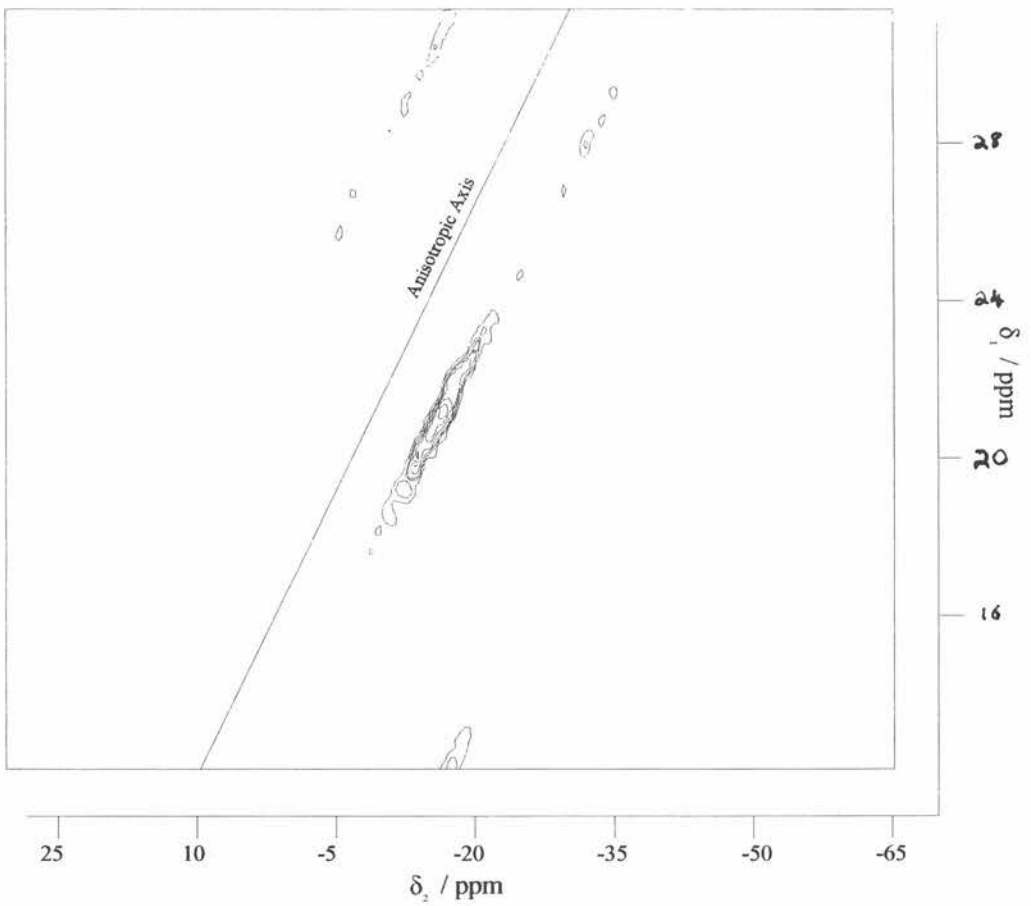

Figure 29 5Q MASNMR spectrum of AlMePO-1.

Aluminium acetophosphonate - AlAcPO

The SQ spectrum (Figure 30) contains two broad peaks (~10 ppm each FWHM) in the octahedral region (-10 – -20 ppm) and a much smaller, less well defined peak at ~-30 ppm. The peak shape of the two larger peaks is consistent with η close to unity. The smallest peak has a very low chemical shift, putting it in a region of uncertain origin. The 5Q spectrum (Figure 31) distinguishes the peaks more clearly, giving isotropic chemical shifts of –25.6 and –30.5 ppm for S1 and S2 respectively. The SOQUE values measured from the multiple quantum spectrum, 7.1 and 6.3, are among the highest observed for any of the samples in this work. The only other species that approaches this is the aluminium in AlMePO-1, also of distorted octahedral symmetry, with $\eta = 1$.

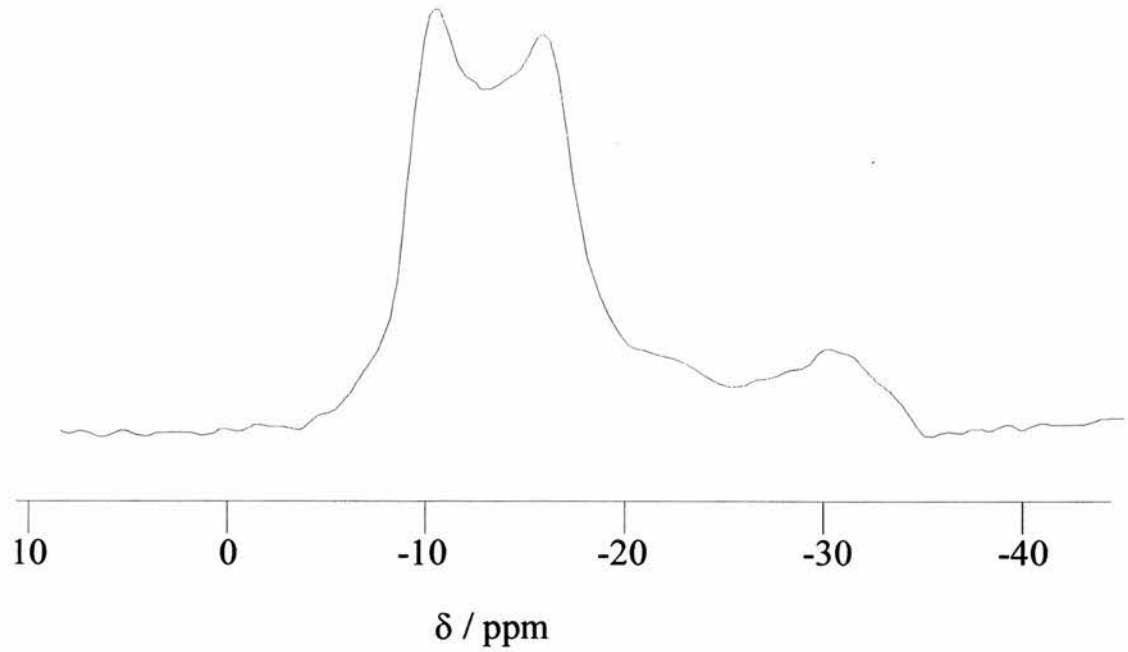

Figure 30 Single quantum ^{27}Al MASNMR spectrum of aluminium acetophosphonate

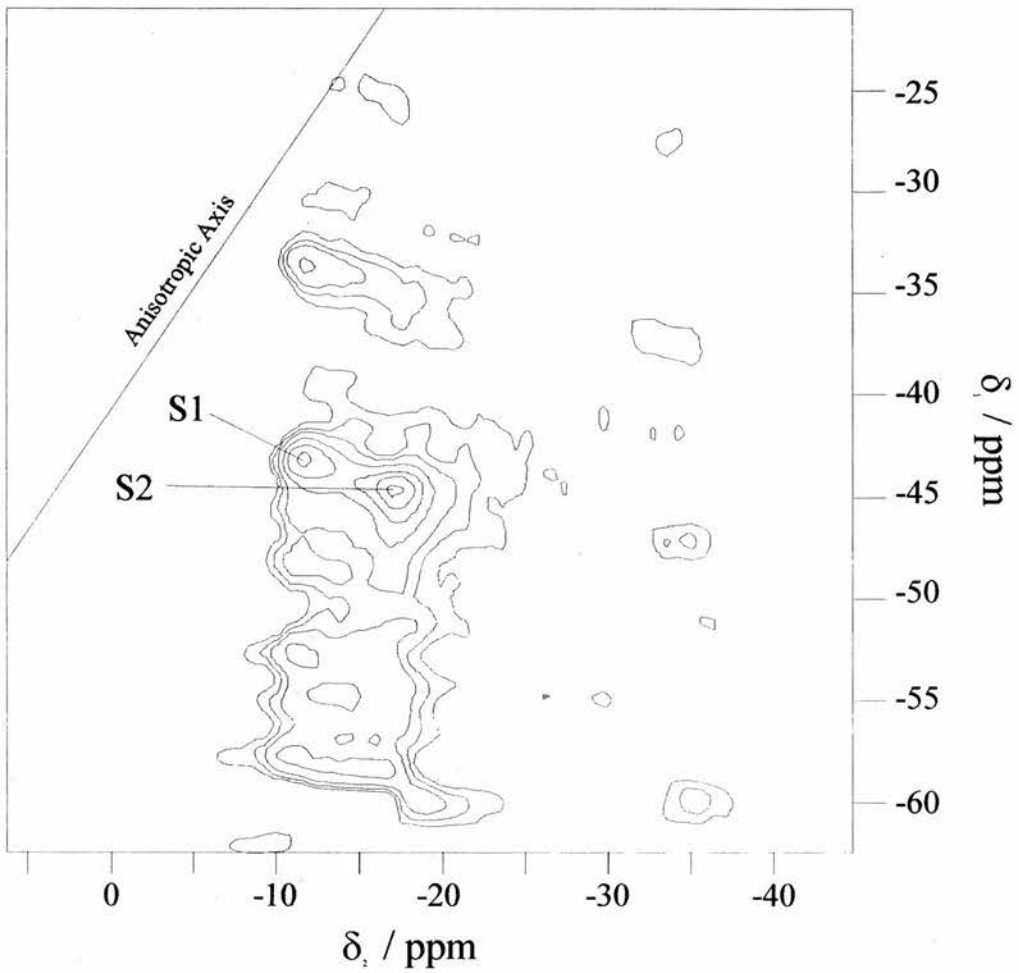

Figure 31 5Q ^{27}Al MASNMR spectrum of aluminium acetophosphonate

The structure of AlAcPO is known, having been solved from single crystal data by Hix *et al*[19] (Figure 32). Inspection of the structure which crystallises in the space group $P\bar{1}$ reveals the origin of the two resonances in the octahedral region. The two aluminium sites are very closely related, having the same ligands but slightly different environments within the cell. The broad shapes of the resonances both in the single and multiple quantum spectra could be attributed to the variety of ligands around the aluminium atoms. Three of the oxygen vertices of the octahedron are attached to phosphorus, one is part of the acetate group and two are unattached, existing either as water or hydroxyl groups. The variety of types of ligand is a characteristic shared by the aluminium in AlMePO-1 which has two vertices shared with other aluminium octahedra, three to phosphonate groups and one as a water molecule. As was mentioned above, this aluminium also gives a very broad resonance.

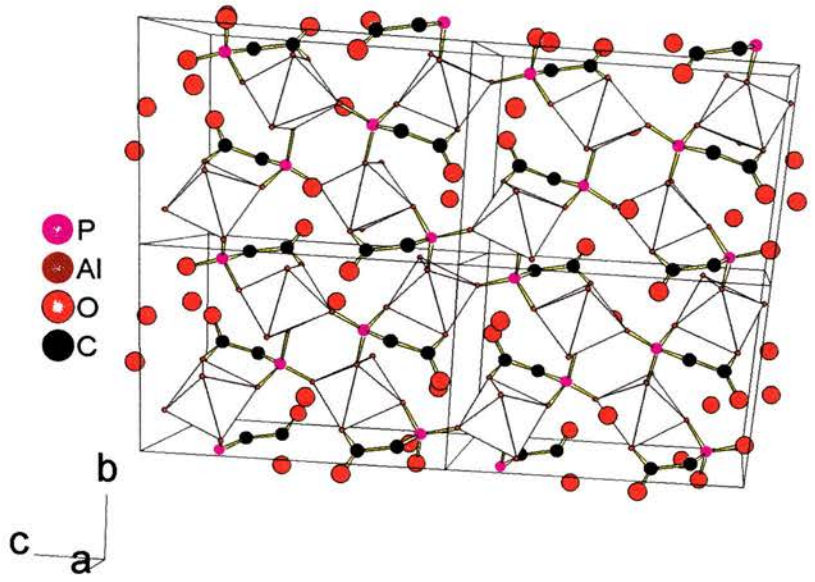

Figure 32 One layer of the structure of the 100% acetophosphonate aluminium phosphonate structure (AcP) described by Hix *et al*[19] (see Chapter 6)

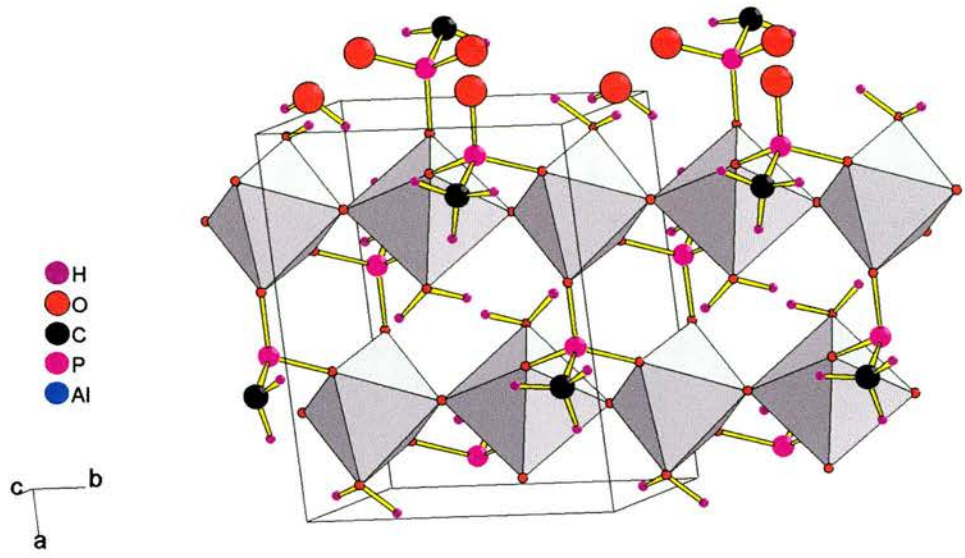

Figure 33 View of part of one layer of AlMePO-1 showing the aluminium octahedra and the different types of oxygen forming its vertices (see Chapter 3 for further details)

AlMePO-2

The ^{27}Al SQ spectrum (Figure 34) shows two lines, the broadest (5 ppm) of Gaussian shape centred at 8 ppm, and the other, at 0 ppm, which has the double peaked structure of a site with $\eta \rightarrow 0$. Assuming $\eta = 0$ the SQ peak splitting (400 Hz under MAS conditions) gives a value of e^2qQ/h = 2.6 MHz. The 5Q spectrum gives a value of 2.7 MHz, assuming a zero asymmetry parameter, sufficient agreement to validate the assumption. The isotropic chemical shift of this line is 3.1 ppm. The broader SQ line gives rise to a peak at 10.8 ppm in the 5Q spectrum (Figure 35) with SOQUE equal to 3.1 MHz. The broad, Gaussian nature of the peak shapes in SQ and MQ indicate a spread of chemical and quadrupolar shifts possibly due to some disorder in the site. There is also another, barely discernible peak in the 5Q spectrum with δ_{iso} = 8.3 ppm. It is possible that this peak is due to the same site as the 10.3 ppm peak and is involved in the disordering of that aluminium.

The chemical shifts of the two sites are in the central region between the tetrahedral and octahedral parts of the spectral range. An attempt to solve the structure of this material has been made (see Chapter 3). Most of the refinement work was performed before the 5Q spectra were available and, as the original SQ spectra were recorded on a Bruker 400, the resolution was somewhat reduced. From the Bruker 400 SQ data it appeared that the chemical shifts of the two lines were more separated with the line having δ_{iso} = 10.8 ppm (from the 5Q experiment) appearing somewhere in the region of 25 ppm.

The structure that has been obtained from the XRD solution in combination with the original NMR data (Bruker 400) contains a penta- and a tetra- coordinate aluminium. The new data from the 5Q measurements does not appear to agree with the presence of the tetrahedral atom. However, the proposed structure is unusual in the presence of a trivalent oxygen, coordinated to two equivalent tetrahedral and the penta-coordinate aluminium atoms. Such an apparently unusual oxygen geometry is encountered in the literature.[30] The 'tetrahedral' aluminium atom is quite distorted (Table 7); one of the Al-O bond ~10 % longer than is normal in undistorted $Al(OP)_4$ polyhedra. In addition the bond angles are distorted from the perfect 109.5° by up to 17° (mean distortion = 10.7 ± 5.5°). It is not surprising that such an unusual 4-coordinate aluminium environment should have a chemical shift outside the normal tetrahedral range. Furthermore, the structure is different from the microporous aluminium phosphonates (AlMePO-β and AlMePO-α) and phosphates since it contains Al-O-Al bonds (as does AlMePO-1 which also has a δ_{iso} that is less negative than one would expect). Each 4 coordinate Al is connected through the 3 coordinate oxygen to another 4 coordinate Al and the pentacoordinate Al, to which also it is connected directly through another oxygen. Perhaps the cumulative effect of these factors has moved the resonance from the normal range for this species.

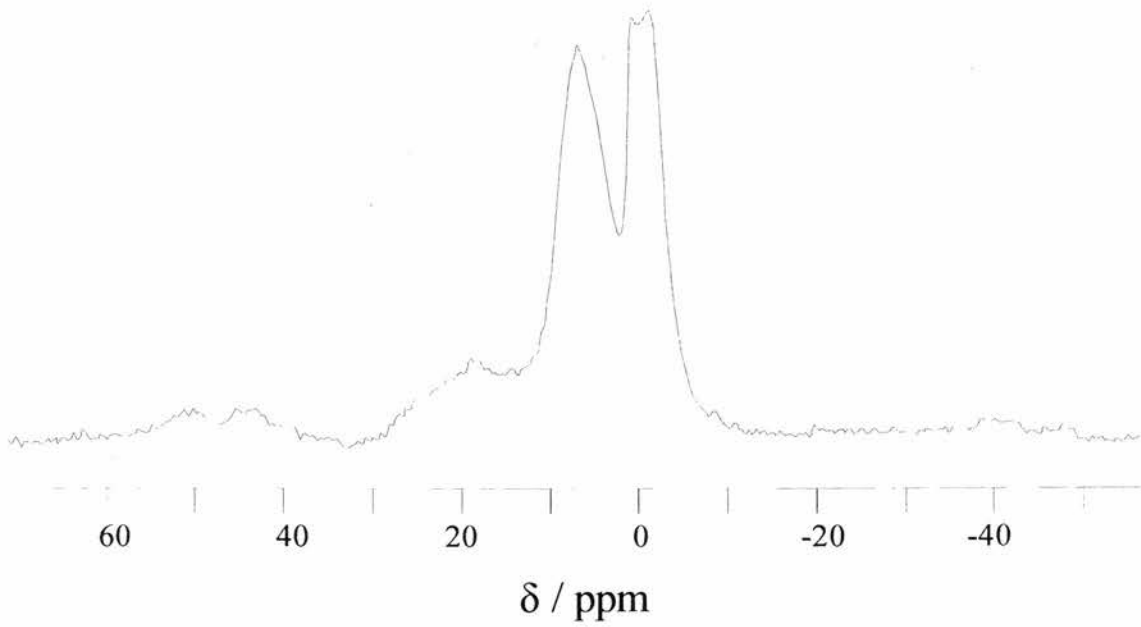

Figure 34 Single quantum ^{27}Al spectrum of AlMePO-2

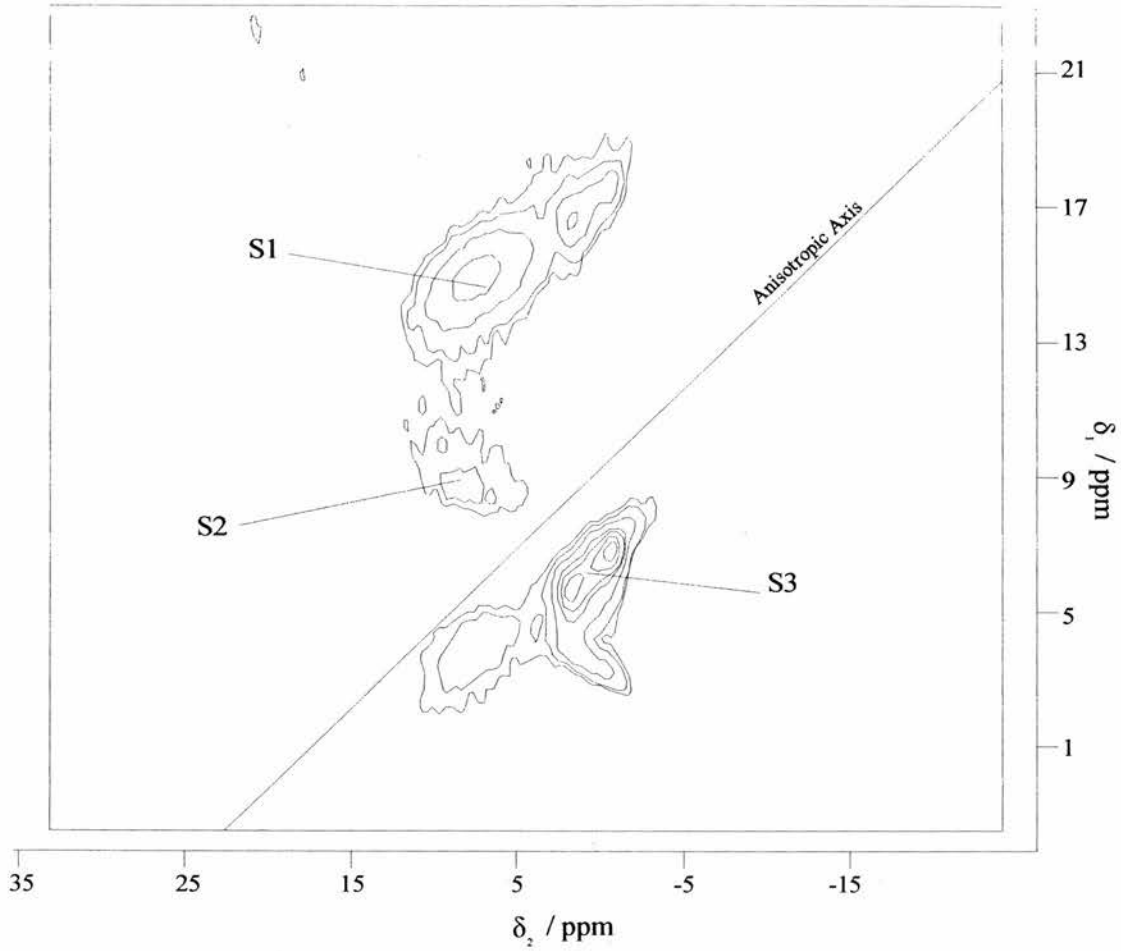

Figure 35 5QMASNMR spectrum of AlMePO-2

Table 7 Table of bond lengths and angles for the 4-coordinate Al atom in AlMePO-2

Bond	Length / Å
AL1_O4	1.77069(5)
AL1_O6	1.88099(5)
AL1_O7	1.81345(5)
AL1_O8	1.81524(9)

Bond Angle	Angle / °
O4_AL1_O6	92.065(3)
O4_AL1_O7	98.795(3)
O4_AL1_O8	100.494(1)
O6_AL1_O7	123.243(2)
O6_AL1_O8	110.714(1)
O7_AL1_O8	121.400(2)

The ^{31}P spectrum for AlMePO-2 shows a single narrow peak 20.8 ppm. As mentioned before, the correlation between the number of aluminium and phosphorus positions in aluminium phosphates does not hold for phosphonates and that extra source of complementary information is not available. In this case there are two independent aluminiums sites and only one phosphorus site.

AlMePO-3

The structure of AlMePO-3 has not been solved at this point although this is a continuing work (Chapter 3). However, the XRD pattern has been indexed to a triclinic cell with lattice parameters of a = 9.68 Å, b = 12.42 Å, c = 5.08 Å, α = 91.2°, β = 90.4°, γ = 92.1° and of space group $P\bar{1}$.

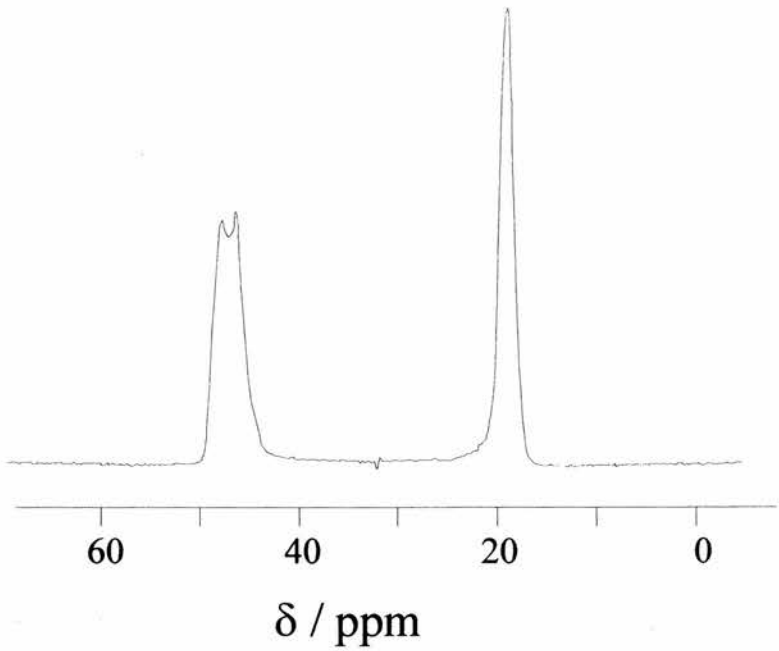

Figure 36 Single quantum ^{27}Al spectrum of AlMePO-3

The SQ aluminium spectrum (Figure 36) shows two lines, one broad at 43 ppm and the other, narrower at 14.5 ppm. The broader line has the peak splitting indicative of an approximately axially symmetric quadrupolar interaction. In the 5Q spectra (Figure 37 and Figure 38) the narrower line gives a sharp resonance with δ_{iso} = 15.5 ppm and the tetrahedral line at δ_{iso} = 44.9 ppm. The latter peak has a SOQUE of 2.5 MHz from the MQ spectrum but of 1.9 MHz (η=0) from analysis of the SQ line splitting. The difference in these parameters can be eliminated if the asymmetry parameter is chosen as 0.3 to give values of e^2qQ/h = 2.4 MHz and 2.3 MHz for MQ and SQ predictions respectively. The peak with δ_{iso} = 15.5 ppm is assigned to a five coordinate aluminium environment. Furthermore, it is postulated that the ligands around the metal are of the same type, i. e. all OP oxygens rather than a mixture of water and OAl. This conclusion is consistent with the results from AlMePO-1 and AlAcPO, both of which have very broad, asymmetric peaks and a range of different groups around the aluminium atoms. The assignment is made both because the peak is very narrow, even in the SQ spectrum. Also, assuming that there are no Al-O-Al bonds, on finds that 6 coordinate aluminium, the only other possible assignment for this peak, does not match the known data concerning the density of the material and the unit cell size (see Chapter 3).

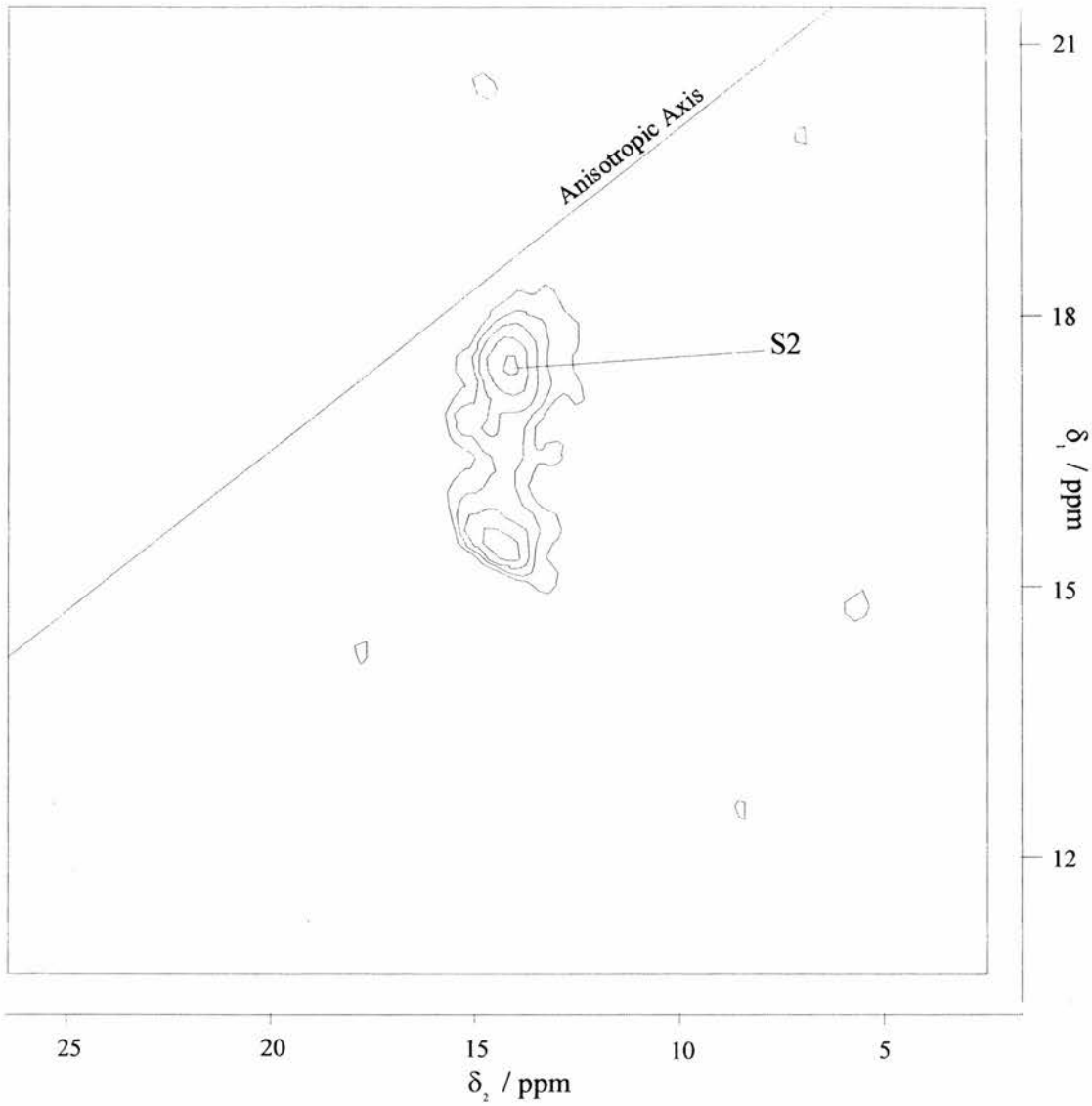

Figure 37 Five coordinate region of the 5Q ^{27}Al spectrum of AlMePO-3

The other signal intensities in the 2-dimensional plot that have not been attributed to 5Q resonances are artefacts. Such artefacts are known to occur in this technique and although their origin is a difficult question, it is likely that they are a result of SQ signal intensity that has not been averaged to zero by the phase cycling. It is possible to test their legitimacy by repeating the experiment using a different value of O1, the irradiation frequency. However, in this case we have not repeated the experiment since the peaks in question appear unambiguously of other than 5Q origin (the gradient of the ridges has a slope of the opposite sign to the MQMAS ratio which is the gradient of real 5Q resonance ridges). Also, it has been possible from the size of the unit cell and a measurement of the density (1.87 ± 0.03 g cm^{-3}) to calculate the Al:P ratio of the material as 1:1.5 (this corresponds to a density of 1.89 g cm^{-3}). The phosphorus spectrum shows three separate sites. Since the density requires 6 phosphonate groups in the unit cell, the presence of three independent sites confirms the identification of the space group as $P\bar{1}$. The density of the material also requires that there be four

aluminium atoms in the unit cell. Since there must be an inversion centre present, there can be only two different aluminium sites. Thus, this supports the identification of the extra peaks in the 2-D plot as artefacts.

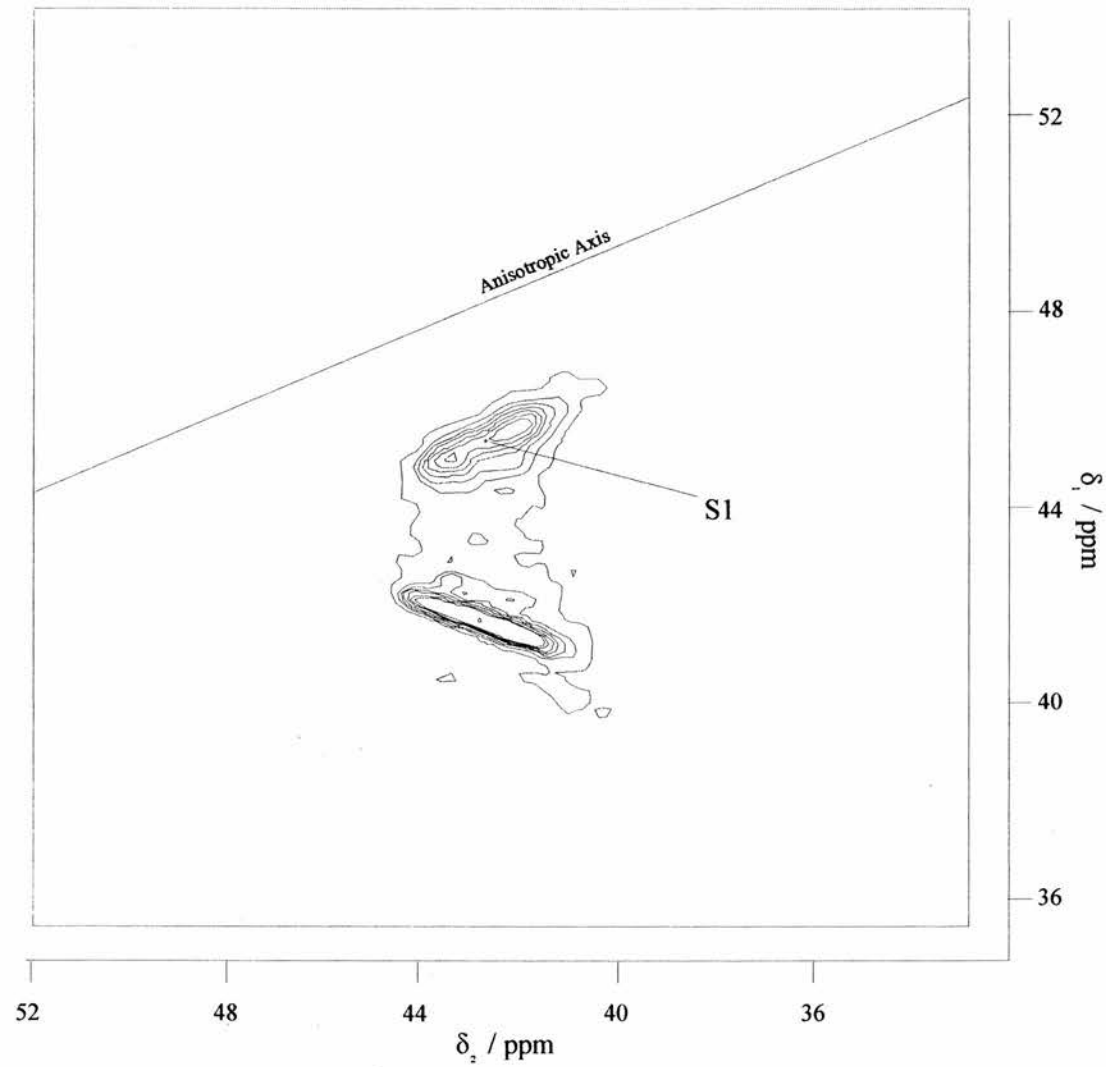

Figure 38 Tetrahedral region of the ^{27}Al 5Q MASNMR spectrum of AlMePO-3

Al[33H]MePO

Of the all the materials discussed in this chapter, one of the most intriguing and, so far, mysterious is Al[33H]MePO. This material was synthesised as part of a series of reactions in which the synthesis gel contained a mixture of phosphonic acids, the aim of which was to isomorphously substitute some of the methylphosphonate groups in a structure with other phosphonates (Chapter 6). In this case, the second type of phosphonate originates from phosphonic acid in which a hydrogen atom is bonded directly to the phosphorus in place of the methyl group. One of the results of the experiment was to produce an unknown phase over a range of different proportions of phosphorous acid in the gel. From the XRD patterns several compositions seemed almost phase pure with the 33% substituted (Al[33H]MePO) being the best. It was decided to record the MQMASNMR spectrum of this compound in an attempt to aid its characterisation.

The SQ spectrum (Figure 39) contains two narrow peaks, the octahedral at -16.3 ppm and the tetrahedral at 42.3 ppm, remarkably similar to those in the spectrum of AlMePO-β except that the octahedral is slightly broader. The reason for this extra width becomes apparent from the 5Q spectrum (Figure 40) which shows the octahedral peak to be made up of two resonances at –14.1 and –16.9 ppm. It is interesting to note that the SQ spectra of other samples of this material show a decrease in the chemical shift in the octahedral line with increasing phosphorous acid in the synthesis gel. It is possible that this is due to a change in the relative size of the two peaks making up the composite lineshape observed in the SQ spectrum (note that the –16.9 ppm line agrees within error limits with the SQ results for AlMePO-β's octahedral site).

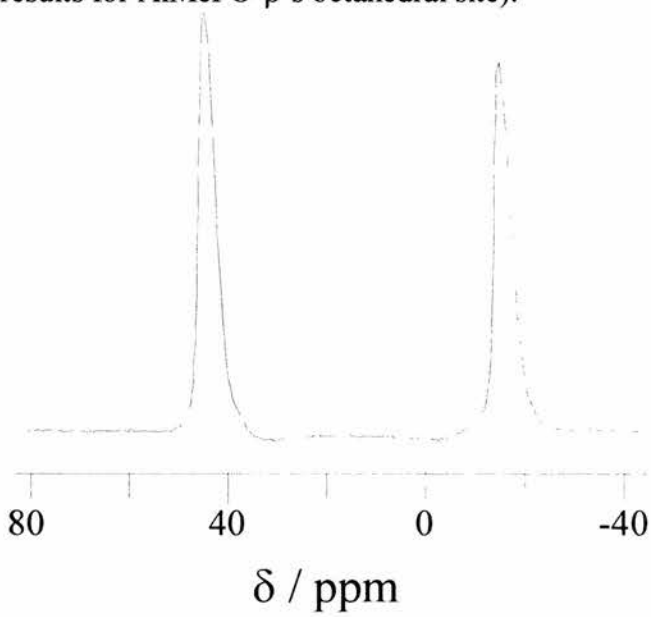

Figure 39 The single quantum aluminium-27 spectrum of Al[33H]MePO

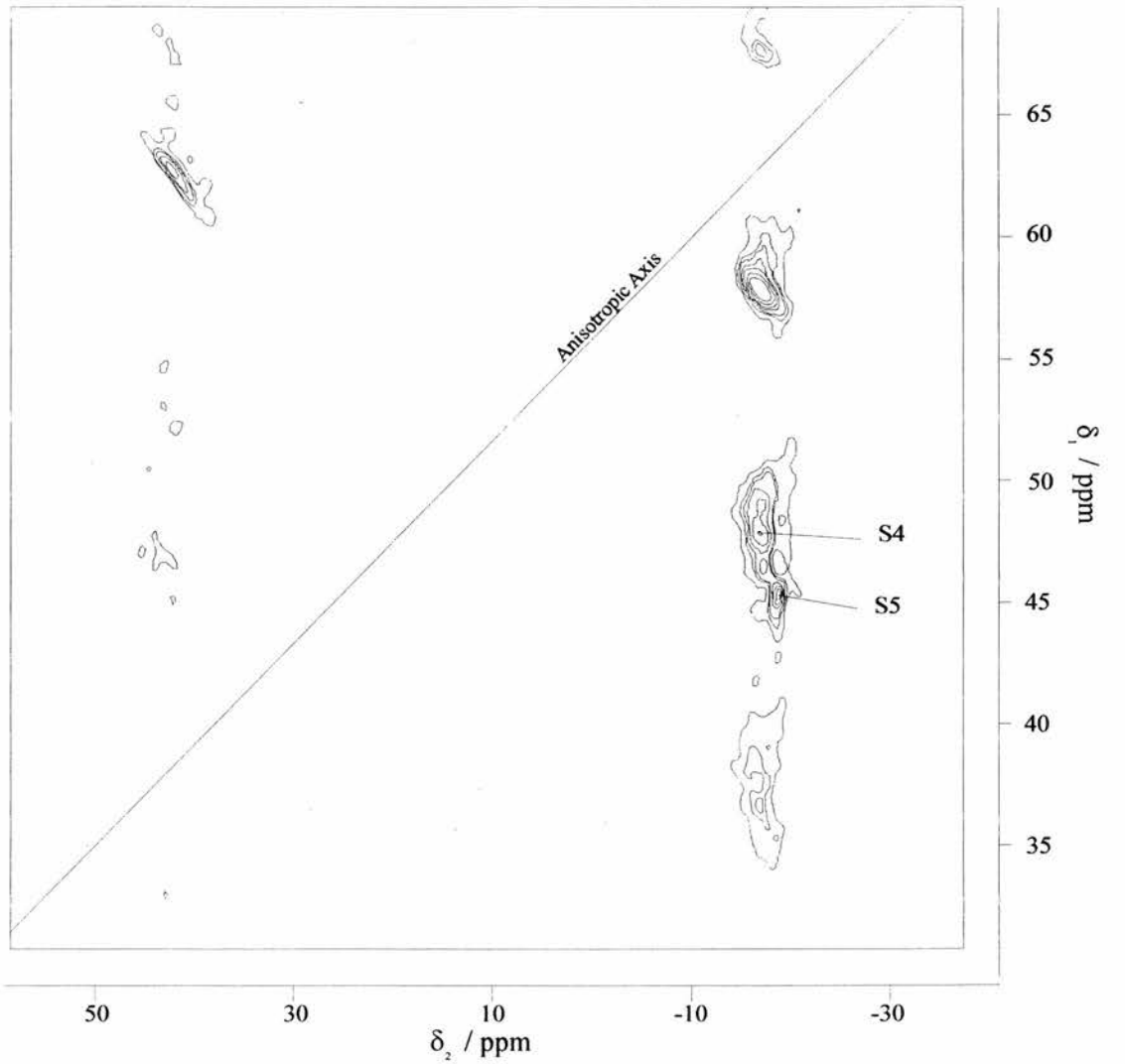

Figure 40 Octahedral region of the 5Q ^{27}Al MASNMR spectrum of Al[33H]MePO

The intriguing similarity to aspects of AlMePO-β's spectrum continues in the tetrahedral region (Figure 41) with three sites of very similar chemical shift and quadrupolar interactions (Table 8). The agreement is so close that it is tempting to assume a relationship between the two structures, although the XRD patterns are quite dissimilar.

It is also worth noting the phosphorus spectrum which shows four resonances, two of which (4.6 and 0.3 ppm) are quite narrow (2-3 ppm), the other two (-8.4 and –20.1 ppm) being much broader (~8 ppm). The last and smallest peak at –20.1 ppm does not appear in other samples of this material with different percentages of the phosphorous acid in the gel. It is instructive to examine a summary of the phosphorus chemical shifts for the materials discussed in this chapter (see Figure 42). As expected, the phosphates and the phosphonates have different ranges of characteristic shifts. The phosphorus resonances

from Al[33H]MePO form a range that overlaps both regions. The resonances at a negative chemical shift (NB chemical shift is given with respect to aqueous 1M H_3PO_4) are likely to be from P-H phosphorus, i.e. those atoms to which a hydrogen is attached rather than a methyl group. However, even allowing for this difference, it is noticeable that the phosphorus spectrum, in contrast to the aluminium, is quite different from AlMePO-β's.

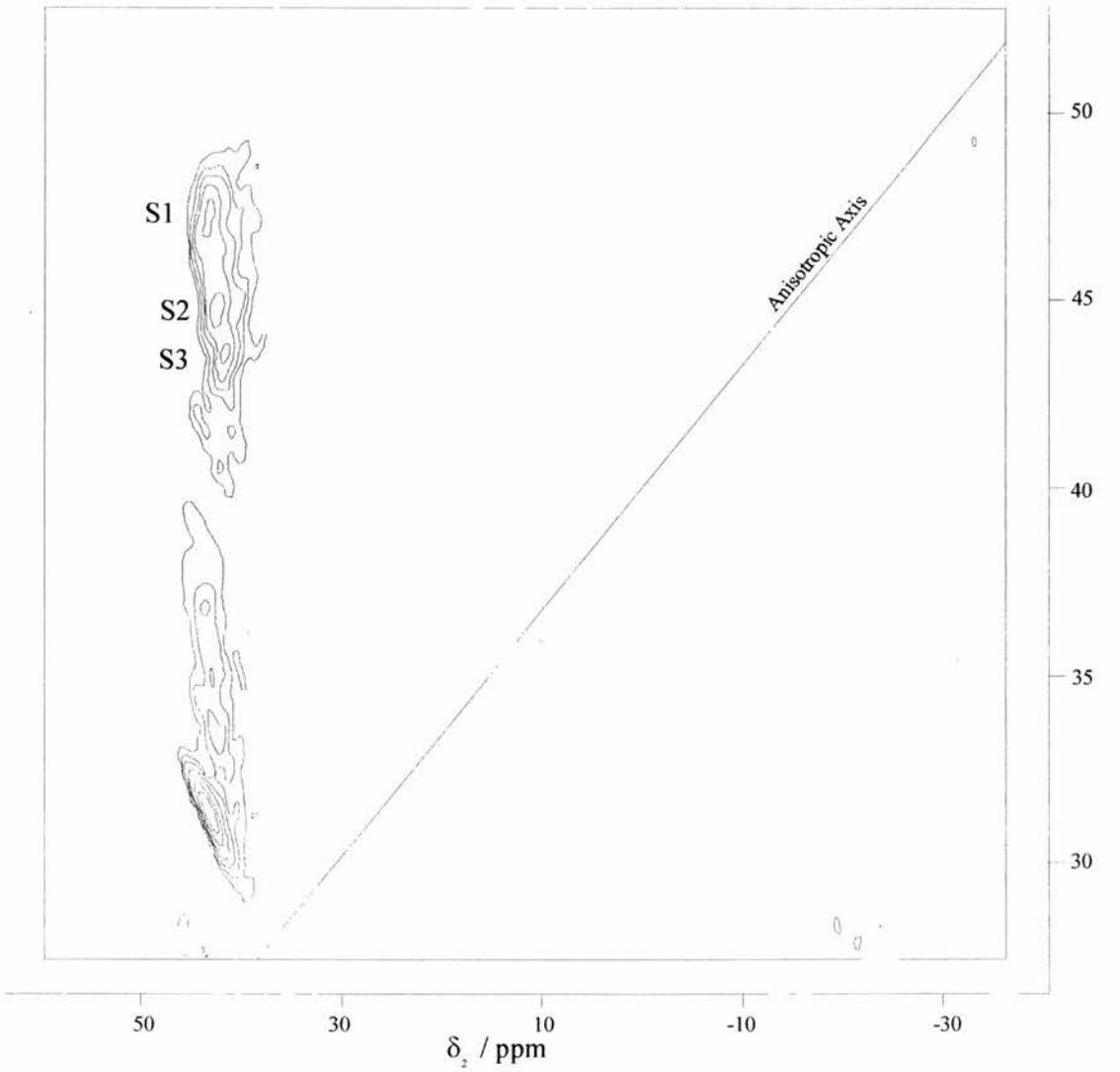

Figure 41 Tetrahedral region of the 5Q ^{27}Al MASNMR spectrum of Al[33H]MePO

Table 8 Comparison of the our data for the tetrahedral sites of AlMePO-β with Al[33H]MePO

	δ_{iso}			SOQUE / MHz		
AlMePO-β	45.3	43.5	42.7	2.4	1.9	0.8
Al[33H]MePO	44.6	43.4	43.0	2.3	1.9	2.3

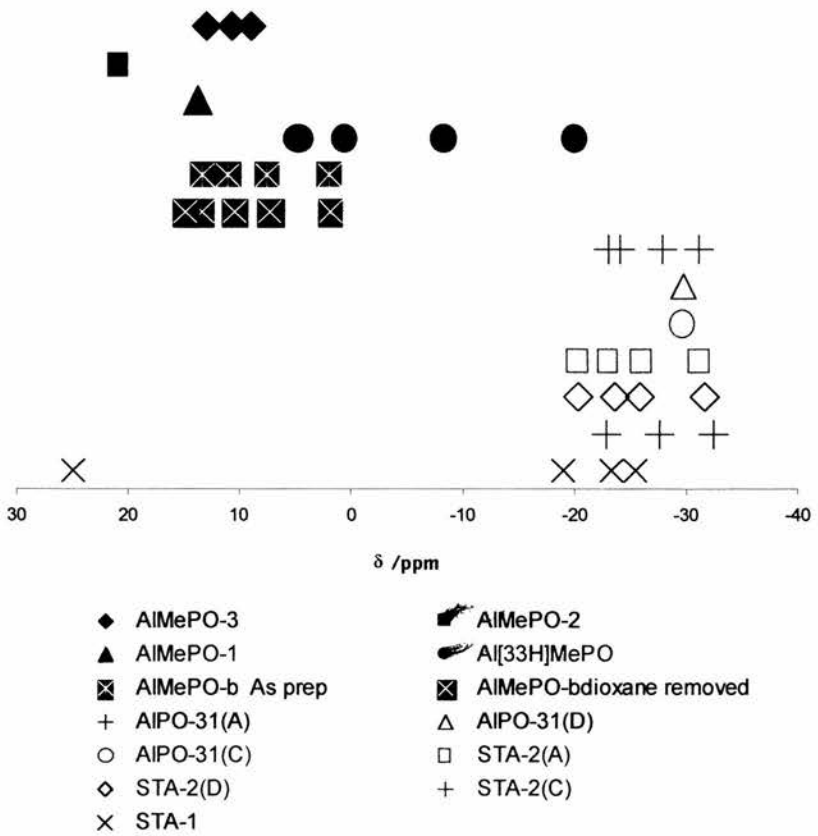

Figure 42 Plot of the ^{31}P chemical shifts for the phosphates and phosphonates in this chapter.

Al-27 Chemical Shift, Quadrupolar Parameters And Site Symmetry

One of the benefits of the MQMASNMR tcchniquc is that thc quadrupolar information is not lost in the process of achieving greater resolution. However, it appears that very little is known in practice about the way in which quadrupolar parameters relate to structure. In order to make use of NMR data, a materials chemist must be able to draw conclusions about the solid's structure from them. To this end, one of the aims of this work was to increase the amount of data available, and to attempt to derive an empirical relationship between the quadrupolar parameters and the known structural characteristics of the materials involved.

A definition of the asymmetry parameter (η) and the quadrupolar coupling constant (e^2qQ/h) in terms of the potentials around the nucleus is[7]

$$\eta = \frac{V_{xx} - V_{yy}}{V_{zz}}$$

$$eq = V_{zz}$$

where $V_{\alpha\alpha}$ are the potential tensors in the principal axis system of the quadrupolar interaction. In the case of an atom surrounded by identical ligands, the coupling constant depends on the extent to which the system has cubic symmetry (since V_{zz} is defined as coincident with the principle axis of the quadrupolar interaction, it will be zero only when perfect cubic symmetry is achieved[7]). In a similar manner, η is a measure of the degree of axial symmetry since only in that case will the x and y potentials be equal, i.e. when $\eta = 0$. Of course, the symmetry is not only a matter of the geometry of the neighbours around the atom in question, there is also the matter of the nature of the ligands to consider. However, it should be possible to correlate some measure of the geometrical symmetry around a nucleus with its quadrupolar parameters, as long as the ligands are kept as similar as possible.

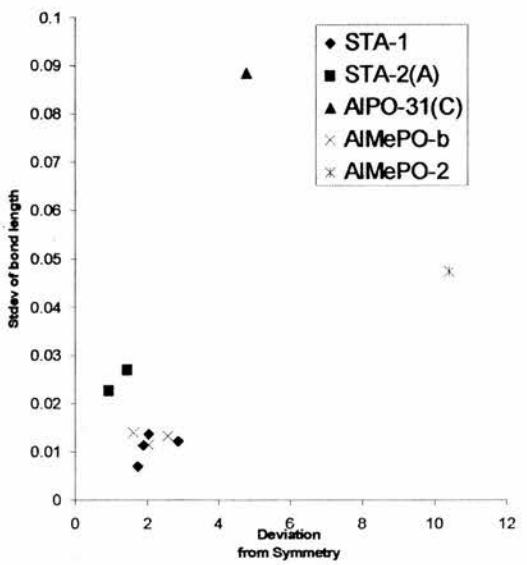

Figure 43 Graph of the correlation between the amount of variation in the Al-O bond length of tetrahedral aluminium atoms and the degree of distortion from 'perfect' symmetry.

Two possible such geometrical measures might be the standard deviation of bond length or the mean deviation from the 'perfect' angle of the bonds around the aluminium (Table 9). Since there is some correlation between these two measurements (Figure 43), either would be acceptable. However, such an empirical analysis is not possible here, even for the tetrahedral aluminium atoms, since there are too many other variables, e.g. the method of structure solution, the presence of phosphonate or phosphate groups and the uncertainty in the values of e^2qQ/h and η. Perhaps in the future, however, such a correlation will be viable.

Table 9 Various geometrical factors for the aluminium atoms in materials of known structure

Compound	Bond mean length / Å	Coordination	Deviation from perfect symmetry angle (109.5° for Tet, 90° for Oct)
STA-1	1.74	4	2.88
STA-1	1.77	4	1.90
STA-1	1.72	4	2.03
STA-1	1.74	4	1.75
STA-2(A)	1.72	4	1.45
STA-2(A)	1.73	4	0.94
AlPO-31(C)	1.69	4	4.79
AlMePO-β	1.73	4	2.05
AlMePO-β	1.73	4	1.63
AlMePO-β	1.74	4	2.57
AlMePO-2	1.82	4	10.40
AlMePO-2	1.88	5	3.05
AlMePO-1	1.90	6	3.81
AlMePO-β	1.89	6	1.57

Conclusions

The MQMASNMR results presented here have demonstrated the advantages of the technique for studies of aluminium containing materials due to its high resolution and facile extraction of field independent isotropic chemical shifts. It has been possible to examine materials with up to 7 different aluminium species with very similar chemical shifts and fully resolve them all.

However, there are several problems with the technique that inhibit its usefulness alone. The first of these is the lack of quantification in the results, a site's MQ signal intensity depending on many factors including the efficiency of excitation, a non-linear function of the quadrupolar coupling constant.[9] In addition, it is as yet impossible to transform the quantitative quadrupolar information that the technique elicits into conclusions of similar quality. Future work should concentrate on investigating ways in which the quadrupolar information can be utilised to provide further insight into the material probed with this technique.

In order to make use of the quadrupolar parameters, even on an empirical basis, a much larger database is required to allow determination of the effects of symmetry on the asymmetry parameter and e^2qQ/h. Such data should be obtained for materials of a very similar chemical nature, in the first instance, so that the number of variables is kept to a minimum. A suitable group of compounds would be the microporous AlPOs since a large number of their structures are known and the aluminium site is always tetrahedrally coordinated, unless water is present. The collection of such a database will be facilitated by the development of the MQMASNMR technique due to the relative ease of its application and speed of spectra collection.

It can not be overemphasised what a huge leap forward this technique is in the usefulness of NMR to materials scientists and many other similar groups. NMR is a technique that is complementary to diffraction techniques in its applicability to non-crystalline or poorly crystalline samples but that has been limited by the poor quality of spectra from quadrupolar nuclei. It has been shown in this chapter that that limit has been removed from many areas of investigation.

References

1 S. P. Elangovan and V. Murugesan, *Journal of Molecular Catalysis A:Chemical*, 1997, **118**, 301-309. P. Kumar, R. Kumar and B. Pandey, *Synlett*, 1995, 289-90.

2 S. H. Park, R. W. G. Kunstleve, H. Graetsch, H. Gies, *Studies in Surface Science and Catalysis*, 1997, **105**(A-C), 1989-1994.

3 *Physical Chemistry*, P. W. Atkins, Oxford University Press, Oxford, 1990.

4 H. Kessler, M. Gehrke and C. Griesinger, *Angewandte Chemie International Edition English*, 1988, **27**, 490-536.

5 *High Resolution NMR in the Solid State*, E. O. Stejskal and J. D. Memory, Oxford University Press, Oxford, 1994.

6 *NMR – A Physiochemical View* by Harris, 1983, pp.143-161

7 *Principles of Magnetic Resonance: with examples from solid state physics*, by C. P. Slichter, Harper & Row (London) 1963.

8 A. Medek, J. S. Harwood and L. Frydman, *Journal of the American Chemical Society*, 1995, **117**, 12779-12787.

9 S. Brown and S. Wimperis, *Journal of Magnetic Resonance*, 1997, **128**, 42-61.

10 L. Frydman and J. S Harwood, *Journal of the American Chemical Society*, 1995, **117**, 5367-5368.

11 *Solved Problems: Gamma and Beta functions, Legèndre polynomials, Bessel functions*, by O. J. Farrell and B. Ross, The MacMillan Company, NewYork, 1963, p 191.

12 *Spherical Harmonics: an elementary treatise on harmonic functions with applications*, by T. M. MacRobert, Metuen & Co. Ltd. (London), 1927, p 86.

13 M. E. Smith and J. H. Strange, *Measurement Science and Technology*, 1996, **7**, 449-475.

14 K. T. Mueller, B. Q. Sun, G. C. Chingas, J. W. Zwanzifer, T. Terao and A. Pines, *Journal of Magnetic Resonance*, 1990, **86**, 470-487.

15 Z. Xu and J. F. Stebbins, *Solid State Nuclear Magnetic Resonance*, 1998, **11**, 243-251.

16 L. Marinelli, A. Medek and L. Frydman, *Journal of Magnetic Resonance*, 1998, **132**, 88-95.

17 J.-P. Amoureux, C. Fernandez and S. Steuernagel, *Journal of Magnetic Resonance, Series A*, 1996, **123**, 116-118.

18 *Principles of Nuclear Magnetic Resonance in One and Two Dimensions*, by R. R. Ernst, G. Bodenhausen, and A. Wokaun, Clarendon Press (Oxford) 1994.

19 G. Hix, R. Morris and P. Wright, *Journal of the Chemical Society, Dalton Transactions*, 1998, in press.

20 L.-J. Sawers, V.J.Carter, A.R.Armstrong, P.G.Bruce, P.A.Wright and B.E.Gore, *Journal of the Chemical Society, Dalton Trans.*, 1996, 3159.

21 P.A.Wright, V.J.Carter and G. W. Noble, *Proceedings of 1996 Symposium, Responsive Inorganic Materials, 3rd Royal Society – Unilever Indo-UK Forum on Materials Science& Engineering*, in press.

22 G. W. Noble, P. A. Wright, P. Lightfoot, R. E. Morris, K. J. Hudson, A. Kvick and H. Graafsma, *Angewandte Chemie International Edition English*, 1997, **36**, 81.

23 G. W. Noble, P. A. Wright and Å Kvick, *Journal of the Chemical Society, Dalton Transactions*, 1997, 4485.

24 H.-L. Zubowa, M. Richter, U. Roost, B. Parlitz and R. Fricke, *Catalysis Letters*, 1993, **19**, 67.

25 K. Maeda, J. Akimoto, Y. Kiyozumi and F. Mizukami, *Journal of the Chemical Society, Chemical Communi*cations, 1995, 1033.

26 G. B. Hix, V. J. Carter, D. S. Wragg, R. E. Morris and P. A. Wright, *Journal of Materials Chemistry*, in press.

27 J. Rocha, Z. Lin, C. Fernandez and J.-P. Amoureux, *Journal of the Chemical Society, Chemical Communications*, 1996, 2513-2514.

28 *Metallic Shifts in NMR*, G. Carter, L. Bennett and D. Kahan, *Progress in Materials Science*, 1997, **20**, Pergammon Press (Oxford)

29 J. Klinowski, in *Encyclopaedia of Nuclear Magnetic Resonance*, Vol 5, Eds D. M. Grant and R. K. Harris, 1995 John Wiley and Sons (London), p 3095.

30 B. Morosin and R. Lynch, *Acta Crystallographica B28*, 1972, 1040.

Chapter 3

The Synthesis, Characterisation and Structure Determination of Novel Aluminium Phosphonate Materials

Introduction

Aluminium phosphonates are a relatively unexplored field of chemistry, particularly when compared to the amount of attention received by other metal phosphonates.[1-3] Many of the known metal phosphonates have lamellar structures, e.g. and zirconium phenylphosphonate,[5] the microporous structures of AlMePO-β[6] and AlMePO-α[7] being rather exceptional. Layered zirconium phosphonates with structures analogous to that of α-zirconium phosphate[8] have been developed for application in sorption and electron transport processes. Similar materials but involving other metals, e.g. V and Fe, have been employed in a variety of areas also, particularly catalysis.[9]

During the course of this work on aluminium phosphonates as potential catalysts, approximately six new phases have been observed by XRD. Of these materials, three were formed sufficiently free from impurities to allow further analysis. This chapter reports attempts made to solve the structures of, and characterise otherwise, these materials. As with most of the materials produced using hydrothermal methods, these samples were available only as powders.

Such microcrystalline solids represent a significant challenge to current methods of structure analysis. The structure solution from laboratory X-ray diffraction data of such solids, particularly for those composed of microporous frameworks or inorganic layers, remains an area of considerable activity in the current literature. Considerable success has been achieved via model-building approaches,[10,11] especially when supplemented by structural data from other sources. It has also been shown that structures of moderate complexity can be solved using direct methods from powder diffraction data. Originally, high resolution data from synchotron sources[12] were required to allow *ab initio* structure solution of powder samples. Recently, however, improvements in the quality of laboratory X-ray diffraction instruments have brought success from this source also.[13-16]

The structural characterisation in this chapter utilises laboratory XRD data together with direct methods, model building and simulated annealing (SA) in attempts to solve the structures of microcrystalline samples. The technique of SA is based upon the idea that a structural model can be changed incrementally with a view to increasing the degree to which the calculated pattern from this structure and the experimental profile fit each other. Such is also the basic premise of Rietveld refinement. The difference between these two methods is that Rietveld refinement relies upon there being a clear, 'downhill' path from the starting model to the global minimum solution of the parametric surface.

Thus, Rietveld refinement requires the starting model to be close to the true solution to avoid being caught in local minima that do not represent the true structure of the material. SA, in contrast, starts from a model that often has very little similarity to the solution of the structure. Progress is made towards a solution by random changes to the model such that either the profile fit improves or the deterioration is within some predetermined limit. It is the ability to accept changes that cause a worsening of the profile fit, below some reasonable limit, which gives the technique its power. Acceptance of changes which cause a reduction in the figure of merit mean that the refinement is able to leave local minima in search of the true global minimum. It is usual to increase the likelihood of reaching the global minimum by reducing the 'temperature' (this is the value of acceptable deterioration in the profile fit for a single step) as a function of the number minimisation steps.[17]

The attempts at solving the structures of the three pure new materials synthesised are reported in this chapter. The first, AlMePO-1, was characterised completely in a very satisfactory manner. The second, AlMePO-2, was rather more difficult and, while an acceptable model has been obtained, there is a little doubt about some of its features. The third material, AlMePO-3, was not solved, despite receiving the greatest attention of all three samples.

Experimental

Density measurements were performed on ~3-5 mg of sample. The material was mixed with 1-2 cm^3 of 1-bromobutane (d = 1.44 g cm^{-3}) in which it sank to the bottom. Iodomethane (d = 2.28 g cm^{-3}) was added very slowly, allowing each drop to mix thoroughly before adding the next, until the sample hung in suspension in the liquid. At this point the liquid is assumed to be of the same density as the solid. Two 1 cm^3 aliquots of the suspension were weighed and the mean value taken as the density of the sample.

Powder X-ray diffraction was performed on a STOE STADIP diffractometer with a linear position sensitive detector covering 6° in 2θ and employing Ge monochromated Cu-Kα_1 radiation (λ=1.54056 Å). Samples were prepared by mounting in a glass capillary or between two sheets of milar as rotating discs in the X-ray beam. X-ray fluorescence analysis was performed using a Philips PW 1450/20 X-ray spectrometer using Rh-Kα radiation. Scanning electron microscopy (SEM) and energy dispersive X-ray (EDX) measurements were performed on a JEOL JSM-35CF microscope with an accelerating voltage of 10kV fitted with a LINK AN 10000 EDX system. For the purposes of determining the Al:P ratio (for AlMePO-3), the ratios of the EDX peak intensities were calibrated with respect to materials of known composition, AlMePO-β, AlMePO-1 and AlMePO-2 whose Al:P ratios had been characterised in a different manner. Thermal gravimetric analysis (TGA) was performed on a TA Instruments SDT 2960 Simultaneous DTA-TGA. Heating rates were 10 °C min^{-1} and inert atmospheres were used in all cases. Infra-red spectra were recorded on a wavelength dispersive instrument, and the sample prepared as a suspension in Nujol mull.

Unless explicitly stated otherwise, ^{13}C, ^{31}P and ^{27}Al NMR were performed using Magic Angle Spinning (MAS) on a Bruker 400 MHz spectrometer. Some MASNMR (mentioned in the text) and all the MQ MASNMR experiments (see Chapter 2) were performed using a Bruker MSL500, at 11.75 T with rf field of approximately 0.01 T.

Synthesis

In general, AlMePO-1, AlMePO-2 and AlMePO-3 were synthesised under hydrothermal conditions from a homogeneous gel made from aluminium hydroxide hydrate (Aldrich), methyl phosphonic acid (Avocado) and water. Exploratory syntheses in the aluminium hydroxide-methylphosphonic acid system using a range of conditions revealed a wealth of new phases. The three materials produced phase-pure, AlMePO-1,[18] AlMePO-2 and AlMePO-3, were synthesised without mineralising agents. In a general form of the synthesis aluminium hydroxide, methylphosphonic acid and water

were reacted in a hydrothermal gel at temperatures of 160 to 210 C, for between 2-3 days, in a PTFE lined stainless-steel autoclave. The contents were filtered, thoroughly washed with distilled water (~40-80 cm^3) and dried in air at ~60 °C.

Table 1 Syntheses in the Aluminium methylphosphonate system

Compound	Al:P:H_2O:R ratio	Temperature / °C	Duration / days
AlMePO-1	1:1:40	160	2
AlMePO-2	1.5:1:52	220	2
AlMePO-3	1:1.5:40	220	3

Results

During the course of the work on AlMePO-β several (6-7) new phases were produced. Of these, three were crystallised in a form pure enough for attempts to determine their structure to be made. These have been named in the order of their discovery as AlMePO-1, AlMePO-2 and AlMePO-3, using a different system than the α, β terminology as the first to be fully characterised was lamellar rather than microporous.

AlMePO-1

Structure Solution[a]

The X-ray powder diffraction pattern was indexed using the Visser indexing package,[19] giving a monoclinic unit cell with a =9.474 Å, b =7.07Å,c =7.865Å and β = 106.6°. Systematic absences indicated the space group to be $P2_1/a$. Subsequent data analysis, structure solution and Rietveld[20] structure refinement were performed using both the GSAS package[21] and the structural modelling routines within the INSIGHT software[22] and also the SIRPOW direct methods program.[23]

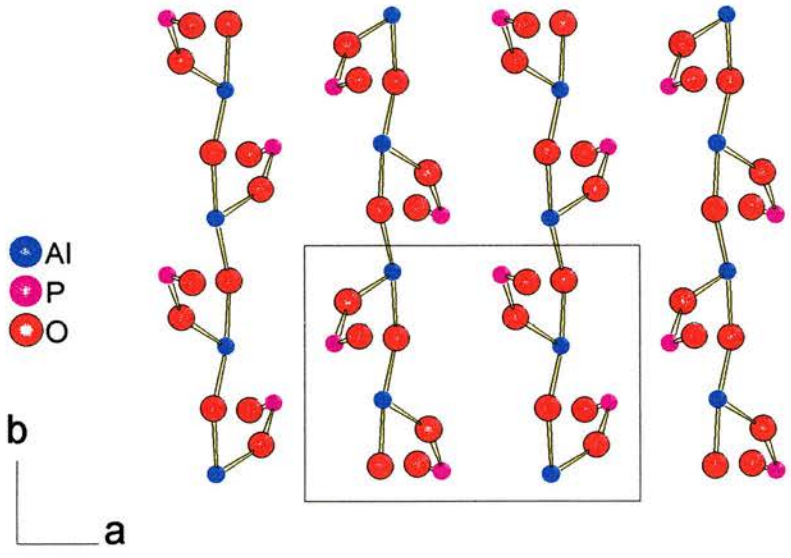

Figure 1 View along (001) of the atom positions obtained from SIRPOW using a range of 10-75° in 2θ.

[a] The work on this material was performed in collaboration with Lesley-James Sawers who performed much of the structure solution analysis.

GSAS was used to extract reflection intensities from the diffraction pattern using the method of LeBail.[24] These were input into SIRPOW for analysis using direct methods and the 2θ ranges 10 - 60°, 10 – 70° and 10 - 80° examined in the default mode. It was necessary to use less than the full range of data because at high scattering angles the overlap of peaks becomes very great reducing the reliability of the extracted intensities. INSIGHT operating on a Silicon Graphics terminal was used to view the resulting sets of suggested atomic positions (Figure 1). It was possible to assign electron density peaks directly to 1 Al, 1 P and 3 O atoms. (On comparing with the complete structure (Figure 5) it is noticeable that one of the most important aspects of the structure, the Al-O-Al chain, was obtained by direct methods alone. The structure solution was much more straightforward as a result of starting from a model containing such a defining characteristic of the final structure.)

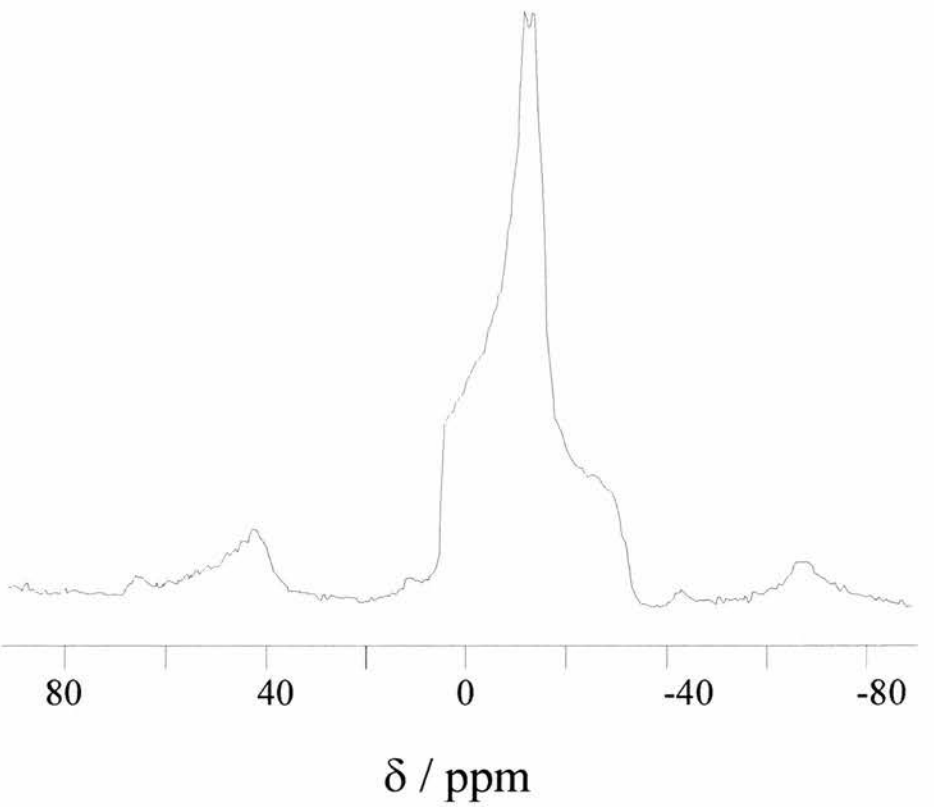

Figure 2 ^{27}Al MASNMR spectrum of AlMePO-1 showing one site of the typical lineshape and chemical shift for a distorted octahedral environment.

^{27}Al (Figure 2), ^{31}P and ^{13}C MASNMR indicated the presence of one aluminium, one phosphorus and one carbon environment. Phosphorus gave a resonance at 13.55 ppm that is within the range of phosphorus resonances observed for other aluminium methyl phosphonates.[6] Aluminium gave an asymmetric peak that is characteristic of a quadrupolar nucleus in a distorted octahedral environment.[25] Fitting of the peak shape gave an asymmetry parameter = 1.0, a quadrupolar coupling constant = 5.86 MHz and an isotropic chemical shift of -0.16 ppm. The carbon signal was a doublet (J = 139.5

Hz) of chemical shift 15.23 ppm. Both the splitting and the chemical shift are within the ranges observed for other aluminium methylphosphonates.[26,27] Since the phosphorus was assumed to be present as methylphosphonate (the conditions of the synthesis are insufficient to break the P-C bond or otherwise greatly change the phosphonic acid species present in the gel), three oxygens and a carbon were required to complete the connectivity of that species. Only two oxygens of the oxygens were present in the starting model obtained from SIRPOW. Therefore the starting model was missing at least one oxygen and a carbon.

The bonds within the model were constrained using soft constraints of the appropriate lengths for this type of material (the structures of AlMePO-β and AlMePO-α and work by Poojary *et al*[28] were used to provide this information). The atom positions were refined to convergence and difference Fourier plots used to find possible positions for electron density so far unaccounted for, i.e. that from the carbon and oxygen known to be missing from the model. Of the several peaks in the plot, only one was consistent with the rest of the structural model. The position of the peak indicated that it was a bridging oxygen rather than a carbon atom. Refinement was continued after adding the extra oxygen to the model together with appropriate constraints. Another difference Fourier plot revealed another consistent peak near the aluminium atom. This was added to the model as an oxygen later found to be part of a water molecule bonded to the aluminium.

After allowing the refinement to reach a point near to convergence, the INSIGHT suite was used to model a tetrahedral arrangement of atoms around the phosphorus such that three of the vertices coincided with the three oxygens. The fourth position was input as the missing carbon atom. Constraints were also added to control the angles between adjacent groups around the phosphorus and aluminium atoms. Refinement was continued until convergence.

Table 2 Bond valence sum calculation results for AlMePO-1

Atom	Valence Sum
Al1	3.09
P1	4.66
O1	1.74
O2	0.33
O2 (assuming modelled hydrogens for H2O)	1.43
O3	1.07
O3 (assuming part of hydroxyl group)	1.63
O4	1.83
O5	1.90

Attempted refinement of the isotropic temperature factors was successful for all but one oxygen and the carbon which tended towards negative values. Bond valence sum calculations[29] (Table 2) indicated that the non-bridging oxygen attached to the aluminium should have two hydrogens bonded to it and that one of the bridging oxygens was a hydroxyl group. Further modelling was used to place hydrogen atoms around the carbon, completing a tetrahedron, and adjacent to the two oxygens to give a hydroxyl group and a water molecule. The distances and arrangements of these atoms were constrained and the hydrogen positions refined, the other atoms having been fixed in place. Subsequent to this refinement it was found that it was possible to refine the isotropic temperature factors of the OH oxygen and the carbon to positive values.

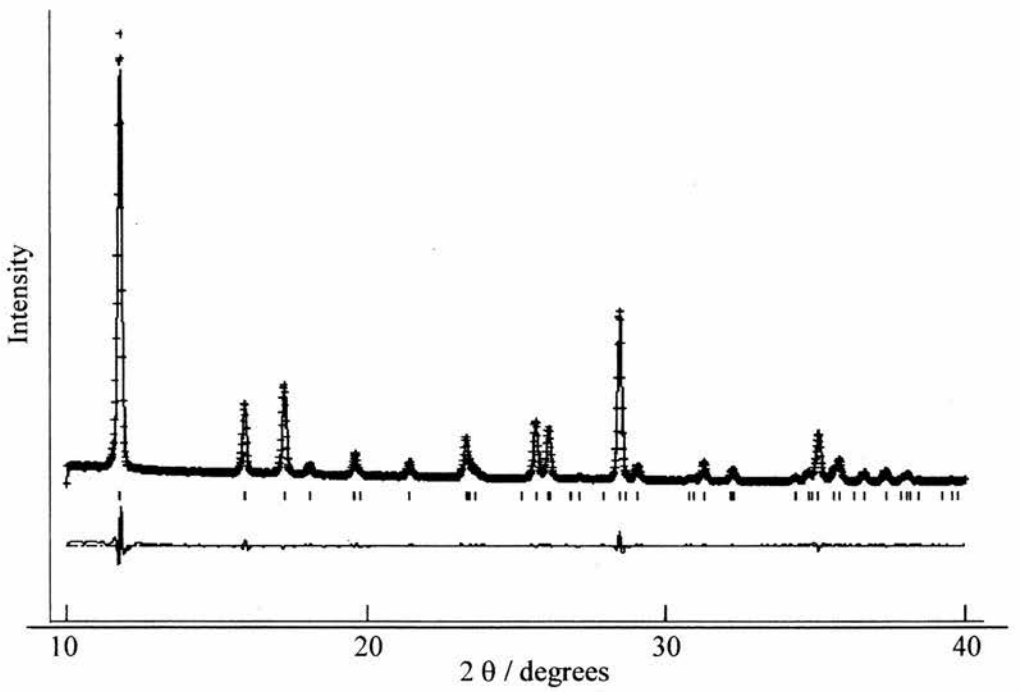

Figure 3 Diagram showing the profile fit (10-40°) from the final Rietveld refinement (χ^2 = 5.39 and RWp = 7.85%).

Finally, all constraints except those on the C-H and O-H bond lengths were removed for the final refinement of 63 variables. The final fit resulted in reduced χ^2 = 5.39 and RWp = 7.85%. The profile fit and difference plot are shown in Figure 3 and Figure 4. Figure 5 shows a representation of the structure of the material.

The final unit cell composition is $[Al(OH)PO_3CH_3.H_2O]_4$. The ratio of aluminium to phosphorus was as determined by X-ray fluorescence measurements (1:1.02). Thermogravimetric and differential thermal analysis (TGA and DTA) revealed two separate endothermic events at 325 °C and 370 °C corresponding to weight losses of 12.5 % and 5.1 % respectively (Figure 6). The first event is assigned to the loss of water from the structure (theoretical mass loss for this is 11.6 %) and the second to a dehydroxylation reaction in which the OH groups combine to create a water molecule

and a oxygen. The newly formed water leaves the structure whilst the oxygen remains bound to the solid. Such a scenario gives a calculated total mass loss of 17.6 % compared with the 17.4 % observed. The presence of O-H bonds within the structure is substantiated further by the infra-red spectrum which reveals two sharp peaks at 3480 cm^{-1} and 3650 cm^{-1} and a broad absorbance characteristic of hydrogen bonded OH at ~3300 cm^{-1}.

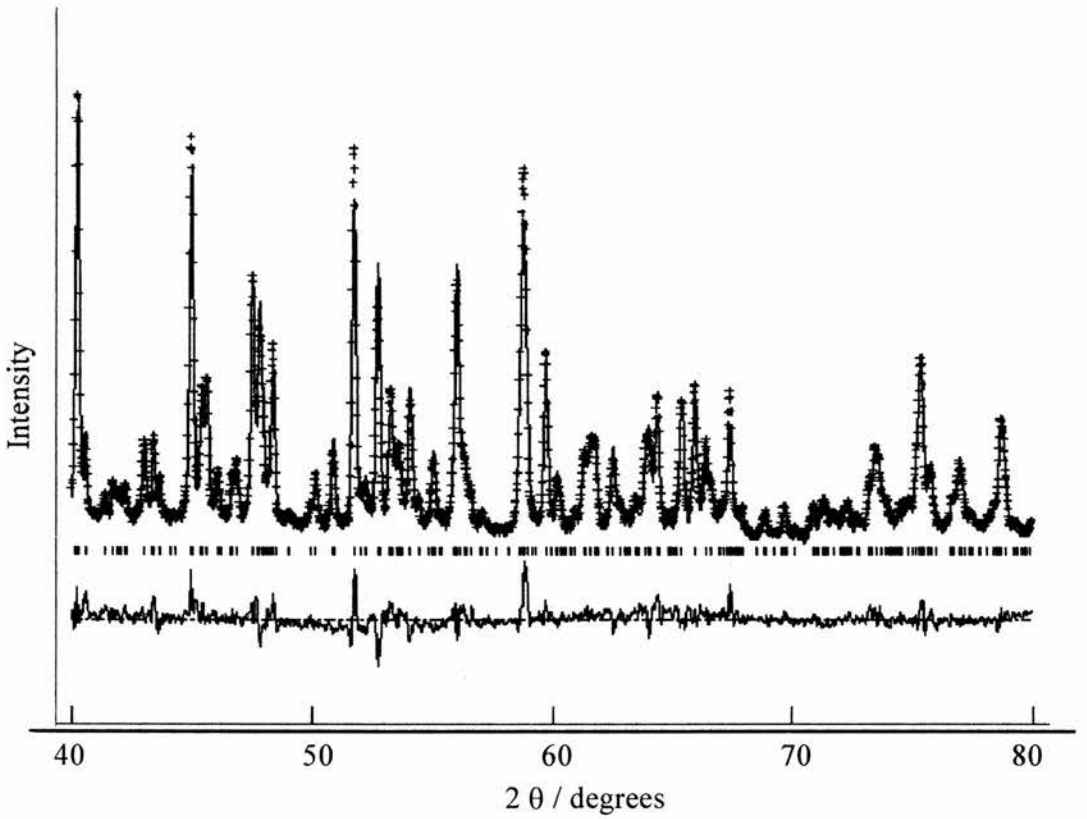

Figure 4 Diagram showing the profile fit (40-80°) from the final Rietveld refinement (χ^2 = 5.39 and RWp = 7.85%).

The AlMePO structure (Figure 5) is made up of layers which contain chains of AlO_6 octahedra, crosslinked by phosphonate groups, the methyl groups of which point upwards and downwards from the inorganic sheet. The chains of corner-sharing AlO_6 octahedra run parallel to the b-axis; the aluminium methyl phosphonate layers are stacked obliquely along the c-axis.

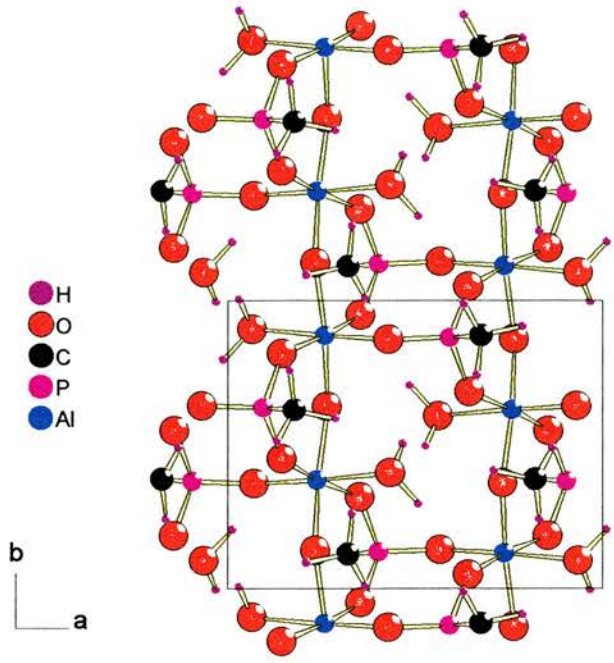

Figure 5 View of one layer of the structure of AlMePO-1 along the [001] axis.

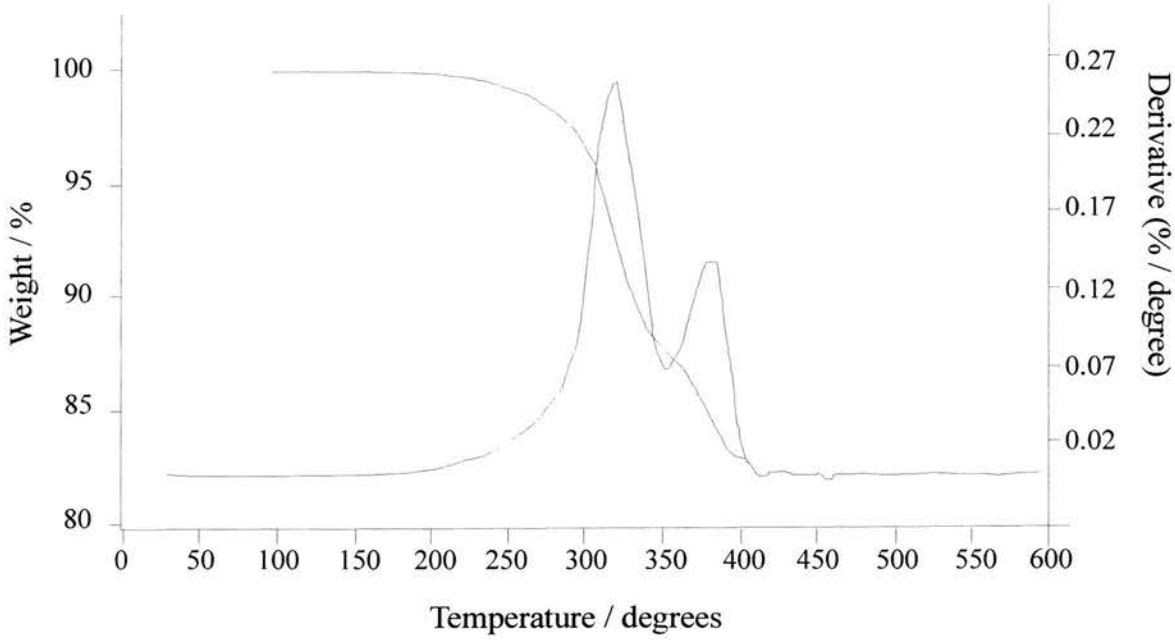

Figure 6 TGA of AlMePO-1 showing two separate weight loss events at 325 °C and 370 °C due to water desorption and dehydroxylation respectively.

Each chain of octahedra consists of a quasi-linear array of aluminiums linked by bridging hydroxyls, with Al-O-Al angles of 140° and Al-Al distances of 3.54Å. In addition to these oxygen links, each aluminium is connected to its two neighbours on the chains by phosphonate bridges (Al-O-P-O-Al). Moving along a chain, each successive phosphonate group is translated and rotated 180° from the last by the screw axis running through the aluminiums. This results in methyl groups pointing up and

down from successive phosphonates. As well as bridging two aluminium octahedra in the same chain, each phosphonate is linked to an octahedron in the chain adjacent. This gives a planar network of stacked chains of aluminium octahedra linked within chains by bridging oxygens and phosphonate tetrahedra and interchain only by phosphonates. The lower and upper surfaces of the layers are covered partially with methyl groups. Within the layers there is a cavity in the framework created by a ring of 12 atoms: two pairs of hydroxyl bridged aluminiums and four oxygens and two phosphorus atoms from two linking phosphonates (Figure 2b) and making up the octahedra coordination of the aluminiums, two water molecules protrude into the cavity.

AlMePO-2

Structure Solution[a]

The structure solution of this material followed a similar route to that of AlMePO-1. The powder XRD pattern was indexed using Visser, as for AlMePO-1, with an orthorhombic unit cell of dimensions : a=19.733 Å, b = 10.154 Å, c = 5.148 Å, volume = 1031 $Å^3$. Determination of the symmetry was ambiguous with there being some doubt about whether *Pmnb* or $P2_1nb$ was the true space group. During the structure solution, however, the centrosymmetric group, *Pmnb*, produced the most chemically sensible model and was used henceforth. Intensities were extracted from the pattern using the method of LeBail[24] implemented within the GSAS[21] package. These were input into SIRPOW[23] and several runs performed using the ranges 10°-80°, 10°-75°, 10°-70°, 10°-65°, 10°-60°, 10°-55° and 10°-50°. The best results (a value of R=23%) were obtained from the 10-80° range. The first five peaks (Figure 7) were examined using the INSIGHT suite running on a Silicon Graphics terminal.

^{27}Al, ^{31}P and ^{13}C MASNMR recorded on a Bruker 400 spectrometer revealed the presence of one phosphorus environment and two aluminium environments. The aluminium signals are broad with apparent, approximate chemical shifts of 25 ppm and 6 ppm. However, it was not possible to model the lineshapes for this spectrum and the chemical shifts are unavoidably inaccurate. These approximate chemical shifts were assigned as a tetrahedral aluminium and a five-coordinate species respectively. Since O3 bridges two other oxygens, each ~1.9 Å away, it was decided that this was more likely to be aluminium and was changed accordingly. [Subsequent work using 5Q ^{27}Al MASNMR (see Chapter 2) has caused some doubt about these conclusions. This will be discussed later. The single quantum ^{27}Al MASNMR spectrum is shown in Figure 8] The

[a] The work on this material was performed in collaboration with Lesley-James Sawers who performed much of the structure solution analysis.

change of O3 from oxygen to aluminium gives a ratio, Al:P, of 1.5:1 which is consistent with the X-ray fluorescence result indicating a ratio of between 1.5 and 1.75.

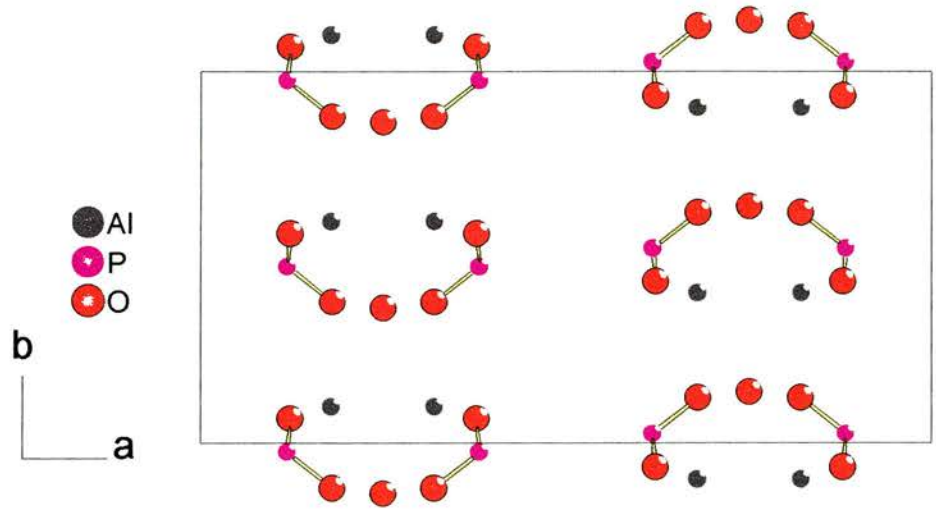

Figure 7 Starting model used - first five most intense peaks output from SIRPOW using the 10-80° range of data for AlMePO-2.

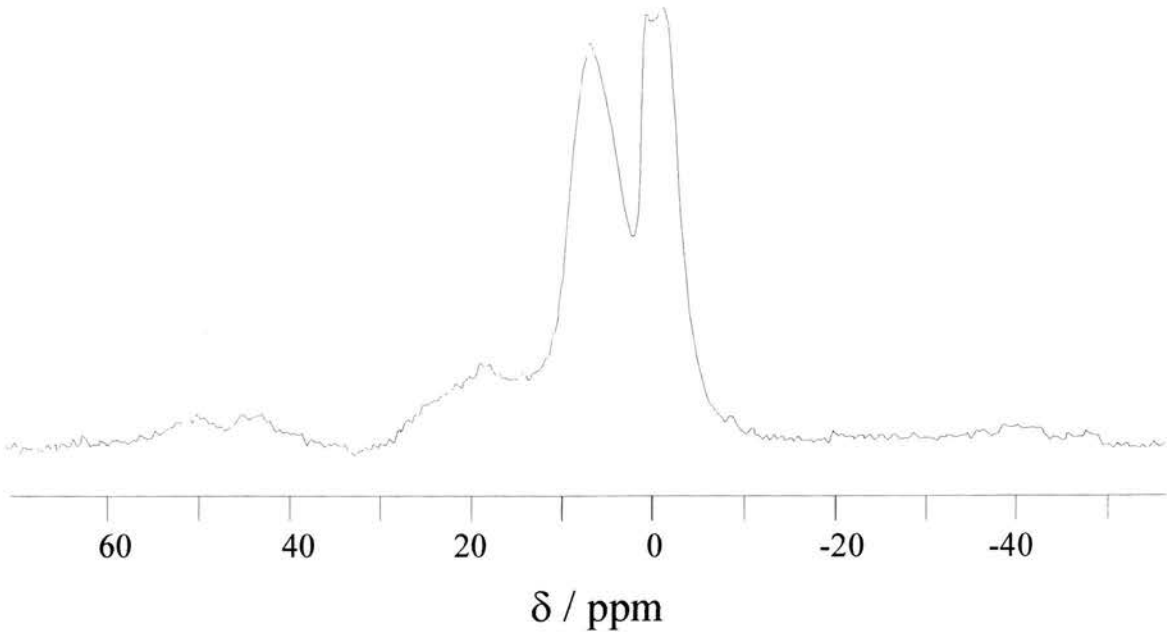

Figure 8 ^{27}Al MASNMR of AlMePO-2 recorded on a MSL500 spectrometer. Note the splitting, on the right hand most peak, indicating an asymmetry parameter of zero.

Due to the lack of firm evidence for the coordination state of each aluminium, constraints were placed only upon the bond lengths, not the geometric arrangement of atoms. Rietveld refinement[20] was carried out under these conditions until convergence giving the structure shown in Figure 9. In a similar manner to that used for AlMePO-1, an iterative process of refinement and difference Fourier plots were used to find atoms that were missing from the model. In total, three more oxygen atoms and the carbon were detected in this way. Again, it was necessary to generate hydrogen atoms around the carbon by modelling using INSIGHT. The inclusion of the hydrogen atoms improved the refinement of the temperature factor for carbon as well as giving a better quality fit to the profile. All the temperature factors were refined (except for the hydrogens) and fractional occupancies were varied. In those cases in which changes in the occupancy caused little improvement in the fit, or when the occupancy change was very low, the values were reset to 1.0 and not allowed to vary henceforth. The only atom found to have an occupancy different from unity was O2, thought to belong to a water molecule (see below). The final fit gave $\chi^2 = 6.5$ and RWp = 10.6%. Difference plots (Figure 10 and Figure 11) are given below. Other data are available in Appendix I.

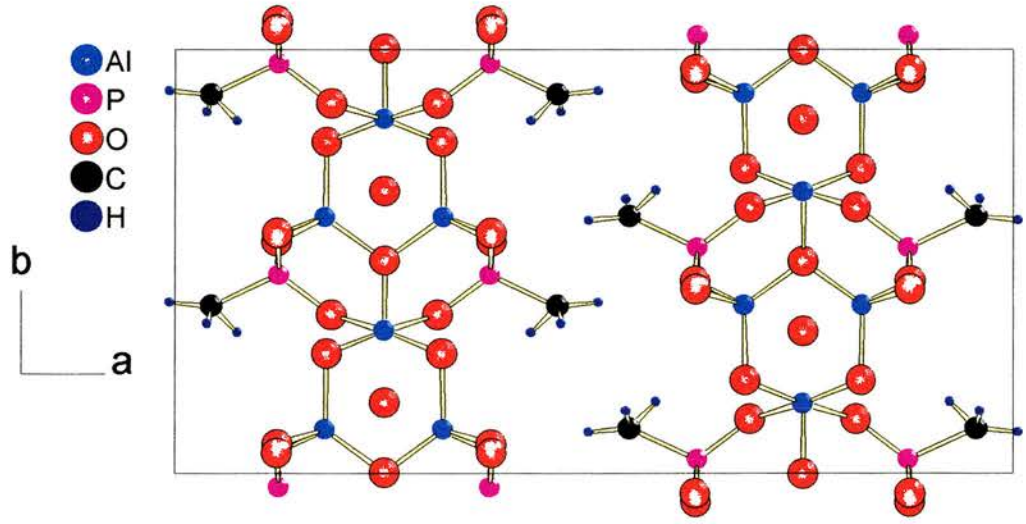

Figure 9 Representation of the structure of AlMePO-2 viewed along the (001) axis. The non-bonded oxygen is part of a water molecule

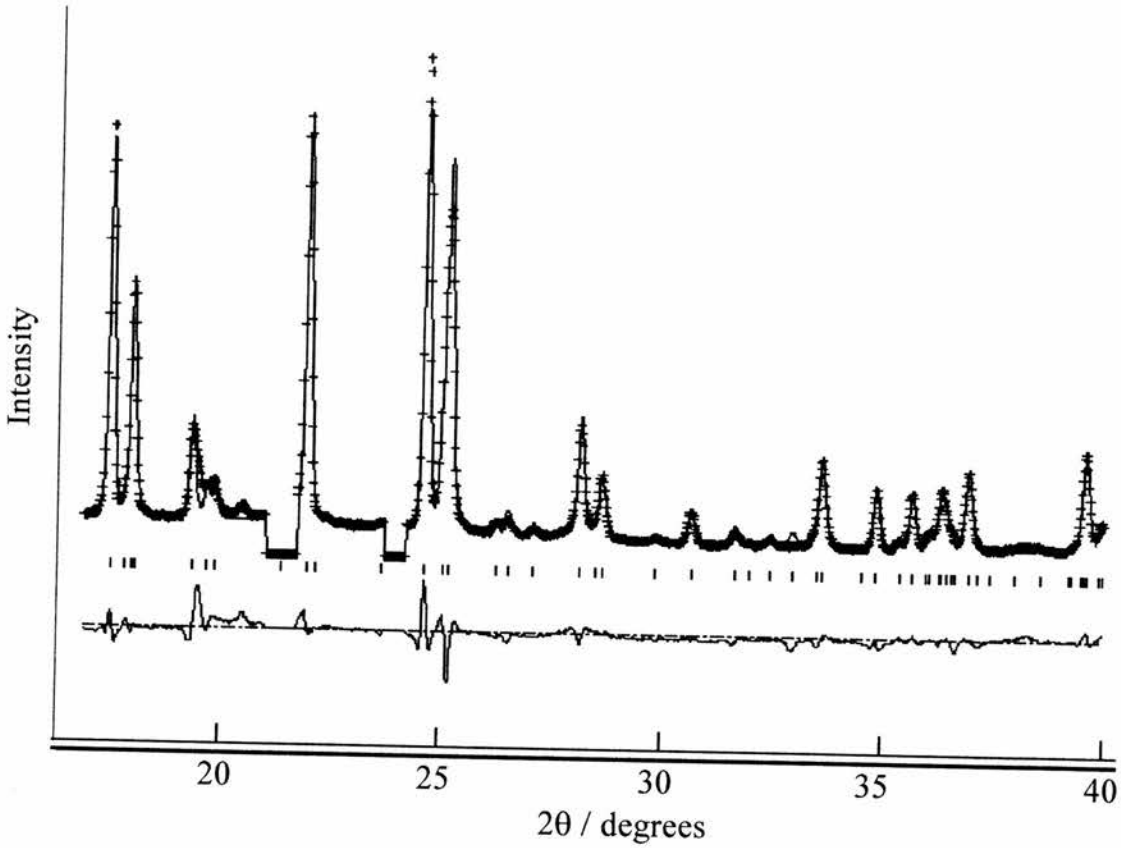

Figure 10 **Final profile fit from Rietveld refinement for AlMePO-2, χ^2 = 6.5 and RWp = 10.6%, range 16-40°.**

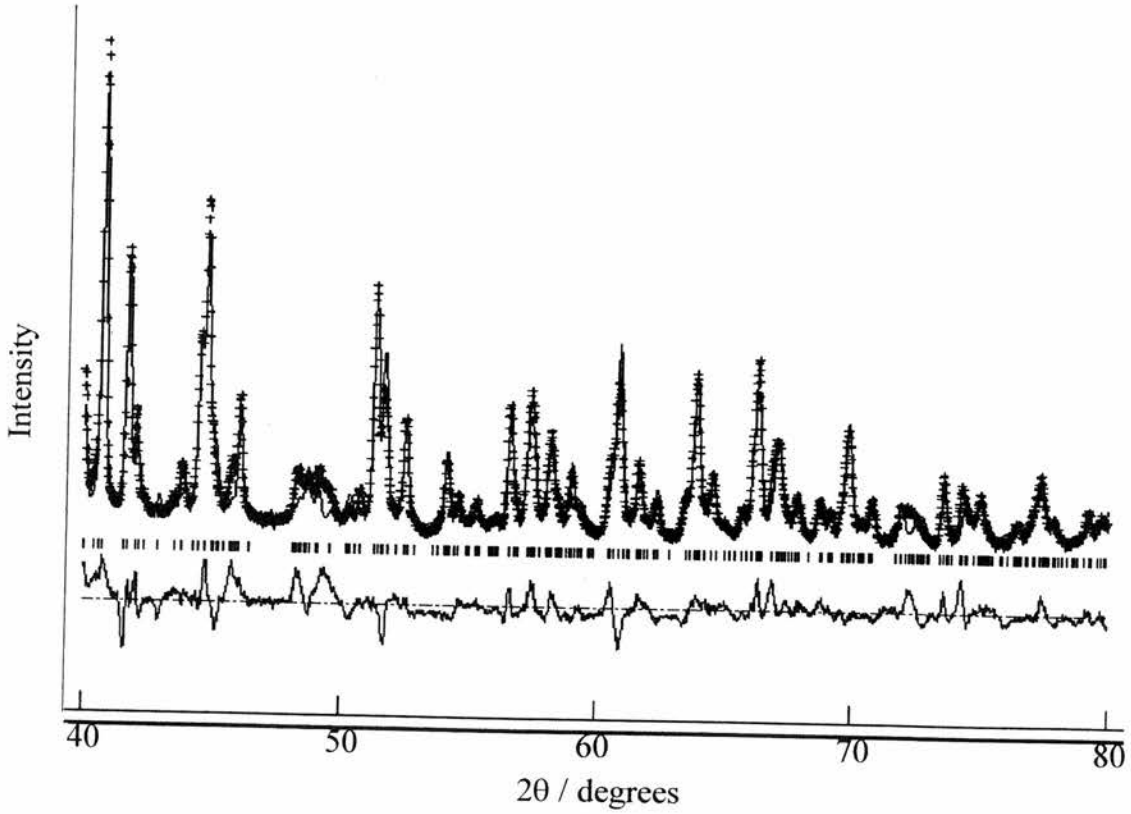

Figure 11 Final profile fit from Rietveld refinement for AlMePO-2, χ^2 = 6.5 and RWp = 10.6%, range 40-80°.

Bond valence calculations were performed on the Al, P and O atoms (Table 3). It was found that O4 and O5 gave better values as hydroxyl groups. Although O4 is unusual in it's triple coordination to aluminium there are examples in the literature of such behaviour for hydroxyl groups. Morosin and Lynch[30] reported the existence of such a species during studies on Al_2TiO_5. Also, three coordinate oxygen species have been encountered in aqueous chromium chemistry in which a wide variety of oligomers are formed.[31] In all these cases, the oxygen is part of a hydroxyl group, supporting the conclusion reached from the bond order calculations. O2 is assumed to be a water molecule and calculations are made on this basis. It is worth noting again that this site appears to be only ~70% occupied.

The structural formula calculated on the basis of the above adaptations to the structure is $Al_{12}[(CH)_3PO_3]_8(OH)_{12}\cdot 3H_2O$. This reduces to $Al_3[(CH)_3PO_3]_2(OH)_3\cdot 0.75H_2O$. The calculated density for this formula is 2.15 g cm^{-3} compared with the experimental value of 2.05 ± 0.1 g cm^{-3} providing very good agreement.

Table 3 Bond order calculations on selected atoms in the AlMePO-2 structure. O2 is assumed to be water (with bond lengths from CRC Handbook of Chemistry and Physics[32]) and calculated accordingly.

Atom	Bond Order
Al1	2.84
P1	4.42
Al2	2.65
O1	1.75
O2	1.92
O3	1.97
O4	1.92
(as hydroxyl)	
O5	1.21
O5	2.00
(as hydroxyl)	
O6	1.61

The structure of AlMePO-2 is a double lamellar material, each layer arranged in an anti-parallel 'herring-bone' fashion. In common with almost all lamellar metal phosphonates, the organic groups line the surfaces of an inorganic core to each layer. Thus the spacing of the layers depends upon the particular phosphonate group present in the material. In AlMePO-2, the layer spacing is ~9.8 Å, considerably larger than for AlMePO-1 (7.85 Å). This difference is due to the unusual arrangement of the methyl groups in AlMePO-1 which fit inbetween each other forming an interlocking array.

Each AlMePO-2 layer is made up of edge sharing aluminium tetrahedra linking, by corner sharing oxygen vertices, single AlO_5 square-based pyramids. The chain of linked aluminium polyhedra is also bridged by a phosphonate group. The phosphonate tetrahedra share vertices with two aluminium polyhedra in the same chain whilst

bridging the distance to another alumina chain adjacent. In this way, it is the phosphonate groups that are responsible for giving a two-dimensional aspect to the structure, rather than an array of one dimensional chains (Figure 12).

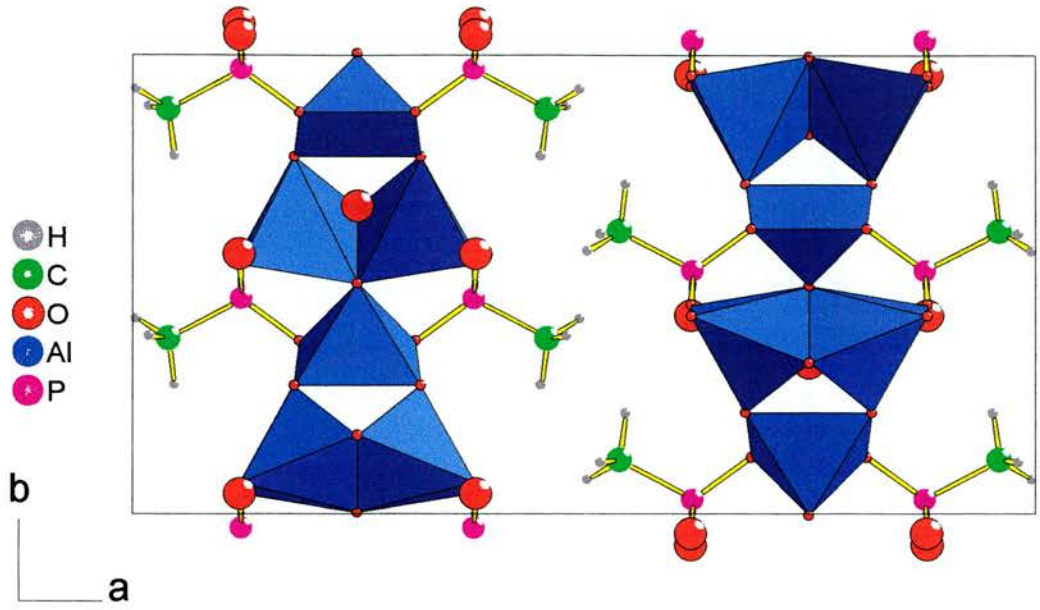

Figure 12 View of AlMePO-2 showing the arrangement of chains of linked aluminium polyhedra which make up the central portion of each layer.

Despite the compelling beauty of the structure, there are several problems with the solution obtained for this material. As mentioned above, more work has been performed using 2-dimensional ^{27}Al 5Q MASNMR spectroscopy to investigate AlMePO-2 since the completion of the structure solution described above (see Chapter 2 for more details). It is possible using this technique to obtain isotropic chemical shifts, even from peaks as broadened by quadrupolar interactions as are those from AlMePO-2. The values obtained for δ_{iso} are 10.8 ppm and 3.1 ppm. The normal range for tetrahedral aluminium is 35-45 ppm and for 5 coordinate 0-15 ppm. Whilst the updated NMR data do support the presence of the five coordinate species, there is no evidence that the material contains tetrahedral aluminium.

In addition to the extremely strong counter evidence of the MQMASNMR, the TGA results (Figure 13) also undermine the proposed structural model. There is a mass loss of ~8 % in an event centred upon 450 °C. It is known that there is no occluded organic material within the crystal as only a single resonance was observed for ^{13}C MASNMR. The desorption is most likely to be due to water molecules leaving the structure. Since this material is very similar to AlMePO-1 in composition it would be expected to decompose under heat in a similar manner. The unit cell contains 3 water molecules and

12 hydroxyl groups. A loss of 8 wt% corresponds to ~6 water molecules per unit cell. If, as in AlMePO-1 at ~350 °C, there is a dehydroxylation reaction, the hydroxyl groups would give rise to 6 molecules of water. However, there are also the 3 water molecules which would desorb more readily than a dehydroxylation would occur so there is not an easy explanation of the TGA results. It is possible to formulate mechanisms to explain the desorption of 6 water molecules from the structure but all such theories rely upon the rather weak assumption that only a fraction of the hydroxyl groups available in the model actually undergo dehydroxylation. Whilst the TGA data do not constitute contradictory evidence of the proposed structure, as do the MQMASNMR data, neither do they support that case.

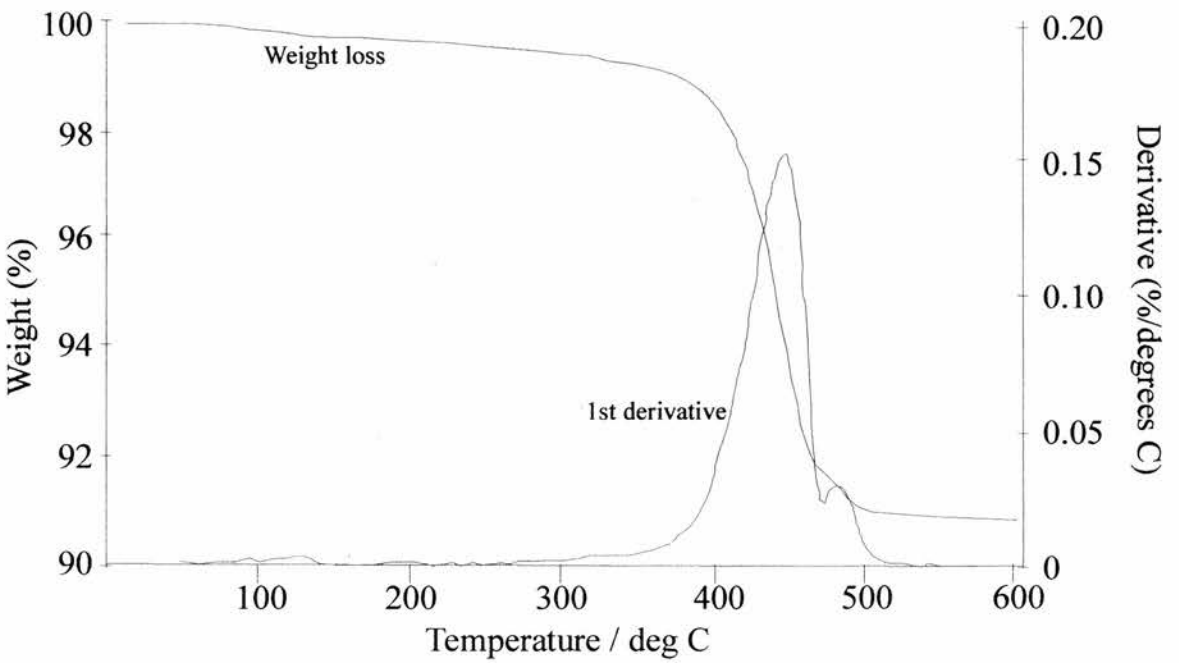

Figure 13 Thermogravimetric analysis (TGA) results of AlMePO-2 in dry N_2.

The proposed structure does give a reasonably good fit to the XRD data and is a self-consistent model. However, the fit is not good enough to be conclusive and the evidence against the model is strong enough to cause considerable doubt, as is the number of unusual, albeit precedented, features of the structure. In view of this further work should include an attempt to solve this material's structure from microcrystal data. It would be instructive to ascertain to what extent the structure proposed in this work is valid.

AlMePO-3

Attempted Structure Solution

The XRD pattern was indexed with the Visser program as a triclinic unit cell with parameters, a = 9.644 Å, b = 12.374 Å, c = 5.063 Å, α = 91.14°, β = 90.36°, γ = 92.13°, volume = 604 $Å^3$. (See Figure 14 and Figure 15 for plots showing the relative positions

of the calclulated reflections and the experimental data.) EDX measurements indicated that the Al:P ratio was the same as for AlMePO-β, i.e. 1:1.5. A measurement of the density (1.87 ± 0.03 g cm^{-3}) is in agreement with the unit cell containing 4 Al atoms, 6 P atoms, 6 methyl groups and 18 oxygens. (Since the TGA shows no significant mass loss the sample does not adsorb water and this can be eliminated from the unit cell contents.) The calculated density of such a system is 1.84 g cm^{-3}. As MASNMR (see below) indicated the presence of 2 aluminium sites and 3 phosphorus sites, the space group must be $P\bar{1}$ in order to generate the correct number of atoms.

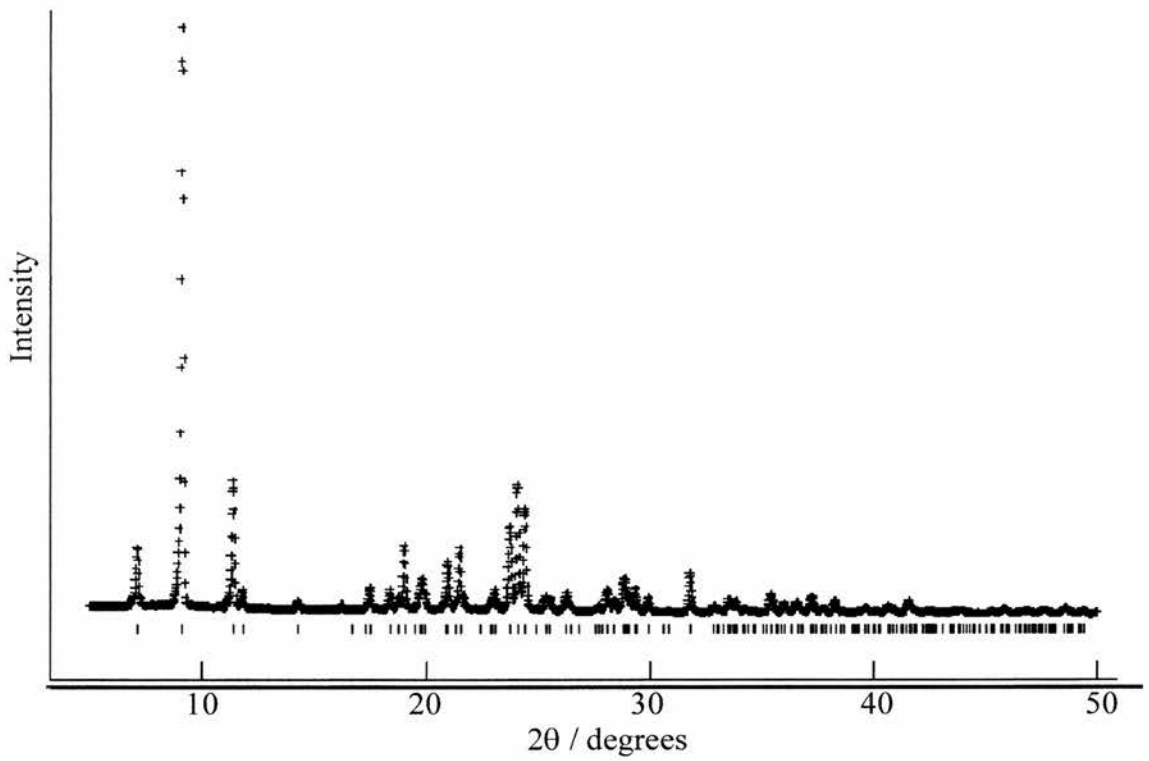

Figure 14 Plot of the XRD for AlMePO-3 showing reflection positions calculated from the indexed cell (a = 9.644 Å, b = 12.374 Å, c = 5.063 Å, α = 91.14°, β = 90.36°, γ = 92.13°).

^{27}Al and ^{31}P MASNMR (Figure 16) indicated the presence of 2 aluminium sites and three phosphorus sites. Aluminium-27 resonances were observed at 43 ppm and 14.5 ppm in the single quantum spectrum. Measurements of isotropic chemical shift were obtained from 5Q MASNMR : δ_{iso} = 44.9 ppm and 15.5 ppm with higher field peak (44.9 ppm) being broader than the other. The chemical shift of this resonance is correct for a tetrahedral environment. The other peak (15.5 ppm), however, is more difficult to assign as it is in the region normally associated with five-coordinate species but is a very narrow and symmetric peak, indicating a high degree of axial symmetry. However, it is very unlikely that this peak is due to an octahedrally coordinated aluminium. Indeed, if one assumes that aluminium is connected, *via* oxygen, to phosphorus only, i.e. rather than there being Al-O-Al bonds in the structure, it is impossible for the

second aluminium environment to be anything but 5 coordinate given the calculated contents. The ratio of Al:O is 1:4.5 which allows for one aluminium to be tetrahedrally coordinated and the other to be penta-coordinate. The assumption of no Al-O-Al bonds is of limited validity since both AlMePO-1 and AlMePO-2 contain examples of these. However, the narrow, symmetric shape of the 15.5 ppm resonance argues that, not only

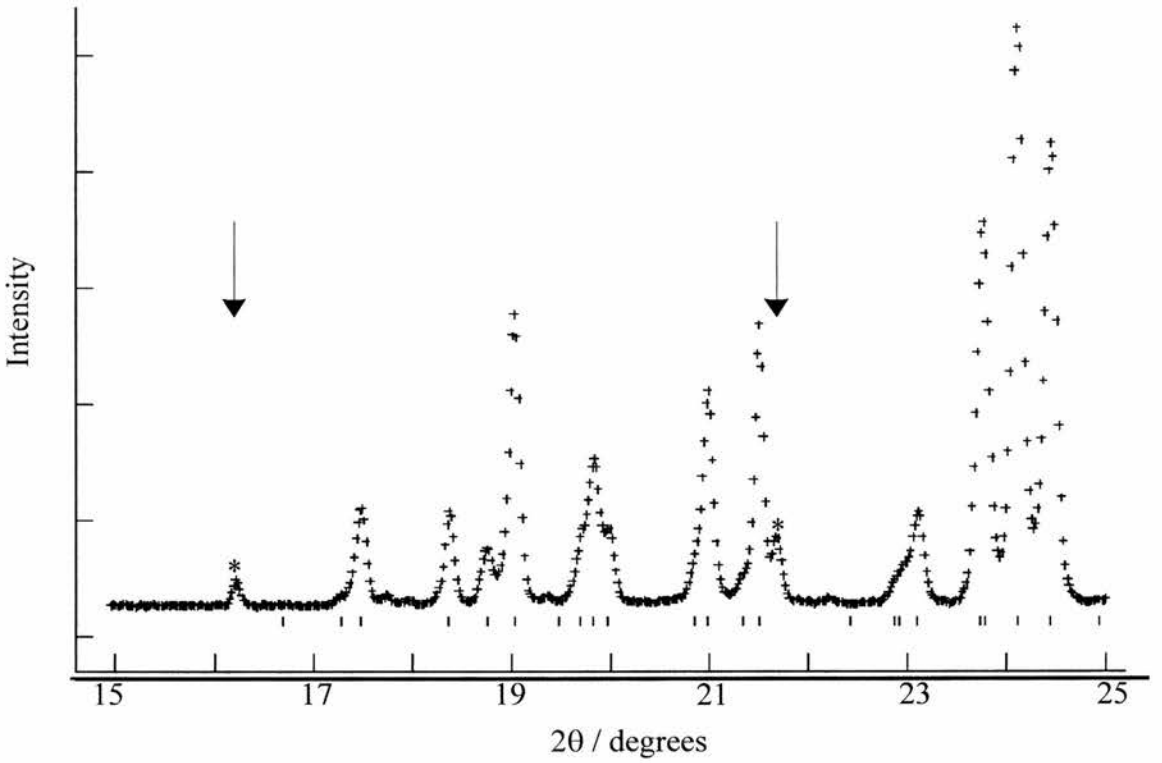

Figure 15 Enlarged plot of the XRD for AlMePO-3 showing unindexed peaks (asterisked).

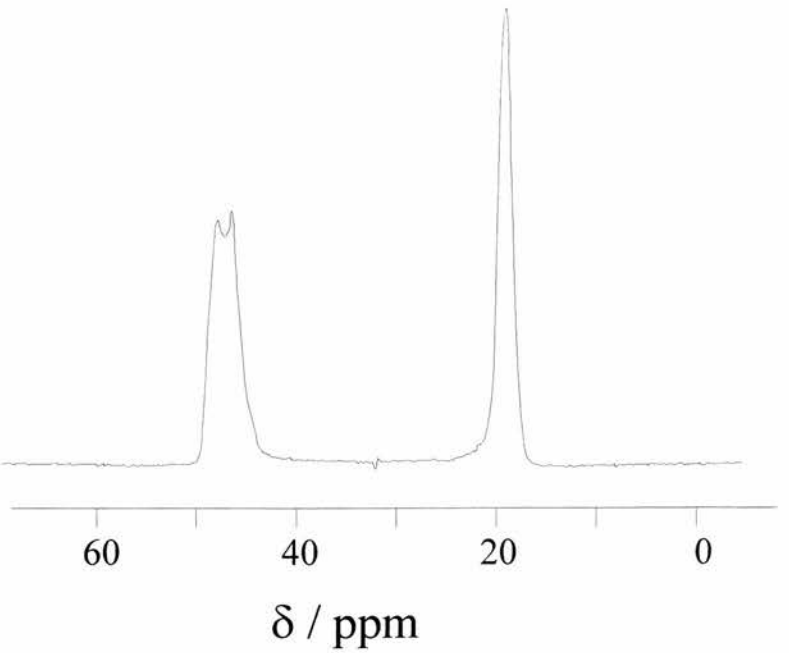

Figure 16 Single quantum ^{27}Al MASNMR spectrum of AlMePO-3.

is the geometry of the site of a roughly cubic character, but also that the ligands are all closely related to each other (see the section on AlMePO-3 in Chapter 2 for a fuller explanation). Therefore, since each aluminium must have some Al-O-P bonds, it likely that all the ligands are of this type. The 15.5 ppm resonance is assigned to a five-coordinate species of relatively high symmetry. It is worth noting, however, that the site has an asymmetry parameter significantly differing from zero, i.e. from axial symmetry.

Three approaches, Direct Methods, Monte-Carlo and Modelling, were used in attempting to obtain good starting models for the Rietveld refinement but none of them was particularly successful.

Direct Methods

A suite of programs known as EXPO[33] was used in an attempt to obtain a starting model from which to refine the structure. This suite of programs includes a routine for extracting the reflection intensities from the powder diffraction data which are passed to the latest version of SIRPOW. One of the advantages of this technique is that there is a high level of automation allowing partial models obtained from one run of SIRPOW to be used by the extraction routine to improve the estimates of reflection intensities.

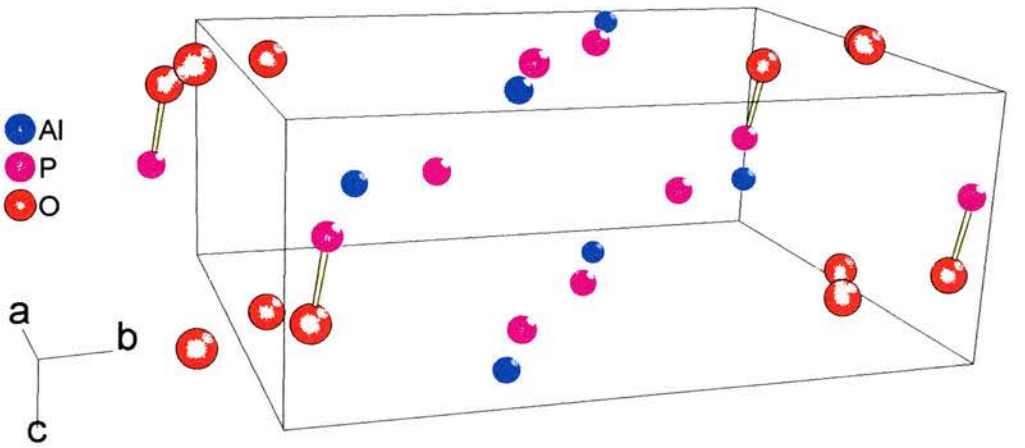

Figure 17 Representation of the model obtained from EXPO using the data range 5-70°.

The data ranges used were 5-80°, 5-70°, 5-60° and 5-50°. The 5-70° range gave the best figure of merit (R=11.3%) and the most intense electron density peaks (Figure 17). Unfortunately, the model does not appear very useful and it is not obvious, despite many attempts to do so, how best to modify it. The problem is that all the heavy atoms are in the centre of the cell with the oxygens at either end along the *b* axis. Obviously

the oxygens should be surrounding the heavy atoms. The bunching of the different types of atom in this way was a feature that recurred many times in the models obtained from EXPO. Indeed, this was also a feature of some of the models obtained from Simulated Annealing (see below).

Simulated Annealing (SA)

The attempts to use SA to solve the structure of AlMePO-3 were carried out in callaboration with Dr Yuri Andreev using an algorithm implemented in custom software designed to allow the solution of crystals containing flexible molecules.[17] Two attempts were made using this technique. The first assumed rigid phosphonate tetrahedra, based upon those found in AlMePO-β, with the aluminiums present as free ions. The second attempt placed oxygens around both P and Al atoms. One aluminium was placed in a tetrahedral environment and the other in a trigonal bipyramidal arrangement (see the discussion of the second set of results below for further information). Using oxygen polyhedra around P and Al atoms results in twice the number of oxygens expected in the cell. Therefore, the occupancies of all the oxygen sites were set to 0.5.

First Attempt to use SA

For the first attempt, the phosphonate groups were entered as rigid units with geometries based upon those of AlMePO-β. The two aluminium atom were entered as free ions. A random starting position was used. The final model is shown in Figure 18. Unfortunately, this model has a similar fault to that from Direct Methods, i.e. the aluminium atoms are all clustered in the centre of the cell. Even if one assumed some sort of chain structure of aluminiums arranged in this way, the oxygens are too far away to be involved in sensible bonding. The changes necessary to rectify this are too large to implement without ruining the fit of the calculated XRD pattern to the experimental profile.

A second attempt was made to use SA to obtain a starting model for the structure. A different approach was used in which oxygen coordination shells were placed around both Al and P atoms. Due to the NMR results discussed above, one aluminium was assumed to be tetrahedral and the other a trigonal bipyramid. (All phosphonate groups were input as rigid tetrahedra based upon those in AlMePO-β's structure.) Bond distances and angles for the aluminium tetrahedron were taken from the structure of AlMePO-β while the trigonal bipyramid was based upon that found in the structure of andalusite[34]. Having full coordination spheres around both the P and Al atoms has the result that the structure contains twice as many oxygen atoms as are truly there.

Therefore, for the purposes of the SA attempt, all oxygen fractional occupancies were set to 0.5. The aluminium oxygens were deleted from the resulting structural model (Figure 21).

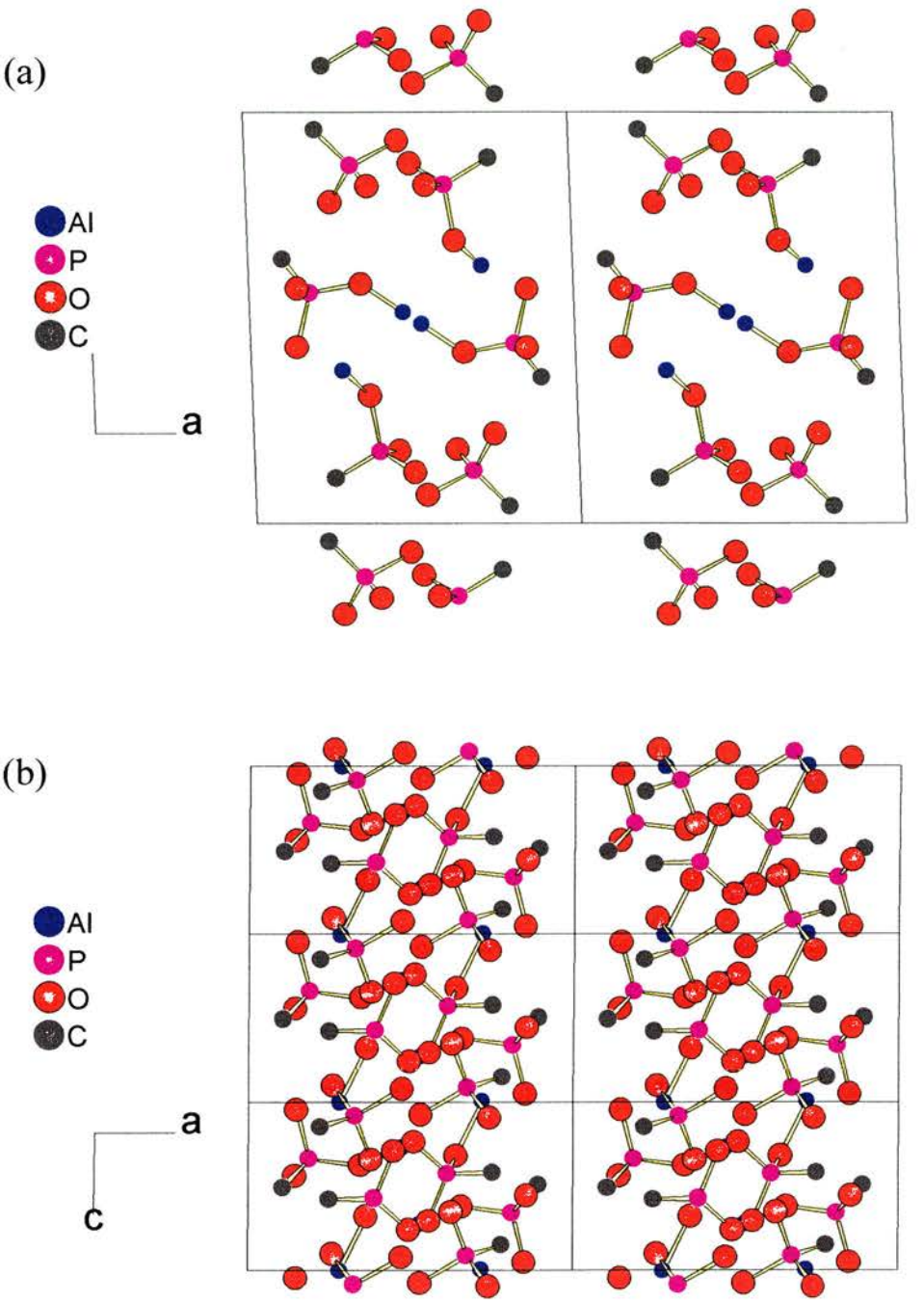

Figure 18 Representation of the starting model obtained from the first attempt using Simulated Annealing (a) viewed along (001), (b) viewed along (010), showing the formation of layers stacking along (100).

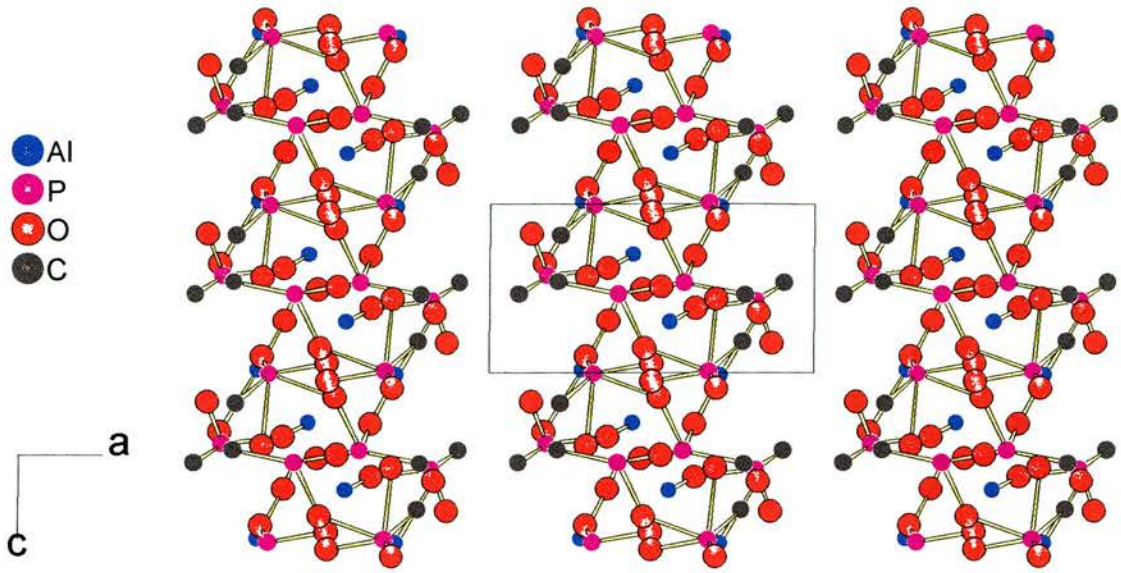

Figure 19 Representation of the first model from Simulated Annealing after refinement without constraints. Notice that the layering of the material is more pronounced than in the original model.

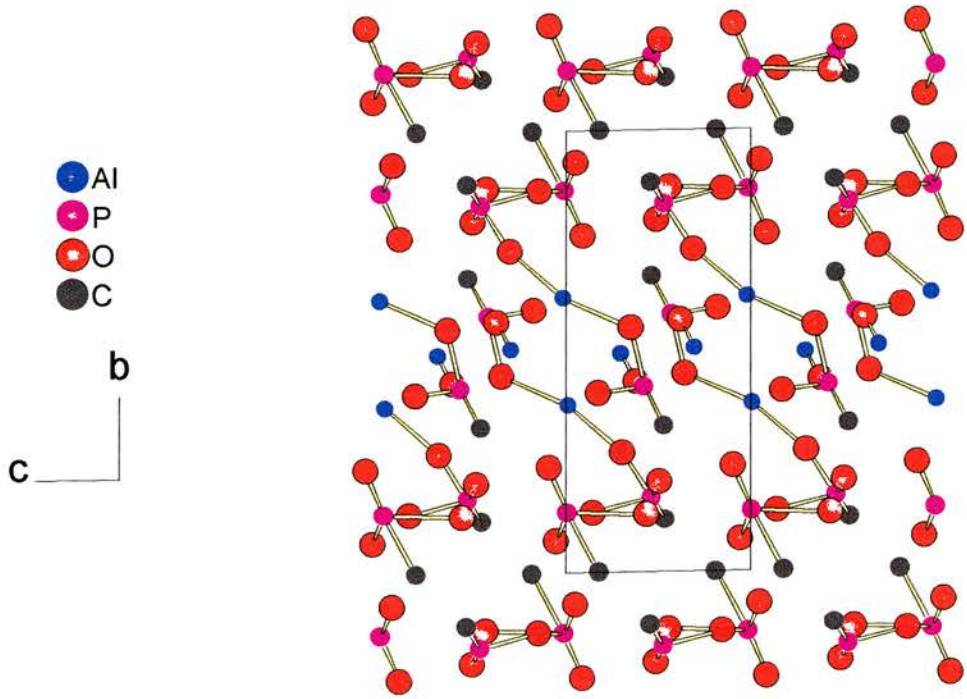

Figure 20 Representation of the first model from Simulated Annealing after refinement without constraints viewed along the stacking axis (100).

Second Attempt to use SA

The model obtained from this use of SA is better than the last because there has been less separation of the aluminium and phosphorus moieties. However, the structure does

not have a realistic connectivity. There are not sufficient oxygens near the aluminium atoms to allow the formation of chemically sensible coordination spheres. Nevertheless, an attempt was made to refine the structure, both with and without constraints on the phosphorus to oxygen distances. When constrained the model did not change very significantly and the refinement tended to be unstable. Unconstrained, the fully refined structure (χ^2 = 13.34, RWp = 15.85%) had changed, becoming that shown in Figure 22.

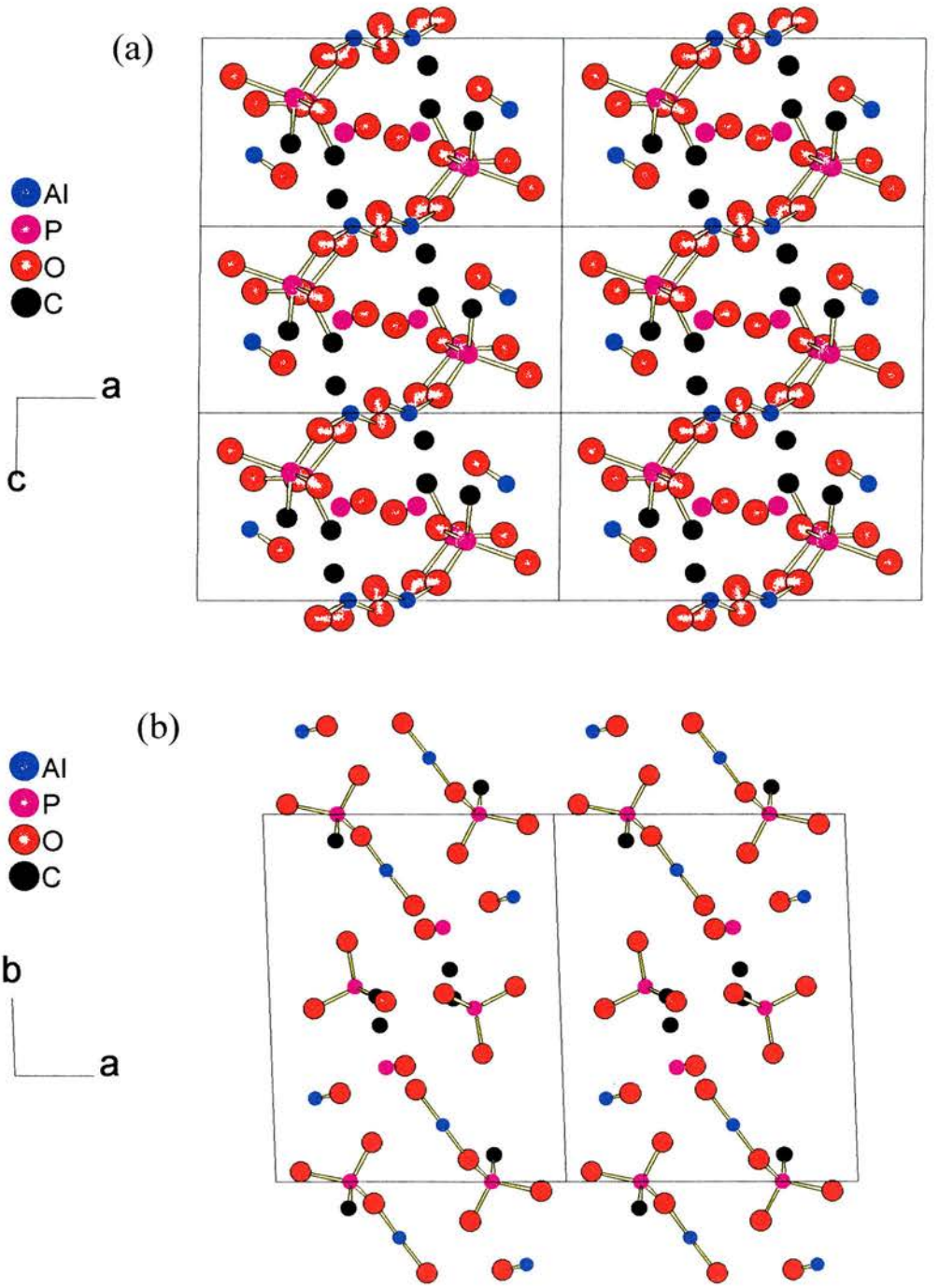

Figure 21 Representation of the model obtained from the second attempt to use Simulated Annealing after the removal of the oxygens from the aluminium polyhedra, (a) viewed along (001), (b) viewed along (010). Notice that here also, the stacking of the layers is along the (100) axis.

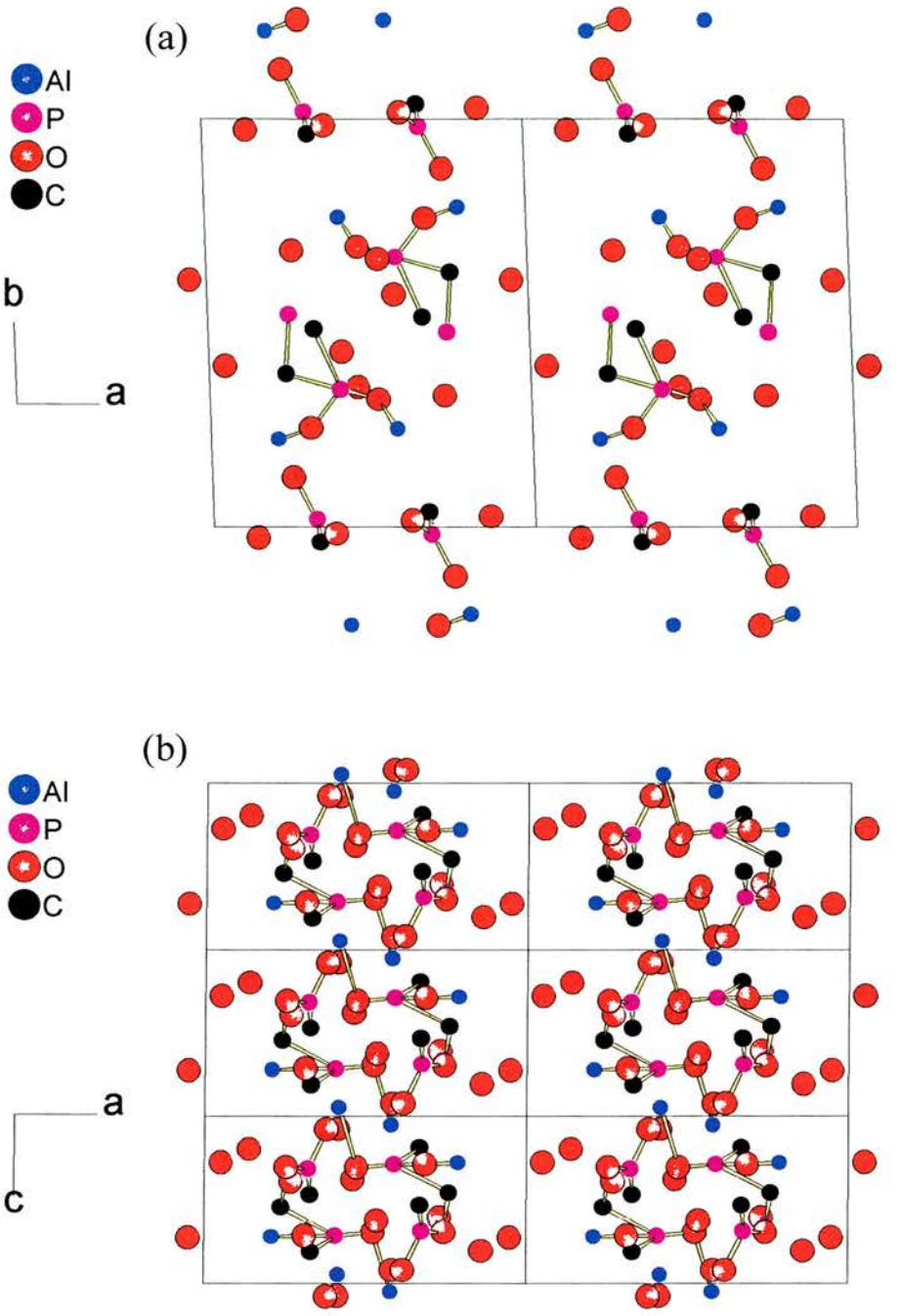

Figure 22 Views of the second model from Simulated Annealing, after Rietveld refinement without constraints (χ^2 = 13.34, RWp = 15.85%), (a) along (001), (b) along (010).

As before, there is marked formation of layers in the *bc* plane, particularly if viewed along the *b* axis rather than the *c* axis. However, further attempts to modify the model, both before and after refinement, to give a more chemically sensible structure were not successful. Either the fit between calculated and experimental profiles became very bad after improvements had been made to the models, or the refinement became unstable. Also, it is not clear which of the huge number of changes that can be made to the

structure would be best. Such a large number of variables makes it very unlikely that a model that is not very close to the true structure can be improved significantly.

The Modelling Approach

In order to find alternative starting models for the refinement step of structure solution, it was decided to attempt to build physical models which fitted the known characteristics of the material. To make this possible, certain assumptions were required. There is a repeat of ~5 Å in the *c* dimension, a relatively common occurrence in metal phosphates / phosphonates. In the majority of cases, such a repeat is formed by 'zigzag' chains of metal atoms linked by a phosphorus unit, i.e. Al-O-P-O-Al in this case. This was also assumed to be the case for this material. In addition, as noted above in the discussion of the NMR data, it is assumed that there are no Al-O-Al type connections within the material. (If one does not assume this, it is hard to build a structure which is either layered or chemically sound with respect to the coordination of aluminium.)

Another necessary adjunct to this approach is in the flexibility of bonds. All structurally important bonds within the material, i.e. excluding P-C and C-H bonds, have been assumed to be of the same type – Al-O-P. Thus, rather than explicitly include oxygens whilst formulating the model, a single flexible tube was used to simulate the Al-O-P bond, allowing some leeway in symmetry of the Al and P atoms and in the strain on the oxygen position. A consequence of this is a certain simplification of the structures produced, a characteristic that is both a positive and negative factor.

The procedure adopted was to build a structure through trial and error whilst observing known or suspected characteristics of the material. Projections of the structure were drawn along each crystallographic axis and these diagrams used to give approximate, but as accurate as possible, fractional coordinates for the asymmetric unit. It was necessary to use great care in positioning the unit cell on the projections so that the origin was correct. The proper position can be determined by reference to the points of inversion within the structure. A point of inversion must be present in the middle of each cell and in the centre of each face. Once a crystallographic description of the Al and P atoms had been obtained, oxygen positions were calculated at the midpoint of a straight line joining the bonded atoms. Whilst this is inaccurate it was felt that it is a sufficiently close approximation of the true oxygen positions to be valid. In addition, since the true position of the oxygen could lie anywhere within a certain radius of the midpoint chosen, an attempt to find more accurate coordinates could have led to a greater error. Carbon atoms were taken to be oriented in the least sterically hindered position given the orientation of the oxygens with respect to the phosphorus.

Having obtained a full set of coordinates for the asymmetric unit (the coordinates were input into Diamond to check that they formed the structure envisaged from modelling), GSAS was used to generate a simulated pattern. Following this, the same experimental file was used to perform Rietveld refinement on the material. In many cases attempts were made to constrain the bond distances and, sometimes, the angles around P and Al atoms. Although these attempts were occasionally successful in giving models in which the P-O and Al-O bond lengths were more appropriate (due to the approximate nature of the process by which crystallographic descriptions of physical models are produced, these bond lengths often differ slightly from the normal values observed in this type of material), the fit to the experimental XRD pattern was very bad in every case (RWp < 25%). Removal of the constraints at this point and subsequent refinement to convergence of the atom positions and other relevant parameters (lattice parameters, zero point shift, background coefficients, scale factor and profile coefficients) gave the same structure as that obtained without any use of constraints. Therefore, in the following discussion, only the structures resulting from refinements without constraints are reported.

A final note on the refinement procedure concerns the indexing of the pattern. Identical peak positions can be obtained from cells which have α', β', or γ' (or any combination of these) set to a value $180 - n$, where n is the original, equivalent angle, α, β, or γ. The consequence of changing the cell thus is to switch the relative intensities among the groups of reflections which would be equivalent in an orthogonal cell of the same dimensions. For each of the models below, the different possible angles for the triclinic cell as described above were investigated during refinements. In all cases in which one option was significantly better than the others, it was the set of parameters in which all the angles are obtuse, i.e. that given at the beginning of the section dealing with AlMePO-3.

Model of a layered material stacking along *b*

The aluminium atoms are connected into chains along the *c* axis, by phosphonate units. The four coordinate aluminiums are linked by one phosphonate and the five coordinate by two phosphonates (Figure 23a). each five coordinate aluminium chain is arranged in a pair with a four coordinate aluminium chain, with links forming between Al and P of adjacent chains. The pairs of chains are themselves joined together in a layer by connections between the phosphonate groups, bridging two five coordinate Al atoms, and a four coordinate Al. Each cell consists of two such layers, one the inversion of the other, stacked on the *b* axis such that a point of inversion lies between them (Figure 23b).

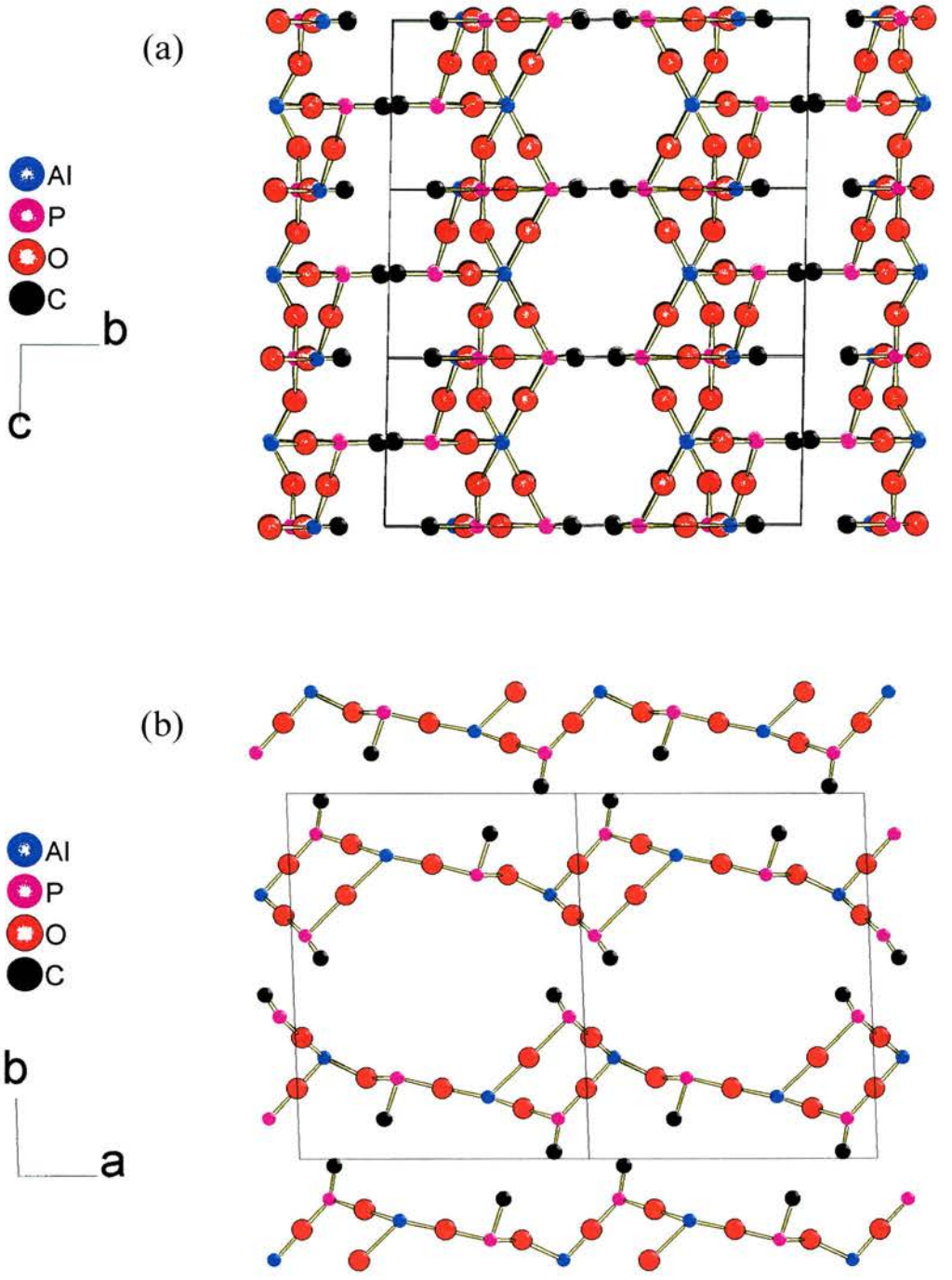

Figure 23 View of the starting configuration of the modelled structure with layers stacking along the (010) axis, viewed along, (a) (100), (b) (001)

The simulated pattern for the starting model is shown in Figure 24. When compared with the true pattern, it can be seen that there is a great deal of difference between this model and the structure of the material. Figure 25 shows the structure after refining to convergence (χ^2 = 8.50, WRp = 15.1%). Attempts to refine the structure were made using constraints on the bond lengths. However, the fit was very bad using this approach and the constraints were abandoned. The fit and final coordinates did not differ

significantly between a refinement involving constraints subsequently removed and another without any constraints.

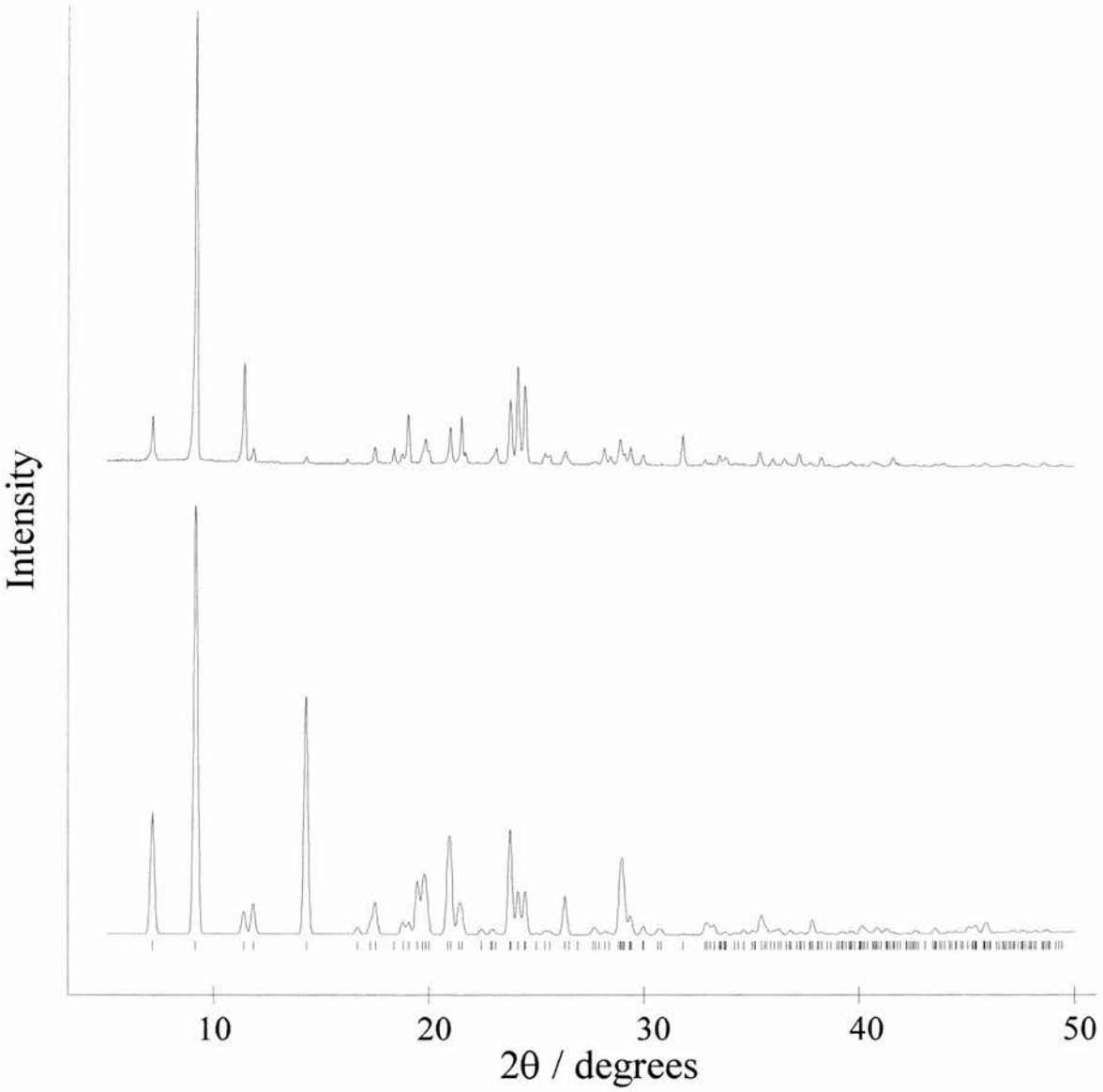

Figure 24 Comparison of a simulated XRD pattern, generated from the starting structure for the model stacking on the *b* axis, with the experimental AlMePO-3 pattern (simulated using GSAS).

Although the model is obviously not correct, it is interesting to note that the refinement causes the emergence of a layering effect stacked along *a* (although the structure above is connected in the *a* direction, this consists solely of an oxygen with two long bonds to each formative layer). This is despite the original layering of this structure in a direction perpendicular to this. The formation of layers in the *bc* plane was also a feature of the models from the Simulated Annealing attempts. Therefore, such a layering structure, along (100) was included in all subsequent models.

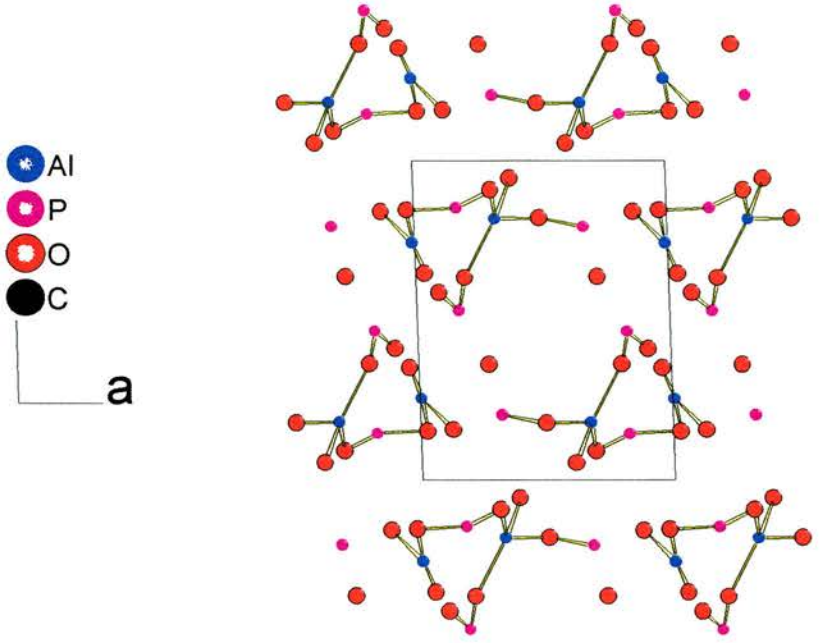

Figure 25 Representation of the *b* stacking model structure refined fully utilising no constraints.

Models of layered materials stacking along the *a* axis

It was possible to find a structure which gave the required stacking along the *a* direction and the correct repeating distances in the other dimensions. Again, the structure consists of layers in which pairs of 'zigzag' chains, of either five or four coordinate aluminium atoms, are connected to each other (Figure 26). In contrast to the previous structure, above, the chains are each connected in pairs in which the aluminium is entirely either in five-fold coordination or four-fold coordination. The pairs of chains alternate in their coordination along the *b* axis. The aluminium atoms in the chains are linked by two phosphonates in the case of five-fold coordination and just one in the case of tetrahedral geometry. Thus each pair of chains forms an arrangement in which four rings (2 P and 2 Al atoms) feature strongly. There is a point of inversion at the centre of each four ring which lies in the centre of a pair of aluminium chains.

When viewed in projection along the *c* axis (Figure 27), the pairs of chains form parallelograms. It is possible to form polymorphic structures in which the parallelograms take up different orientations. There is one alternative orientation for each of the two pairs of chains, thus giving rise to four polymorphs. The four structures are arbitrarily designated polymorph a, b, c and d for the purposes of this discussion.

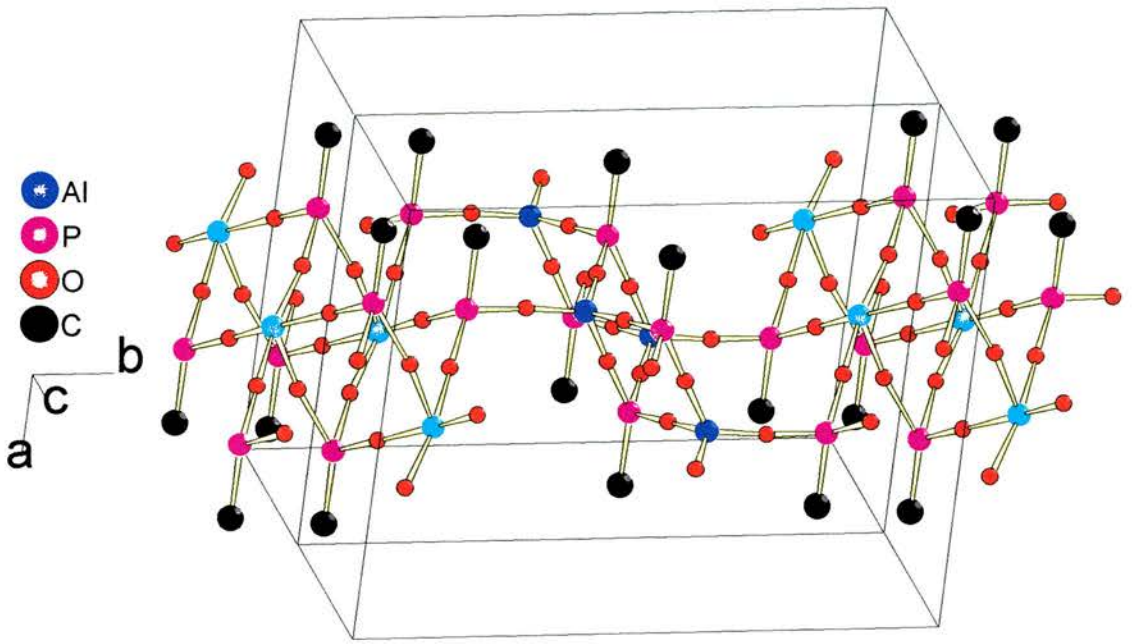

Figure 26 View showing one layer of polymorph b of the modelled structure. Five coordinate aluminiums are shown in cyan, four coordinate as blue.

Polymorph a

The starting model used for polymorph a is shown in Figure 27. Comparison of the simulated XRD pattern with the experimental pattern (Figure 28) shows that there is little similarity between this material and AlMePO-3. Rietveld refinement gave final RWp = 15.6% and χ^2 = 12.1. However, the fully refined structure (Figure 29) is not viable as the central phosphonate moieties have moved away from the centre and one another, while the tetrahedral aluminium atoms have become very close. Therefore, the polymorph a model is not the correct structure.

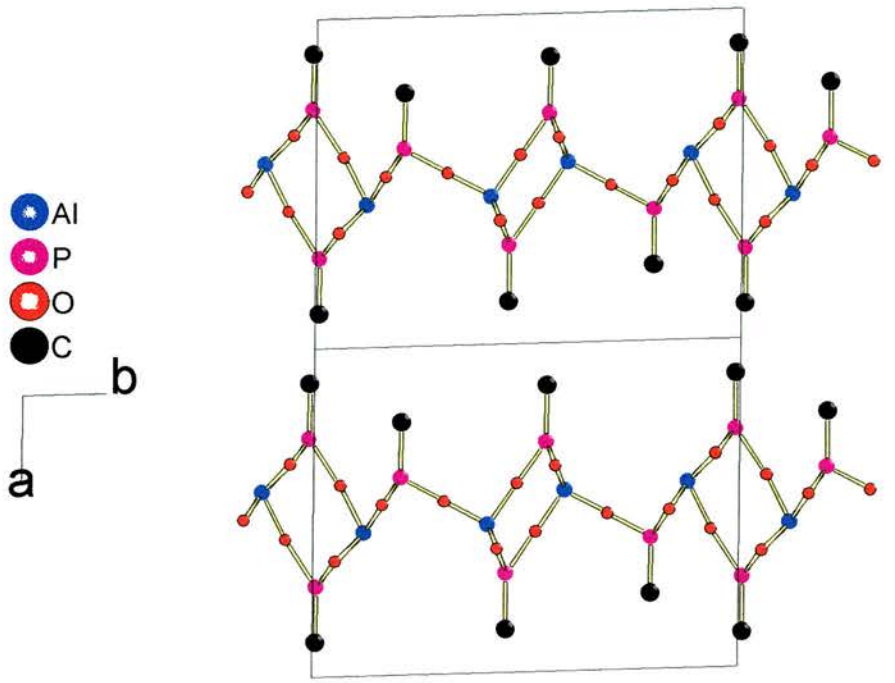

Figure 27 Original starting model of polymorph a.

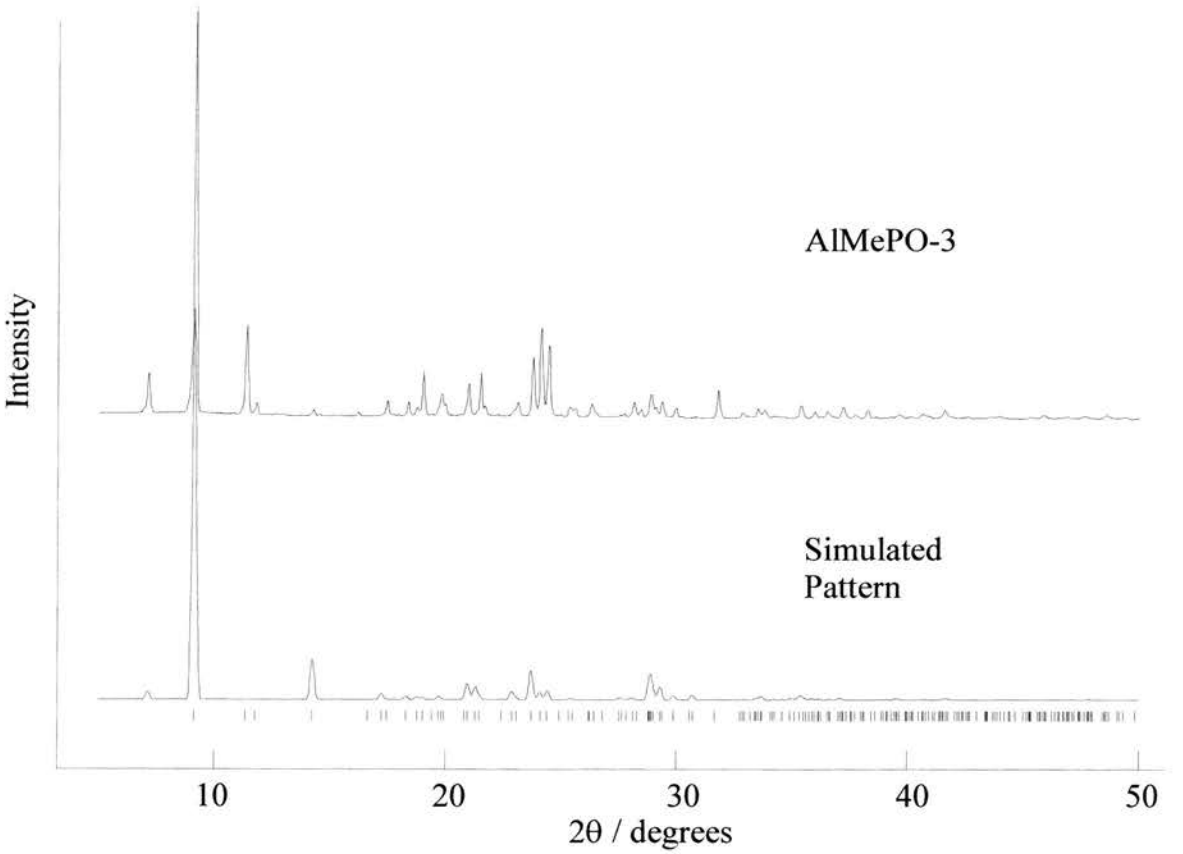

Figure 28 Comparison of a simulated XRD pattern for polymorph a with the experimental AlMePO-3 pattern (simulated using GSAS).

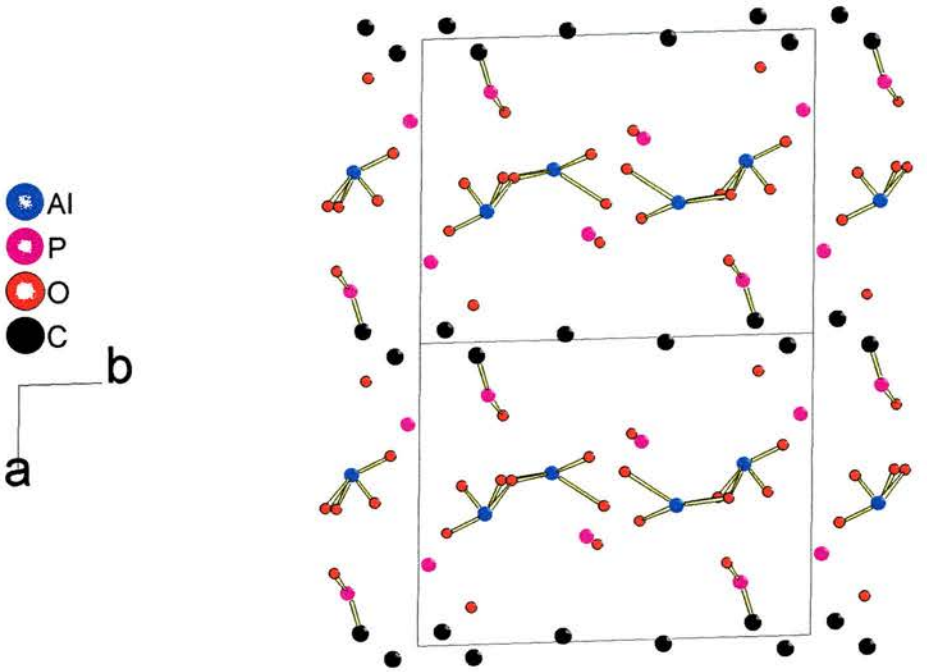

Figure 29 Representation of the fully refined structural model of polymorph a.

Polymorph b

The starting model used to represent this polymorph is shown in Figure 30. The XRD pattern simulated from this structure, compared with the experimental data for AlMePo-3 in Figure 31, indicates that this is not the correct structure. However, it is arguably the closest fit of any of the starting structures obtained from the modelling procedure. Unfortunately, refinement of the structure did not give significantly better results than for polymorph a.

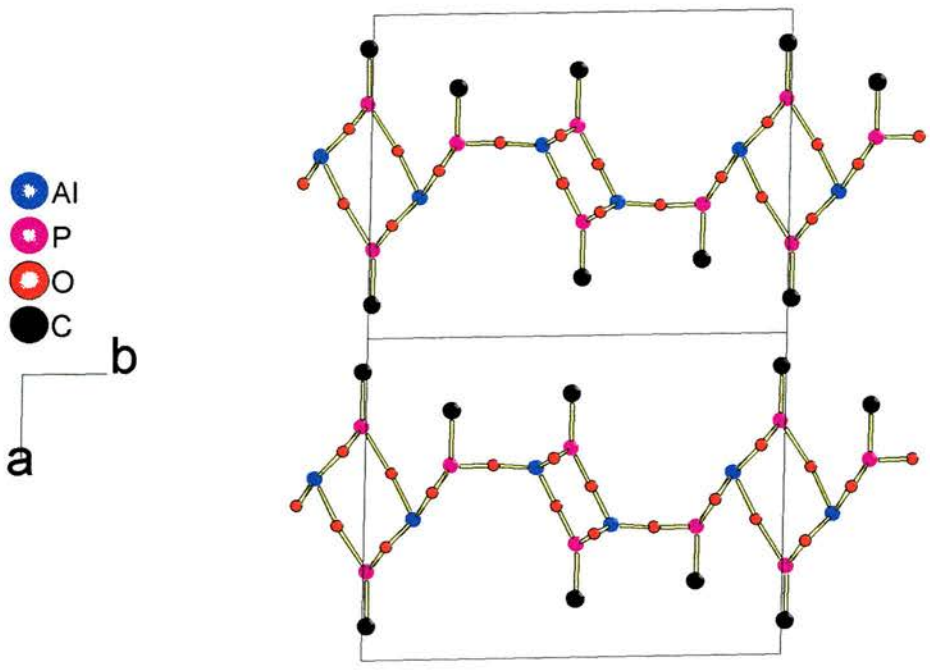

Figure 30 Representation of the structure of polymorph b used as the starting model for refinement.

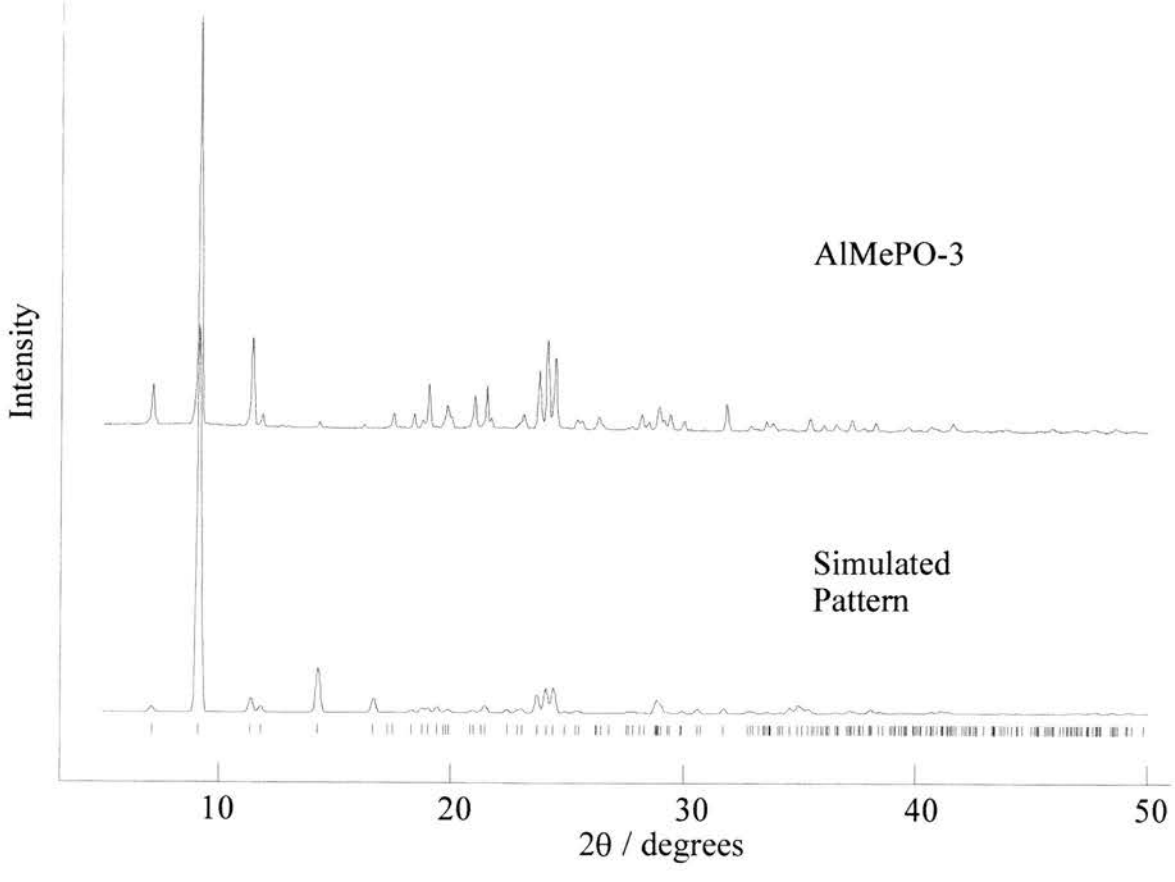

Figure 31 Comparison of a simulated XRD pattern for polymorph b with the experimental AlMePO-3 pattern (simulated using GSAS).

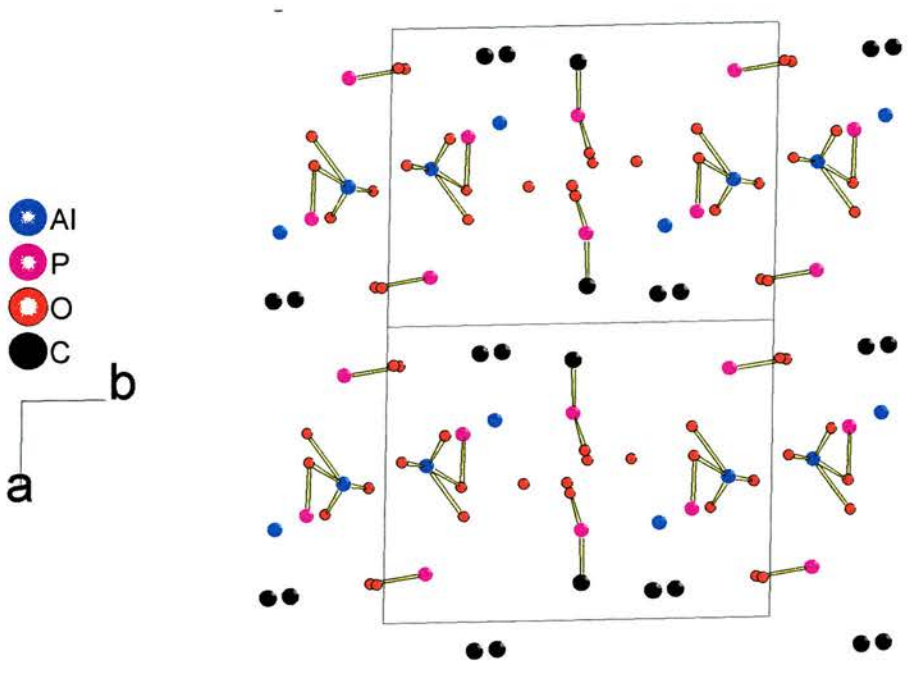

Figure 32 Representation of the fully refined model from polymorph b.

Polymorph c

This structure was deemed to be the most likely of the polymorphs to be correct as it most easily accommodated the correct spacing along the *b* axis. All the other models favour a configuration in which the *b* repeat distance is slightly too long. This structure,

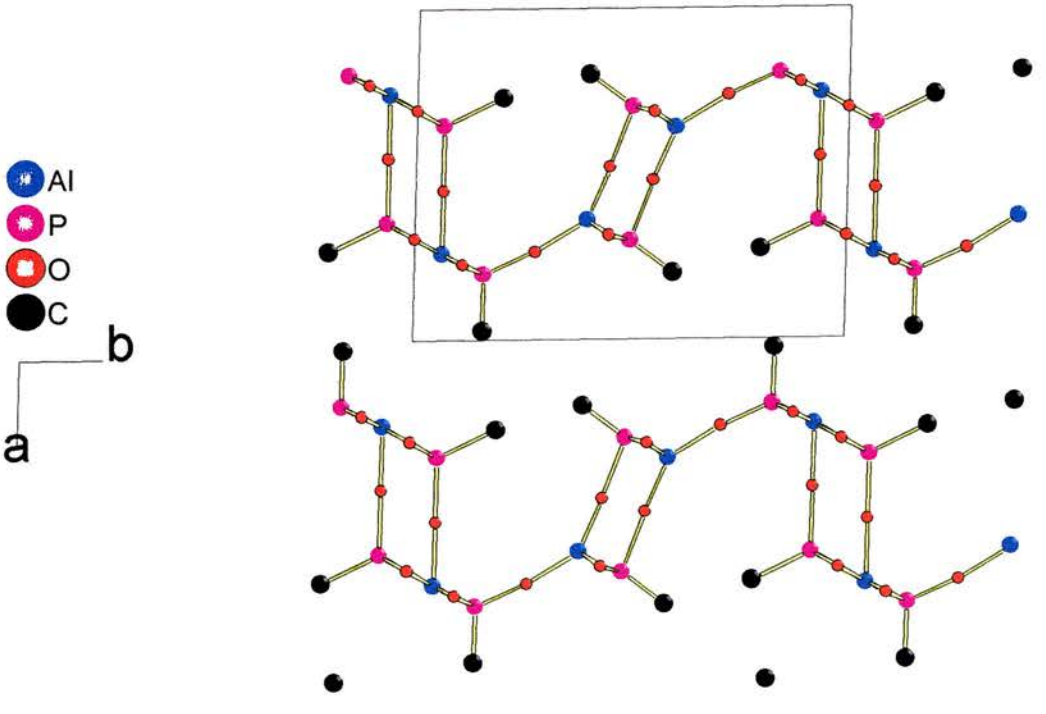

Figure 33 Representation of the starting structure of polymorph c.

however, is able to compress and expand such that a relatively wide range of values for *b* are possible. Unfortunately, consideration of the comparison between the simulated and actual XRD patterns (Figure 34) reveals this to be an incorrect structure. Rietveld refinement gives a final value of χ^2 = 13.7 and RWp = 16.4%. Consideration of the refined structure reveals certain similarities to that of the other refined polymorphs of this type. Two heavy atoms, phosphorus in this case, have remained in the centre and moved closer to one another while the other heavy atoms that did reside close to the middle of the cell have moved towards the corners. As a result of this movement, layers appear to have formed along the $(1\bar{1}0)$ direction. Although the layers are not completely convincing, they do have a central portion of aluminium with the phosphonates moving to the outside in a manner characteristic of metal phosphonates. In addition, the carbon atoms have formed a line marking the edge of layers. Although these carbons are quite close to each other, only a relatively small reorientation with respect to the phosphorus atoms would be necessary to correct this.

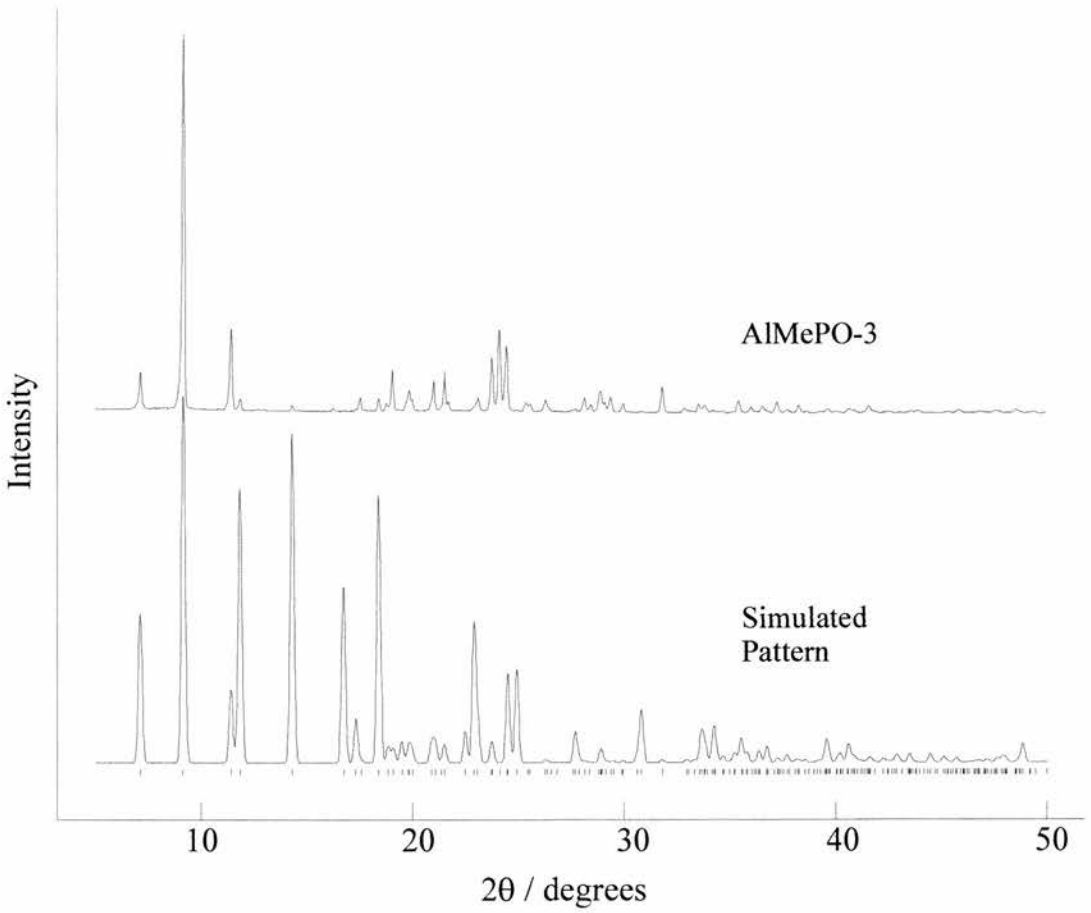

Figure 34 Comparison of a simulated XRD pattern for polymorph b with the experimental AlMePO-3 pattern (simulated using GSAS).

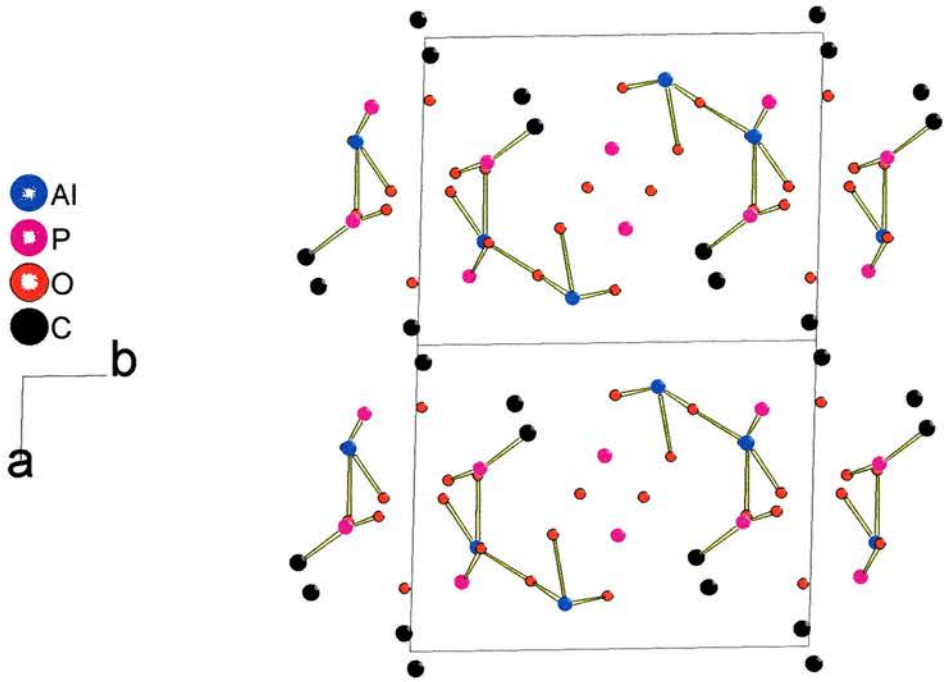

Figure 35 Representation of the fully refined structure for polymorph c.

Polymorph d

The starting model for polymorph d is shown in Figure 36. Although the comparison of the simulated and experimental XRD data (Figure 37) show some agreement, refinement of this model proved unstable and always diverged despite several attempts to stabilise it with increased damping and different combinations of the parameters which were allowed to vary.

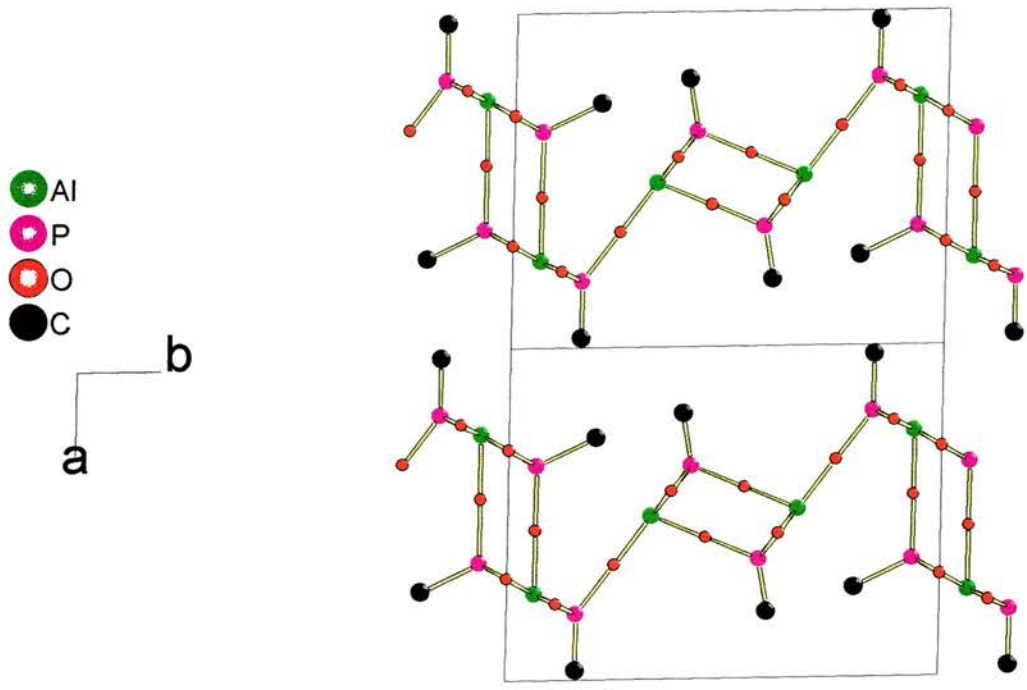

Figure 36 Representation of the starting structure of polymorph d.

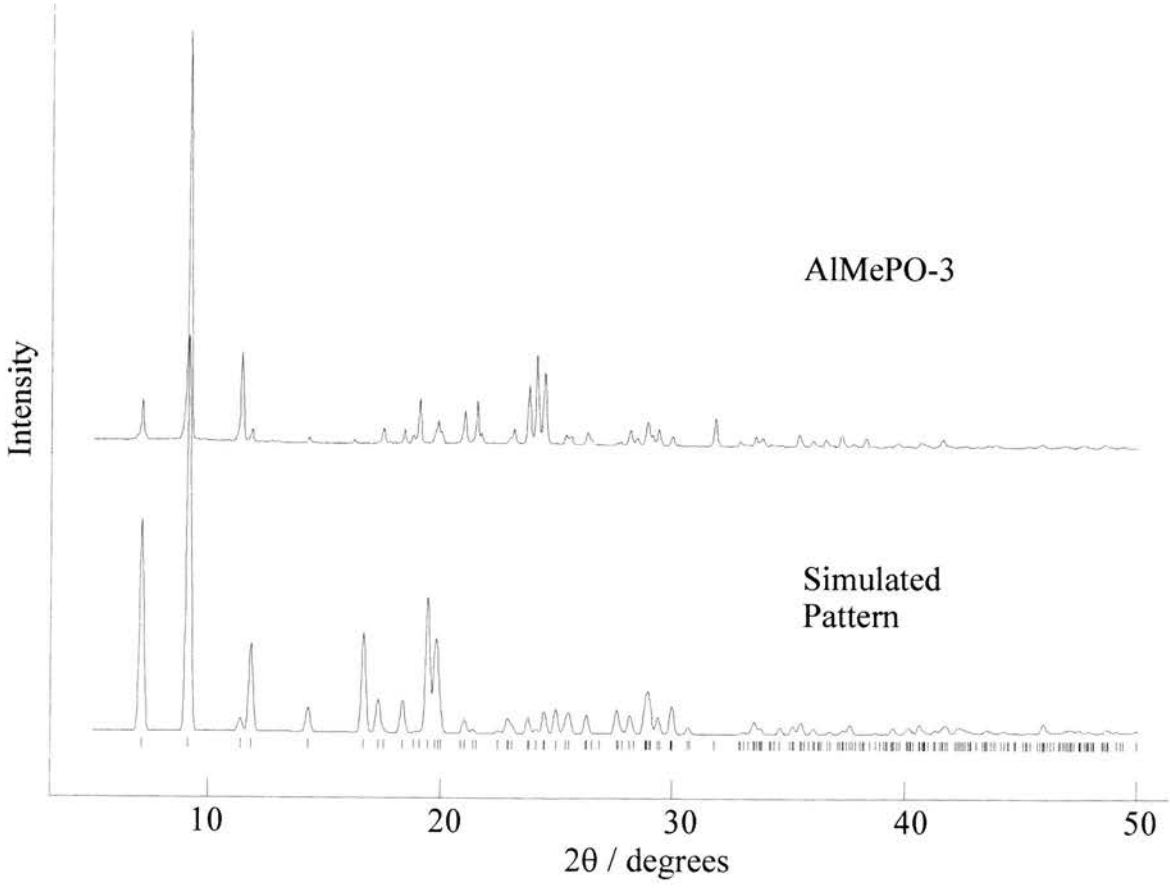

Figure 37 Comparison of a simulated XRD pattern for polymorph d with the experimental AlMePO-3 pattern (simulated using GSAS).

Conclusion

AlMePO-1

Laboratory X-ray data was used to solve the structure of this material *ab initio*. The data were sufficient to determine the structure unambiguously. Complementary techniques, including ^{27}Al, ^{31}P and ^{13}C MASNMR, X-ray fluorescence and TGA, were used to aid in the solution process. The structure was both the first reported layered aluminium methylphosphonate and also the first of that group to have a Al:P ratio of 1:1. In common with other layered metal phosphonates, this structure could have applications as a catalyst or sorbent.

AlMePO-2

A reasonable structural model giving a good fit to the experimental XRD profile was produced through similar *ab initio* techniques to those used to solve AlMePO-1. There is some doubt about the proposed structure, however, due to more recent ^{27}Al 5Q MASNMR evidence contravening the presence of tetrahedral aluminium. Also, the fit between the calculated and experimental XRD plots is not of sufficient quality to be incontrovertible, particularly at 45-50° and higher 2θ angles. This could be due to a small amount of impurity however.

AlMePO-3

It has been impossible to solve the structure of this material despite a great deal of effort in this direction. The structure is very difficult to characterise, possibly because of the lower symmetry of the unit cell. Such symmetry results in more reflections than for AlMePO-1 and AlMePO-2 and, hence, greater overlap of the peaks. Also, the low symmetry necessitates a greater number of atoms in the asymmetric unit, even for a cell of relatively low volume such as this is.

Attempts to solve the structure by model building were unsuccessful, although the refinement of polymorph c has given rise to an interesting possibility, that of layers lying obliquely across the cell, parallel to the *c* axis. The structural models used were described quite inaccurately by the process of transforming the physical model into crystallographic coordinates. The model building approach relied upon many assumptions (stated earlier) but perhaps most importantly upon the expectation that this approximate description of the structure, if correct, would refine easily to a good fit. It is not known to what degree the inherent inaccuracies of this approach would complicate the refinement. It is possible that a refinement of the correct model inaccurately described would fail as the Rietveld technique relies upon there being a 'downhill'

gradient to the global minimum without any local minima inbetween. A possible approach for the future would be to use the models, particularly polymorph c, as the starting point for Simulated Annealing procedures in order to avoid becoming trapped in a local minimum.

Summary

It is likely that the ease with which it was possible to solve AlMePO-1 was due to the relatively small number of atoms in the asymmetric unit. A similar argument explains the difficulty in solving AlMePO-3 and the doubt about the solution of AlMePO-2. Further work should include both a simulated annealing treatment of some of structures obtained from model building for AlMePO-3, and microcrystal diffraction studies of AlMePO-2 and AlMePO-3. It would be interesting to compare a structure solved by such a method with the existing model for AlMePO-2. Unfortunately, the crystals of AlMePO-2 are very small (<1 μm) making it impossible to carry out microcrystalline diffraction. Attempts have been made to use this technique to solve the structure of AlMePO-3 but the crystals were of insufficient quality. More work needs to be performed to obtain larger, good quality crystals of both of these phases.

References

1 V. Soghomonian, R. Diaz, R. Haushalter, C. J. O'Connor and J. Zubieta, *Inorganic Chemistry*, 1995, **34**, 4460-4466.

2 R. LaDuca, D. Rose, J. R. D. DeBord, R. C. Haushalter, C. J. O'Connor and J. Zubieta, *Journal of Solid State Chemistry*, 1996, **132**, 408-412.

3 V. Soghomonian, Q, Chen, Y. Zhang, R. Haushalter, C. J. O'Connor, C. Tao and J. Zubieta, *Inorganic Chemistry*, 1995, **34**, 3509-3519.

4 Y. Zhang and A. Clearfield, *Inorganic Chemistry*, 1992, **31**, 2821-2826.

5 A. Clearfield, J. D. Wang, Y. Tian, E. Stein, C. Bhardwaj, *Journal of Solid State Chemistry*, 1995, **117**, 275-289.

6 K. Maeda, J. Akimoto, Y. Kiyozumi and F. Mizukami, *Journal of the Chemical Society, Chemical Communications*, 1995, 1033.

7 K. Maeda, J. Akimoto, Y. Kiyozumi and F. Mizukami, *Angewandte Chemie, International Edition English*, 1995, **34**, 1199.

8 J. M. Troup and A. Clearfield, *Inorganic Chemistry*, 1977, **16**(12), 3311.

9 G. Cao, H. Lee, V. M. Lynch and T. E. Mallouk, *Inorganic Chemistry*, 1988, **27**, 2781-2785.

10 J. M. Thomas, *J. Phys. Chem. Solids*, 1989, **50**, 449.

11 L. B. McCusker, *Acta Crystallographica;* 1991, **A47**, 297.

12 J. P. Attfield, A. W. Sleight, A. K. Cheetham, *Nature (London)*,1986, **322**, 620.

13 P. R. Rudolf, C. Saldariagga-Molina and A. Clearfield, *Journal of Physical Chemistry*, 1986, **90**, 6122.

14 P. Lightfoot, C. Glidewell and P. G. Bruce, *Journal of Materials Chemistry*, 1992, **2**, 361.

15 A. Le Bail, *Journal of Solid State Chemistry*, 1993, **103**, 287.

16 D. Poojary, A. Cabeza, M. Aranda, S. Bruque and A. Clearfield, *Inorganic Chemistry*, 1996, **35**, 1468.

17 Y. G. Andreev and P. G. Bruce, *Materials Science Forum*, 1998, **Vols 278-281**, 14-19.

18 L.-J. Sawers, V. J. Carter, A. R. Armstrong, P. G. Bruce, P. A. Wright and B. E. Gore, *Journal Chemical Society, Dalton Transactions,* 1996, 3159-3161.

19 J. Visser, *Journal of Applied Crystallography,* 1969, **2**, 89.

20 H. M. Rietveld, *Journal of Applied Crystallography,* 1969, **2**, 65.

21 A. Larson and R. Von Dreele, Los Alamos National Lab. Rep. No. LA-UR-86-748, 1987.

22 Biosym Technologies Inc., San Diego, 1993.

23 G. Cascarano, L. Favia, and C. Giacovazzo, *Journal of Applied Crystallography,* 1992, **25**(2), 310.

24 A. Le Bail, *Journal of Solid State Chemistry,* 1989, **83**, 267.

25 C. Blackwell and R. Patton, *Journal of Physical Chemistry*, 1988, **92**, 3965.

26 K. Maeda, J. Akimoto, Y. Kiyozumi and F. Mizukami, *Journal Chemical Society, Chemical Communiations,* 1995, 1033.

27 K. Maeda, J. Akimoto, Y. Kiyozumi and F. Mizukami, *Angewandte Chemie, International Edition English,* 1995, **34**(11), 1199.

28 M. D. Poojary, A. Clearfield, *Materials Chemistry and Physics*, 1993, **35**, 301.

29 I. D. Brown, and D. Altermatt, *Acta Crystallographica,* 1985, **B41**, 244.

30 B. Morosin, R. W. Lynch, *Acta Crystallographica*, 1972, **B28**, 1040.

31 H. Stunzi, L. Spiccia, F. Rotzinger, W. Marty, *Inorganic Chemistry*, 1989, **28**, 66.

32 CRC Handbook of Chemistry and Physics, 73rd Edition, 1992-1993, Editor-in-Chief, D. R. Lide, CRC Press (London).

33 A. Altomare, M. C. Burla, G. Cascarano, C. Giacovazzo, A. Guagliardi, A. G. G. Moliterni and G. Polidori, *Journal Applied Crystallography,* 1995, **28**,842-846.

34 C. W. Burnham and M. J. Buerger, *Zietchrift fur Kristallographie, Bd.*, 1961, **115**, 269-290.

Chapter 4

Studies on the Solid-State Transformation of Aluminium Methylphosphonate-β (AlMePO-β) to its Polymorph Aluminium Methylphosphonate-α (AlMePO-α)

Introduction

Microporous materials such as AlMePO-β[1] have many potential uses in a wide variety of applications. In order to be suitable for many of these, the material must be stable under quite harsh conditions. One can imagine instances of AlMePO-β's use in a sorptive capacity, e.g. as effluent filters, or a catalytic material, the development of which would require detailed knowledge of the behaviour of this compound under thermal and mechanical stress.

This chapter reports investigations of AlMePO-β at elevated temperatures under a variety of atmospheres. The original aim was to ascertain the stability of this material in inert atmospheres only. However, as the work progressed a more in-depth study of the processes taking place under these circumstances was warranted and a variety of atmospheric conditions were used. The results not only confirmed the presence of occluded 1,4-dioxane molecules within the material, first indicated by ^{13}C MASNMR, but also brought to light that AlMePO-β undergoes a rare and interesting topotactic solid-state transformation to its microporous polymorph AlMePO-α. The transformation, which is favoured in a humid atmosphere, is of interest not only in itself but also practically as a means of preparing AlMePO-α, the more difficult polymorph to synthesise, directly.[2]

Solid-state transformations between microporous materials are very rare because even those involving compounds of closely related structures, such as the cubic and hexagonal stacking variants of zeolite Y, require many bond breaking and reforming steps. Under conditions in which the necessary thermal energy is available to activate such a process, more thermodynamically favourable, dense recrystallisation phases become accessible. Thus, the usual response of microporous materials under thermal treatments sufficiently extreme to cause bond rearrangements is to transform into dense phases, e.g. the conversion of microporous aluminium phosphates to the form of $AlPO_4$ isostructural with tridymite and the conversion of the zeolite Mg-B to cordierite.[3,4]

The solid-state transformation of AlMePO-β is reported here, having been studied using a combination of complementary techniques including powder X-ray diffraction (XRD), pulsed spallation neutron diffraction (Chapter 5), both single quantum (SQ) and multiple quantum (MQ) ^{27}Al magic-angle spinning nuclear magnetic resonance

(MASNMR) and conventional ^{31}P MASNMR. Detailed discussions of the changes taking place are given together with a proposed mechanism for the transformation.

Experimental

Synthesis of AlMePO-β

The aluminium methylphosphonate-β was-prepared according to the published method[1] and its phase purity confirmed from the XRD pattern. In general, $Al(OH)_3.xH_2O$ (Aldrich) and 1,4-dioxane (Aldrich) were added to a solution of methylphosphonic acid (Aldrich) and stirred for 30 minutes. The molar ratios of the components {$Al(OH)_3$: $CH_3PO(OH)_2$: H_2O : 1,4-dioxane} in the mixture were 1:1.5:40:0.5 respectively and the pH was 3-3.5. The gel was sealed inside a Teflon-lined stainless steel autoclave and heated at 160°C for 48 hours. On removal, it was filtered, washed with distilled water (~60 cm^3) to remove any remaining reactants and dried at 60 °C in air. To confirm the role of the organic molecule in structure direction, a preparation was performed in its absence, producing some AlMePO-β but mainly another polymorph of $Al_2(PO_3CH_3)_3$ without microporosity. In the case of the preparations performed in the absence of dioxane, all other reaction parameters were unchanged.

Characterisation techniques

Conventional thermogravimetric analysis (TGA) was carried out under nitrogen (for which no special measures had been taken to remove trace amounts of water) on a TA Instruments SDT 2960 Simultaneous DTA-TGA. Thermogravimetry with mass-spectrometry (TG-MS) was carried out under helium on standard commercial equipment as a service. Larger scale heating experiments were performed in a silica glass tube in a tube furnace under a flow of nitrogen in which the water vapour content was controlled. Samples were heated at a rate of 10°C min^{-1} in all cases. For the larger scale preparation the material was kept at the desired temperature and held for the reported period of time at that temperature (between 400 - 600°C). The temperature measured at the sample, using a K-type thermocouple, was between 3 - 4°C higher than the setpoint temperatures over the range used. Experiments requiring controlled, high humidity were performed by bubbling a stream of high purity nitrogen through distilled water at 25 °C and hence through the silica glass tube and over the sample. Under typical conditions this gave approximately 20 cm^3 min^{-1} H_2O / 500 cm^3 min^{-1} N_2 at 25°C and 1 atm.

Energy dispersive X-ray (EDX) measurements with scanning electron microscopy (SEM) and were performed on a JEOL JSM-35CF microscope with an accelerating voltage of 10kV fitted with a LINK AN 10000 EDX system. X-ray diffraction of products was performed on a STOE diffractometer with a linear position-sensitive detector covering 6° in 2θ and employing Ge monochromated Cu-$K\alpha_1$ radiation (λ = 1.540 56 Å). Samples were prepared by mounting between two sheets of milar as

rotating discs in the X-ray beam. ^{13}C, ^{31}P and ^{27}Al NMR were performed using Magic Angle Spinning (MAS) on a Bruker 400 MHz spectrometer unless otherwise stated.

Results and Discussion

Inclusion of Dioxane Molecules

Needle shaped crystals of approximate dimensions 0.1 - 0.05 mm long by 0.005 mm across were formed in 69% yield (calculated w.r.t. phosphorus or aluminium theoretical yield). EDX of samples before and after heating revealed, as expected, no significant change in the Al:P ratio. Thermogravimetric analysis (TGA) of AlMePO-β in nitrogen up to 600°C revealed a small initial weight loss followed by two main weight loss peaks at around 190°C and 460°C. The first peak was broad and it is likely that it is formed by the combination of several desorption peaks resulting from a range of sites with similar binding energies. The higher temperature peak is much more sharply defined, probably resulting from desorption from a single, more strongly binding site. X-ray analysis subsequent to the TGA revealed the sample had completely transformed to AlMePO-α.

In order to determine the nature of the weight loss events, a similar thermal treatment was applied under helium with on-line mass spectrometric analysis (TG-MS) (although, to ascertain the ultimate thermal stability of the sample, the maximum temperature was increased to 850°C with the same ramp rate). TG-MS in a helium atmosphere (Figure 1) shows the two weight loss events with peaks at 190°C and 450°C and matching of the mass spectra at these times reveals these to be due to the removal of dioxane molecules. At temperatures of 600°C and above, a weight loss of 8 % is observed and this can be attributed mainly to the loss of methane as indicated by mass spectroscopy. It is clear, however, that there are some higher hydrocarbons produced also, including C_2 and aromatic species. Comparison of thermal treatments in air and helium show a similar weight loss below 300°C but the air treated sample shows more weight loss at higher temperatures up to 600°C, and less at temperatures greater than this. (Total weight loss: air treated = 11.7 wt% compared to He treated = 15.8 wt%).

The TGA data indicate that in the as-prepared sample (air dried at 60°C) the chemical composition of AlMePO-β is $Al_2(PO_3CH_3)_3.0.25C_4H_8O_2$ (this corresponds to 9 dioxane molecules per unit cell). Heating in an inert gas results in the removal of 33% of the dioxane in the first, broad event peak and the remainder in the second, sharper event. If one assumes the decomposition in an inert atmosphere to follow Scheme 1, removal of the CH_3 group as methane only would permit a maximum weight loss of 10.7 % of the AlMePO framework. A value of 9.8 % weight loss is observed. Heating in air followed by XRD reveals AlMePO-β is air stable up to 350°C. Although calcination at higher temperatures in air might be expected to remove all the CH_3 groups the observed weight loss is less than the theoretical maximum. The reduced weight loss observed must arise

from the oxidation of the phosphonate units, involving take up of oxygen and, therefore, a weight gain offsetting that lost as methane.

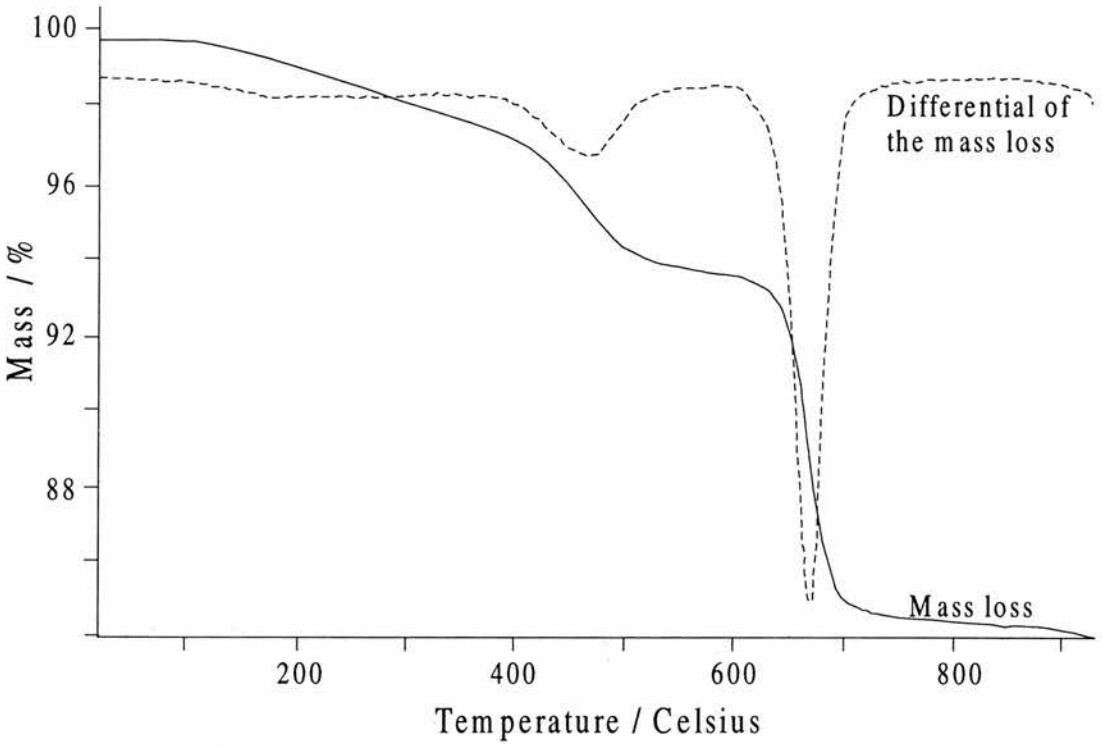

Figure 1 TG-MS of AlMePO-β in a helium atmosphere. The differential of the mass loss profile is on an arbitrary axis.

$$4\ \text{-}CH_3 \longrightarrow 3\ CH_4 + C$$

Scheme 1 Proposed mechanism for the pyrolysis of methyl groups in an inert atmosphere.

To confirm the presence of the dioxane molecules and to attempt to locate two chemically distinct sites corresponding to the two TGA events, ^{13}C and ^{31}P MASNMR (Figure 2 and Figure 3) were performed on a sample of as-prepared AlMePO-β and on a sample heated at a temperature sufficient to remove the dioxane without causing the -β to -α transformation. One expects to see extremely complex ^{13}C MASNMR resonances in the methyl region for AlMePO-β because there are six crystallographically distinct species, each split into a doublet by coupling with the attached phosphorus. The 1,4-dioxane, however, should give a single powerful resonance due to its highly symmetrical structure (Figure 4). ^{13}C MASNMR with cross-polarisation (CP) reveals a poorly resolved cluster of resonances at around 13.5 ppm, characteristic of $-CH_3$ groups attached to P. Also, there is one extremely sharp resonance at 67.65 ppm corresponding to the carbon of the dioxane. The ^{13}P MASNMR of the sample containing dioxane shows broader resonances than does the sample from which dioxane has been removed. Since the peaks are broadened rather than split, the dioxane molecules cannot be well ordered with respect to the AlMePO framework, at least on the timescale of the NMR

experiment. This is confirmed by the single site observed for dioxane rather than a set split by the local framework interaction. The two types of site indicated by the TGA are consistent with this observation since the rapid interchange of the dioxane molecules would not be expected to affect greatly the thermal energies necessary to effect desorption. It is noted, however, that a part of the ^{31}P resonance broadening effect could be due to the proximity of dioxane protons causing a through-space interaction. Proton decoupling was not used on the as-prepared sample so one cannot estimate the extent of the proton effect.

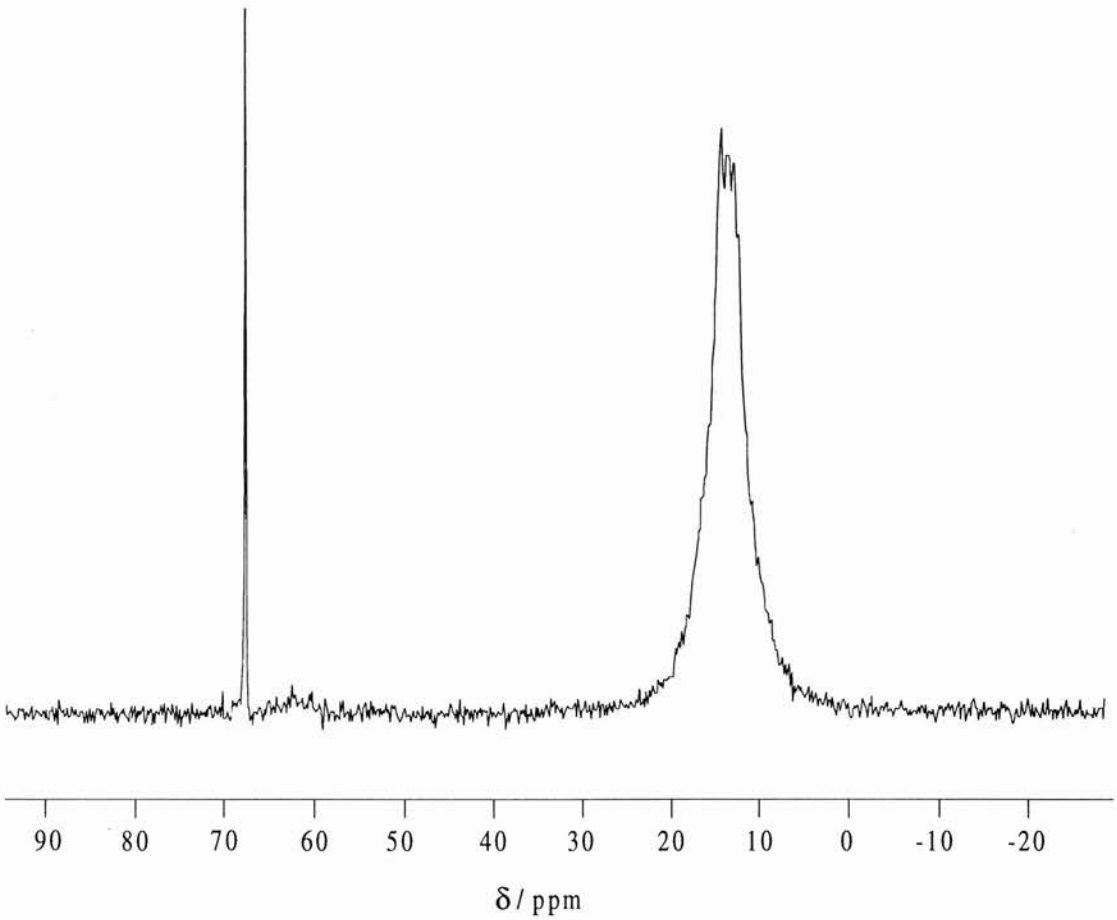

Figure 2 The ^{13}C CP MASNMR of as prepared AlMePO β showing both complex resonances in the methyl region due to P-CH3 and a sharp resonance downfield due to the 1,4-dioxane. No significant difference in the ^{13}C MASNMR was observed between the as-prepared and heated samples except for the absence in the latter of the dioxane resonance at 68 ppm.

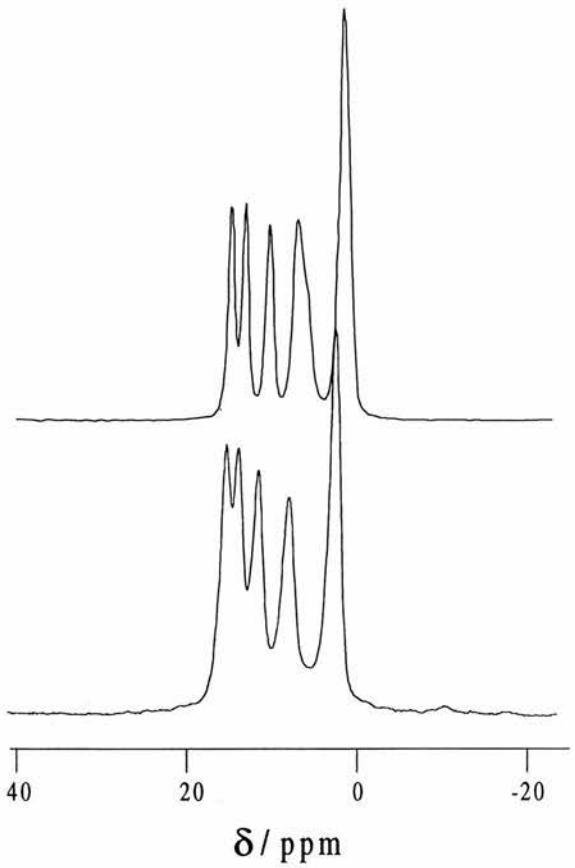

Figure 3 The ^{31}P MASNMR of AlMePO-β, before and after the removal of the dioxane. Note the broadening effect of the dioxane molecules on the phosphorus resonances.

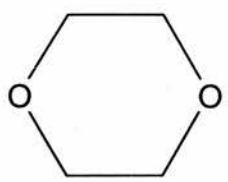

Figure 4 Structure of 1,4-dioxane. Note the high symmetry giving only one distinct carbon species and one oxygen species.

Topotactic Transformation

Examination by XRD of the sample used in the series of heating experiments designed to remove dioxane and assess the thermal stability of AlMePO-β revealed the formation of AlMePO-α (Figure 5). At temperatures below 450 °C, heating for 8 hours in a flowing nitrogen atmosphere (from which efforts had been made to remove water vapour) caused no change in the AlMePO-β sample except the aforementioned loss of occluded dioxane. The same period of heating at temperatures greater than 450 °C caused variable degrees of transformation from AlMePO-β to AlMePO-α. At 475 °C some AlMePO-α had been produced, a significant amount at 500 °C and, at 550 °C,

~90% of the sample had transformed (as measured by XRD). At temperatures greater than 600 °C the material turned black and lost all crystallinity.

The literature[5] reporting the original synthesis asserted the stability of AlMePO-β in a vacuum at temperatures of up to 500 °C. Therefore, as the only parameter to be changed in the current work was the presence of a nitrogen atmosphere, some characteristic of that atmosphere must have had a role in facilitating the transformation. As nitrogen is usually considered to be an inert gas for this type of thermal treatment, it was suspected that the transformation catalysing effect was due to a trace amount of water vapour.

To confirm the role of water a series of experiments was conducted in which the humidity of the nitrogen stream was increased in a controlled manner. A stream of nitrogen saturated with water vapour (approximately 20 cm^3 min^{-1} H_2O / 500 cm^3 min^{-1} N_2 at 25°C and 1 atm) was passed over samples heated at temperatures in the range 450 - 525 °C (see Figure 6 for typical results). Different samples of AlMePO-β transformed at differing temperatures so that the ranges reported show some variation for the general case (see below). The results shown in Figure 6 relate to one sample of AlMePO-β. The sample transformed completely to AlMePO-α at 500 °C with a range of conversions at intermediate temperatures. At T > 550 °C the sample lost all crystallinity and turned black – this is ~50 °C lower than the temperature at which this occurs in the drier nitrogen used previously. Investigations of the effect of the duration of the heat treatments on the extent of transformation revealed no effect.

It is interesting that the bulk of the material has transformed in the 480 °C treated sample, yet the 460 °C sample is predominantly still AlMePO-β. Such a large change over a relatively small temperature range indicates that the transformation, once it has been activated by a sufficient amount of thermal energy, continues to completion very quickly. Also, both the temperature at which the transformation is just observable and that at which it has gone almost to completion differed between preparations of AlMePO-β by more than 30 °C, some samples being mostly stable until the destructive decomposition limit was reached. It is reasonable to assume therefore that there would be a range of optimum activation temperatures for the crystallites within one sample, with the majority lying within a small range. Such an 'all or nothing' process is consistent with the independence of the extent of reaction on duration of heating and with the small dependence of the extent of transformation on temperature at the extremes of the investigated range.

The transformation is accompanied by a change in the local environment of the octahedral aluminium that it is possible to follow by ^{27}Al MASNMR (Figure 7). The octahedral aluminium resonance in AlMePO-β (δ = -19.2 ppm) reduces as the AlMePO-

α signal (δ = -22.6 ppm) increases. The sharpness of the peaks indicates a fast, 'coherent' reaction mechanism that does not involve a stable intermediate. The original and the transformed materials were examined under cross-polars in an optical microscope for evidence of topotacticity. Each of the crystal fibres examined was found to go into extinction uniformly when it was parallel and perpendicular to the polarised direction of the incident light, indicating that the transformation is indeed topotactic.

The heating procedure also resulted in a reduction in the N_2 adsorption capacity, at 77 K and $P_{N_2} / P^0_{N_2}$ = 0.2, from 2.6 x 10^{-3} mol g^{-1} for AlMePO-β to 4.6 x 10^{-4} mol g^{-1} for the product AlMePO-α. This reduction in adsorption capacity is presumably the result of defects produced during the transformation which act to block some of the channels in the structure. Maeda *et al*[6] have reported the adsorption properties of AlMePO-α transformed in a similar way from AlMePO-β through the use of steam treatments. Under these conditions of reaction, the AlMePO-α produced shows no drop in adsorption capacity for nitrogen. Presumably this indicates that the transformation is cleaner due to the greater amount of water vapour present to catalyse the bond rearrangements leaving fewer discontinuities. Interestingly, they also report that AlMePO-β adsorbs water at a $P_{H_2O} / P^0_{H_2O}$ value of ~0.7 whereas AlMePO-α shows no uptake, a difference they ascribe to the different sizes of the water clusters formed and the differences in the shapes of the channels. Such a result also shows the completeness of the transformation in the presence of steam since any faults within the structure of AlMePO-α would be expected to leave clusters of OH groups free, thus increasing the ability of the material to adsorb water.

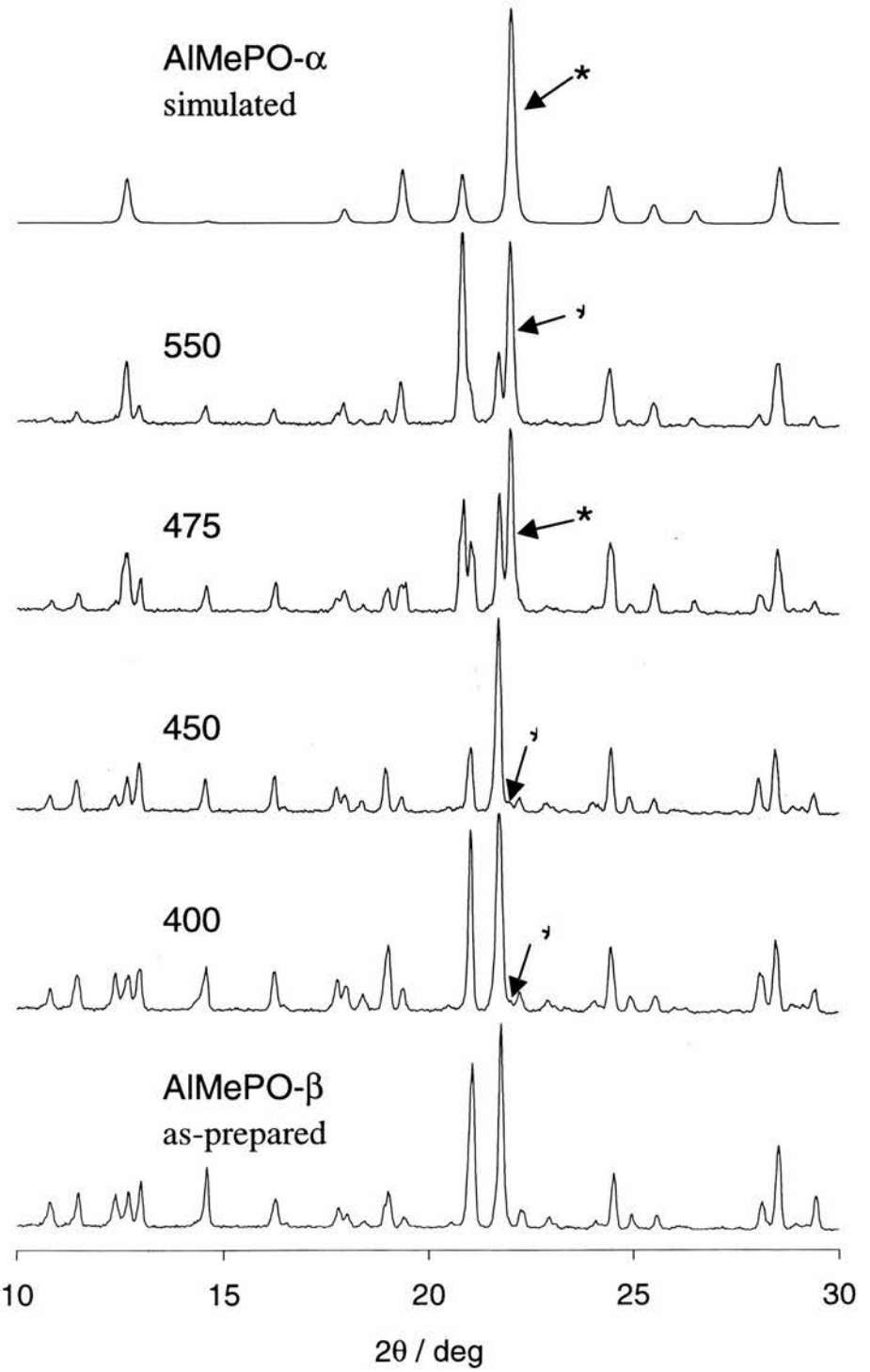

Figure 5 Showing XRDs of AlMePO-β samples heated in N_2, from which had been passed through a moisture trap, for 8 hours at the temperatures shown.

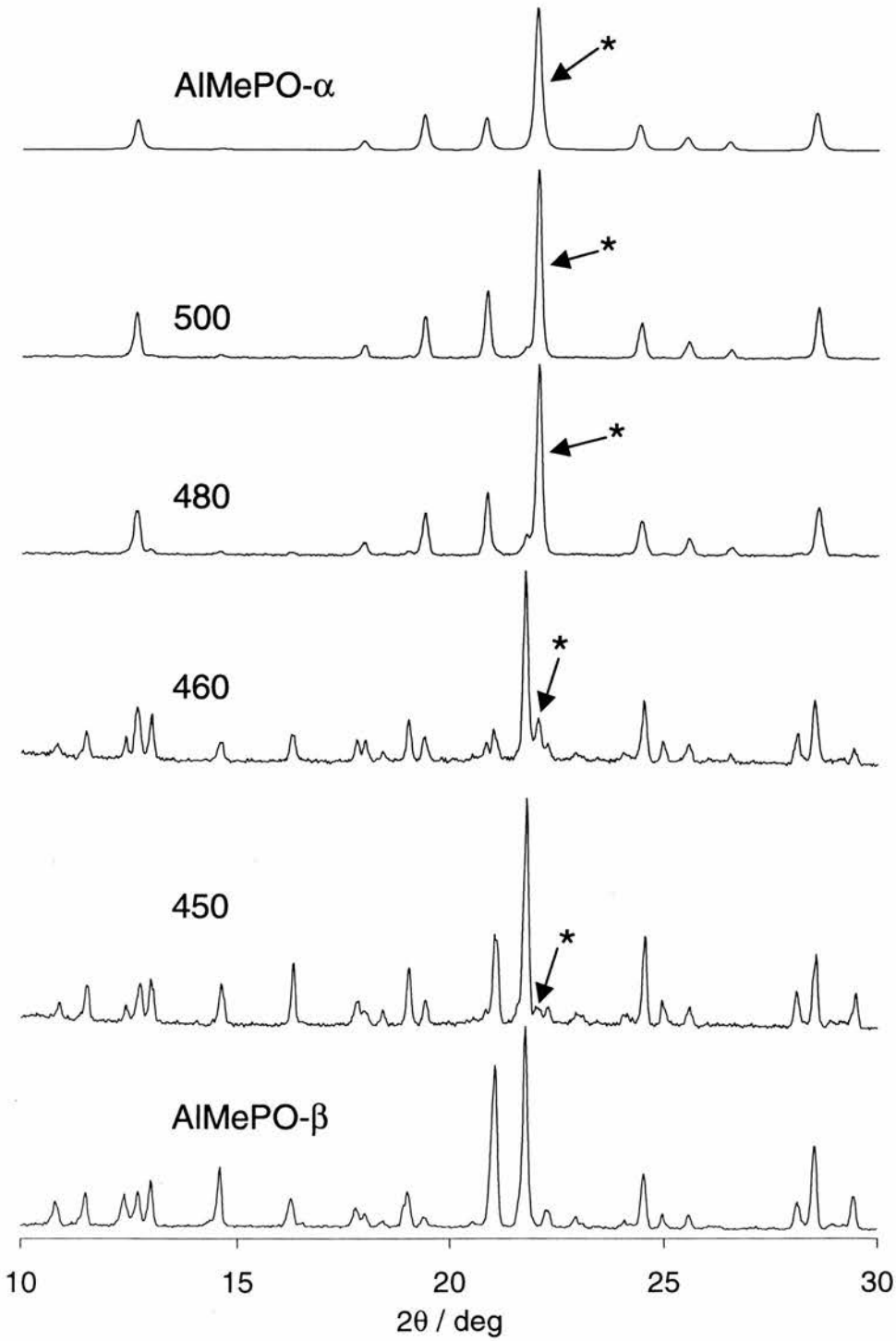

Figure 6 Showing XRDs of AlMePO-β samples heated in saturated water vapour for 8 hours at the temperatures shown.

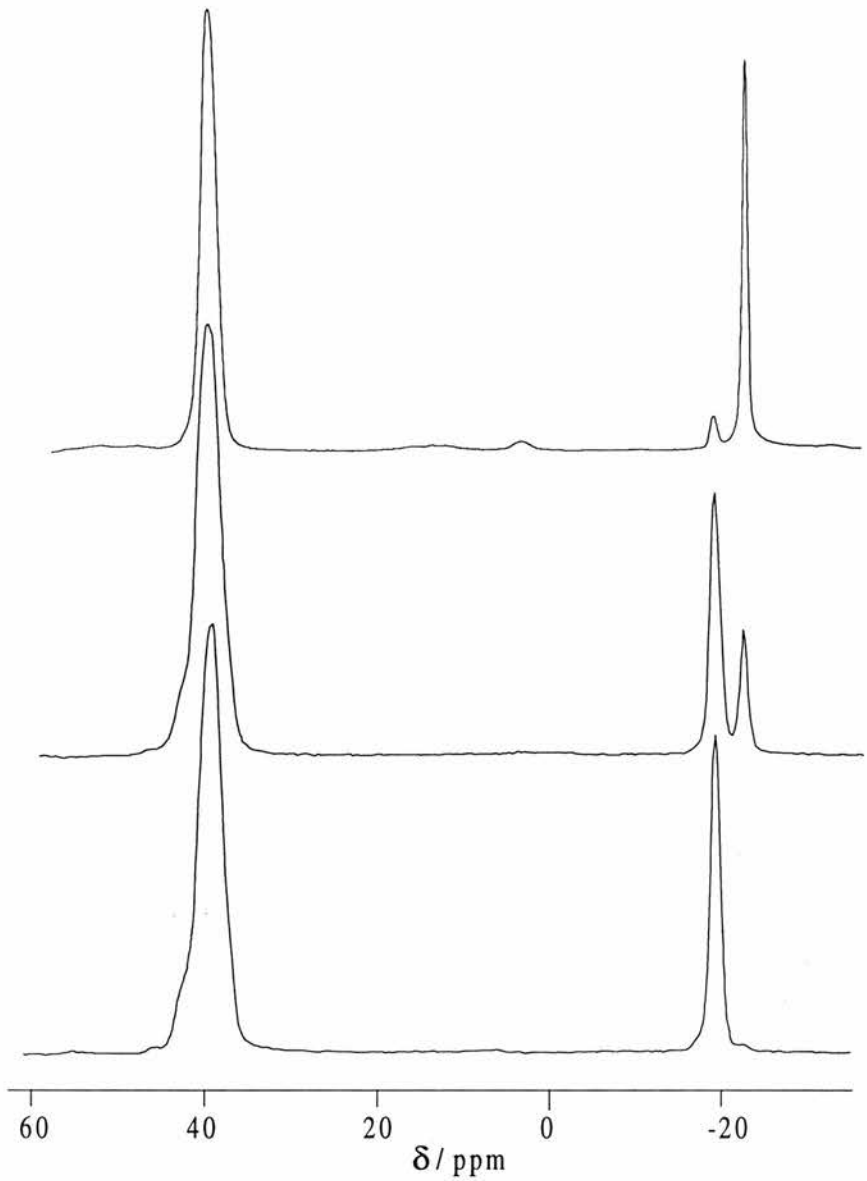

Figure 7 ^{27}Al MASNMR of AlMePO-β samples after a range of heat treatments.

Computational Studies

Since the two polymorphs are very similar and the heating experiments suggest that AlMePO-α is more stable than AlMePO-β, it was decided to attempt to confirm this using computational methods. The following computational work was performed by J. Gale at Imperial College, London, and is acknowledged with gratitude. The following details of the calculation were provided by Dr Gale also. It was decided to use a new periodic implementation of the semi-empirical quantum mechanical Hamiltonian AM1[7] as written in the program GULP.[8] While interatomic potential methods have been successfully used to model aluminophosphate structures and their relative energies,[9] they are not readily amenable to the AlMePOs because of having to blend a shell model for the inorganic component with a covalent model for the methyl groups.

In order to handle the long range summation of the Coulomb terms in this approach the integrals are evaluated exactly out to 12 Å, beyond which the integral formula is expanded as a power series in inverse powers of the distance. These terms become negligible after the fifth power and so the series is truncated here. Each term in the series can be summed by a partial transformation into reciprocal space in the same fashion as for the Ewald summation.[10] In the long range limit the integrals are evaluated in a point multipole approximation and the exact integrals are tapered to the approximate region to avoid discontinuities. All overlap integrals can be truncated similarly at the 12 Å cut-off as they become negligible. Given the large unit cells involved, the wavefunction is sampled at the gamma point of the Brillouin zone only as this should be sufficient. All structures are minimised fully with respect to the cell strains and the fractional coordinates using analytical first derivatives and a BFGS update of the hessian which is initialised as a unit matrix. See work by Gale[11] for further details.

While semi-empirical methods, including AM1, are generally known to have a weakness for the prediction of the relative energies over changes in coordination number, particularly for hypervalent compounds, they should be far more reliable in this case as we are comparing two structures which are closely related and have the same connectivities and environments for all atoms. Results from the calculations on the energy minimised structures indicate that AlMePO-α is ~12.6 kJ mol^{-1} per formula unit $[Al_2(CH_3PO_3)_3]$ more stable than AlMePO-β, supporting the experimental observations. The calculated fractional coordinates of the two materials show excellent agreement with the experimentally determined values and the calculated cell parameters (AlMePO-α; *a(calc)* = 14.188 Å, *c(calc)* = 8.6532 Å, AlMePO-β; *a(calc)* = 24.7701 Å, *c(calc)* = 25.9097 Å) are all within ~ 2% of the published observed values.[2,5]

Discussion

These studies of the behaviour of as-prepared AlMePO-β when heated are best treated in two sections : firstly the removal of 1,4-dioxane molecules entrained during synthesis and secondly the topotactic transformation to AlMePO-α.

Magic angle spinning ^{13}C NMR shows the presence of 1,4-dioxane as a single sharp resonance, indicating that the molecules are mobile on the NMR timescale and do not occupy distinct sets of crystallographic sites. This is supported by the ^{31}P MASNMR because the ^{31}P resonances, arising from different crystallographic environments, are broadened, rather than split. Combined thermogravimetry and mass-spectrometry,

however, reveal that dioxane molecules are evolved in two steps. We suggest that these steps correspond to the removal of dioxane molecules that exist in two kinds of environment at different distances from the framework, but that can exchange between these positions. Continued heating in the presence of water vapour in an inert gas results in the transformation to the -α polymorph. The methyl groups are removed from the framework, largely as methane, at temperatures of 500°C and above, depending on the partial pressure of water vapour.

The transformation between the polymorphs is observed by X-ray diffraction and optical microscopy reveals it to be topotactic. The thermodynamic driving force for the reaction is revealed by the higher thermal stability of -α polymorph and confirmed by computational energy minimisations that indicated that the -α form is more stable per $Al_2(PO_3CH_3)_3$ unit than the -β form by 12.6 kJ mol^{-1} (2.52 kJ mol^{-1} per framework cation). The significance of this energy difference is best seen in comparison with the energies of aluminophosphate polymorphs. The difference in the lattice enthalpies between highest and lowest energy structures in the series AlPO-5, -11, -42 , VPI-5 is 4.5 kJ mol^{-1} per tetrahedral atom (experimental)[12] and 7.3 kJ mol^{-1} (computed).[9] The value of 2.52 kJ mol^{-1} per framework cation calculated for the AlMePO polymorphs is around a half of the difference between VPI-5 and AlPO-8, computed value = 4.6 kJ mol^{-1} and experimental value = 4.3 kJ mol^{-1}, which also undergo a topotactic interconversion (from VPI-5 to AlPO-8).

To understand how such a topotactic transformation is possible the structures are compared in Figures 5 and 6. The materials have the same composition, $Al_2(CH_3PO_3)_3$, and have channels, lined with methyl groups, of almost exactly the same dimensions. In both structures the phosphorus is exclusively tetrahedral and the coordination around the aluminium atoms is octahedral and tetrahedral in the ratio 1 : 3. The crystal structure of AlMePO-α is conventionally described in the trigonal space group P31c, with unit cell parameters a = 13.995 Å and c = 8.531 Å. However, the structure can be described[a] using the space group R3c with $a' = \sqrt{3} \cdot a = 24.240$ Å and $b' = 3 \cdot b = 25.293$ Å (see Appendix II for atom coordinates of AlMePO-α in this description, and for other supplementary data). This is equivalent to the conventional description of AlMePO-β in space group R3c with unit cell $a = 24.650$ Å and $c = 25.299$ Å, allowing direct comparison of atomic positions in the two structures. The orientations of the unit cells are shown in Figure 5. Ensuring that the origins of both structures are fixed with respect to the octahedrally coordinated aluminium atoms (in space group R3c the origin is not

---

[a] The transformation of the conventional unit cell for AlMePO-α to the equivalent R3c description to allow comparison of the two structures was carried out by R. Morris, University of St Andrews.

fixed by symmetry and can lie anywhere along the three-fold axis), it can be seen that the major difference in the two structures lies in the position of one of the tetrahedrally coordinated aluminium atoms (labelled Al(4) in the atomic numbering scheme of Maeda et al[1]). Al(4) is shifted by ~2.4 Å in AlMePO-β relative to its position in AlMePO-α, while the other two tetrahedral aluminium atoms are shifted by only very small amounts ($\Delta < 0.4$ Å). The structures of both AlMePO-β and AlMePO-α can conveniently be described in terms of columns of cage-like building units having aluminium centred (AlO_6) octahedra as vertices that are linked parallel to the channels along the c - direction (these are seen in Figure 9). The cages are made up of four 4-, one 6- and one 8- ring in -β (Figure 10a) and of three 4- and three 6- rings in the more symmetrical -α (Figure 10b). The columns of cages are joined in the *xy* plane by 'channel walls' comprising 4-, 6- and 8- rings in -β and 6- rings only in -α (Figure 11a, b).

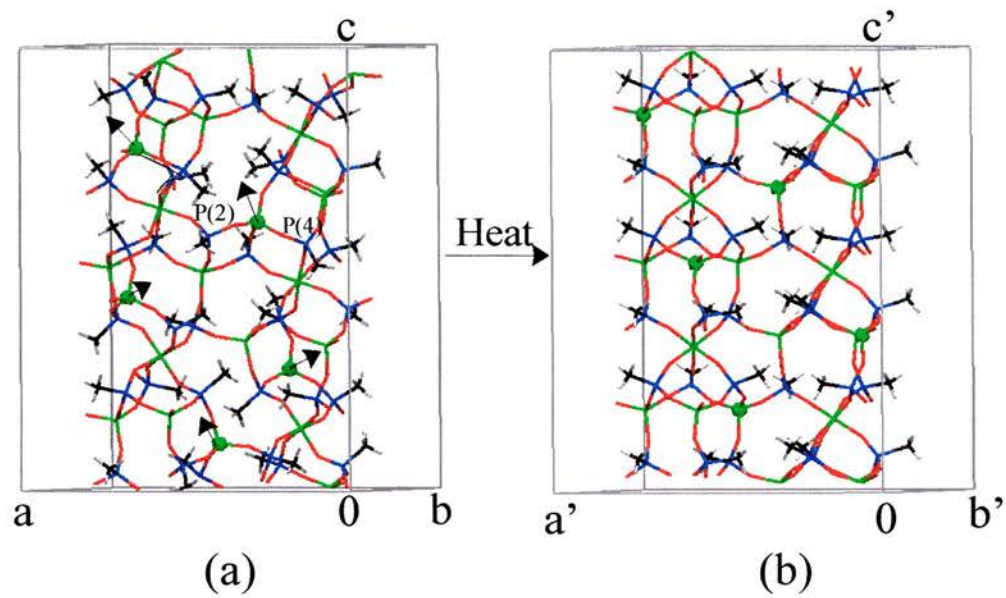

Figure 8 Views of AlMePO-β (left) and AlMePO-α (right) showing the distribution of Al(4) atoms (solid spheres) in the unit cell and the shift that occurs during the transformation of AlMePO-β to AlMePO-α. The direction of this shift is shown by the straight arrows. The phosphorus atoms, P(2) and P(4), which show the largest reorientation during the transformation are also labelled.

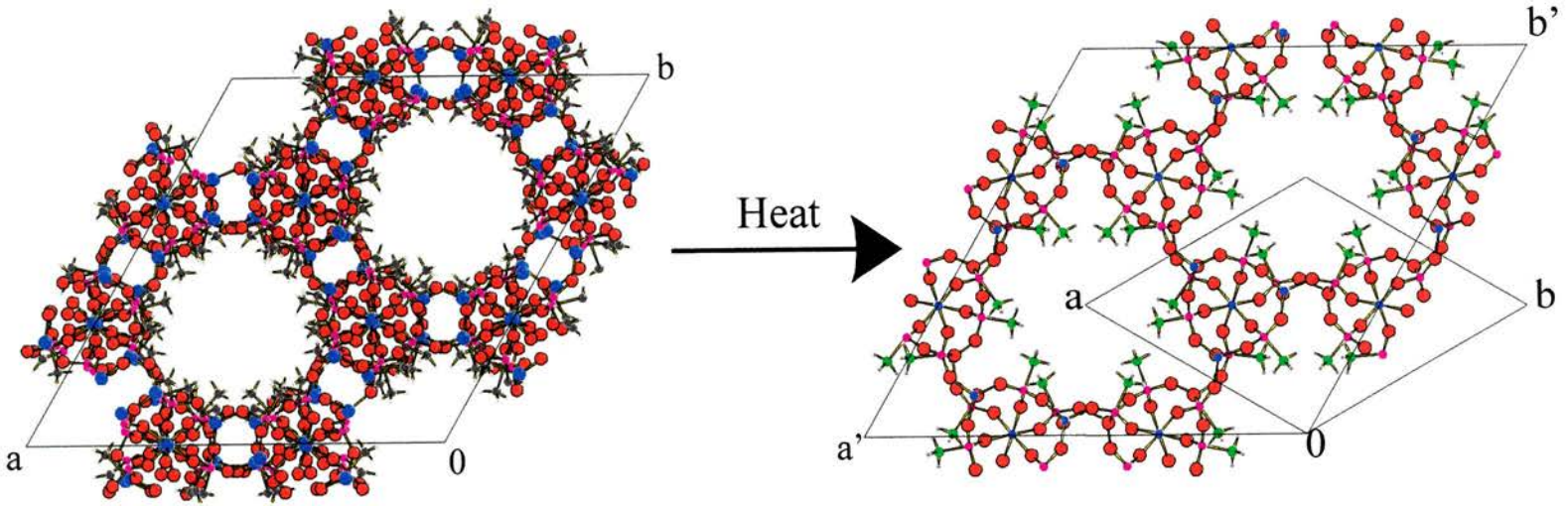

Figure 9 Views of AlMePO-β (left) and AlMePO-α (right) down the crystallographic [001] axis. The relationship between the unit cells of AlMePO-β and the conventional (abc) and unconventional (a'b'c') descriptions of AlMePO-α are shown. One can also see the columns of cage-like building units (parallel with the channels) and the difference in the way they are linked in the two polymorphs.

In order to understand what occurs during the transformation detailed consideration of the structure is necessary. Possibly the most informative section to examine is the cage-like building unit between two aluminium octahedra. This is represented by a ball and stick diagram in Figure 10 where a large sphere has been chosen to show Al(4). If the aluminium coordinations are shown as polyhedra (Figure 12) we can more readily appreciate the overall nature of the reaction and the greater symmetry of the product. To summarise the transformation - the first stage consists of the breaking of two of Al(4)'s Al-O bonds (the two furthest from the arrow on the diagram), leaving it free to move. This process leaves two phosphonate tetrahedra with an unattached oxygen vertex each. The second stage is the movement of Al(4), which retains its two Al-O-P bonds and moves to form two new bonds to two oxygens of different phosphonate groups. The phosphonate tetrahedra thus bonded to that Al(4) must have broken their bonds with Al(4)s further on in the structure to have been able to realign and form the new bonds. During this process the phosphonate group involved (top right of Figure 11) undergoes inversion (the -CH_3 orientation is greatly different).

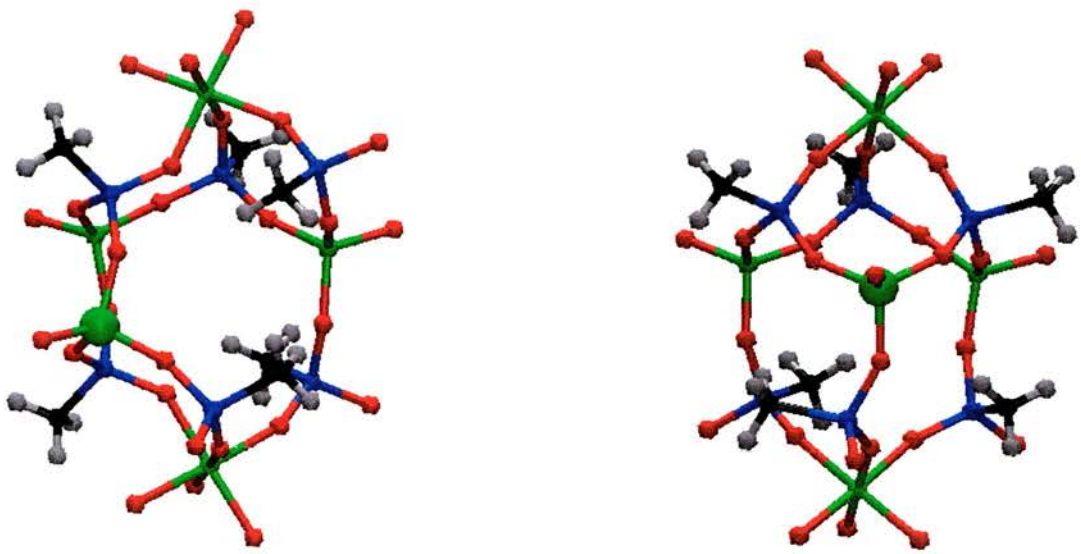

Figure 10 Diagram showing the cage-like building units and the movement of Al(4) (large sphere) during the transformation (a) AlMePO-β and (b) AlMePO-α. Note that only half of -β's cage-like units are shown as there are also mirror image cages to consider. One should also note the inversion of the phosphonate group in the top right of the diagram. Green denotes Al, pink denotes P, orange denotes O, grey denotes C and white denotes H.

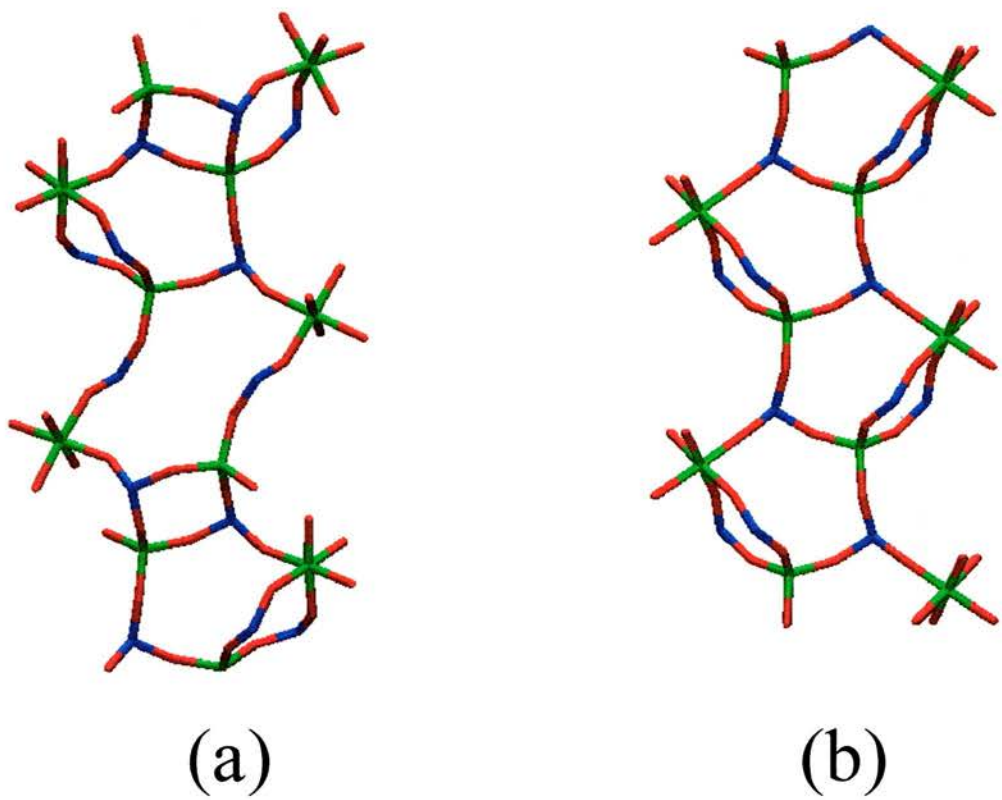

Figure 11 Diagram comparing the different rings connecting the columns of cage-like building units in the two polymorphs, (a) AlMePO-β linked by 4, 6 and 8 rings, (b) AlMePO-α linked by 6 rings only. Green denotes Al, pink denotes P, orange denotes O.

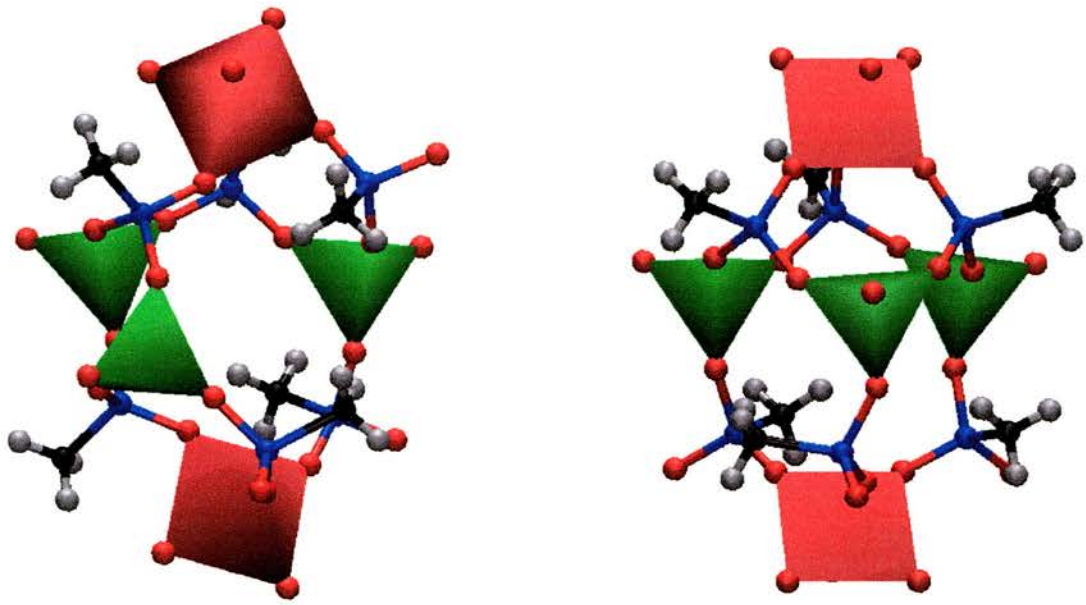

Figure 12 Diagram showing the cage-like building units and the overall rearrangement of the two polymorphs showing the aluminium coordination as polyhedra, (a) AlMePO-β and (b) AlMePO-α. One can see the overall change in geometry of the cages and the greater symmetry of the product. The green polyhedra are tetrahedral AlO_4 units, the red are octahedral AlO_6 units, pink denotes P, orange denotes O, grey denotes C and white denotes H.

Of course, the description above ignores the role of the water vapour in the reaction. As described the transformation would be very unlikely as there are many unstable transition states generated, i.e. P-O^- and 3 coordinate aluminium. A more likely scenario is that water coordinates to Al(4), hydrolyses the Al-O bond, protonating the P-O^- and leaving a hydroxyl attached to the metal (aluminium is known to be able to coordinate to become fivefold and sixfold in aluminophosphates). Al(4) can migrate to its new position as a stabilised intermediate and form a new bond with a phosphonate by condensation. In this way, water would act in a catalytic role, permitting Al(4) and the relevant phosphonate groups to move into a more stable configuration, that of AlMePO-α, with a reduced activation energy.

Since the reaction involves of all the aluminiums only movement of Al(4), it might appear, therefore, that Al(4)-O bonds have a greater vulnerability to hydrolysis than those of the other tetrahedral Al. However, it is likely that the driving force that causes Al(4), rather than the other aluminium atoms, to migrate is the existence of a more

stable alternative position for this atom, rather than any particular instability in its environment. However, although there is relatively little to distinguish the three tetrahedral aluminium species on the basis of their bond valence sums (Al(2) = 3.19, Al(3) = 3.23, Al(4) = 3.21 as calculated by the procedure of Brown *et al.*[13]), there is a slightly higher degree of distortion around Al(4) (mean deviation from tetrahedral: Al(3) - 1.63°, Al(2) - 2.0° and Al(4) - 2.6°). The slightly greater distortion around Al(4) is indicated also by the 5Q MASNMR results (Figure 13), both those reported in Chapter 2 and those of Rocha *et al*[14] (Al(2) and Al(3) at δ_{iso} = 42.8 ppm and 42.3 ppm respectively, and Al(4) at δ_{iso} = 45.0 ppm). This distortion may play a role in reducing the activation energy for this process.

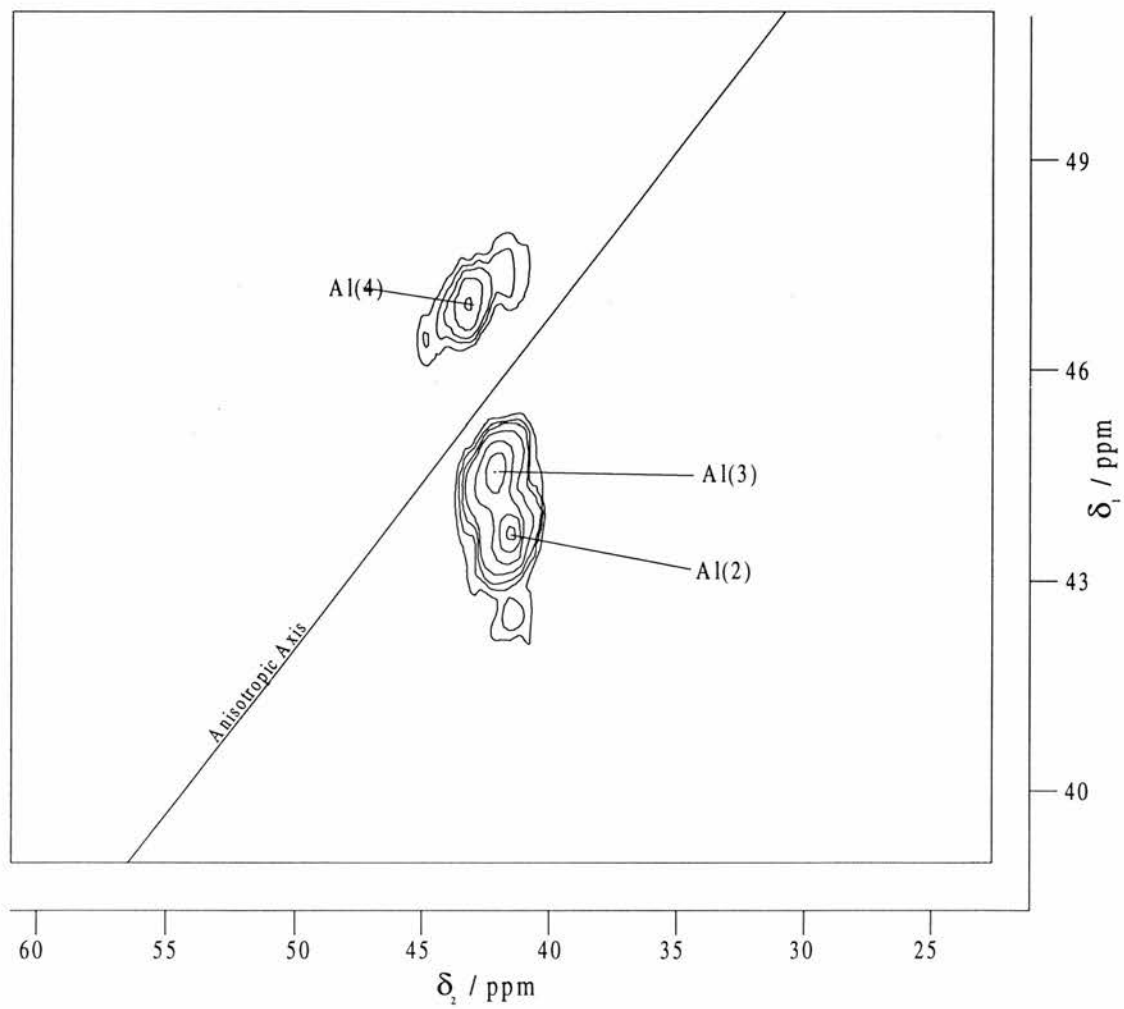

Figure 13 ^{27}Al 5Q MASNMR results of the tetrahedral chemical shift region of AlMePO-β.

A further consideration in understanding this phase transformation is the way in which the reaction spreads through the crystal. For every Al(4) that migrates, two phosphonate tetrahedra are left with unattached vertices (possibly OH groups), and another two form bonds with the migrating aluminium. This forces them to break bonds and rotate leaving two more Al(4)'s in low coordination, probably stabilised by the action of water. Thus,

every time an aluminium migration takes place the possible progress of the transformation can take two directions, both of which can occur at the same time.

Due to this branching effect, one can imagine, if the transition states are sufficiently stabilised by the coordination of water molecules, the reaction fanning out through the structure with ever increasing area of boundary. Such a mechanism of reaction is consistent with the 'all or nothing' character of the transformation of which we found considerable evidence. For example, there is the large increase in extent of transformation between the 460°C and 480°C heated samples in Figure 6. Over this temperature range the transformation goes from a very low to a very high conversion. Indeed, during all our investigations of this phenomenon we found very few samples that had transformed by approximately 50%. In addition, the XRD peak width of the product, AlMePO-α, is always narrow, even in the early stages of the transformation, indicating crystalline domains of diameter > 1000 Å, whereas some broadened X-ray diffraction peaks would result if domain size were growing slowly.

Conclusion

The reconstructive transformation of AlMePO-β to AlMePO-α is a rare type of structural change in a novel class of solids. It will be important to consider this transformation when using AlMePO-β in applications in adsorption and catalysis when reduction of adsorption capacity might result as a consequence of channel blocking due to defect formation. It is possible, under suitable conditions, to transform -β to -α without loss of adsorption capacity.[6] In that case changes in adsorption and, for appropriately substituted materials, catalytic properties would result from differences in the accessible framework topology (see, for example, Figure 11). This would not only enable differences in physical properties of the solids to be examined purely as a function of structure (and not particle size), but would also offer an alternative preparative route to the AlMePO-α polymorph which is the more difficult of the two materials to synthesis by direct hydrothermal methods.

References

1 K. Maeda, J. Akimoto, Y. Kiyozumi and F. Mizukami, *Journal of the Chemical Society, Chemical Communications*, 1995, 1033.

2 K. Maeda, J. Akimoto, Y. Kiyozumi and F. Mizukami, *Angewandte Chemie, International Edition English*, 1995, **34**, 1199.

3 M. A. Subramanian, D. R. Corbin and U. Chowdry, *Bulletin of Materials Science*, 1993, **16**, 665.

4 G. Sankar, P. A. Wright, S. Natarajan, J. M. Thomas, G. N. Greaves, A. J. Dent, B. R. Dobson and R. H. Jones, *Journal of Physical Chemistry*, 1993, **97**, 9550.

5 K. Maeda, Y. Kiyozumi and F. Mizukami, *Angewandte Chemie, International Edition English*, 1994, **33**, 2335.

6 K. Maeda, Y. Kiyozumi and F. Mizukami, *Journal of Physical Chemistry B.*, 1997, **101**, 4402-4412.

7 M. J. S. Dewar, E. G. Zoebisch, E. F. Healy, J. J. P. Stewart, *Journal of the American Chemical Society*, 1985, **107**, 3902.

8 J. D. Gale, General Utility Lattice Program (GULP) Version 2.0, Imperial College, London, 1996.

9 N. Henson, A. Cheetham, J. Gale, *Chemistry of Materials*, 1996, **8**, 664.

10 D.E. Williams, *Crystallographic Reviews*, 1989, **2**, 3.

11 J. D. Gale, *Faraday Discussions,* **106**, in press.

12 A. Navrotsky, I. Petrovic, Y. Hu, C.-Y. Chen, M. Davis, *Microporous Materials*, 1995, **4**, 95.

13 I. D. Brown, D. Altermatt, *Acta Crystallographica., Section B*, 1985, **41**, 244.

14 J. Rocha, Z. Lin, C. Fernandez, J.-P. Amoureux, *Journal of the Chemical Society, Chemical Communications*, 1996, 2513.

Chapter 5

Neutron diffraction study of the low temperature structure of AlMePO-β

Introduction

For a catalytic application, one of the most important characteristics of AlMePO-β would be the amount of access to the oxygen ions possible from the channels. In order to obtain a good estimate of this and to be able to map out the internal surface of the channel wall, it is necessary to obtain data on the positions of the methyl groups. Previous single crystal, X-ray diffraction work,[1] has been able to place the carbons of the methyl groups with some degree of accuracy. However, such attempts are limited in success because of the high speed rotation of the methyl groups at room temperature (the data mentioned above were collected at room temperature) and because the very light hydrogen atoms scatter X-rays very inefficiently.

In order to identify the position of all the atoms in the methyl groups, the best method is to use neutron diffraction at low temperatures. Neutron diffraction is more suitable than X-rays because the scattering factors for each element are not monotonically dependent on the atomic number. In addition, neutron diffraction gives very accurate data as it is possible to collect reflections from much smaller *d* spacings than it is using X-rays (see below). At low temperatures, the rotation of the methyl groups should be reduced greatly, thus allowing a better chance obtain accurate positions. The experiment was carried out at the High Resolution Powder Diffraction (HRPD) station at the ISIS neutron spallation source, Rutherford Appleton Laboratory.

Another aspect of the neutron study is that it should be possible to observe the solid-state transformtion of AlMePO-β to AlMePO-α (see Chapter 4) *via* this technique *in situ*. It would be necessary to use higher flux than is available on the HRPD station since fast collection of patterns at each temperature would be necessary. A successful neutron diffraction study aimed at a slightly different set of results would provide the necessary background information to allow an *in situ* reaction study to be carried out, giving the HRPD experiment a further aim.

In order to use neutron diffraction to its best advantage, it is necessary to remove ^{1}H from the sample because it has a large incoherent scattering factor. In the case of AlMePO-β this involves synthesising a deuterated material, using the Arbutzov reaction (see below). This chapter reports the preparation of such a sample and the refinement of the structural parameters to fit the subsequently recorded neutron diffraction pattern. Also part of this work is a deuterium NMR measurement of the rotational dynamics of

methyl groups in this compound. This data is used to form an idea of the internal surface of the channels in AlMePO-β.

Neutron Diffraction

Neutrons are heavy particles which, unlike X-rays, are diffracted from the nuclei of atoms. Although capable of many complex interactions with the angular momenta and magnetic fields of the atoms they diffract from, it is the availability of high resolution in atomic positions and the fact that scattering factors vary non-monotonically with atomic number that will be of importance in this work. The scattering factor for deuterium is among the highest of all the elements making this technique particularly suitable for the probing of the methyl groups in AlMePO-β.

The accuracy in atomic positions allowed by neutron diffraction is a result of the diffraction from the atomic nuclei, rather than the electron clouds around them. The interaction is governed by forces having a range of the order of 10^{-13} cm and the radius of the nucleus is ~10^{-15}cm. The wavelength of the neutrons is several orders of magnitude greater than this and, therefore, the atoms behave as points with respect to the diffraction. Since the pathlength of the neutron beam will not vary in diffraction from a single atom, as it would for the diffraction of X-rays, there is no dependence of the reflected intensity with sin θ/λ. Thus, it is possible to collect data from very low *d* spacings, giving rise to very precise refinement of atomic coordinates.[2]

Two types of neutron source are available, nuclear reactors and pulsed spallation. Reactors produce high energy, 'white' neutrons, i.e. a wide energy band. The flux is generally low because the reactor source is continuous. The build up of heat would be a problem under these conditions if the flux were high. Spallation sources, such as that at ISIS (Figure 1), operate by firing pulses of high energy protons at a heavy metal, e.g. ^{238}U, which releases neutrons as a result.[2] The neutron flux lasts for ~0.4 μs and is pulsed at between 24 – 50 Hz. As the pulse length is so small, high flux is possible, there being no problem in removing heat. The neutrons released have a range of energies, velocities and, hence, wavelengths. The scatter of energies is exaggerated by the moderation of the pulse, designed to slow the neutrons to thermal energies. In order to limit the effect of this and make the pulse of a more well defined length, beam choppers are used. These are rotating discs, a section of which has been cut away. As the disc rotates at a set frequency, the beam of neutrons can pass through only when the gap coincides with the beam path. Consequently, the pulse is shortened and the spread of energies, and wavelengths, reduced.

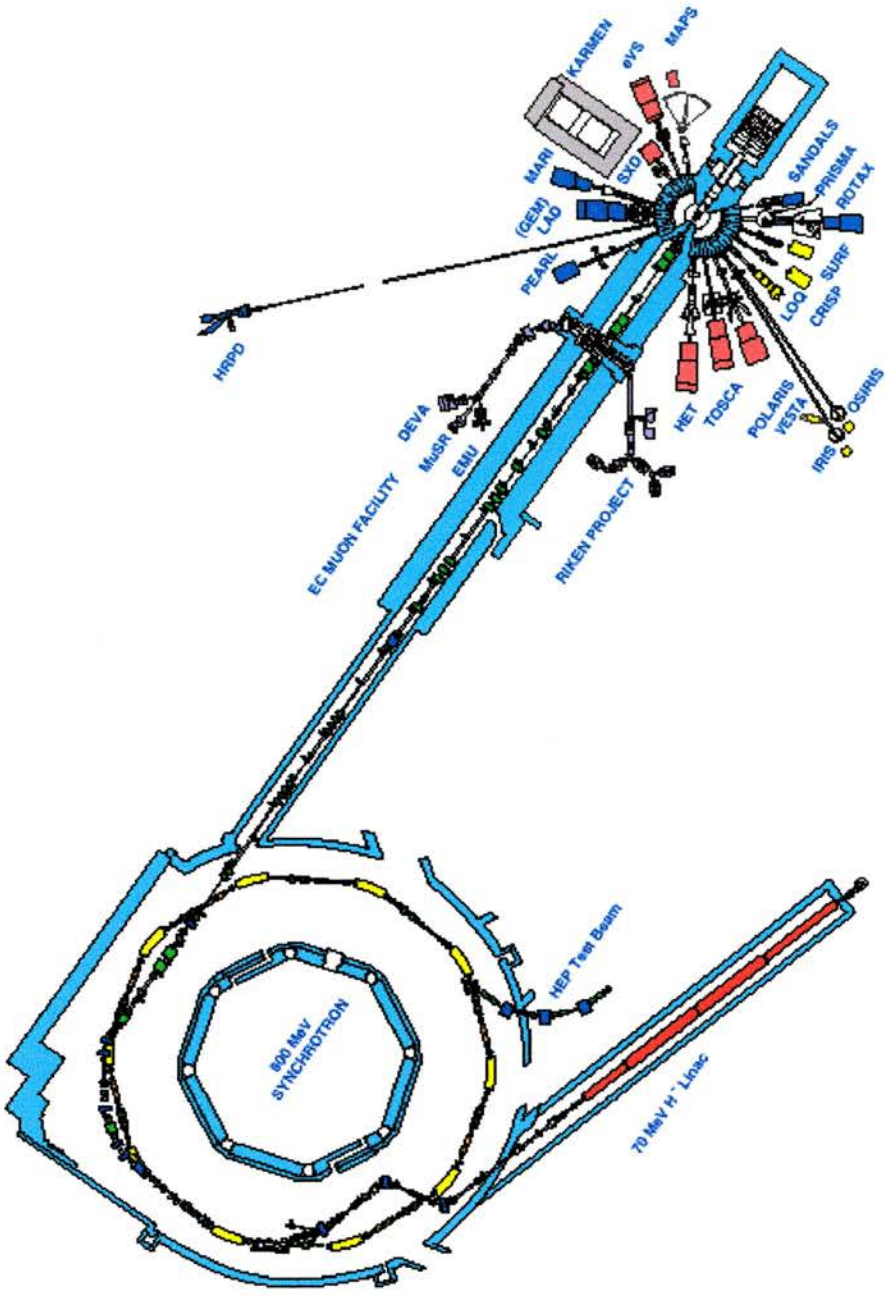

Figure 1 Diagram of the particle accelerator and target at ISIS. Note the pathlength to the HRPD station, designed to increase the resolution.[3]

As spallation sources operate with very short pulses with relatively long pauses between each one, all the neutrons arrive at the detector before the next pulse is fired. The beam chopper reduces the spread of energies but it does not give a monochromated source of neutrons. Therefore, the reflections cannot be discriminated on the basis of their 2θ

value. Instead, the time of flight (TOF) is used to discriminate between wavelengths at a single point in 2θ. De Broglie's equation relates the velocity and mass of a particle to its wavelength. Since the diffraction condition for a reflection is $\lambda = 2d\sin\theta$, it is possible to derive the reflection positions in terms of TOF. The relationship is[2]

$$t = 505.555Ld\sin\theta_0$$

where t is the TOF at which the reflection intensity occurs at angle θ_0. d is the spacing (in Å) such that the reflection condition above is true and L is the flight path (in metres).

It can be seen that, for a given time discrimination, resolution can be improved by increasing the flight path. Figure 1 shows the arrangement of the stations at ISIS with respect to the source. Notice that the HRPD station is a long way, ~100 m, away from the source to improve the performance of the instrument.

Experimental

Instrumentation

Neutron diffraction data were collected at 4.6 K on the High Resolution Powder Diffraction (HRPD) station at ISIS, Rutherford Appleton Laboratory which has a resolution, $\Delta d/d$, of ~ 5×10^{-4}. Data were recorded on two banks of detectors positioned at 90° and 168° in 2θ, during two time of flight windows, 30-130 ms and 100-200 ms, resulting in four diffractograms (see the summary in Table 1). Data were normalised by Dr Kevin Knight, an instrument scientist at HRPD, and refined using GSAS[4] (see Results for details).

Table 1 List of the parameters of the data sets collected at the High Resolution Powder Diffraction station at the Rutherford Appleton laboratory.

Bank	Data series	TOF window / ms
168°	histogram 1	100-200
168°	histogram 2	30-130
90°	histogram 3	100-200
90°	histogram 4	30-130

The deuterium NMR experiments were carried out on a MSL500 machine at 11.75 T with rf field of approximately 0.01 T. T_1 measurements were carried out at temperatures between 100 – 400 K.

Synthesis

Deuterated methylphosphonic acid was synthesised *via* the Arbutzov reaction[5,6] (Scheme 1). All chemicals were obtained from Aldrich and used without further purification. 7.0 cm^3 of iodomethane (0.11 moles) was mixed with 17.2 cm^3 triethylphosphite (0.10 moles) and refluxed for 4 hours. The excess iodomethane and the iodoethane produced were distilled away leaving a viscous oil $[(D_3C)P(O)(OEt)_2]$. 45.3 cm^3 of chorotrimethylsilane (0.38 moles), 72 g of potassium bromide (0.61 moles) and 100 cm^3 of acetonitrile (solvent) were added to the oil and refluxed for 48 hours. The reaction mixture was filtered on celite and washed with CH_3CN. The solvent was removed by rotary evacuation. ~50 cm^3 of water were added to the oil and stirred at room temperature for 3-4 hours then extracted with 3 aliquots of dichloromethane. The organic layer was discarded (it contains the silane) and the water removed from the aqueous layer by rotary evacuation leaving a crystalline solid. While the solid was white in the majority of cases, occasionally it became brown, particularly if left warm or open to air for more than 1 hour. Further extraction with dichloromethane removed the colour

although this sometimes had to be repeated several times (the brown colour was thought to be due to iodine formed by oxidation of iodide ions trapped in the product). The yield was ~70% based upon the amount of phosphorus in the first step.

The product was characterised by ^{31}P and ^{13}C NMR in D_2O and by FTIR. One resonance was observed for the carbon NMR, split due to coupling with the phosphorus. The phosphorus NMR also showed one narrow signal indicating that the material was not contaminated by any of the phosphorus containing intermediates. The FTIR spectrum showed neither the CH_3 deformation absorbance at 1315cm^{-1} nor the C-H stretch at ~3000 cm^{-1} confirming the purity of the reaction and the lack of significant exchange of the deuterium with protons from the solvent and reagents.

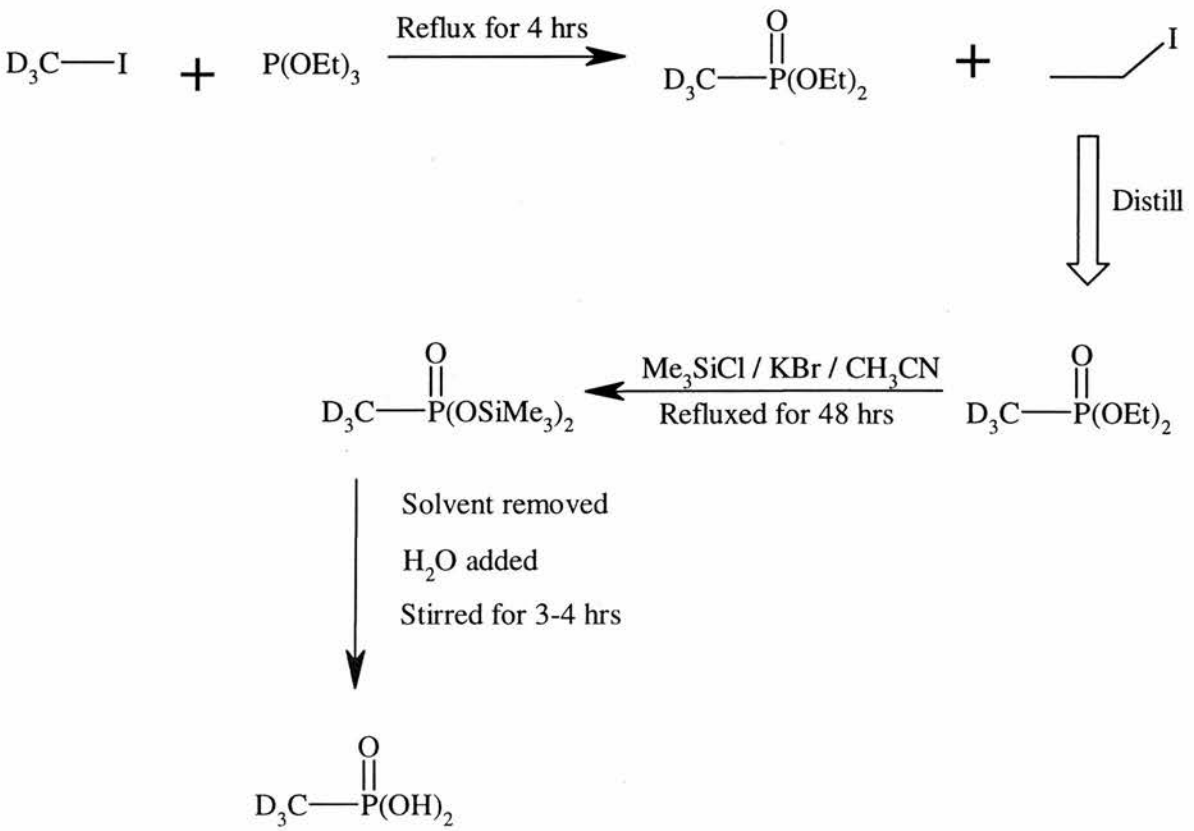

Scheme 1 Showing the Arbutzov reaction used to produce deuterated methylphosphonic acid.

Deuterated AlMePO-β was prepared from a modified version of the published procedure[7] by mixing $(CD_3)P(O)(OH)_2$: $Al(OH)_3$: D_2O : 1,4-dioxane in the ratio 1:1.8:40:0.5 until the gel was homogeneous. The gel reacted hydrothermally in a PTFE lined stainless steel autoclave for 48 hours at 160 °C. The product was filtered and

washed in distilled water (~60 cm^3) before drying in air at ~60 °C. The yield, based on the amount of aluminium in the gel, was ~55 %, on average.

Results

Refinement of the Neutron Diffraction Data

General considerations

Data were collected from two banks at the HRPD station of ISIS, at 90° and 168°, using two time windows (see Appendix III for plots of the patterns indexed on the published lattice parameters from room temperature, single crystal data[1]). The higher angle detectors yield data that gives the smallest *d* spacings, leading to more precise positioning of the atoms but, unfortunately, only over a small (0.8 – 4 Å) range. In using the 168° bank data to refine the lattice parameters during the early stages of the refinement, care must be taken because of the high density of reflections. At each reflection position there is the possibility of diffraction intensity. Since the positions are very close together, small shifts in lattice parameters will move the reflection markers along the pattern but are unlikely to cause any peaks to be missed. In the early stages of the refinement when the fit is poor and the calculated peak intensity is low, movements of the calculated peak positions do not cause the fit to change to a great degree. A result of this is that several sets of lattice parameters give similar fits to the pattern and the particular choice is likely to be random. Therefore, it is wise to include data from higher *d* spacings in the early stages, despite the lower resolution, because the density of reflections is much lower, helping to fix the lattice parameters in the correct configuration. At later stages of the refinement, when the calculated pattern is closer to the experimental pattern, the less accurate, higher *d* spacing data sets can be discarded as the lattice should be fixed within very small margins. This is the procedure that has been followed in this work.

Part 1 of the refinement - refinement of non-atomic parameters

A starting model was created from the published single crystal data and the defaults from the instrument parameter file supplied by a HRPD instrument scientist, Dr Kevin Knight of the Rutherford Appleton Laboratory (See Appendix II for a copy of the instrument parameter file). The first stage of the refinement was to find good values for instrument constants, such as profile function coefficients and the background function, and for lattice parameters. A 6 term cosine Fourier series was used to model the background, this having been found to be the optimum of a range from 3-8 terms of all the available functions implemented within GSAS. All six terms were refined for each histogram together with the scale factors and the lattice parameters. The fit parameters after convergence are shown in Table 2.

Table 2 Fit parameters after refinement of the background parameters.

Histogram	WRp	Rp
1	0.2513	0.1753
2	0.3314	0.3095
3	0.4133	0.3051
4	0.2210	0.1927
Total	0.2821	0.2331

At this point the fit was not as good as expected, particularly for Histogram 3. Examination of the plots of the diffractograms and the fit revealed that the calculated peaks were far too narrow for the experimental data. The profile parameter Sig-1 was refined to convergence, greatly improving the overall fit, especially that of Histogram 3 which gave a weighted profile fit, WRp of 8.54 % subsequent to this. Further refinement of the lattice parameters, background, scale factors and Sig-1 resulted in convergence with the profile fit shown in Table 3. After this point, Histograms 3 and 4 were excluded from further refinements.

Table 3 Profile fit parameters after preliminary refinement of lattice, background, scale factor and peak shape parameters. Reduced $\chi^2 = 16.57$.

Histogram	WRp	Rp
1	0.0752	0.0555
2	0.1202	0.0975
3	0.0870	0.0810
4	0.0706	0.0596
Total	0.0956	0.0720

Part 2 – Refinement of Atomic Parameters

The space group in which AlMePO-β crystallises, *R3c*, has no fixed origin on the *z* axis. In order to stop the origin moving without limit during refinement of the all the atom positions, it is necessary to fix the position along *c* of 1 atom. In this case, the *z* parameter of Al1 was fixed.

Several refinement strategies were used in an attempt to arrive at the best refinement possible.

Unconstrained Refinement

The first approach was to allow all the atom positions to vary under the maximum level of damping without any constraints. Although the lattice and background parameters were varied at the same time, the profile coefficients Sig-1, Gam-1 (and near the end of the refinement, Sig-2 and Gam-2 also) were refined iteratively with the atom positions,

i.e. the atom positions would be held constant and the peak shape varied then *vice versa*. The final fit parameters are shown in Table 4. Further results such as the atomic coordinates are reported later in this chapter as this is the model that was adopted for the most thorough treatment. (The background coefficients, peak parameters, etc can be found in Appendix II.) See below for a discussion of the merits of this fit with respect to the constrained approach. (Also see the discussion of Isotropic versus Anisotropic temperature factors for the deuterium atoms – this structure is the isotropic model).

Table 4 Final profile fit results for the unconstrained refinement using isotropic temperature factors for the deuterium atoms.

	WRp / %	Rp / %	Reduced χ^2
Histogram 1	5.26	4.41	-
Histogram 2	5.09	4.63	-
Total	5.13	4.55	4.24

Constrained Refinement

This approach involved refining the atomic positions having constrained the bond lengths of the aluminium-oxygen, phosphorus-oxygen and carbon-deuterium polyhedra as well as the vertex-vertex distances (in order to constrain the bond angles) to the values of the single crystal starting model. The constraints were input in the first instance as very harsh limits with sigmas of 0.001 Å (GSAS does not allow, to my knowledge, the overt setting of the 'softness' of the constraints – therefore the most effective way to achieve harsh constraints is to decrease the amount of expected spread of the distances from the set limit to the lowest possible value, 0.001 Å). Under these conditions the polyhedra behave almost as rigid bodies under refinement.

All atom coordinates, except *z* of Al1, were refined together with the lattice, background and scale factor. However, the fit did not improve to any significant degree. The constraints were re-entered with larger sigmas, i.e. as softer constraints, and the refinement repeated. This process was repeated with ever softer constraints as the fit failed to achieve the same quality as for the unconstrained refinement. Finally, with sigmas of 0.1, the constraints were considered to be of almost negligible effect and were entirely removed. Further refinement to convergence gave a fit of similar quality to the totally unconstrained refinement.

Comparison of the constrained and unconstrained structures

During the last stage of its refinement, all the constraints were removed from the constrained model. It was felt that the difference in the fit between the fully unconstrained model (WRp ~ 5%) and that containing constraints (WRp ~ 7%) was so great as to cast doubt upon the validity of the latter structure. Hence, it was decided that it was necessary to allow the structure the chance to move to the best fit configuration unconstrained.

It should be noted that, despite the fact that the constrained model was refined, eventually, without constraints, it is not equivalent to the fully unconstrained model in which bond distances were not controlled in any way. Placing constraints upon the structure whilst allowing it to change gives the refinement the chance to take a different path across the parametric surface. Thus, a constrained refinement, even one from which constraints are removed at a later point, experiences a different set of parameters to the unconstrained refinement. In this way, a constrained refinement has the chance to avoid certain local minima in the value of $\chi 2$ which might trap the unconstrained model into a false result.

In this case, however, the different pathways to the minimum resulted in quite similar structures. A comparison of the structures (Table 5) shows that there is little difference in the position of most of the atoms, and of those that do move significantly, all are deuterium or carbon atoms. Such a change is not surprising when one considers that the published structure that was used to create the starting model contained H positions modelled after the refinement had been completed. This was done because the single crystal data were not of sufficient quality to allow the refinement of such light atoms.[1] The C-H bond lengths in the structure from the single crystal experiment are ~0.96 Å, whereas the refinement of the neutron data gave values of ~1.09 Å. The modelled positions for the hydrogens given in the published data were calculated using a shorter than normal C-H bond. As the constraints were based upon the single crystal data, the shorter length was used, forcing the deuterium positions to be too close to the carbons. The shift of the deuterium atoms in the unconstrained model includes a substantial factor to account for this error.

Table 5 Difference in the atomic positions of the structures from the constrained and unconstrained refinements

Atom	Difference in position / Å
D39	0.34
D32	0.32
C31	0.21
D35	0.21
D41	0.20
D44	0.19
D47	0.18
D37	0.17
D52	0.17
D45	0.14
D53	0.13
C34	0.13
C30	0.13
Al3	0.12
Al4	0.12
Al2	0.12
D49	0.12
C38	0.11
P7	0.11
D36	0.10
O11	0.10
C42	0.08
D48	0.08
D51	0.08
Al1	0.07
P8	0.07
O19	0.07
C50	0.07
O23	0.07
O25	0.07
D40	0.06
C46	0.06
P10	0.06
P9	0.06
O16	0.06
P5	0.06
O20	0.06
O15	0.06
D43	0.06
O21	0.06
D33	0.05
O22	0.05
O29	0.05
O17	0.05
O14	0.05
O18	0.04
P6	0.04
O28	0.04
O27	0.04
O13	0.04
O24	0.04
O26	0.03

Given that the two strategies result in structures that do not differ very greatly from each other the unconstrained approach is used henceforth.

Isotropic versus Anisotropic temperature factors for the deuteriums atoms

The second point that requires attention in the refinement of the structure is the question of the best way in which to model the deuterium atom positions. At room temperature, the methyl groups are rotating at a high frequency (see later for details of the NMR measurement of the spinning dynamics of the methyl groups) and, therefore, it is impossible to obtain definite positions for the hydrogen atoms. At 4.6 K, however, the motion of the methyl groups is much reduced allowing the possibility of locating the hydrogen (or deuterium in this case) atoms with some degree of accuracy. Although the NMR measurements suggest that there is negligible rotation at 4.6 K, they were made at temperatures > 100 K and there is considerable scope for error at temperatures so close to absolute zero when different mechanisms of motion might become important. Thus, an attempt was made to model the motion of the methyl group using anisotropic temperature factors. It was thought that rotation of the group might be modelled by elongated ellipsoids placed upon the D atom positions of lowest energy and oriented so that the longest axis of each formed one side of a triangle coincident with the plane of the deuterium atoms. Subsequently, this refinement will be compared to the unconstrained model using isotropic temperature factors only.

Refinement of the temperature factors, both of deuterium and non-deuterium atoms, and the atomic positions, lattice and background parameters of such a model resulted in a much better fit to the experimental diffraction pattern (shown in Table 6 – compare with Table 4). However, the validity of using anisotropic temperature factors is doubtful as many of the coefficients obtained are physically meaningless, either through being too small or by describing ellipsoids that can't exist. Of those that are possible, e.g. those shown in Figure 2, the results seem to support the lack of rotation at this temperature since the ellipsoids are very small and not oriented in the plane in which deuterium would move if the methyl group were rotating.

Table 6 Final profile fit results for refinement using anisotropic temperature factors for the deuterium atoms.

	WRp / %	Rp / %	Reduced χ^2
Histogram 1	5.11	4.31	-
Histogram 2	4.21	3.98	-
Total	4.46	4.10	3.20

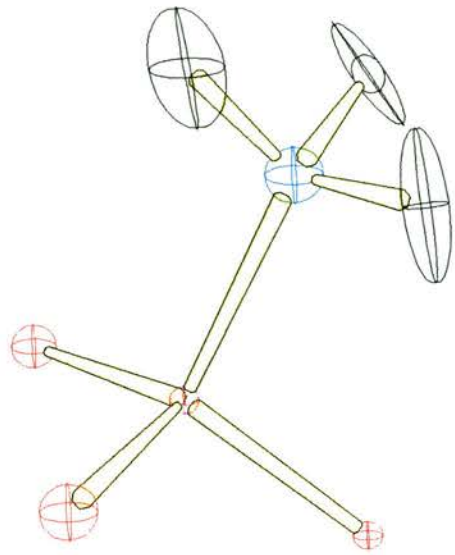

Figure 2 Diagram showing the orientation and size of a phosphonate group with the thermal ellipsoids. The deuterium atoms are modelled with anisotropic temperature factors but the ellipsoids obtained do not lie along the plane in which rotation, if it were to occur, would take place.

Therefore, it is not possible to refine the structure using anisotropic thermal parameters for the deuterium atoms in the sample. Either the data is not good enough to allow the extraction of these extra variables or the deuterium atoms have a very small amount of thermal motion. These two explanations are mutually supportive since the smaller the temperature factors, the smaller the effect on the pattern and the harder it is to extract them by refinement. Also, AlMePO-β has over fifty atoms in the asymmetric unit making it a very complex refinement. The more degrees of freedom available in the refinement the less certainty there is in any particular variable. Of course, the increase in degrees of freedom on going from isotropic to anisotropic temperature factors for the 18 deuterium atoms is considerable and it is not surprising that it is not possible to fit them perfectly in this way.

The results of refinement using anisotropic parameters are given in Appendix II. Atomic position from the refinement using isotropic temperature factors only are given in Table 7. Plots of the diffractograms and the calculated profiles for the isotropic fit are given in the figures below (Figure 3 - Figure 9). A summarised comparison of the structures obtained from the anisotropic and isotropic temperature refinements is given in Table 8 and Table 9.

Table 7 Atom coordinates and temperature factors of the fully refined structure utilising isotropic temperature factors for the deuterium atoms.

Atom	x	y	z	U_{iso}
AL1	0.3394(8)	0.3343(7)	0.4726(10)	0.01900
AL2	0.4781(9)	0.4277(10)	0.3398(9)	0.02581
AL3	0.2432(7)	0.3699(7)	0.3272(5)	0.00028
AL4	0.4234(8)	0.4798(8)	0.6082(6)	0.00235
P5	0.4049(5)	0.2992(5)	0.3858(5)	0.01000
P6	0.2050(5)	0.2676(5)	0.4101(4)	0.00755
P7	0.3712(5)	0.4505(5)	0.3886(4)	0.00536
P8	0.2913(6)	0.4047(6)	0.5590(6)	0.02546
P9	0.4701(4)	0.4106(4)	0.5329(4)	0.00020
P10	0.2763(4)	0.2122(4)	0.5393(4)	0.00077
O11	0.3543(4)	0.3118(4)	0.4061(4)	0.00194
O13	0.2544(5)	0.3056(4)	0.4459(4)	0.01074
O14	0.3547(4)	0.4187(4)	0.4385(4)	0.00923
O15	0.3124(5)	0.3621(5)	0.5331(4)	0.00949
O16	0.4202(5)	0.3765(4)	0.4918(4)	0.00848
O17	0.3198(4)	0.2647(4)	0.5005(4)	0.00509
O18	0.4636(4)	0.3581(4)	0.36601(35)	0.00233
O19	0.4322(4)	0.4605(4)	0.3645(4)	0.00989
O20	0.2455(4)	0.3727(5)	0.6035(4)	0.01212
O21	0.2590(4)	0.1488(4)	0.5139(4)	0.01049
O22	0.2119(4)	0.2998(4)	0.3569(4)	0.00476
O23	0.3217(4)	0.4213(4)	0.3457(4)	0.01125
O24	0.5334(4)	0.4605(4)	0.5068(4)	0.01467
O25	0.3084(5)	0.2167(5)	0.5918(4)	0.01348
O26	0.3800(4)	0.2540(4)	0.3371(4)	0.00466
O27	0.1398(4)	0.2414(4)	0.4323(4)	0.00666
O28	0.3493(5)	0.4662(5)	0.5767(4)	0.01419
O29	0.4548(4)	0.4444(4)	0.5745(4)	0.00353
C30	0.4290(5)	0.2597(4)	0.4311(4)	0.01575
D31	0.4719(7)	0.2609(6)	0.4177(6)	0.05900
D32	0.3853(7)	0.2151(7)	0.4405(5)	0.04575
D33	0.4397(6)	0.2851(7)	0.4676(6)	0.05638
C34	0.2090(4)	0.1982(4)	0.3928(4)	0.00701
D35	0.1684(6)	0.1655(5)	0.3665(5)	0.03711
D36	0.2020(7)	0.1679(7)	0.4263(7)	0.06468
D37	0.2537(6)	0.2131(7)	0.3713(5)	0.05135
C38	0.3834(4)	0.5256(4)	0.39766(34)	0.01480
D39	0.4225(5)	0.5529(5)	0.4305(5)	0.04850
D40	0.3417(5)	0.5277(5)	0.4107(5)	0.04386
D41	0.4012(7)	0.5556(7)	0.3608(5)	0.06365
C42	0.2537(4)	0.4261(5)	0.5112(4)	0.00817
D43	0.2433(4)	0.4585(4)	0.5258(4)	0.01887
D44	0.2094(6)	0.3871(6)	0.5030(5)	0.03937
D45	0.2799(7)	0.4446(7)	0.4740(7)	0.06829
C46	0.4859(4)	0.3578(4)	0.5647(4)	0.01288
D47	0.5210(6)	0.3798(6)	0.5984(4)	0.05135
D48	0.5030(6)	0.3326(6)	0.5401(5)	0.05118
D49	0.4437(5)	0.3190(5)	0.5829(4)	0.04157
C50	0.2095(5)	0.2134(6)	0.5530(4)	0.02541
D51	0.2136(5)	0.2555(6)	0.5654(5)	0.03719
D52	0.1766(5)	0.1761(6)	0.5774(5)	0.04321
D53	0.1788(6)	0.2075(7)	0.5161(6)	0.05083

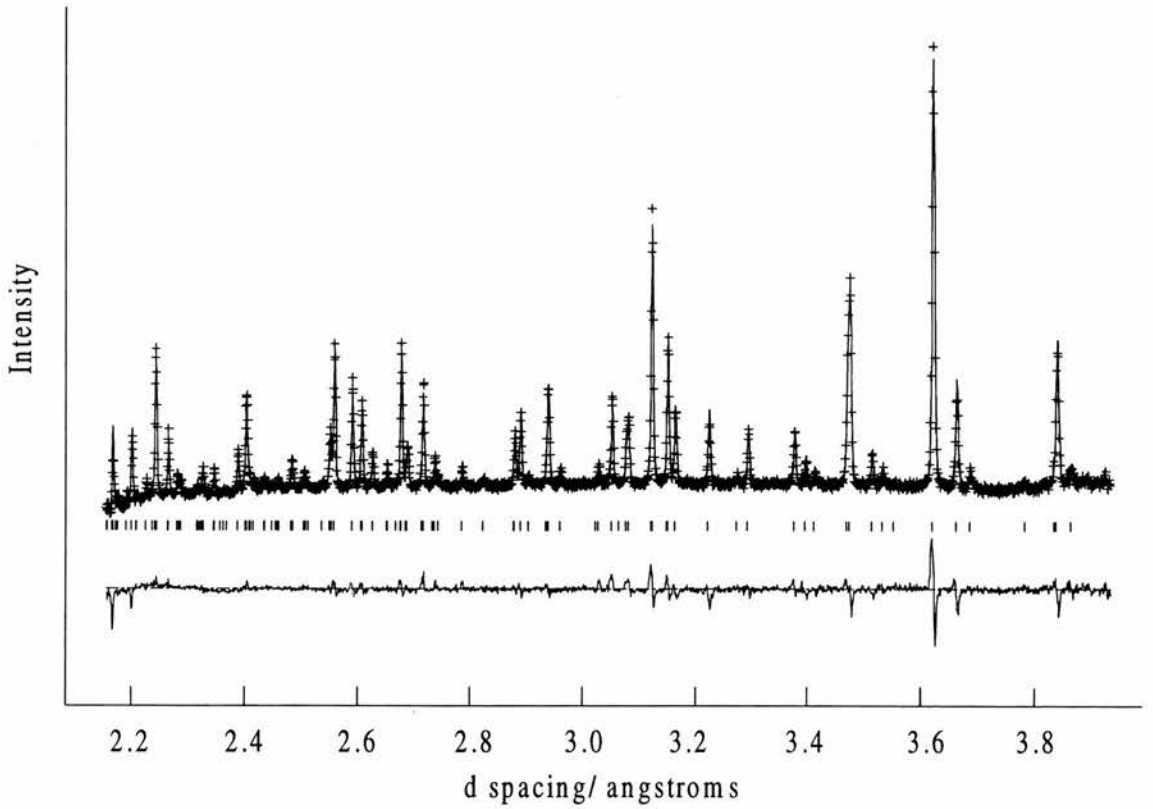

Figure 3 Histogram 1 (isotropic fit)– 100-200 ms time window collection from the 168° bank, 2.1 – 3.95 Å.

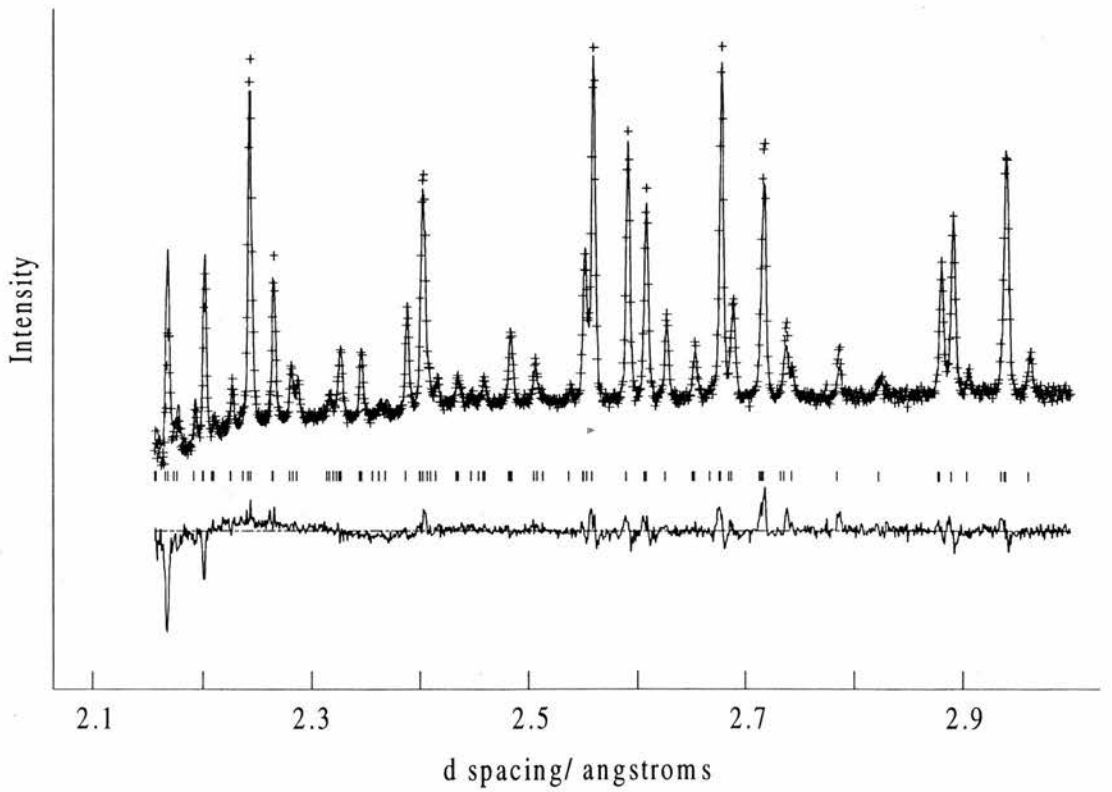

Figure 4 2.1 – 3.0 Å enlargement of Histogram 1 (isotropic fit for 100-200 ms from the time window collection from the 168° bank)

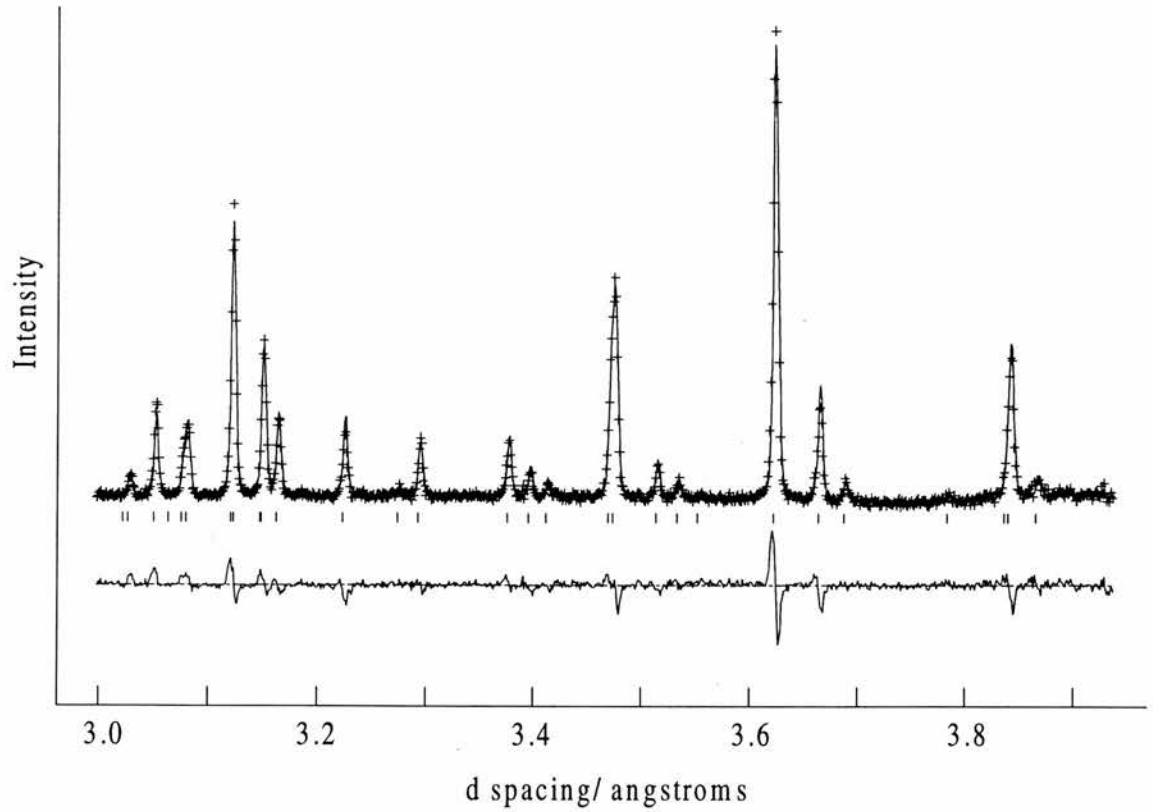

Figure 5 3.0 – 3.95 Å enlargement of Histogram 1 (100-200 ms from the time window collection from the 168° bank)

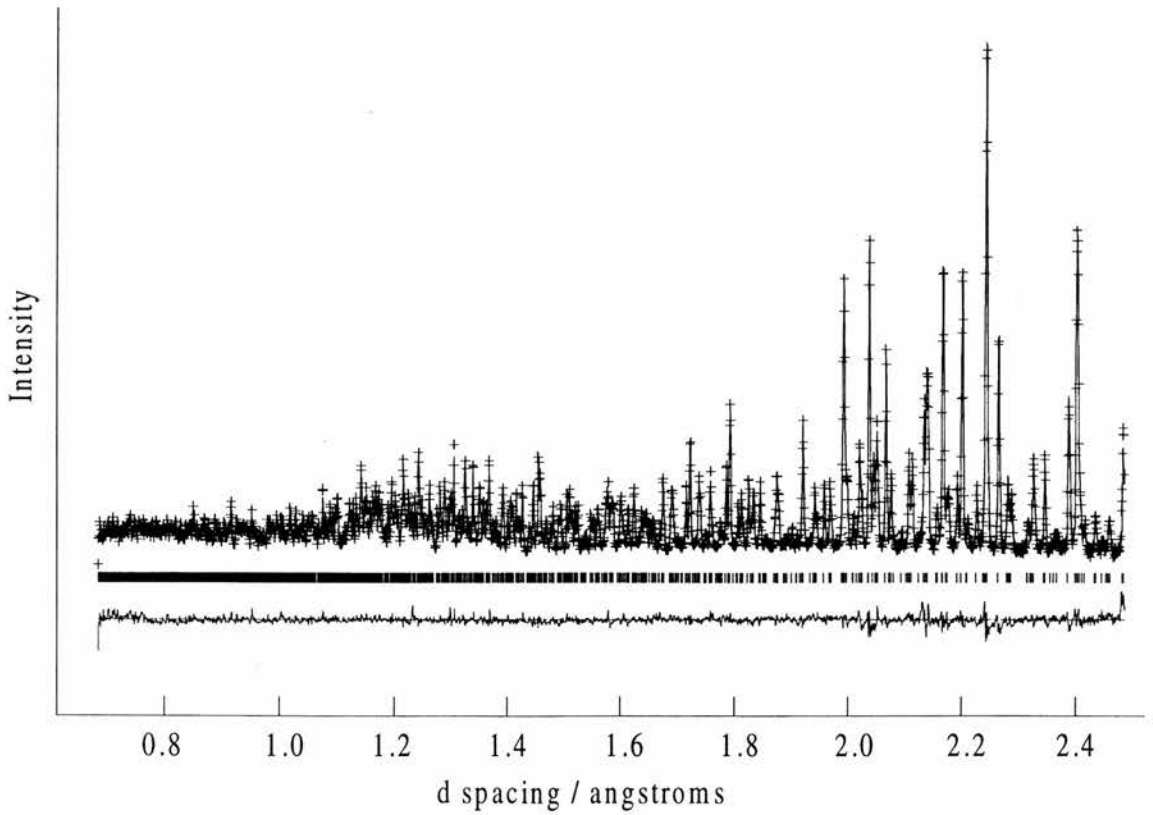

Figure 6 Histogram 2 – 30-130 ms time window collection from the 168° bank, 0.7 – 2.5 Å.

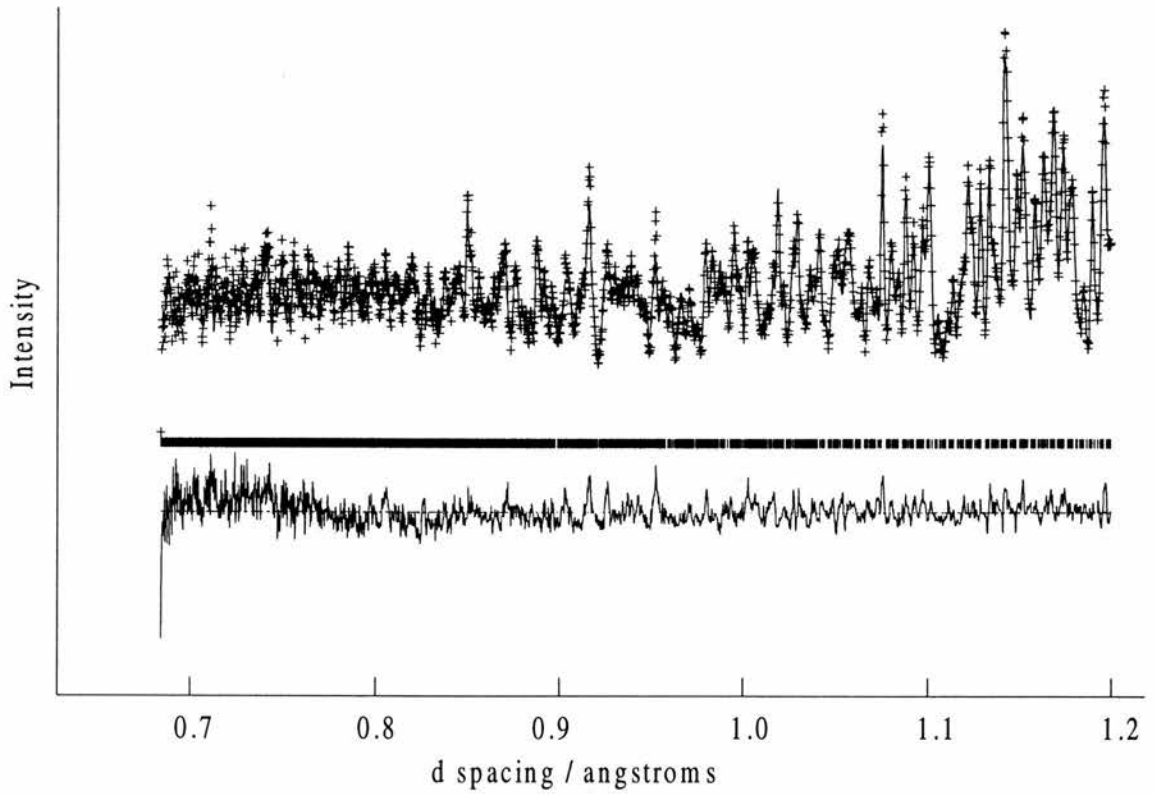

Figure 7 0.7 – 1.2 Å enlargement of Histogram 1 (30 – 130 ms from the time window collection from the 168° bank)

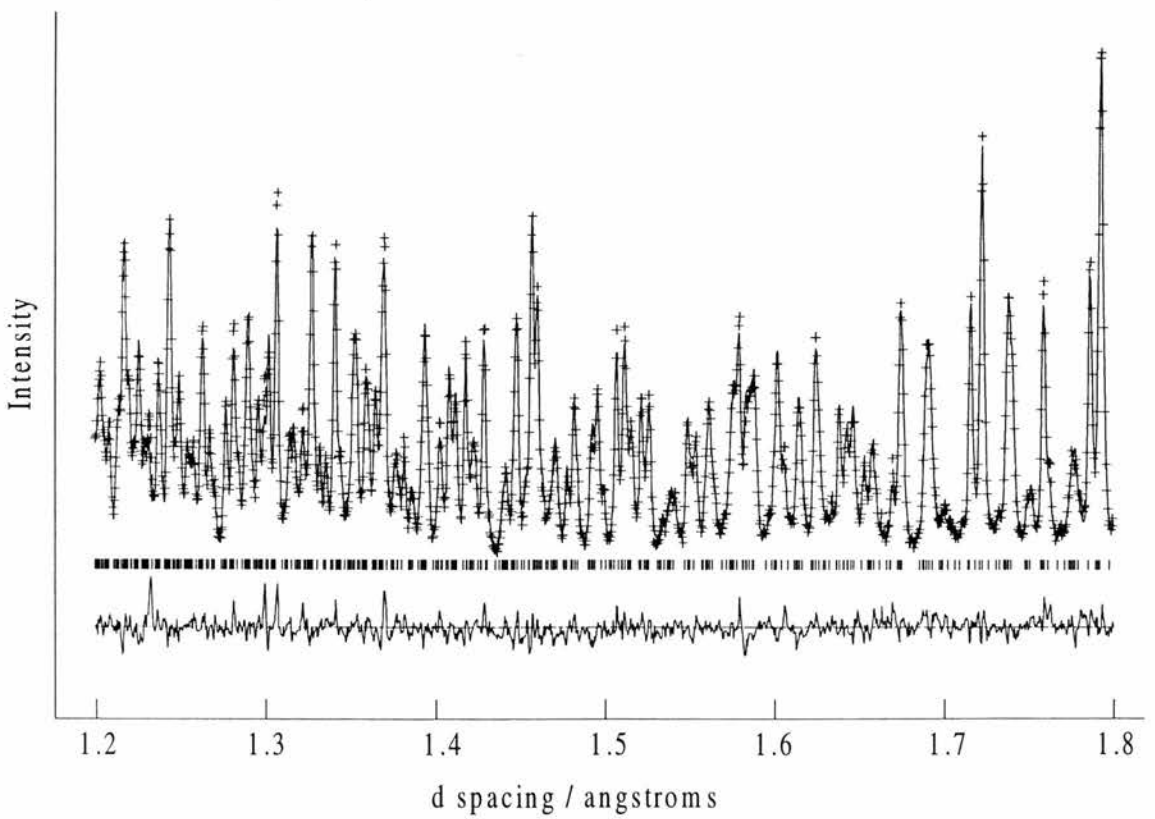

Figure 8 1.2 – 1.8 Å enlargement of Histogram 1 (30 – 130 ms from the time window collection from the 168° bank)

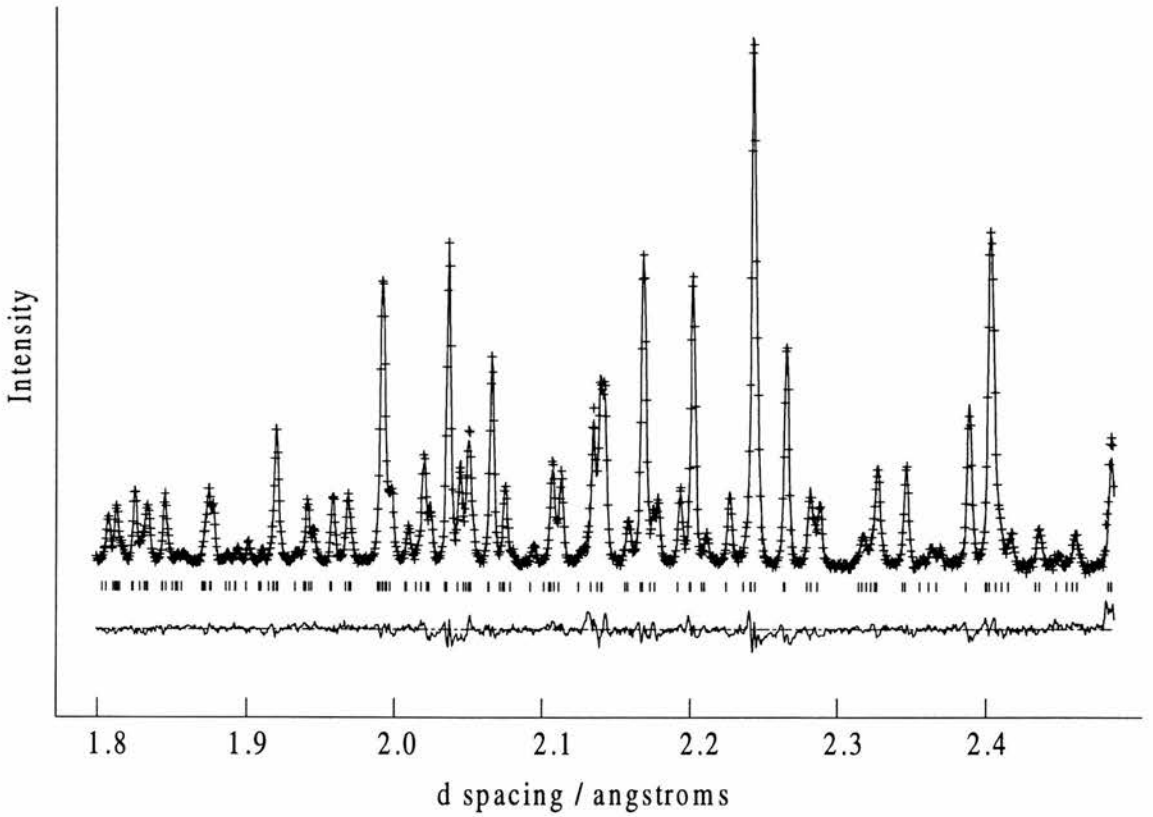

Figure 9 1.8 – 2.5 Å enlargement of Histogram 1 (30 – 130 ms from the time window collection from the 168° bank)

Table 8 Summary of the bond length comparison of the final structure refined with anisotropic temperature factors for the deuterium atoms with final structure refined with isotropic temperature factors (See Appendix II for the full list of bonds).

Final structure refined using anisotropic temperature factors for the deuterium atoms				**Final structure refined using isotropic temperature factors for the deuterium atoms**		
Bond	**Mean length / Å**	**Range (std dev) / Å**		**Bond**	**Mean length / Å**	**Range (std dev) / Å**
AL1_O11	1.88	0.083		Al1_O11	1.89	0.14
AL2_O18	1.76	0.068		Al2_O18	1.76	0.05
AL3_O22	1.74	0.072		Al3_O22	1.73	0.04
AL4_O26	1.74	0.107		Al4_O26	1.75	0.12
P5_O11	1.55	0.049		P5_O11	1.60	0.12
P6_O13	1.51	0.035		P6_O13	1.57	0.17
P7_O14	1.50	0.010		P7_O14	1.55	0.13
P8_O15	1.52	0.030		P8_O15	1.58	0.12
P9_O16	1.52	0.036		P9_O16	1.58	0.11
P10_O17	1.52	0.016		P10_O17	1.57	0.08
C30_D31	1.11	0.04		C30_D31	1.09	0.02
C34_D35	1.07	0.04		C34_D35	1.11	0.03
C38_D39	1.12	0.06		C38_D39	1.14	0.05
C42_D43	1.05	0.02		C42_D43	1.06	0.04
C46_D47	1.10	0.03		C46_D47	1.11	0.02
C50_D51	1.09	0.03		C50_D51	1.07	0.03

Table 9 Summary of the bond angle comparison of the final structure refined with anisotropic temperature factors for the deuterium atoms with the final structure refined with isotropic temperature factors. The deviation from perfect symmetry column measures the difference of the angle from the angle normally associated with geometry of the central atom, i.e. 90° between adjacent ligands of octahedral geometry and 109.5° between ligands of a tetrahedral geometry (see Appendix II for the full list of bond angles compared).

Final structure with anisotropic temperature factors				**Final structure with isotropic temperature factors**			
	Deviation from perfect geometry / °	**Mean deviation from symmetry / °**	**Standard Deviation of distortion / °**		**Deviation from perfect geometry / °**	**Mean deviation from symmetry / °**	**Standard Deviation of distortion / °**
O13_Al1_O14	5.4	2.8	1.6	O13_Al1_O14	8.8	4.9	2.0
O18_Al2_O19	7.2	3.9	3.7	O18_Al2_O19	7.5	3.4	3.4
O22_Al3_O23	7.0	3.4	2.3	O22_Al3_O23	3.7	1.9	0.9
O26_Al4_O27	0.9	2.9	3.1	O26_Al4_O27	3.3	3.2	2.9
O11_P5_O18	1.9	2.9	2.4	O11_P5_O18	3.9	3.5	2.3
O13_P6_O22	1.4	2.8	1.6	O13_P6_O22	2.8	3.8	2.3
O14_P7_O19	4.8	4.1	2.1	O14_P7_O19	5.8	4.1	1.9
O15_P8_O20	1.4	2.6	1.5	O15_P8_O20	3	2.1	1.4
O16_P9_O24	2.8	2.7	1.3	O16_P9_O24	1.8	2.7	2.0
O17_P10_O21	1.6	1.5	1.3	O17_P10_O21	1.5	2.0	0.9
H31_C30_H32	13.2	19.5	4.2	H31_C30_H32	12.9	7.2	5.4
H35_C34_H36	4.7	14.6	2.5	H35_C34_H36	8.5	4.4	3.9
H39_C38_H40	6.7	14.1	3.2	H39_C38_H40	3.7	3.7	0.6
H43_C42_H44	10.0	15.5	5.1	H43_C42_H44	6	2.5	3.1
H47_C46_H48	5.4	16.9	1.0	H47_C46_H48	3.4	5.0	2.2
H51_C50_H52	0.1	14.8	4.5	H51_C50_H52	0.3	7.6	6.8

Deuterium NMR measurement of the methyl group rotation dynamics

Powder ^2H NMR was performed by Jukka Kusanpää using a MSL500 spectrometer. The rotation parameters were measured in two samples of AlMePO-β, one of which contained 1,4-dioxane molecules occluded during the synthesis and the other of which had been heated to remove the dioxane. The procedure used was that of Sidhu *et al*[8] and Torchia *et al.*[9] Activation energies for the spinning process, assuming an Arrhenius dependence on temperature, were measured for both samples. Also, estimates were made of the frequency of rotation of the groups both at room temperature and at 4.6 K (Table 10). It was found that the activation energy for the process was 10.0 ± 0.2 kJ mol^{-1} for the heated sample and 10.8 ± 0.3 kJ mol^{-1} for the sample containing dioxane. These values are almost identical, within experimental error. The estimated correlation time, τ, was very low in the fast limit, i.e. at room temperature, giving a frequency of 4.48 x 10^{12} Hz. The estimated correlation time at 4.6 K was so great that it is safe to assume that all movement according to this mechanism has stopped at that temperature. Of course, this does not preclude the rotation that might take place through more esoteric mechanisms.

Table 10 Results of deuterium NMR studies to measure the rotation dynamics of methyl groups in AlMePO-β, both with and without occluded 1,4 –dioxane molecules.

Sample	**E_a / kJ mol^{-1}**	**τ_∞ / 10^{-13} s**	**τ (4.6 K) / s**
No dioxane	10.0 ± 0.2	2.23	5 x 10^{111}
With dioxane	10.8 ± 0.3	2.21	5 x 10^{121}

Discussion and Summary

The attempt to synthesise deuterated AlMePO-β was very successful, giving sufficient, very pure material for a neutron diffraction experiment at Rutherford, on the HRPD station of ISIS. The data obtained at ISIS was of very good quality and it was possible to refine the structure of AlMePO-β using this with very good agreement, although it was found that constraints designed to stabilise the minimisation were detrimental to the fit and were not used. Two main refinements were performed, one using isotropic temperature factors for the deuterium atoms, the other anisotropic. Although using anisotropic parameters improved the fit, the unreasonable values obtained indicate that it is not appropriate to use them in this case. Furthermore, the deuterium atoms for which the refinement produced reasonable values seemed to have very little thermal motion and it was not oriented in the plane in which rotation would take place. Therefore it was decided that the methyl groups were not rotating to any detectable degree and that isotropic thermal parameters were the most appropriate for modelling all the atoms in this sample.

In addition to the neutron diffraction experiment, deuterium NMR was used to study the dynamics of the methyl rotation. It was possible to estimate the activation energy for this process and the frequency at which it occurs. A very small difference, almost negligible within the experimental errors, was found between the rotation activation energies of a sample containing dioxane and a sample from which it had been removed by heating.

Given the evidence it has been concluded that the methyl groups are stationaryat the temperature at which the diffraction experiment was carried out, thus allowing the deuterium atoms to be located accurately. Previous work[1] on AlMePO-β has failed to characterise the methyl groups' positions fully due to a combination of the high rotation frequency at room temperature and the difficulty in locating hydrogen atoms using X-ray diffraction techniques.

Figure 10 shows a view along the P-C bond of all six phosphonate sites present in AlMePO-β, allowing the conformation of the group to be viewed. Without exception the methyl groups have adopted an anti-conformation so that the deuterium atoms are staggered between the oxygens attached to the phosphorus. The original structure solution of this compound by single crystal X-ray diffraction[1] was unable to locate the hydrogen atoms on the methyl group and, therefore, they were put in calculated positions around the carbon. Whilst the choice of position was wise in also adopting a staggered conformation, the bond length chosen was too short. Since the deuterium atoms have moved so little from their original positions in this refinement it was

decided to check the validity of the result. Individually, single deuterium atoms were moved ~0.2 Å away from their refined positions. The WRp value increase by ~2 % in every case, from ~5 % to ~7 %. Also, when the atom positions were allowed to refine, the deuterium returned to its former location. Since there are 18 deuterium atoms in the structure, it seems remarkable that such a small change in the position of one of them gives such a large effect on the quality of the fit. However, it does considerably strengthen the conclusion that the methyl groups are stationary at 4.6 K and that they adopt an anti conformation with respect to the PO_3 moiety of the phosphonate group. It is also interesting to note that a similar view along the P-C bonds of the phosphonate groups from the refinement using anisotropic temperature factors for the deuterium atoms is indistinguishable from that in Figure 10.

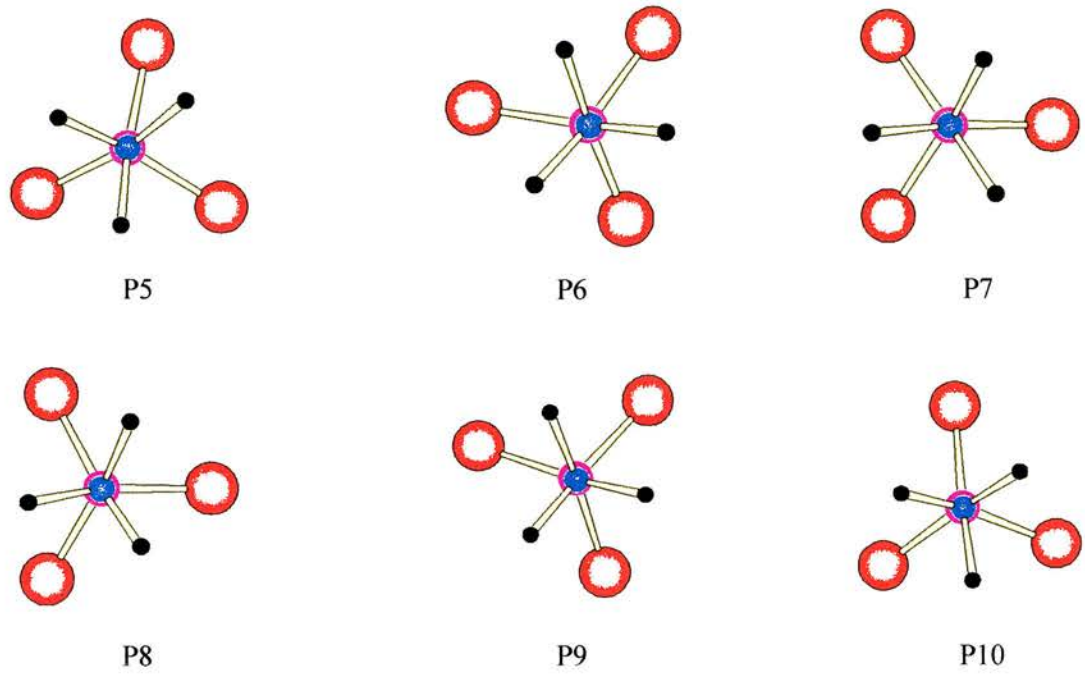

Figure 10 Diagram showing the conformation of the phosphonate groups in AlMePO-β. The data is taken from the refinement using isotropic temperature factors for the deuterium atoms.

A space filling diagram of the structure (Figure 11) with the refined coordinates shows the actual positions of the methyl groups on the internal surface of the channel wall. Allowing for the fact that the groups are rotating under normal conditions of adsorption or catalysis applications, it can be seen that there is not complete coverage of the walls. Although the aluminium atoms are well hidden from the internal surface of the channel (those that can be clearly viewed are part of the wall and would not be uncovered if the structure had not been cut away to show the inside of the channel) the oxygen atoms are

quite prominent in two areas of the portion shown. This must affect the hydrophilic properties of the sieve. Also, it might be supposed that the oxygens hiding the aluminiums in the areas bare of methyl groups could change their position as the aluminium, or heteroatom in its place, changes its coordination geometry to accommodate another member. The fact that there are areas bare of methyl groups indicates that redox metal centres dispersed in the aluminium positions might be able to interact with substrate molecules within the channel space.

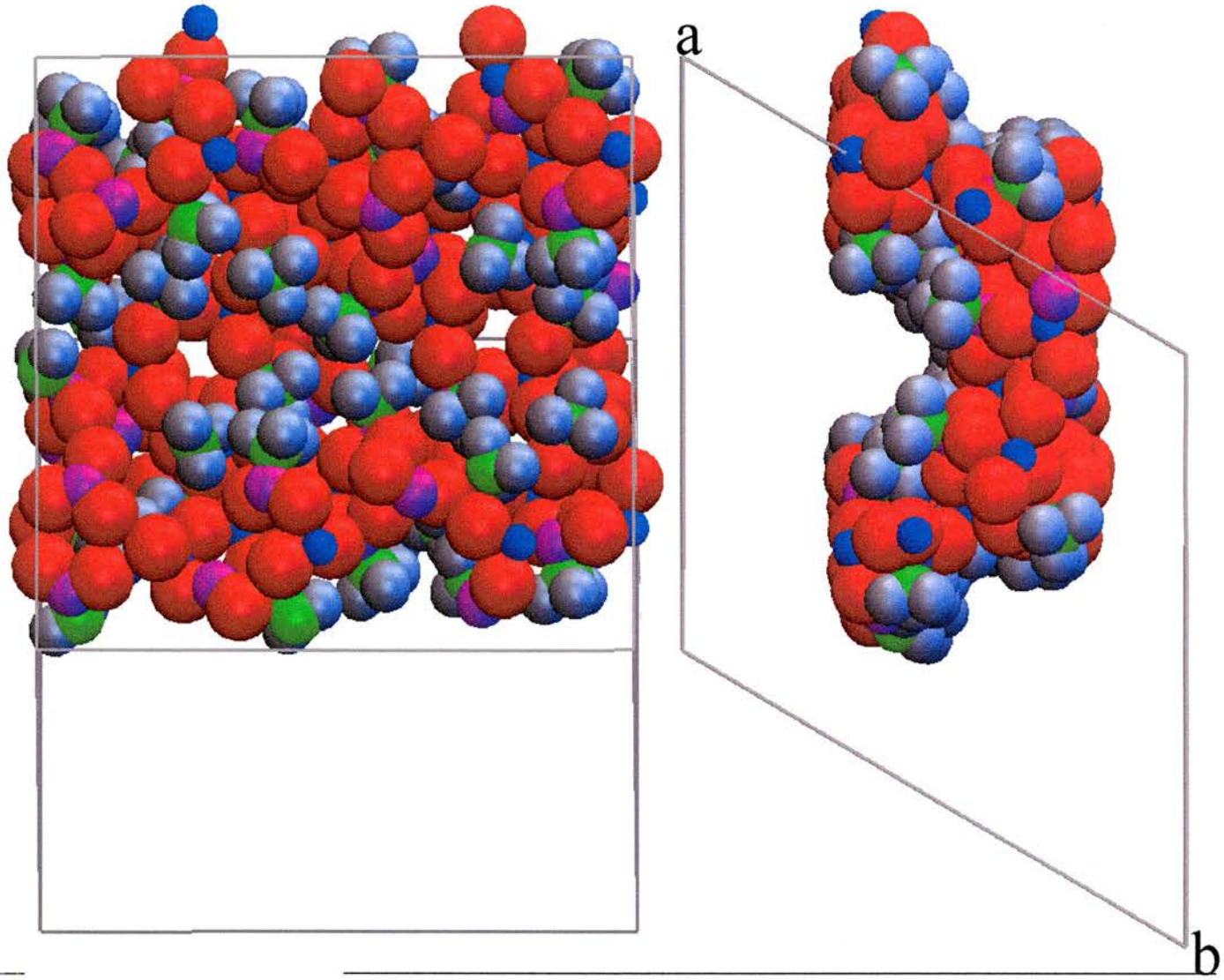

Figure 11 Diagram showing the inside of the channel in AlMePO-β. The atom parameters are taken from the isotropic refinement of the structure. The portion of structure on the right is viewed along the *c* direction while, on the left, the same portion is viewed having been rotated by 90° around the *b* direction. The top and bottom portions of the left hand view are cross sections of the wall included to provide a demarcation to the channel. Grey – D, green – C, red – O, blue – Al, and purple – P.

References

1 K. Maeda, J. Akimoto, Y. Kiyozumi and F. Mizukami, *Journal of the Chemical Society, Chemical Communications*, 1995, 1033.

2 *Fundamentals of Crystallography,* Edited C. Giacovazzo, p.199, Oxford University Press (Oxford), 1992.

3 *ISIS 1998 Report,* Rutherford Appleton Laboratory.

4 A. Larson and R. Von Dreele, Los Alamos National Lab. Rep. No. LA-UR-86-748, 1987.

5 A. K. Bhattacharya and G. Thyagarajan, *Chemical Reviews*, 1981, **81**, 415.

6 T. B. Brill and S. J. Landon, *Chemical Reviews*, 1984, **84**, 577.

7 K. Maeda, Y. Kiyozumi and F. Mizukami, *Angewandte Chemie International Edition English*, 1994, **33**, 2335.

8 P. S. Sidhu, J. Bell, G. H. Penner and K. R. Jeffrey, *Canadian Journal of Chemistry*, 1996, **7**, 1784.

9 D. A. Torchia and A. Szabo, *Journal of Magnetic Resonance,* 1982, **49**, 107.

Chapter 6

Attempts to Substitute Aluminium Phosphonate Structures Isomorphously with other Phosphonate Groups

Introduction

The structures of the two microporous aluminium phosphonates known at the present time, AlMePO-β[1,2] and AlMePO-α,[3] both contain unidimensional channels of ~6.5 Å diameter partially lined with an organic layer made up of methyl groups (Figure 1). As mentioned in the Introduction (Chapter 1), in contrast to the microporous aluminium phosphates (AlPOs), whose pore walls have a surface largely made up of oxygens, the presence of the methyl groups in AlMePO-β and AlMePO-α imparts a hydrophobic character to the internal surface of the channels.

The novelty of an aluminium and phosphorus based molecular sieve with a hydrophobic character is intriguing in itself when considering potential applications in catalysts and sorption materials. The most attractive facet of this structure, however, is the possibility of controlling the character of the sieve by choosing the organic groups which line the channel. Such control would lead to a class of materials with a practically continuous range of affinities for water, solvents and other organic molecules and, perhaps, even gases, for use in sorption applications such as chromatography or filters for effluents released into the environment. Also, it should be possible to create ion exchange materials through the use of organic groups containing metal binding heteroatoms such as nitrogen, oxygen and phosphorus itself. The ability to choose the make up of the organic lining of the channel would be very useful in catalysis also, giving materials that are not only size and shape selective but also sensitive to the chemistry of the substrate or product.

Finally, an understanding of the methodology necessary to change the channel lining might help to solve a potential problem in using these organic-inorganic materials as catalysts. In order to make AlMePOs or AlPOs active for oxidation or acid catalysis, it is necessary to modify the framework by isomorphously replacing metals. For acid catalysis a metal with a lower valence than Al^{III} is necessary since this creates a charge imbalance and, hence, an acid site. For oxidation materials,[4] some of the aluminium atoms are exchanged for redox active metals such as Ti, Cr or Fe. It is in connection with the latter case that a problem might arise. The very aspect of the AlMePO structure that makes the them so interesting, the covering of the channel walls with an organic layer, could act to inhibit such catalysis by separating the substrate within the channel from the active metal centre within the framework. In such a scenario it would be desirable to replace some of the organic groups with much smaller moieties, e.g. H, in order to expose the metal ions.

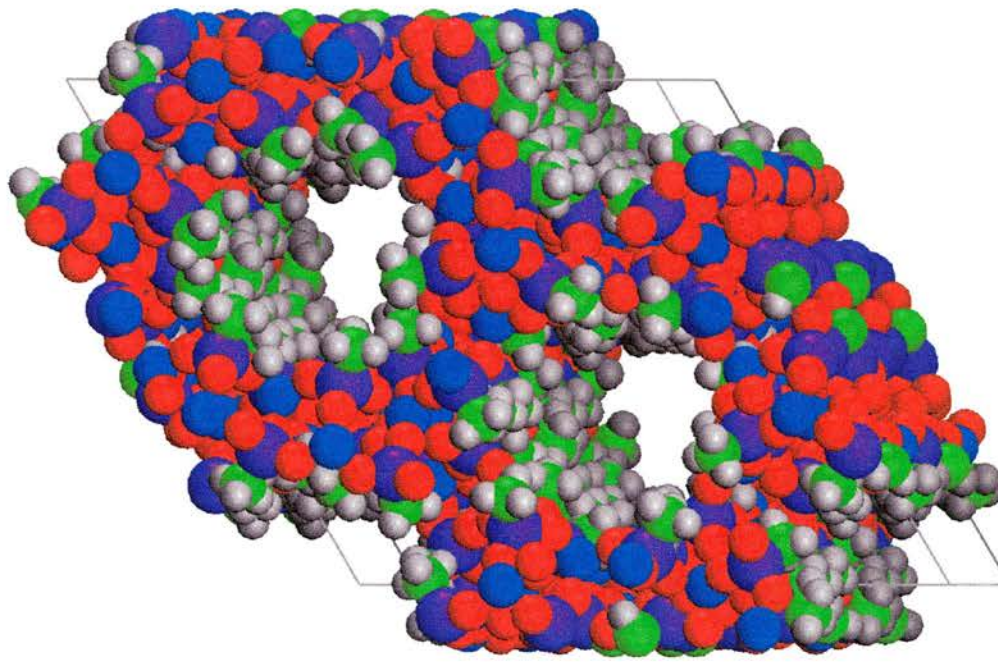

Figure 1 AlMePO-β viewed along an axis just askew from [001], showing internal surface of the channels. White spheres – H, green – C, small blue – Al, large purple – P, red – O.

Two approaches can be used to effect isomorphous phosphonate substitution within aluminium phosphonate materials, either one can attempt to synthesise the desired material directly (synthesis substitution), or one can attempt to modify a preformed material (post-synthesis substitution). Substitution during synthesis usually uses a procedure modified from the normal method such that the reaction mixture (a gel for hydrothermal preparations or a mixture of pure reactants for melts) contains a mixture of the phosphonates that are required in the final product. Modification methods are varied but, in general, the metal phosphonate is contacted by a liquid form, either a solution or a melt,[5] of the exchange phosphonate, usually in the acid form. Heat can be employed to hasten the substitution process depending upon the stability of the material. As many metal phosphonates are hydrolysed in the presence of acid and, occasionally, neutral water, a compromise must be reached in choosing the temperature since heat will hasten this process.[6] Unfortunately, it is necessary to use a solvent in which the material is slightly unstable or the substitution is unlikely to take place.

Other factors also influence the choice of solvent. The layers in lamellar metal phosphonates, for example, are usually made up of an inorganic central portion covered by organic groups. it is possible to induce the layers to separate, a process known as exfoliation, if a solvent is used with which the organic covering can interact favourably.[7] Exfoliation increases the rate of phosphonate substitution since the transport to the reaction site is far faster without the steric hindrance of an adjacent layer.[8] Another common characteristic of such phosphonate replacement reactions is that they are reversible, causing there to be an equilibrium point at which no further net substitution takes place.[7] In order to obtain complete substitution one must negate the effects of Le Chateliers' Principle by removing the phosphonate, displaced from the framework, from the solution.

The work in this Chapter concentrates on attempts to substitute isomorphously methylphosphonate groups in AlMePO-β (or AlMePO-α) with one of three other phosphorus moieties. The replacement groups are phosphite – HPO_3 – (although the correct name is phosphonate, phosphite is used here to avoid confusion with the other phosphonates used), phosphate – $HOPO_3$, and phosphonoacetate – $HO_2CCH_2PO_3$. These have been chosen for the following reasons :

Phosphite : as mentioned above, it could be necessary to uncover some of the AlMePO framework to allow better access to catalytically active metal centres. Replacing methylphosphonate with phosphite removes a relatively bulky methyl group with the smallest replacement possible, hydrogen.

Phosphate : The replacement for the methyl group in this case is a hydroxyl group. Whilst being approximately the same size as a methyl group, OH is much more hydrophilic, changing the character of the channels considerably.

Phosphonoacetate: The intention here is to create a material in which acid groups are attached 'permanently' to the inorganic framework. The acid group could have many uses, for example, as a binding site for a metal, as a powerful hydrophilic modifier for sorption, or as a catalytic acid site in dehydroxylation reactions, e.g. methanol to hydrocarbons.

In each case, a series of hydrothermal preparations was performed, based upon the method of Maeda *et al,*[2] in which all the parameters were kept constant except the ratio of the two phosphorus compounds in the gel. In the case of phosphonoacetate, another series was performed in which the composition of the gel was unchanged (15% $AcP(O)(OH)_2$) but the duration of heating was varied. (The motivation for performing this last series is explained in the text at the appropriate point.)

The products are referred to using the form Al[*n*R]MePO, where *n* is the percentage of the phosphorus compound $RP(O)(OH)_2$ in the gel from which the material was formed, and where R can be OH, H or Ac (meaning CH_2COOH) for phosphoric acid, phosphorous acid and phosphonoacetic acid respectively. For each series of gels, the products are characterised, chiefly by XRD and FTIR, with the aim of establishing as much as possible about the success of substitution. A new material formed during the phosphite series is characterised also by ^{27}Al MQ and ^{31}P MASNMR.

Experimental

Synthesis and sample preparation

Reagents were obtained from Aldrich and used without further purification unless stated otherwise. A method adapted from that of Maeda *et al*[2] was used to synthesise series of AlMePOs from gels containing methylphosphonic acid mixed with another phosphorus source in a range of proportions such that the total amount of phosphorus remained the same. The components of the gel were $Al(OH)_3$: $CH_3P(O)(OH)_2$: $RP(O)(OH)_2$: H_2O : 1,4-dioxane where R was H, CH_2COOH or OH, and the ratio of the materials was 1 : 1.5-x : x : 40 : 0.5 respectively ($0 \leq x \leq 1.5$). Gels were stirred until homogeneous and reacted in PTFE-lined stainless steel autoclaves of 24 ml volume at 160 °C for 48 hours. (A series of gels containing phosphite was heated for 120 hours also, although the results were rarely significantly different from the 48 hour treatment. Explicit mention will be made if such a difference occurred.) Immediately before heating the gels had a pH of 2-3.5 depending upon the identity of the substituting acid and its ratio to methylphosphonic acid. Products were filtered, washed with 40-60 cm^3 distilled water and dried in air at 60°C. The materials were characterised by powder X-ray crystallography (XRD), single quantum (SQ) magic angle spinning NMR (MASNMR), ^{31}P and ^{13}C MASNMR and FTIR. Also, one material was investigated using ^{27}Al multiple quantum (MQ) MASNMR (see Chapter 2 for further details).

Instrumentation

The majority of the MASNMR and MQMASNMR experiments were run on a Bruker MSL500, at 11.75 T with rf field of approximately 0.01 T (for the maximum power pulses). Some ^{31}P MASNMR spectra were collected on a Bruker 400 spectrometer, at 9.4 T.

Powder x-ray diffraction was performed on a STOE diffractometer with a linear position sensitive detector covering 6° in 2θ and employing Ge monochromated Cu-$K\alpha_1$ radiation (λ=1.54056 Å). Samples were prepared by mounting in a glass capillary or between two sheets of milar as rotating discs in the X-ray beam.

FTIR was performed on a Perkin Elmer 1710 FT-IR Spectrometer. Samples were run as KBr discs prepared from 0.056g of finely ground mixtures of KBr and the sample in the

mass ratio 20:1. The KBr was dried in air at 120 °C for several hours before use and the spectra were run as soon as possible after disc formation to avoid absorbance of moisture.

Heat treatments were performed in a silica glass tube in a tube furnace. Samples were heated at a rate of 10°C min^{-1} in all cases. The temperature in the furnace was measured at the sample using a K-type thermocouple and found to between 3 - 4°C higher than the setpoint temperatures over the range used. Thermal gravimetric analysis (TGA) was performed on a TA Instruments SDT 2960 Simultaneous DTA-TGA. Heating rates were 10 °C min^{-1} and inert atmospheres were used in all cases.

Results and Discussion

Phosphite substitution

Al[*n*H]MePO samples were prepared in two series, one heated for 48 hours, the other for 120 hours. The Al[*n*Ac]MePO and Al[*n*OH]MePO series' were heated for 48 hours only. The XRD results of the 48 and 120 hours heating series for Al[*n*H]MePO are reported separately at first and then discussed together and in the light of other characterisation techniques.

48 hours heating duration

The XRD patterns for Al[*n*H]MePO are shown in Figure 2 and summarised in Table 1. At low H_3PO_3 gel loadings, the main phase is AlMePO-β although, even at 5%, there is always an impurity phase also. (Indeed, it is interesting to note that even the pure methylphosphonate preparation has a small shoulder at slightly lower 2θ than the most intense peak. This shoulder may owe more to the asymmetry of low 2θ peaks on the STOE diffractometer than to the presence of a small amount of impurity however.) At 5% H_3PO_3 loadings a small amount of an unknown compound (Unknown1) is produced which increases in the 10% sample until almost equal to the amount of AlMePO-β. At 10% the first occurrence of a material that comes to dominate the product at higher loadings is observed, giving the peak at 6.38° (Unknown2). At 15% there is almost no Unknown1 but there is a slight increase in the amount of Unknown2. At 20% no Unknown1 is produced and again there is a slight increase in Unknown2 although the amount of AlMePO-β does seem to have decreased markedly.

At 33% and greater H_3PO_3 loadings, AlMePO-β is no longer produced and the main phase is Unknown2. The Al[33H]MePO sample also contains a small amount of AlMePO-1 (Figure 4). However, from comparative inspection of the patterns, both the Al[50H]MePO and Al[66H]MePO samples appear to be phase pure, though this cannot be determined absolutely as none of the patterns of any of the new phases from this series of experiments has been indexed. It is interesting to note that increasing H_3PO_3 content in the gel is accompanied by a decrease in *d* spacing of the Unknown2 peaks (Table 2). This is consistent with there being an increase in the substitution of the relatively large methyl groups by hydrogens. The change of peak position is seen more clearly in an enlargement of the pattern (Figure 3). Where an assignments of the low 2θ peaks was ambiguous it was resolved by reference to the whole pattern.

The Al[75H]MePO sample shows some of the pure phosphite phase, $Al_2(O_3PH)_3.4H_2O$, which appears phase pure in the Al[90-100H]MePO samples. The structure of the phosphite material has been characterised previously, at first as a gallium analogue of this material[9] and, more recently, in this, the aluminium form.[10] The XRD pattern for Al[100H]MePO has been fitted with a wR_p of 15% to the single crystal data[10] for this phase without changing the atom positions.

Table 1 Identifying peak 2θ values and corresponding phase identifications for samples heated for 48 hours. Identifying peaks are normally the lowest 2θ, high intensity peaks unless this coincides with another peak from another phase. Amounts are approximated purely from peak intensities and should not be relied upon to any great degree.

Composition (Amt of H_3PO_3 in the gel)	**Peak (2θ / °)**	**Est normalised amount in sample / %**	**Phase name**
0% (AlMePO-β)		100	AlMePO-β
5%	7.14	85	AlMePO-β
	7.22	15	Unknown1
10%	7.00	45	AlMePO-β
	7.1	45	Unknown1
	6.88	10	Unknown2
15%	6.38	70	AlMePO-α
	7.28	15	Unknown1
	7.02	15	Unknown2
20%	6.42	80	AlMePO-α
	7.28	20	Unknown2
33%	6.44	100	Unknown2
50%	6.4	100	Unknown2
66%	6.5	100	Unknown2
75%	6.6	95	Unknown2
	6.66	5	$Al_2(O_3PH)_3.4H_2O$
90%	11.78	100	$Al_2(O_3PH)_3.4H_2O$
100%	11.76	100	$Al_2(O_3PH)_3.4H_2O$

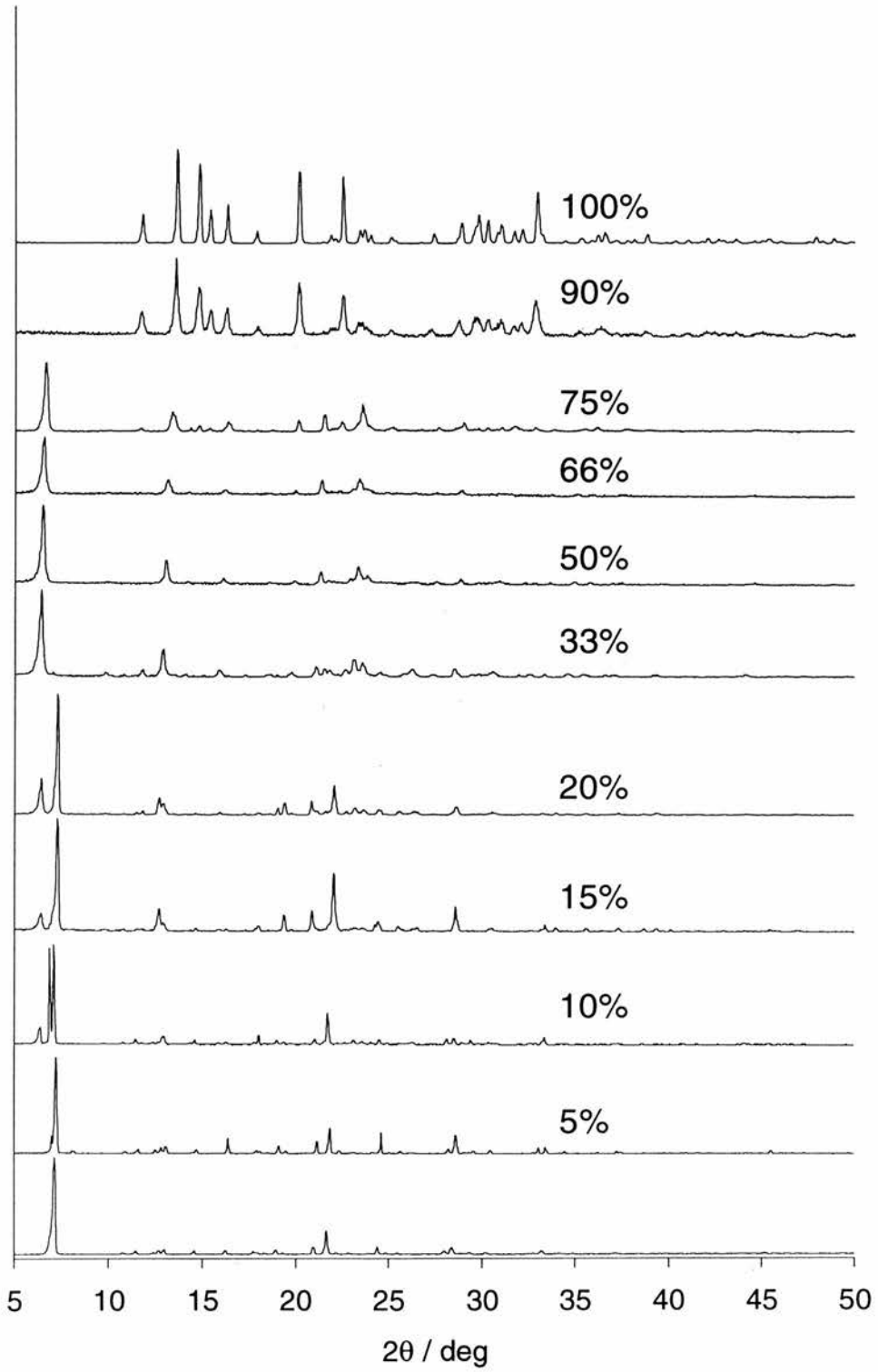

Figure 2 Showing the XRD patterns for the products from the range of gel compositions for 18 hours heating at 160 °C. Samples are labelled according to the proportion of H_3PO_3 in the gel.

Table 2 **Change of *d* spacing with increased H_3PO_3 gel loadings, 48 hour heating**

H_3PO_3 loading / %	Low 2θ peak / ° (Å)	Decrease in *d* spacing / Å
33	6.4 (13.80)	
		0.21
50	6.5 (13.59)	
		0.21
66	6.6 (13.38)	
		0.12
75	6.66 (13.26)	

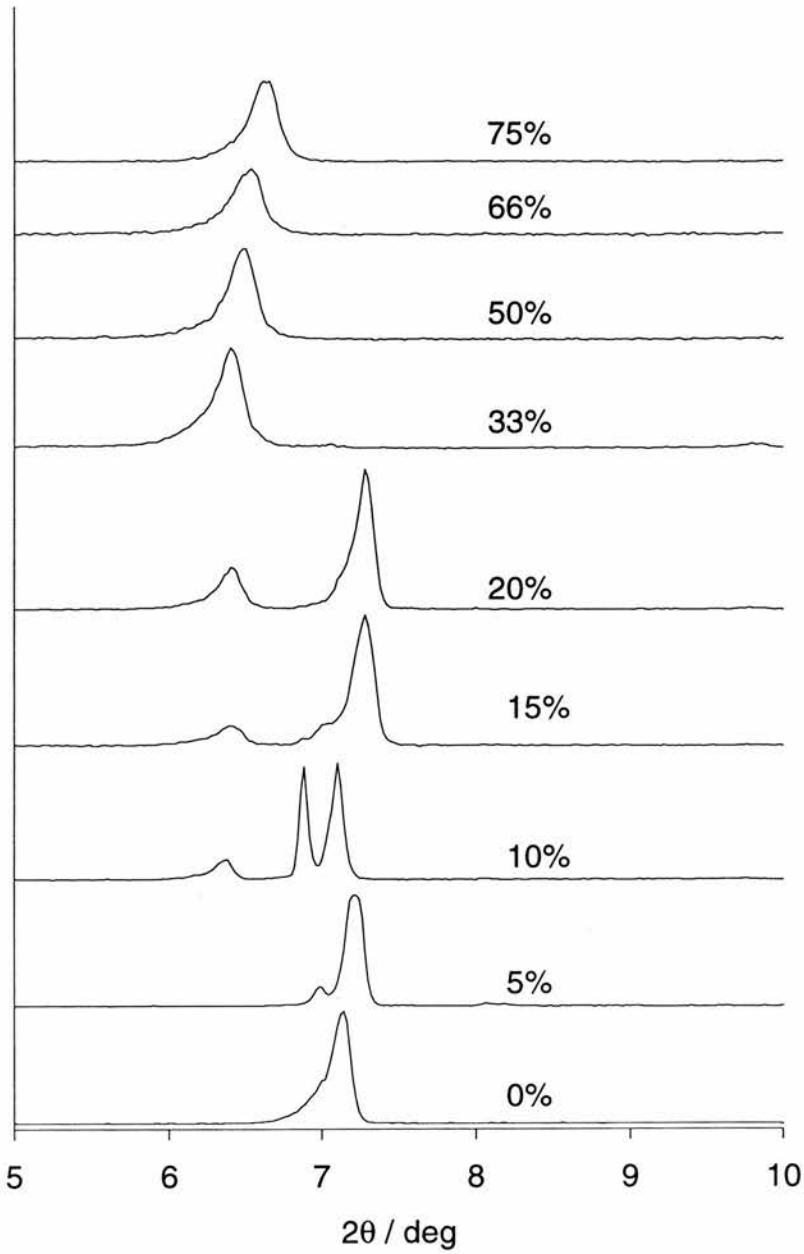

Figure 3 Enlargement of the low 2θ range of the XRD patterns of products from 48 hrs heating at 160 °C.

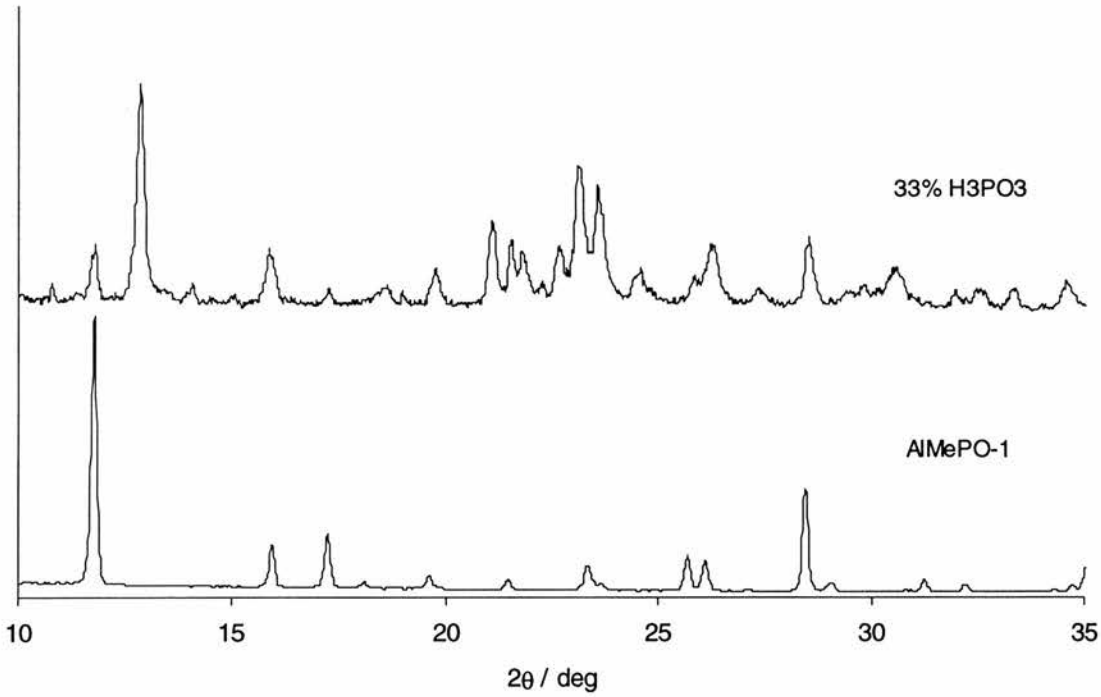

Figure 4 Showing the enlarged portions of the XRD patterns of AlMePO-1 and the 48 hour, 33% H_3PO_3 sample

120 hour heating duration

The results of heating (Figure 5) for 120 hours rather than for 48 show almost no change at most gel compositions (see Table 3 for a summary). However, some differences are noticed. The 48 hour, Al[33H]MePO experiment shows the presence of some AlMePO-1 in minor quantities, in contrast to the 120 hour heated sample which appears to be solely the new phase, Unknown2. Also, the Al[15H]MePO and Al[20H]MePO samples are very different between the two durations of heating. The longer heating time favours the formation of the Unknown2, this being the dominant phase. The 48 hours heating not only produces very little of the Unknown2 material, it also gives some Unknown1 and AlMePO-α rather than AlMePO-β.

The enlargement shown in Figure 6 allows the effect of composition of the major product and its lattice parameters to be seen more clearly.

Table 3 Identifying peak 2θ values and corresponding phase identifications for samples heated for 120 hours. Identifying peaks are normally the lowest 2θ, high intensity peaks unless this coincides with another peak from another phase. Amounts are approximated purely from peak intensities and are intended as an indication of relative size, not as a quantitative measure of each component.

Amount of H_3PO_3 / %	Peak (2θ / °)	Amount of component / %	Phase
0%	7.14	100	AlMePO-β
5%	7.10	85	AlMePO-β
	6.84	15	Unknown1
10%	7.12	45	AlMePO-β
	6.86	10	Unknown1
	6.38	45	Unknown2
15%	7.16	10	AlMePO-β
	6.40	80	Unknown2
20%	7.14	15	AlMePO-β
	6.4	85	Unknown2
33%	6.44	100	Unknown2
50%	6.48	100	Unknown2
66%	6.64	100	Unknown2
75%	6.64	100	Unknown2
90%	11.76	100	$Al_2(O_3PH)_3.4H_2O$,
100%	11.76	100	$Al_2(O_3PH)_3.4H_2O$

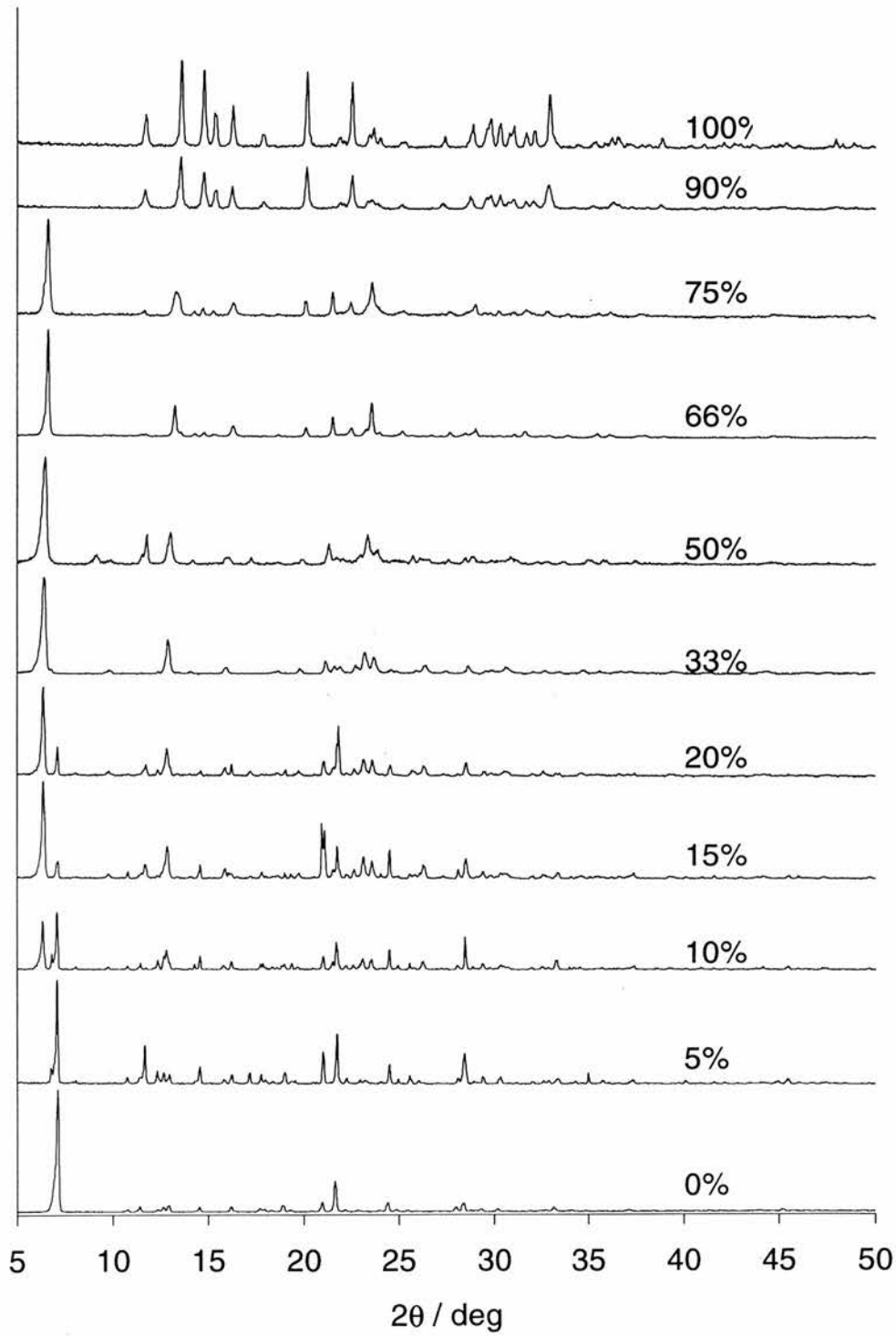

Figure 5 Showing the XRD patterns for the products from the range of gel compositions for 120 hours heating at 160 °C. Samples are labelled according to the proportion of $HP(O)(OH)_2$ in the gel

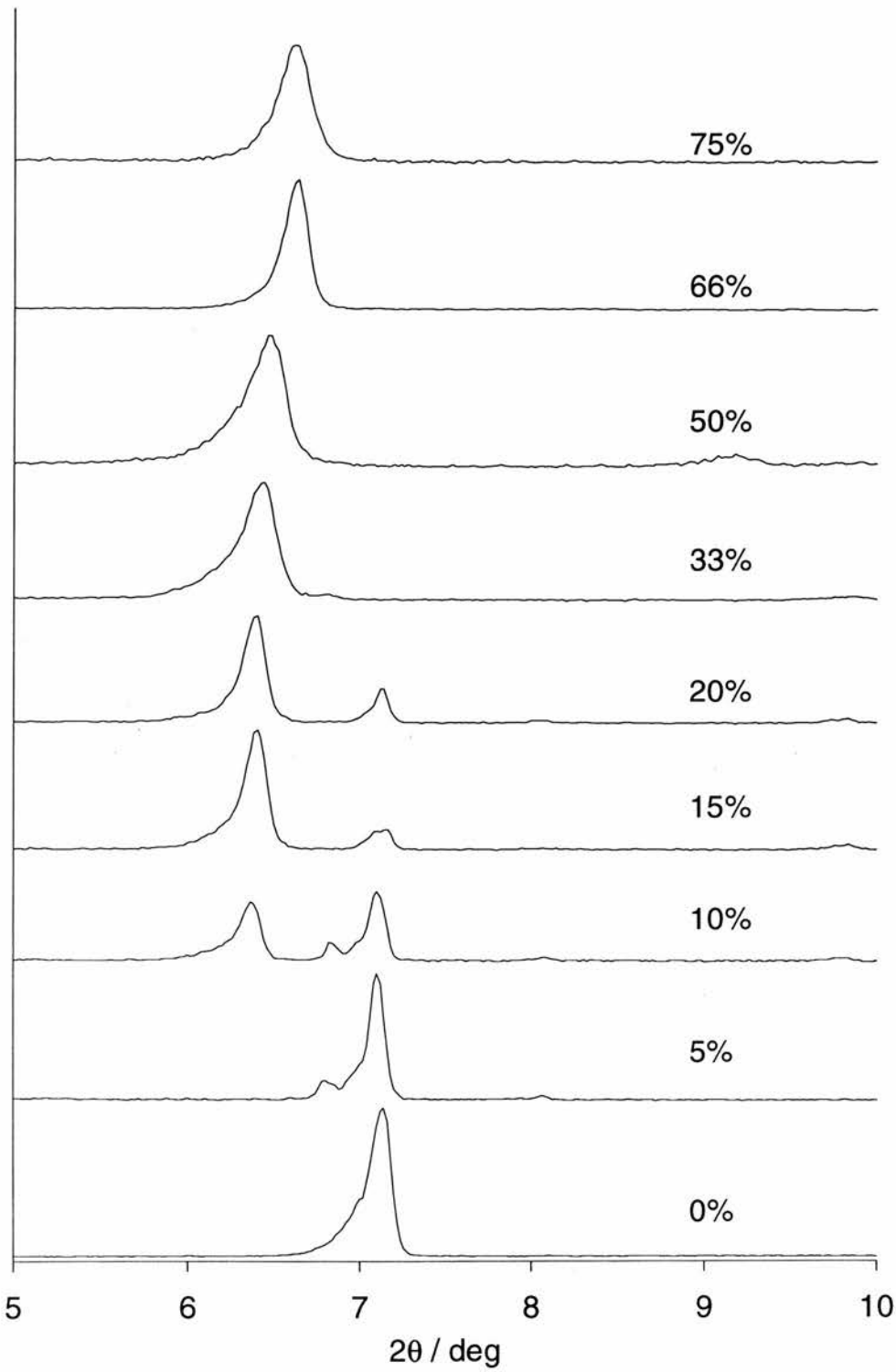

Figure 6 Enlargement of the low 2θ range of the XRD patterns of products from 120 hrs heating at 160 °C (NB. the Al[90-100H]MePO samples do not have peaks in this range and are not shown.)

Table 4 **Change of *d* spacing with increased H_3PO_3 gel loadings, 120 hour heating**

H_3PO_3 loading / %	Low 2θ peak / ° (Å)	Decrease in *d* spacing / Å
33	6.44 (13.71)	
		0.08
50	6.48 (13.63)	
		0.33
66	6.64 (13.30)	
		0.0
75	6.64 (13.30)	

As with the 48 hour series, the Al[33-75H]MePO samples exhibit a reduction in *d* spacing of the lowest 2θ peak (Table 4), albeit smaller than before. Since the patterns have not been corrected for zero point errors, the degree of uncertainty in the magnitude of the change is quite high. However, the fact that both series exhibited an overall decrease in *d* spacing of 0.41 Å (120 hour) and 0.54 Å (48 hour) confirms the effect.

Summary of 48 and 120 hour heated series

In attempting to establish the principle of hydrothermal, isomorphous substitution of methylphosphonates by phosphite, there are two aspects that need to be addressed; whether isomorphous substitution of the methyl groups by hydrogen has taken place in AlMePO-β, and whether the new material in the Al[33-75H]MePO samples is a mixed phosphonate phase.

The materials produced from the low loading of H_3PO_3 gave a significant proportion of AlMePO-β. However, there was an impurity phase present in every substituted preparation. The amount of impurity is difficult to measure but an estimate from the XRD pattern is possible (as shown in Table 1and Table 3). If the amount of impurity observed is comparable to the amount of phosphorous acid in the synthesis, it is not possible to determine if substitution has occurred, despite the observation of phosphite within those samples. The only possible course of action would be to separate the two phases but it is difficult to do so when one is present in a very small amount. This is the case in both the 48 hours and 120 hours heating experiments. All of the samples that gave AlMePO-β contained an impurity in a similar amount to the phosphorous acid in the reaction gel.

Therefore, although it has not been possible to examine separately the AlMePO-β and the impurity in these cases, the coincidence of the increase of impurity with the increase in H_3PO_3 content of the gel indicates that there has been no phosphonate substitution of the AlMePO-β framework.

A further interesting result of this work is the appearance of a new phase formed in the Al[33-75H]MePO preparations. The XRDs for these samples show very little change as the proportion of H_3PO_3 is increased, leading us to believe that the predominant material is phase pure. Optical and scanning electron microscopy (SEM) support this belief showing the samples to be dominated by the presence of polycrystalline spheres (40-80 μm in diameter) with the only impurity phase observed being a small number of needle-like crystals bearing a resemblance to AlMePO-β's preferred morphology (Figure 7). The material is particularly interesting as its lowest 2θ peak corresponds to a *d* spacing 1.6 Å greater than that for AlMePO-β (13.7 Å compared with 12.1 Å for AlMePO-β). Given that the difference in the preparation has been to substitute a smaller phosphonic acid it is very interesting that such an increase should occur, and might indicate that a more open, and hence porous, material has been synthesised.

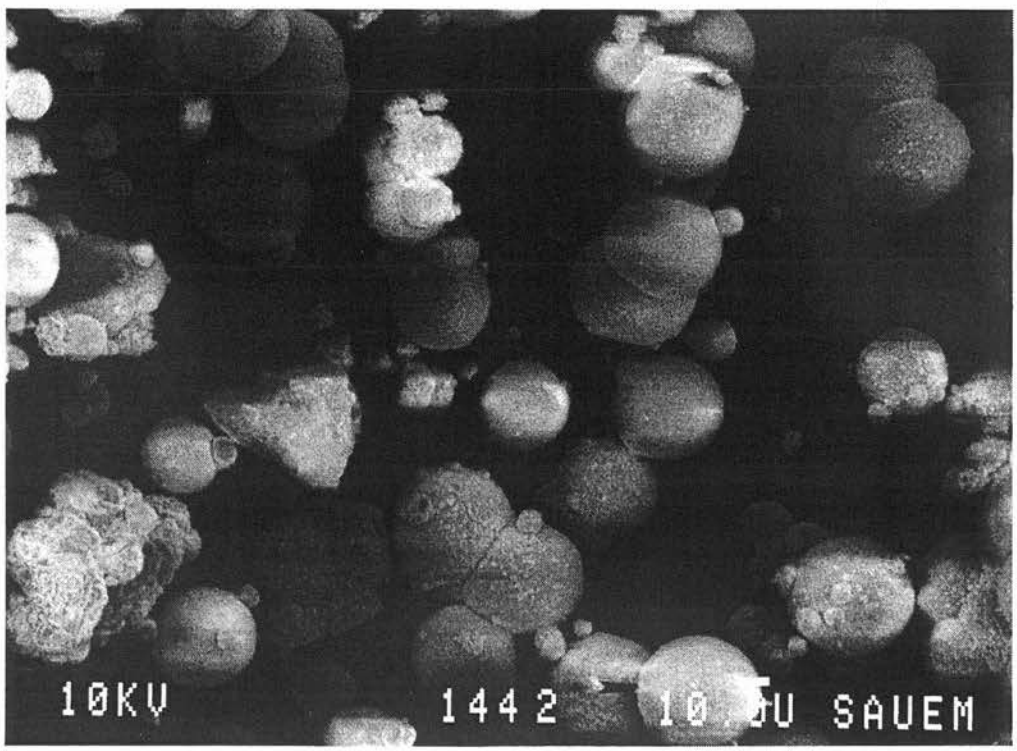

Figure 7 Micrograph from SEM of the Al[33H]MePO sample.

Although we have not been able to characterise the new phase by indexing its XRD pattern other characterisation has taken place. EDX indicates an unusually high aluminium to phosphorus ratio of 2-3:1. The ^{27}Al SQ spectrum of the Al[33H]MePO sample contains two narrow peaks, the octahedral at -16.3 ppm and the tetrahedral at 42.3 ppm, remarkably similar to those in the spectrum of AlMePO-β except that the octahedral is slightly broader. The 5Q spectrum shows the octahedral peak to be made up of two resonances at –14.1 and –16.9 ppm. The SQ spectra of the Al[50-66]MePO samples show more positive values for the octahedral peak as the phosphate ratio increases (see Chapter 2 for more details on all the NMR data mentioned here). It is likely that this is due to a change in the relative size of the two peaks making up the composite lineshape observed in the SQ spectrum (the –16.9 ppm resonance agrees within error limits with the SQ results for AlMePO-β's octahedral site). Also, as has been noted the *d* spacing of the lowest 2θ peak decreases with increasing H_3PO_3 content of the gel, a fact consistent with the material having a variable methyl:H ratio depending upon the synthesis conditions. The tetrahedral region has three sites of very similar chemical shift and quadrupolar interactions to those of AlMePO-β (Table 5). The agreement is so close that it is tempting to assume relationship between the two structures, although the XRD patterns are quite dissimilar. It is also worth noting the phosphorus spectra for the Al[33-66]MePO materials which are also quite different from that for AlMePO-β (Figure 8).

Table 5 Comparison of the 5QMASNMR data for AlMePO-β with Al[33H]MePO

	δ_{iso}			SOQUE / MHz		
AlMePO-β	45.3	43.5	42.7	2.4	1.9	0.8
Al[33H]MePO	44.6	43.4	43.0	2.3	1.9	2.3

Finally, the FTIR spectra confirm the conclusion that the Al[33-66H]MePO materials contain P-H bonds and, thus, are mixed phosphonate materials. Figure 9 shows the P-H stretching region of the spectra for the unsubstituted material (AlMePO-β), the Al[33-66H]MePO samples and Al[100H]MePO. (N.B. Despite the method used to prepare the KBr discs which attempted to standardise all the quantities, the spectra are not totally quantitative with respect to each other and only general trends can be extracted from them.) It is noticeable that the higher percentage substituted compounds have more intense absorptions in the P-H region. Also, some of the Al[33-66H]MePO absorbance bands are different to those from Al[100H]MePO. This indicates that at least some of the P-H groups in the Al[33-66H]MePO samples are not due to a purely phosphitic phase. As the XRDs for

these samples do not show any impurities and the FTIR bands change very little in frequency over the range of H_3PO_3 loadings, the identification of this as a single phase is strengthened. Again, there is evidence that the extent of substitution within the material depends upon the gel ratios of the phosphonic acids.

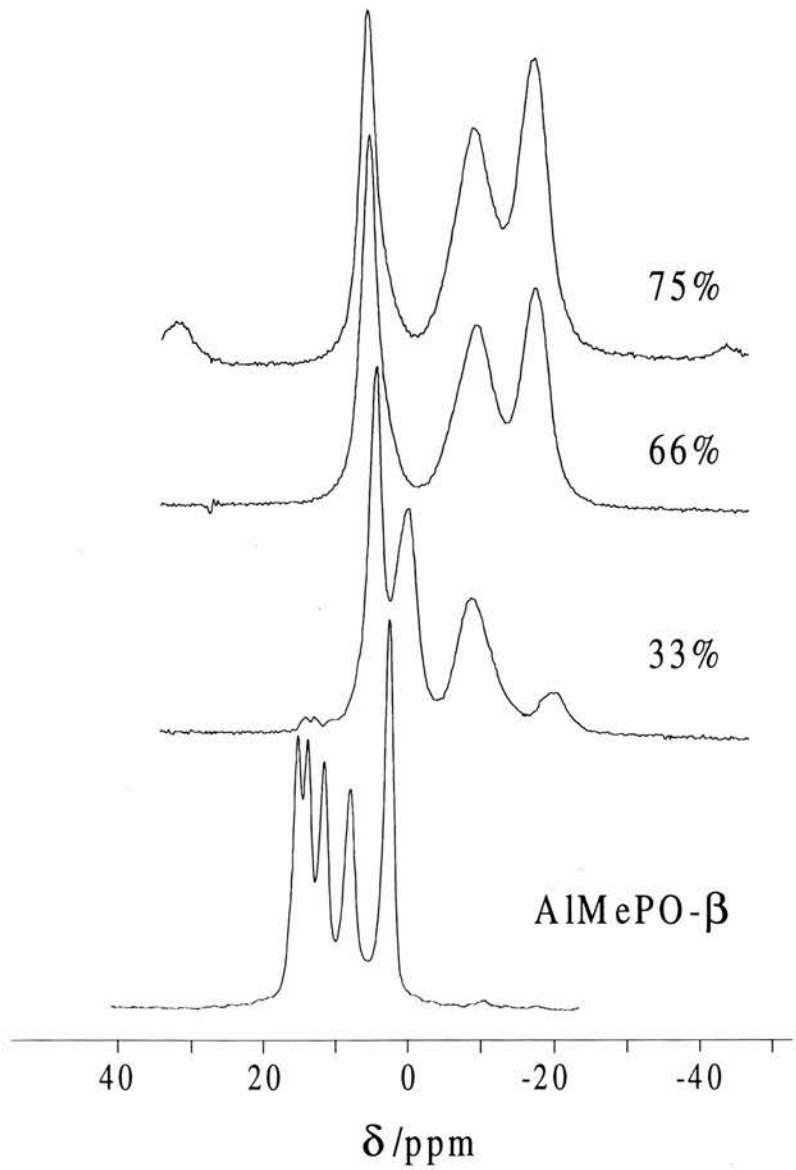

Figure 8 ^{31}P spectra of AlMePO-β and the Al[33-66]MePO samples of the 120 hours heated series.

Therefore, it must be concluded that the variable substitution of methyl groups by phosphitic groups within an aluminium phosphonate has been achieved. Unfortunately, we have no structural data, at this time, as to whether the material is microporous. However,

the TGA shows a 5.5% mass loss centred on 225 °C which we believe to be water since the ^{13}C MASNMR shows there to be no dioxane within the material. In itself, the fact that there is no structure directing agent within the material points to any pores that might be present being small (<4 Å).

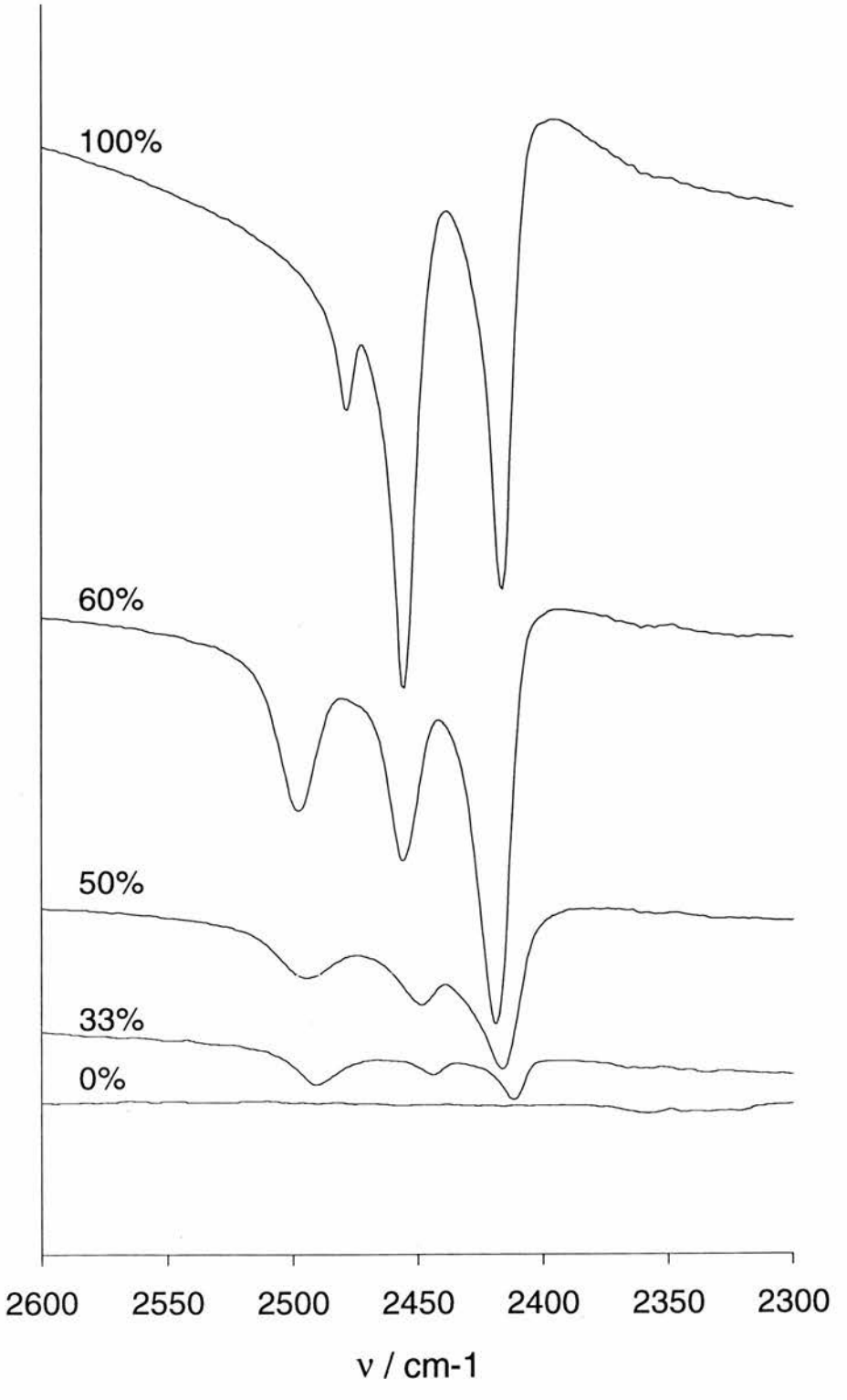

Figure 9 P-H stretching region of the FTIR spectrum of unsubstituted AlMePO-β, Al[33-75H]MePO and Al[100H]MePO samples.

Phosphonoacetate substitution

Broadly speaking, the XRDs (Figure 10 and Figure 11) may be summarised by dividing the phase system into four regions. The first, consisting of the lower dopings of $AcPO_3$ (Al[0-20Ac]MePO), is characterised by the production of phases with the AlMePO-β or AlMePO-α structures. The second region (Al[33-50Ac]MePO) consists of gel compositions that did not produce any crystalline material at the conditions used. Third (Al[66-75Ac]MePO) is a two phase region in which the pure phosphonoacetate phase is mixed with an unknown material with a large *d* spacing in at least one dimension. Lastly, the sole phase to condense in the fourth region (Al[90-100Ac]MePO) is a pure aluminium phosphonoacetate of known structure[11] (Figure 12), which will be known as 100% AcP henceforth. The materials given by each preparation are summarised in Table 6.

Table 6 Identifying peak 2θ values and corresponding phase identifications for phosphonoacetic acid doped gel samples heated for 48 hours. Identifying peaks are normally the lowest 2θ, high intensity peaks unless this coincides with another peak from another phase. Amounts are approximated purely from peak intensities and are intended as an indication of relative size, not as a quantitative measure of each component. 100% AcP refers to the pure phosphonoacetate phase the structure of which has been solved recently.

Amount of AcP / %	Peak (2θ / °)	Amount of component / %	Phase
0%	7.14	100	AlMePO-β
5%	7.22	85	AlMePO-β
	6.78	15	Unknown3
10%	7.26	100	AlMePO-α
15%	7.30	100	AlMePO-α
20%	7.30	100	AlMePO-α
33%	7.22 (very poorly crystalline)	50	AlMePO-β
	7.34 (very poorly crystalline)	50	AlMePO-α
50%	5.28 (very poorly crystalline)	100	Unknown4
66%	5.3 (poorly crystalline)	~50	Unknown4
	11.38	~50	
75%	5.22 (very poorly crystalline)	~30	Unknown4
	11.40	~60	100% AcP
90%	11.38	100	100% AcP
100%	11.40	100	100% AcP

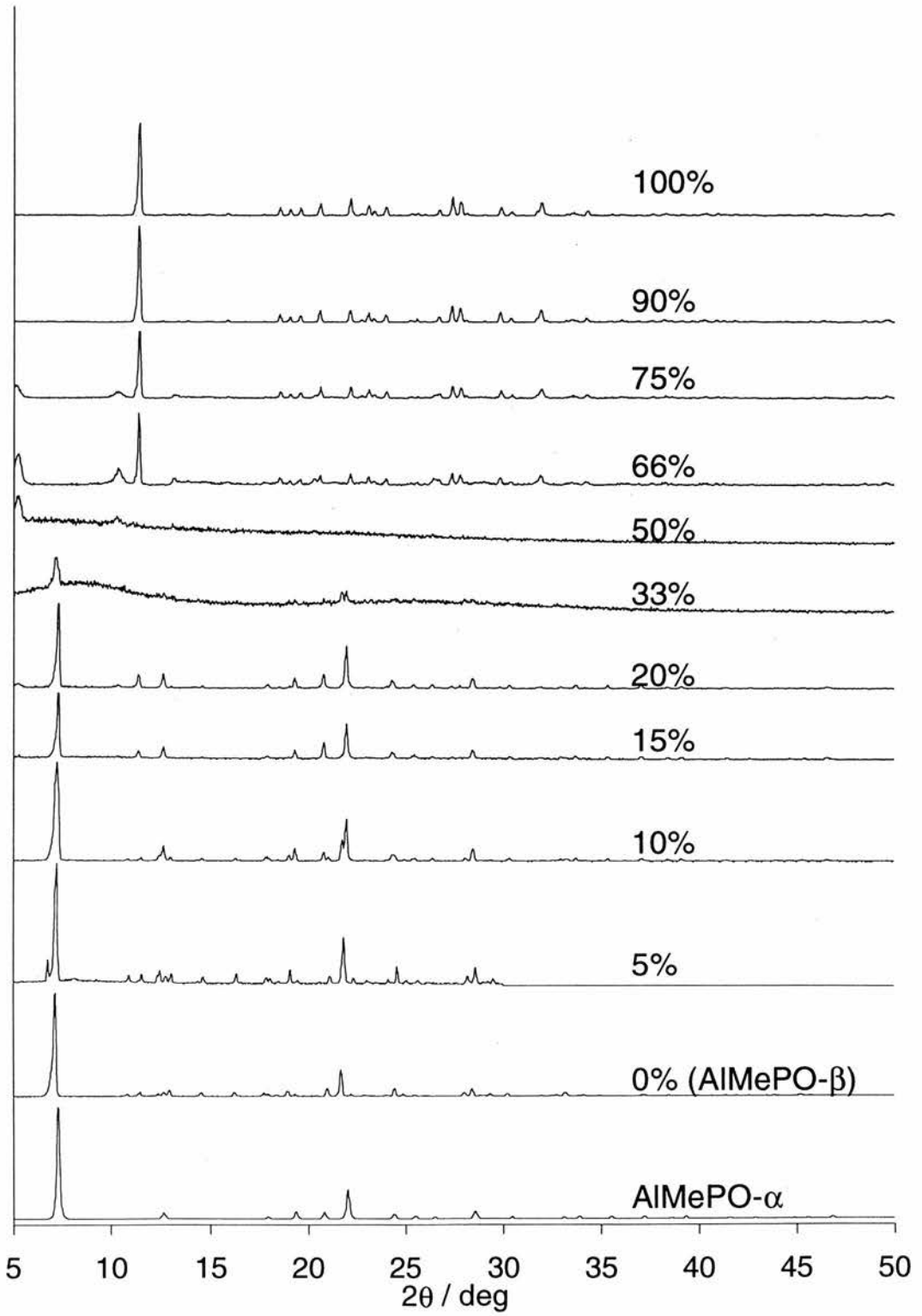

Figure 10 Full plot of the XRD patterns for the range of Al[*n*Ac]MePO.

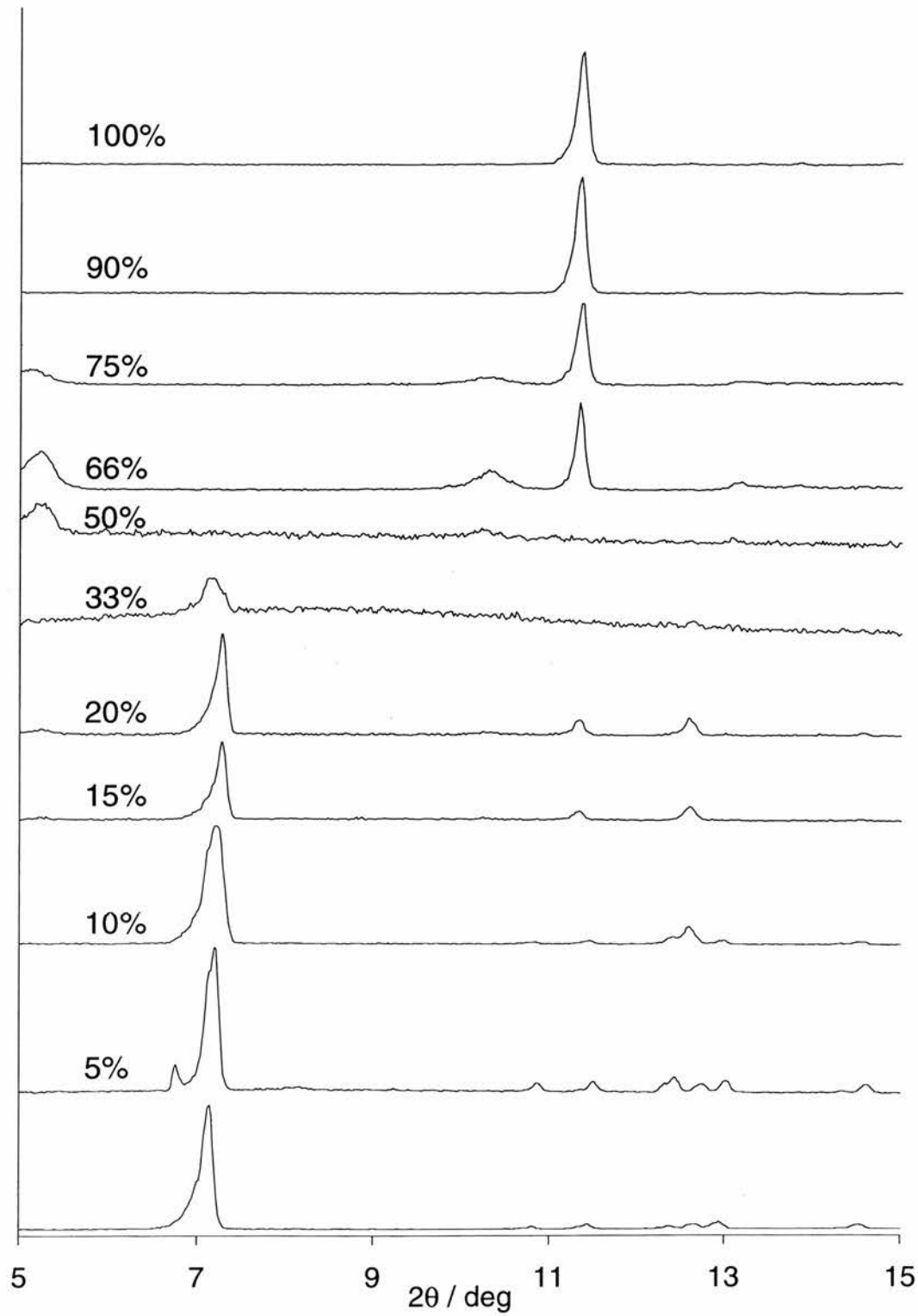

Figure 11 Enlarged region of the XRD patterns for various samples formed from different gel proportions of AcP.

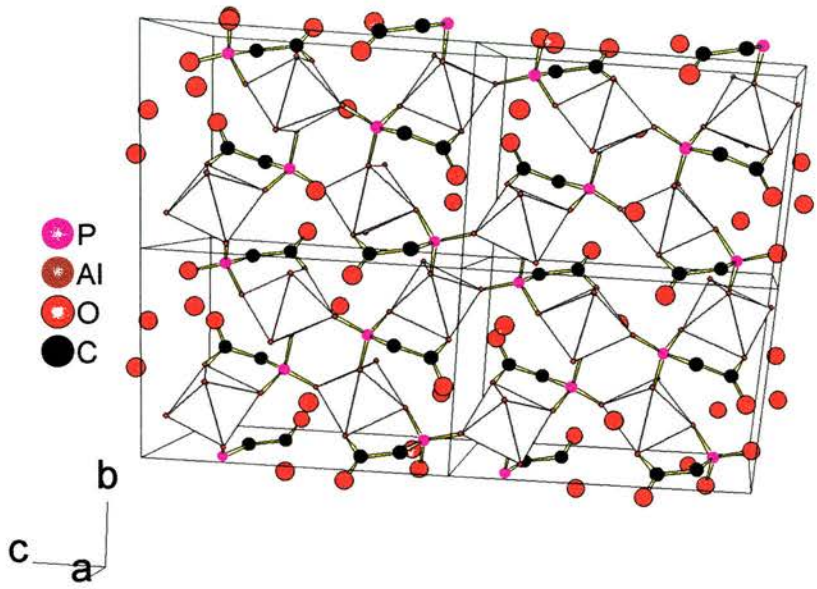

Figure 12 One layer of the structure of the 100% AcP described by Hix *et al.*[11]

Thus, there are four materials under consideration. The first two are AlMePO-β and AlMePO-α, the third an unknown phase that appears to have low crystallinity, and fourth the pure aluminium phosphonoacetate phase of known structure. The question of whether certain of these compounds contain mixed phosphonate groups must be addressed. Figure 14 shows the carbonyl, CH_3 deformation (1320-1280 cm^{-1}) and C-O regions[12a,13] of the FTIR spectra. Although the characteristic band of a carboxylic acid is the strong C=O stretch absorbance in the 1650-1850 cm^{-1} range, it is possible that the carboxyl group in this compound is bending back to coordinate to the aluminium as it does in the 100% AcP material (Figure 12). In this material, there are two Al and two P crystallographic positions. In each case, the acetate group links the phosphorus and the aluminium through one of the oxygens. This has the effect of lengthening the C-O bonds to a value between that for conventional C=O and C-O (Table 7). Thus it is not possible to assume that the IR band will appear in the carbonyl region associated with crystalline carboxylic acids. On the contrary, the absorption is likely to appear between the carbonyl region (1650-1850 cm^{-1}) and the C-O region (900-1300 cm^{-1}). However, the region below 1300 cm^{-1}, with many overlapping peaks, is too complex to allow it to be used to determine the presence or

absence of various phosphonate functional groups. Thus, the discussion will be confined to the 1300-1800 cm^{-1} region of the spectra.

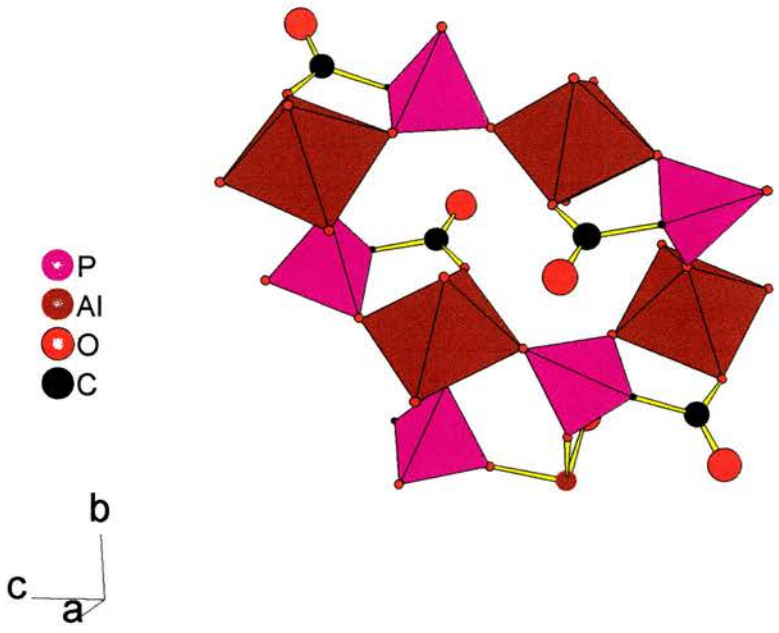

Figure 13 Portion of one layer of the 100% AcP structure, viewed obliquely onto that layer. Note the two types of CO_2 carbon, one [C(1)] linking around the outside of the 'cavity' like structure, the other [C(2)] inside (there are two of each type shown).

Table 7 A summary of the bond lengths of the acetate group within the 100% aluminium phosphonoacetate structure[11] together with the standard values for sp^2 hybridised carbon to oxygen bonds in crystalline carboxylic acids,[14] and various Al-OP bond lengths from aluminium methylphosphonates.[2,11,15] (The value given for the length corresponds to the explicitly shown bond).

Source	Bond	length / Å
Ref 11	C(1)-OAl	1.278
-	C(1)-O	1.248
-	C(1)O-Al	1.890
-	C(2)-OAl	1.284
-	C(2)-O	1.247
-	C(2)O-Al	1.945
Ref 14	C(OH)=O	1.214
-	C(O)-OH	1.34
100% AcP (ref 11)	Al-OP	1.834
AlMePO-1 (ref 15)	Al-OP	1.866
-	Al-OH2	2.068
AlMePO-β (ref 2)	Al-OP	1.893

Although it is beyond the scope of this study to assign definitively the resonances within the particular region of interest, careful examination and comparison of the bands from the different materials does allow correlation with the structures. Table 8 shows a summary of the values of various bands within the relevant regions of the IR spectra. Care should be taken in interpreting the tabulated data as they do not convey the change in intensity of the bands. It is clear from Table 8 that bands 2 and 6 are due to a framework vibration and should not be considered further. Band 1 is closely correlated to the presence of methyl groups since it correlates both to the gel composition and to the methyl deformation resonance, bands 8 and 9. There are also a group of bands, 3 and 7 that correlate to the presence of acetate groups. Band 5 appears solely in the samples, Al[66-75Ac]MePO, which are a mixture of the partially crystalline material and the 100% AcP compound.

On consideration of the bands with respect to the compositions producing AlMePO-β and AlMePO-α (Al[0-20Ac]MePO) it can be seen that all the bands except 3 are common to all of the samples. Band 3 falls within the expected asymmetric stretch region for O-C-O in metal carboxylates.[12b] Also, it is obvious from Figure 16 that the intensity of band 3 increases in the Al[5-20Ac]MePO samples with increasing phosphonoacetate. This result indicates that the samples do contain acetate groups. Since the bands indicating the presence of methyl groups are observed for these compounds in addition, one concludes that the samples contain a mixture of the two phosphonate groups within the structures of AlMePO-β and AlMePO-α.

Table 8 Showing selected FTIR absorption bands for different regions of the spectrum (b – broad: sh – shoulder: w – weak: v.w – very weak).

	Resonances / cm^{-1}								
%	**Carbonyl Region**				**Mid C-O Region**			**Methyl Deformation**	
Band	**1**	**2**	**3**	**4**	**5**	**6**	**7**	**8**	**9**
100		1631	1596			1422	1381	-	
90		1630	1594			1422	1383	-	
75	1736	1624/1609	1572		1439	1423	1387	1313(b)	
66	1735	1613	1572		1441(s)	1424? (sh?)	1389	1314(b)	
20	1720	1615	1573		1436(v.b)	1424	1390	1314(b)	
15	1717(sh)	1637	1618	1580(sh)		1424(b)	1391(w)	1315(b)	
10	1740	1637	1618			1424(b)		1314(b)	
5	1740	1637	1617			1422(b)		1320	1305
0	1650	1631			1454(v.w)	1421		1318	1307

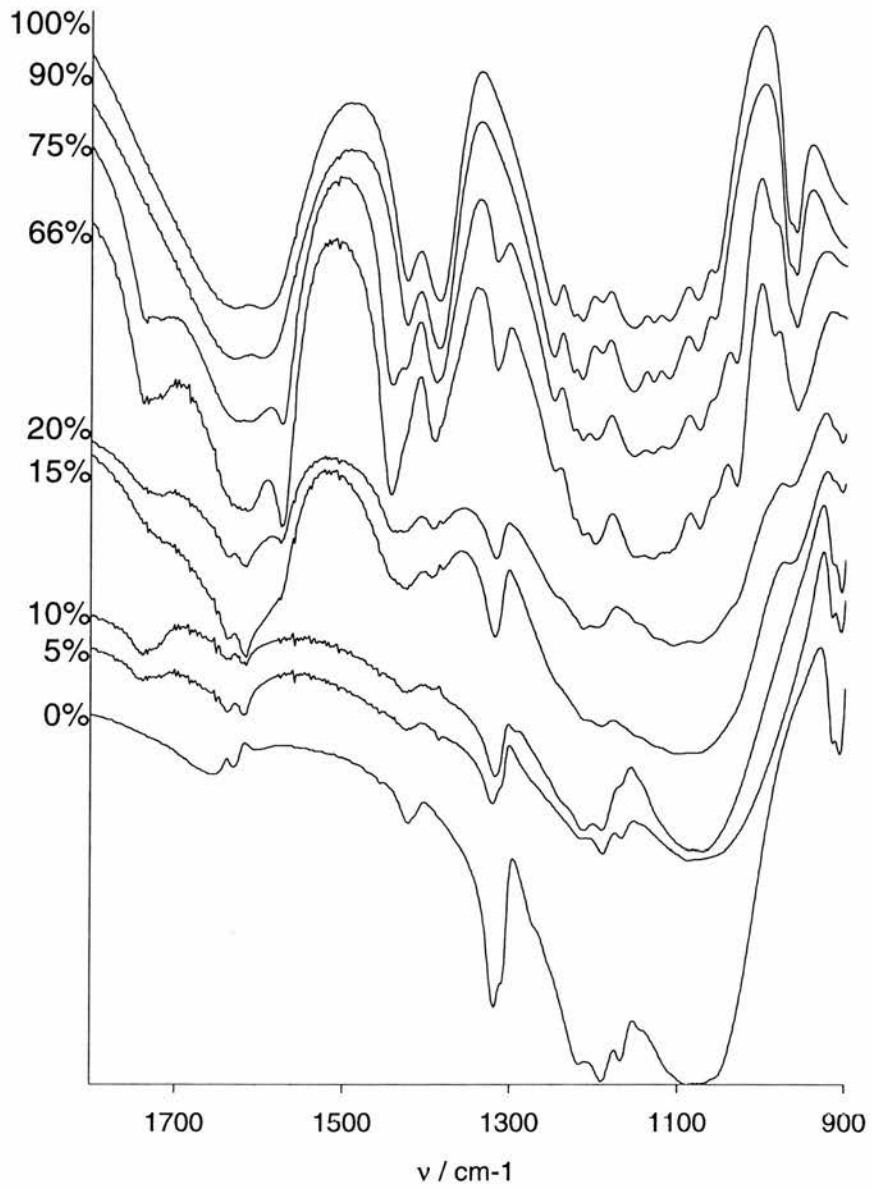

Figure 14 Carbonyl, C-O and methyl deformation regions of the FTIR spectra of the crystalline samples of various phosphonoacetic acid gel compositions.

As mentioned above, the Al[66-75Ac]MePO samples conform exactly to 100% AcP except for band 5 which is unique to these preparations and must be produced by the unknown material with large *d* spacing. Since these samples also show the methyl bands it is likely that this new material contains not only some phosphonoacetate but also the small amount of methylphosphonic acid that was present in the synthesis gels. Estimates of the amounts of the material produced, from the XRD peak sizes, agree with this conclusion. This does not shed light on the origin of band 5 however.

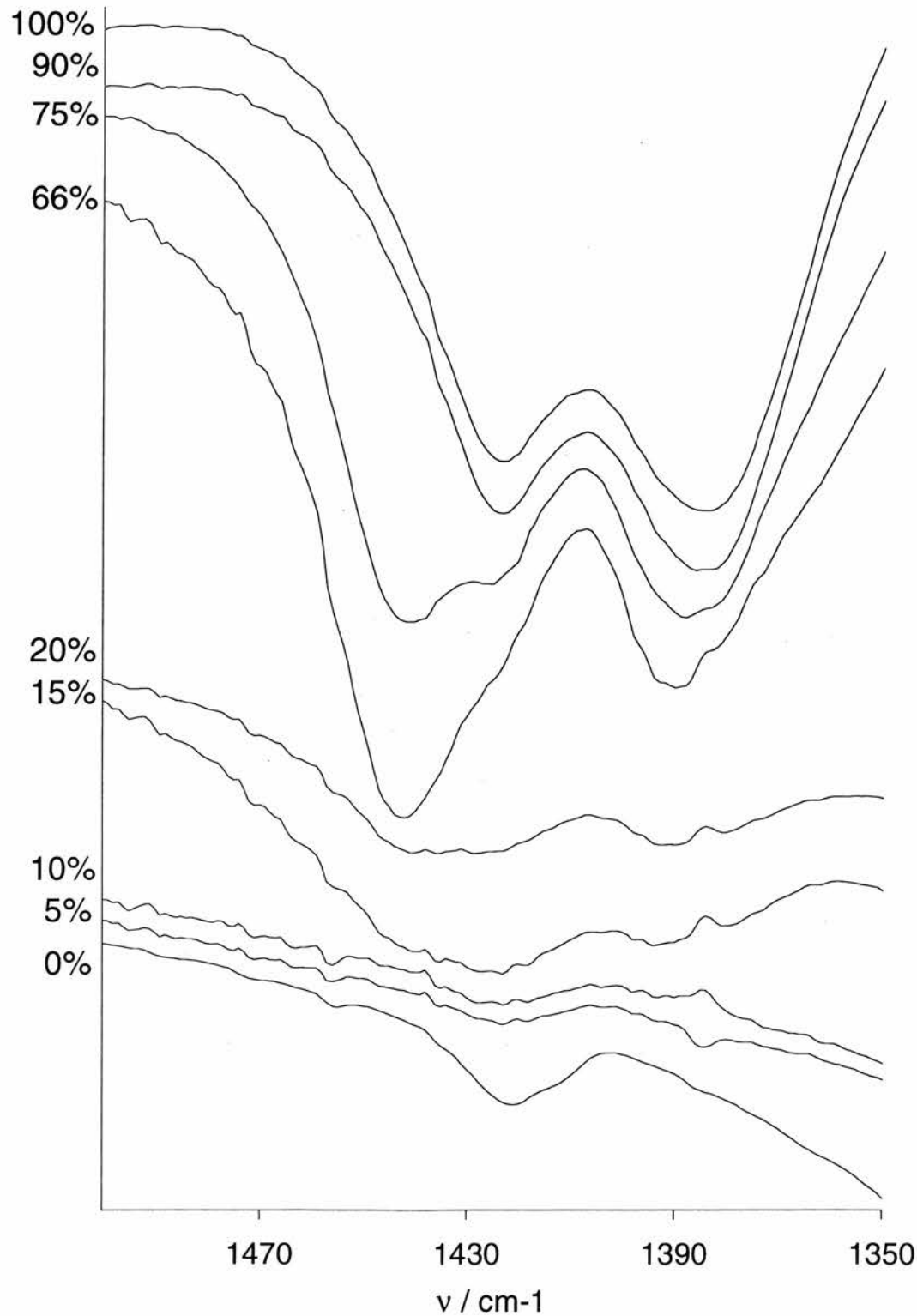

Figure 15 Enlarged region showing several bands characteristic to the different phases

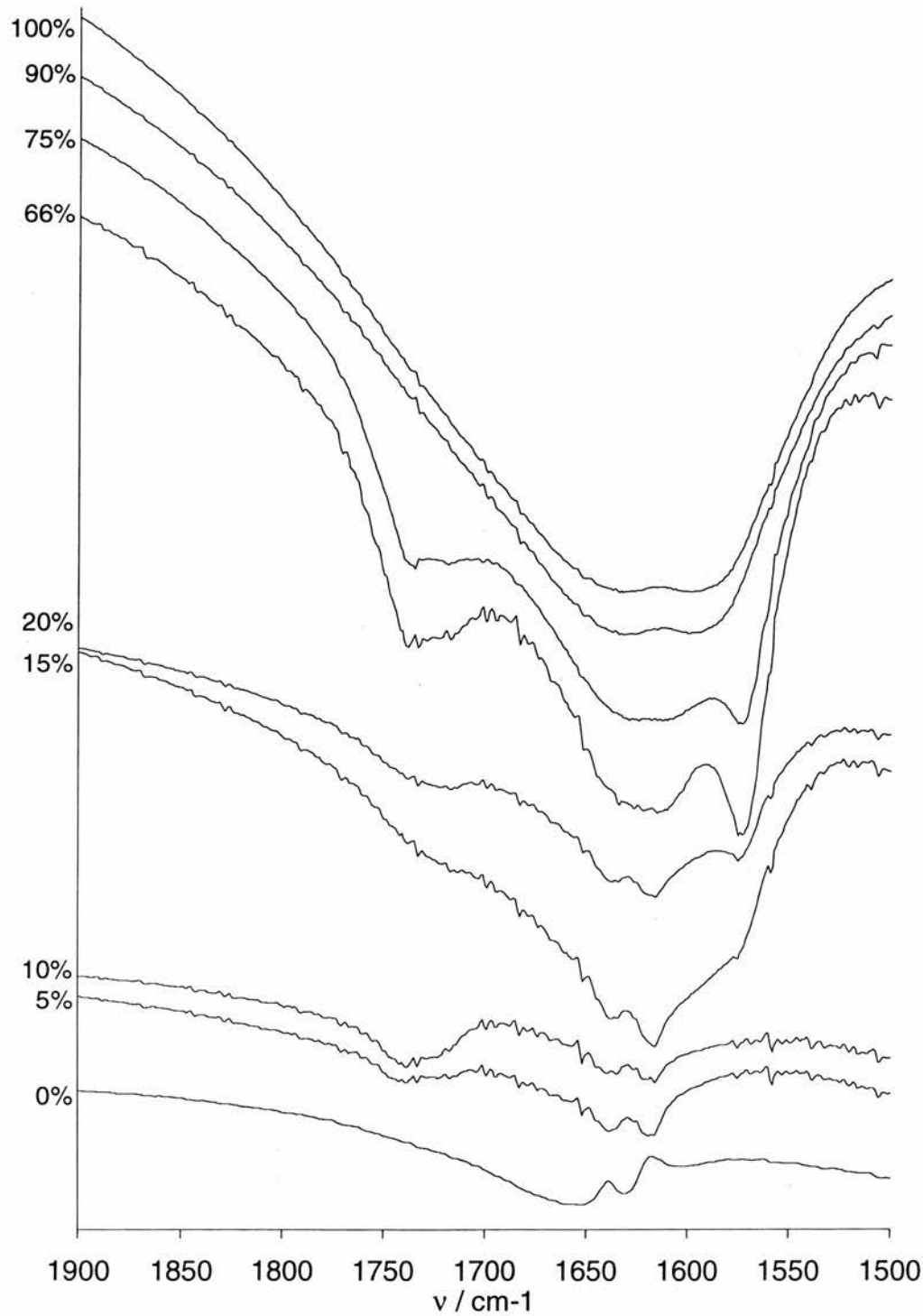

Figure 16 Enlargement of the carbonyl region of the FTIR spectra for different gel compositions.

Finally, the Al[90-100Ac]MePO samples produce only 100% AcP. There is no evidence to suggest that this material is different in any way from the published structure.[11] Figure 17 shows a comparison of the XRDs for these samples with that of 100% AcP.

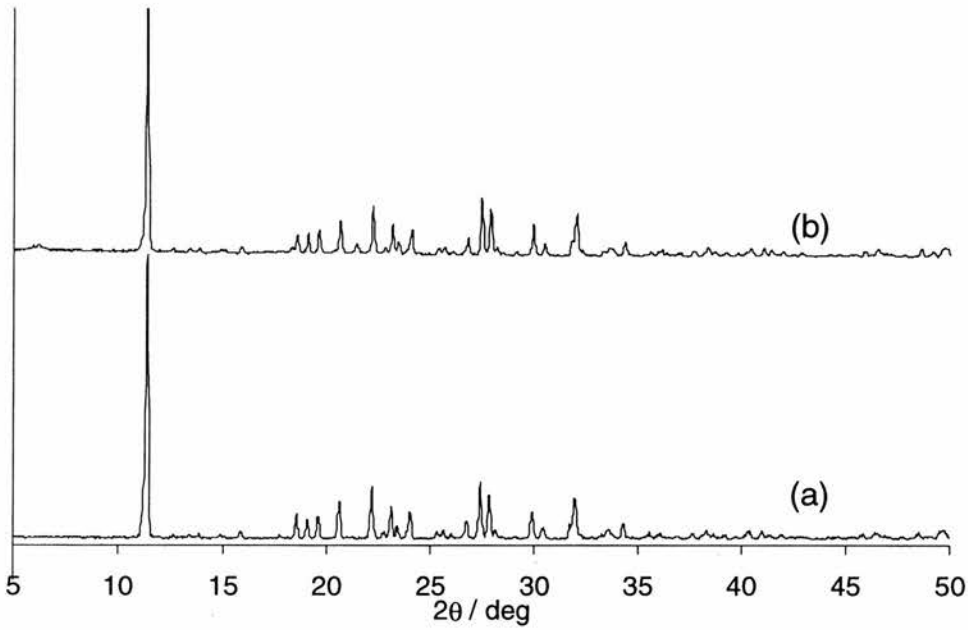

Figure 17 Comparison of the XRD pattern for Al[100Ac]MePO (a) with that of the sample from which the single crystal used in the published structure solution was taken (b).[11]

Another point worthy of note is the fact that the phosphonoacetic acid series produced, on the whole, AlMePO-α rather than AlMePO-β. In their original paper on the structure solution of AlMePO-β, Maeda *et al*[2] report that the presence of 1,4-dioxane strongly directs the synthesis towards this material rather than its polymorph, AlMePO-α. This result has been our experience also. However, modelling calculations (Chapter 4) reveal that the AlMePO-α structure is more thermodynamically stable than AlMePO-β.

It was decided that the formation of AlMePO-α in this series of experiments warranted investigation. To this end, a further series of preparations was performed in which the gel composition was constant (15% $AcP(O)(OH)_2$) but the duration of heating was varied from 1 to 4 days. Two points can be extracted from the comparison of XRDs (Figure 18). AlMePO-α is the dominant phase in all the preparations, even in the 3 day in which substantial AlMePO-β is produced. The consistency of AlMePO-α production at both extremes of the time range makes it likely that the 3 day result is an anomaly, demonstrating the sensitivity of hydrothermal syntheses of this and, indeed, many other,

types of system. However, since the general result of AlMePO-α is confirmed, it is interesting to speculate upon the reason. Neglecting the effect of the phosphonoacetate groups upon the stability of the structure, it is known that AlMePO-α is more stable than AlMePO-β. The presence of 1,4-dioxane must act to increase the rate of AlMePO-β crystallisation in order for it to be the dominant phase. The only effect of adding phosphonoacetic acid to the gel, other than changing the type of phosphorus present, is to decrease the pH by 1-2. Such an increase in acidity could be responsible for the catalysis of either AlMePO-α formation, a hydrothermal equivalent of the transformation of AlMePO-β into AlMePO-α known to take place in the solid-state[16] (see also Chapter 4), or a mixture of the two. The action of the acidity is supported by the presence in the 4 day preparation of a peak at ~5.2°, a phase that is present at 50-75% compositions in the two day series. As observed, a catalytic effect dependent upon acidity should be less pronounced at 15%, taking 4 days to produce the 5.2° phase, than at 50-75% where 48 hours is sufficient.

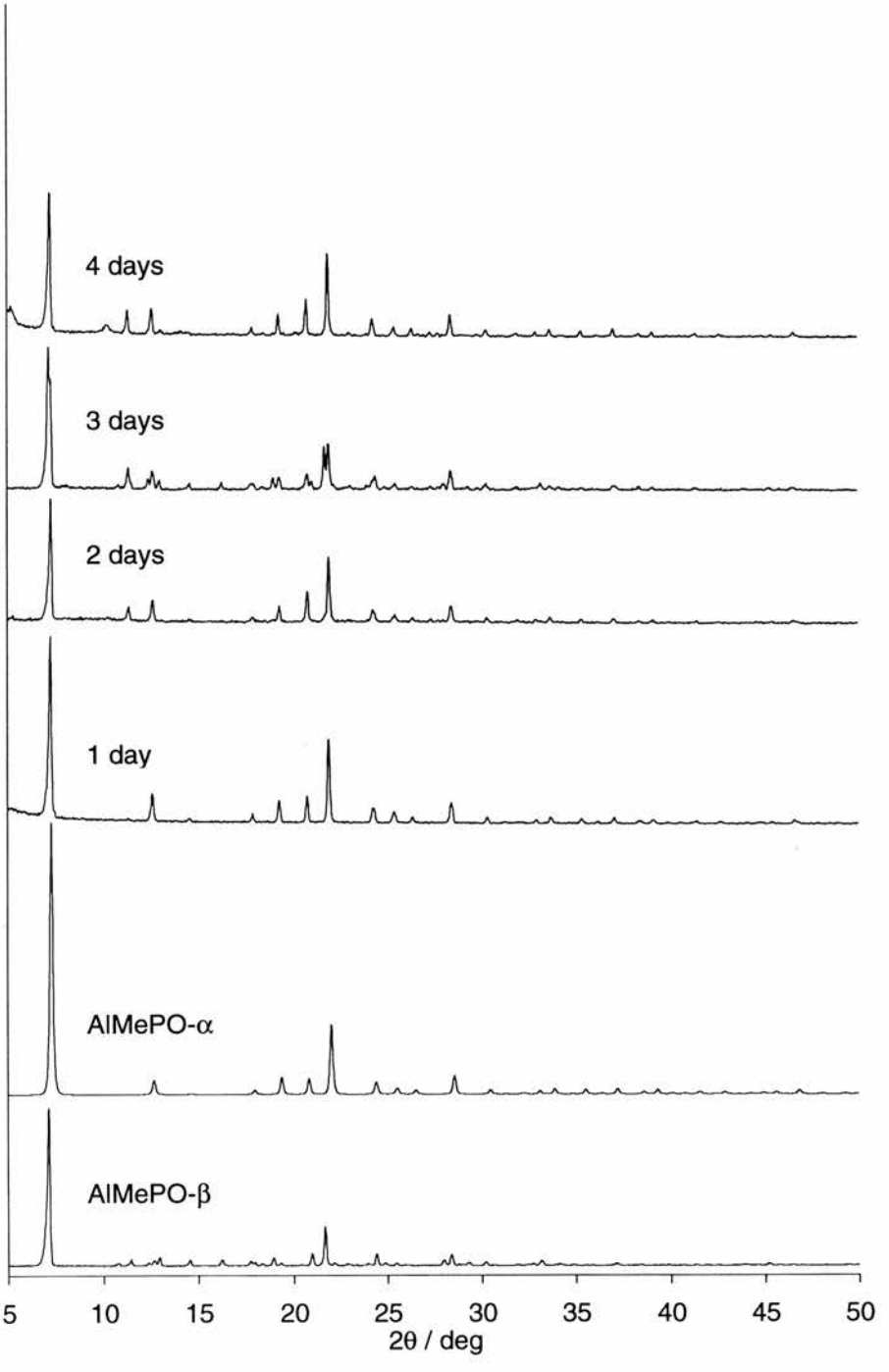

Figure 18 Comparison of the XRDs for different heating durations of the 15% AcP gel composition.

Phosphate substitution

This series of experiments gave the fewest crystalline samples of all the attempted substitutions. Figure 19 and Table 9 summarise the results of this series of experiments. As with the other two substitutions, only the Al[0-20OH]MePO samples produce AlMePO-β,

with no other crystalline phase formed until the pure aluminium phosphate phase is produced in the Al[90-100OH]MePO samples. The AlMePO-β samples produced do not appear to contain any impurities although an enlargement of the lowest 2θ peaks (Figure 20) shows some change in the line shape, possibly due to a small distribution of lattice constants. This would be consistent with the substitution of the methylphosphonate by P-OH type phosphorus which is indicated by the FTIR spectra (Figure 22).

Table 9 Identifying peak 2θ values and corresponding phase identifications for phosphoric acid doped gel samples heated for 48 hours. Identifying peaks are normally the lowest 2θ, high intensity peaks unless this coincides with another peak from another phase. Amounts are approximated purely from peak intensities and are intended as an indication of relative size, not as a quantitative measure of each component.

Amount of AcP / %	Peak (2θ / °)	Amount of component / %	Phase
0%	7.16	100	AlMePO-β
5%	7.12	100	AlMePO-β
10%	7.22	100	AlMePO-β
20%	7.20	100	AlMePO-β
33%		Amorphous	
50%		Amorphous	
66%		Amorphous	small amt of starting material
75%		Amorphous	small amt of starting material
90%	12.22	100	100% AlPO phase
100%	12.20	100	100% AlPO phase

Enlargements of the O-H stretch region of the FTIR spectra (Figure 23) shows a broad absorbance band for the Al[0-20OH]MePO samples that does not reveal particular sites. However, as with the other series of materials, the FTIR spectra suffer from high absorption by water in this region, due to the KBr used in the discs. Although precautions were taken to use dry KBr and to prepare discs with the same sample:KBr ratio of the same thickness, there remained always some absorbance in the 3000-4000 cm^{-1} region. Thus, the absence of particular bands is not surprising. The important observation is that the total intensity of the absorbance in the O-H region increases as the amount of phosphoric acid in the gels increases. Either this increase in absorption is due to more OH groups attached to phosphorus within the material, or to there being higher water content. If it is the effect of water that is being observed, this also indicates the presence of a greater number of OH groups which are making the channels sufficiently hydrophilic to adsorb H_2O.

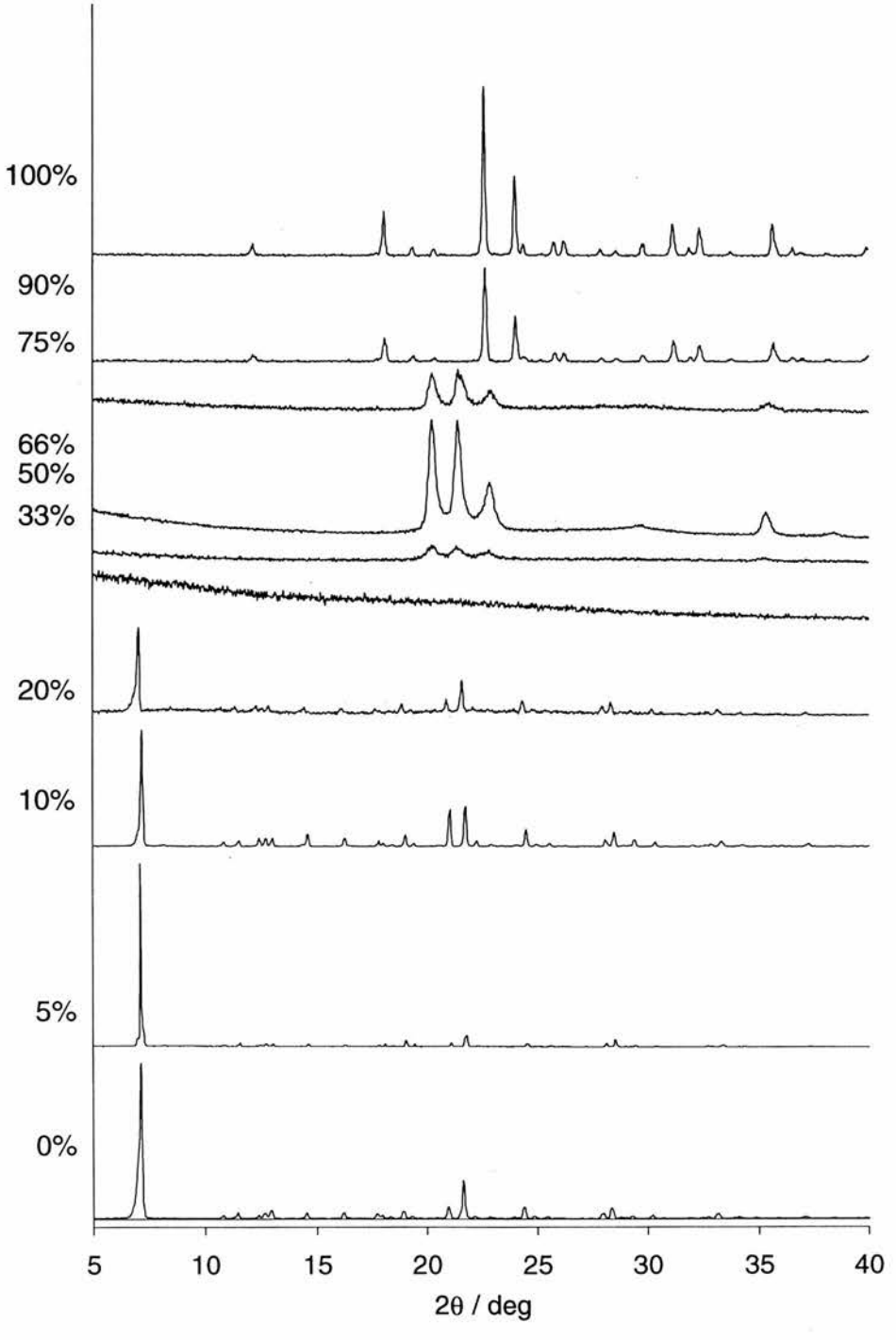

Figure 19 XRD patterns for the range of H_3PO_4 gel compositions.

The evidence of substitution within the material is increased on inspection of the methyl deformation region of the FTIR spectra (Figure 24). The bands positioned at ~1320 cm^{-1} (Table 10) decrease in intensity with increasing H_3PO_4 concentration in the gels, consistent

with methylphosphonate groups being substituted to a varying degree dependent upon the content of the synthesis gel.

Table 10 Showing the methyl deformation FTIR absorption bands for the 0-20% samples of H_3PO_4 substituted gels.

Sample / % sub[a]	Frequency of Band / cm^{-1}	
0	1317	1308
5	1318	1308
10	1320	1308
20	1320	Band is still present but hidden by the 1320 cm^{-1} absorbance creating a broad peak.

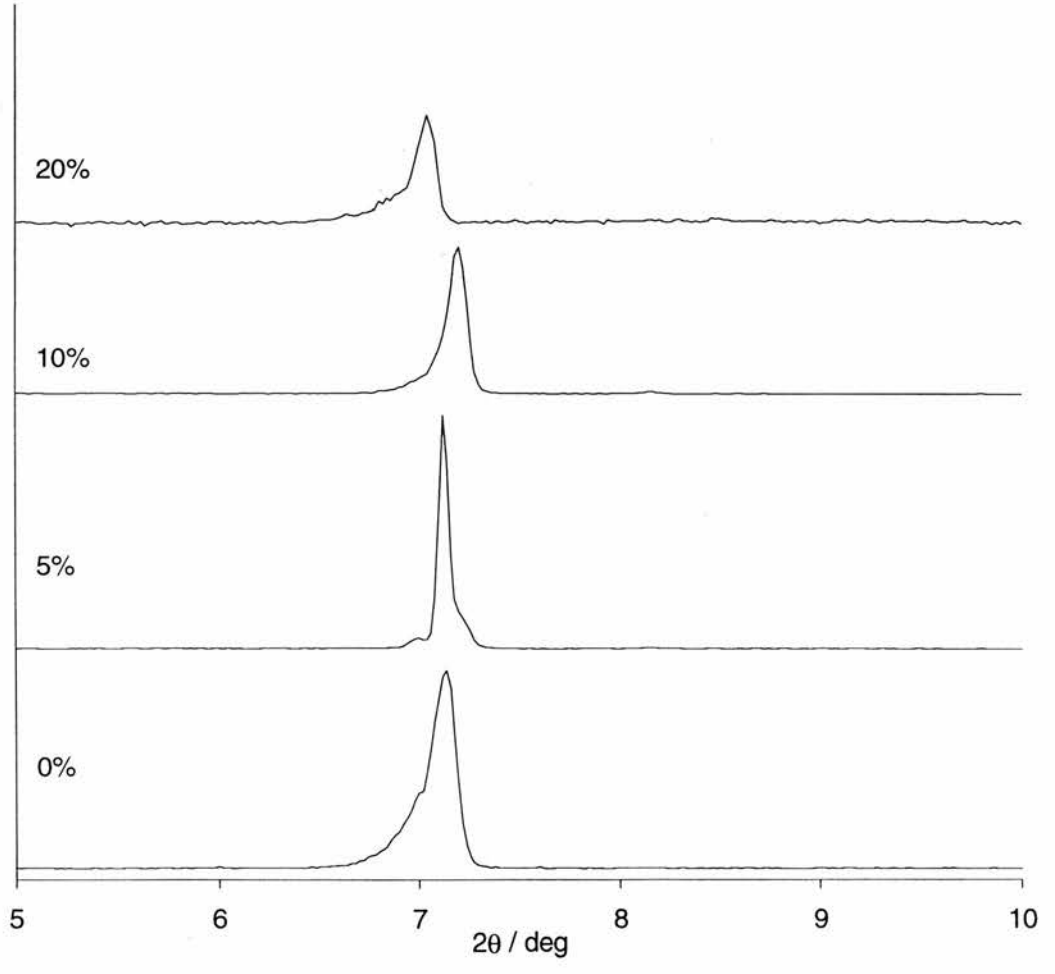

Figure 20 Enlargement of the low 2θ region of the AlMePO-β products from the H_3PO_4 series of gels.

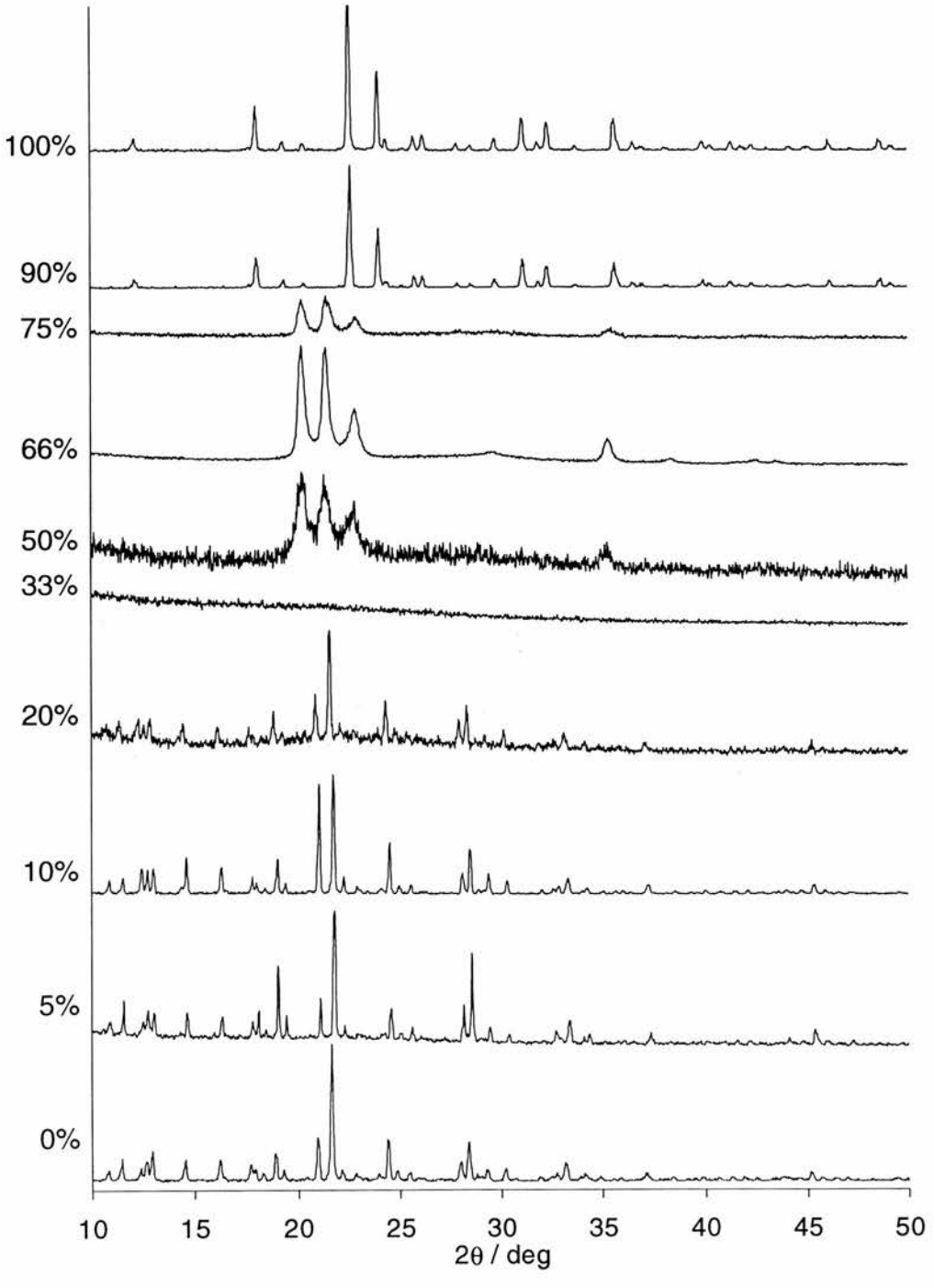

Figure 21 Enlarged sections of the XRDs for the H_3PO_4 substituted series of preparations.

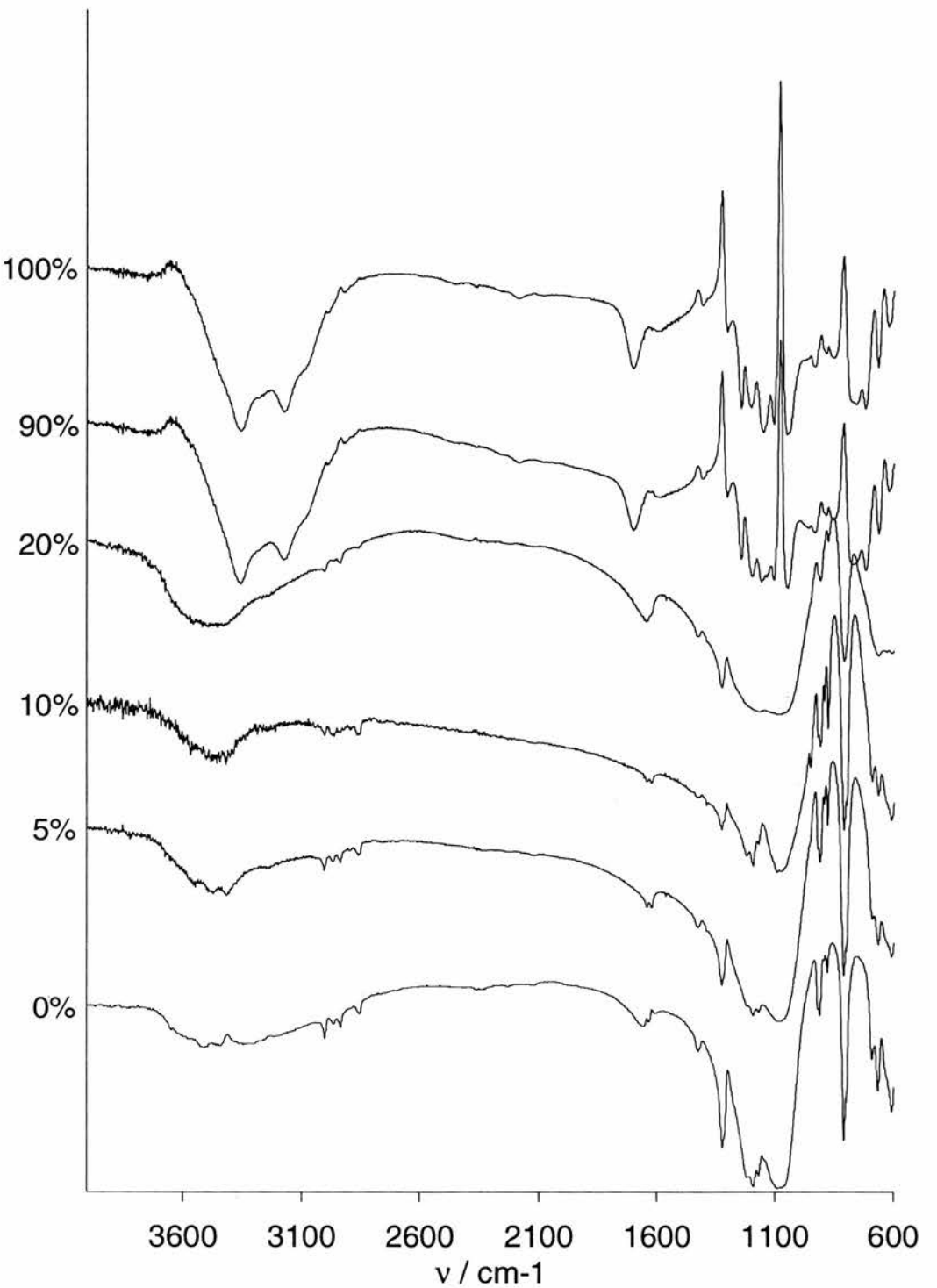

Figure 22 FTIR spectra for the phosphoric acid gel compositions producing crystalline materials.

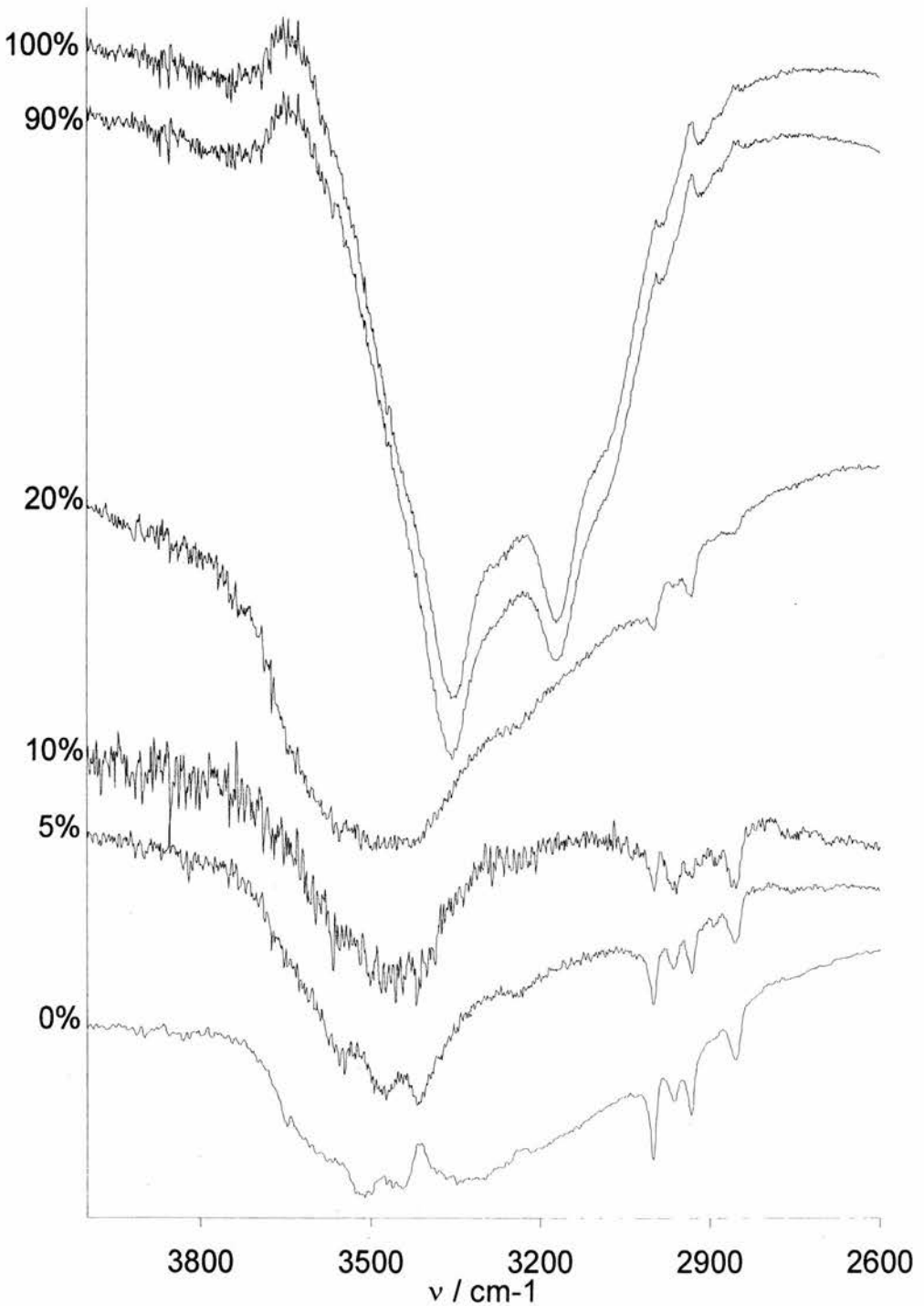

Figure 23 O-H stretch region of the FTIR spectra of various phosphoric acid gel compositions.

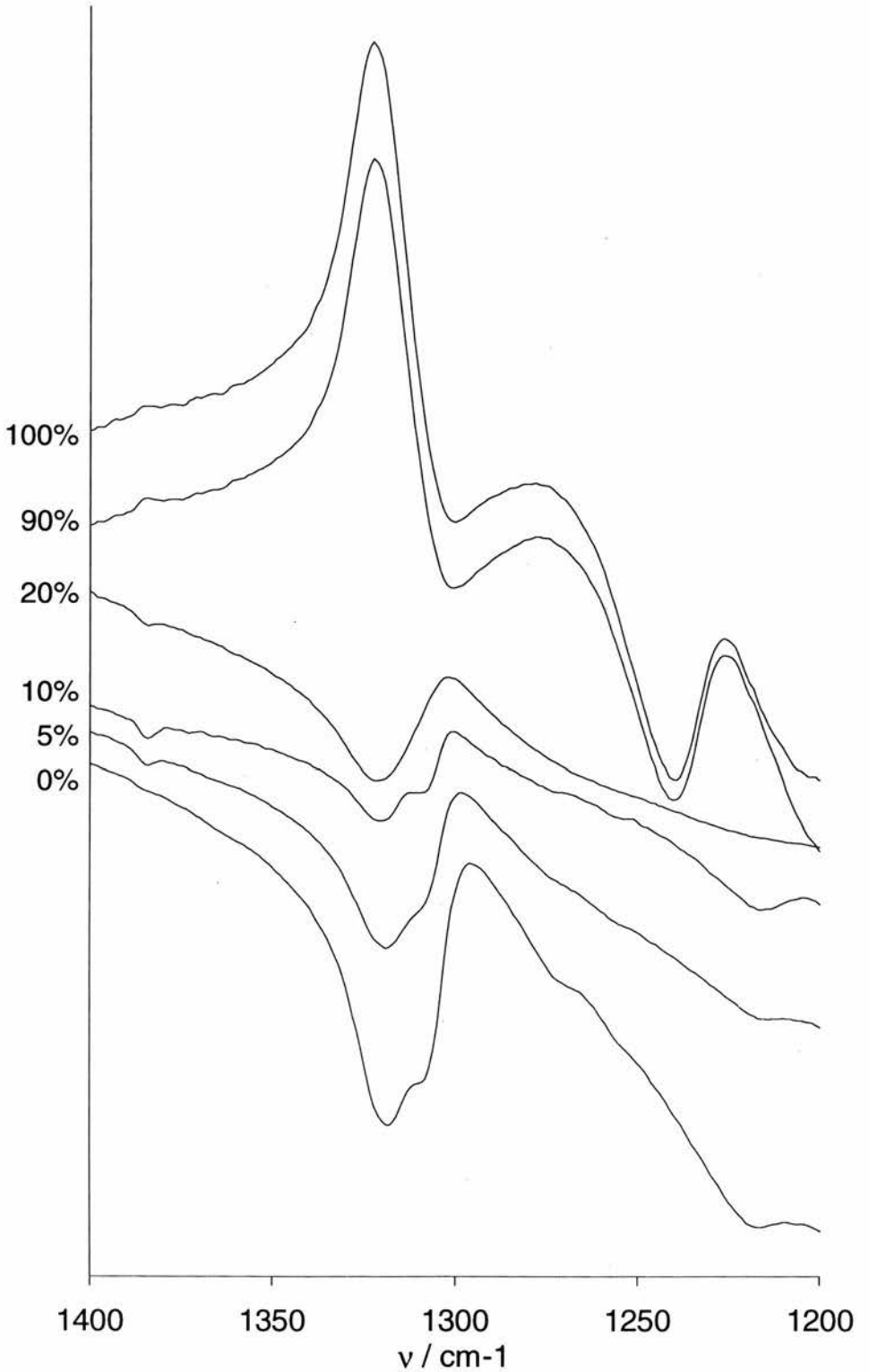

Figure 24 Enlargement of the methyl deformation band of the phosphoric acid gel dopings.

Testing of Solid-Acid strength by catalysis of methanol conversion to light alkenes and dimethylether (DME) by Solid Acid

The attempts to substitute phosphonoacetic acid and phosphoric acid into the framework of AlMePO-β had a two-fold aim. Primarily, it was the purpose to investigate methodologies for controlling the internal environment and coverage of the channel walls of the sieve. However, the presence of such acidic groups bound to the channel wall has the potential to form solid acid sites and, therefore, to catalyse the reaction of methanol, either to dimethyl ether or, at higher temperatures, to light alkenes.[17] Preliminary catalytic testing using this reaction has been carried out. (See Chapter 7 for Experimental details of the analysis technique). A brief summary of the results is given.

The two most crystalline samples one from each acidic substitution series were tested in this way, 15% AcP and 10% H3PO4 substituted materials which both gave mostly AlMePO-α. 0.25 g of sample were used in both cases. A graph of the various levels of material in the reactor system for 15% AcP is shown in Figure 25. This is compared with the results for AlMePO-β in Figure 26.

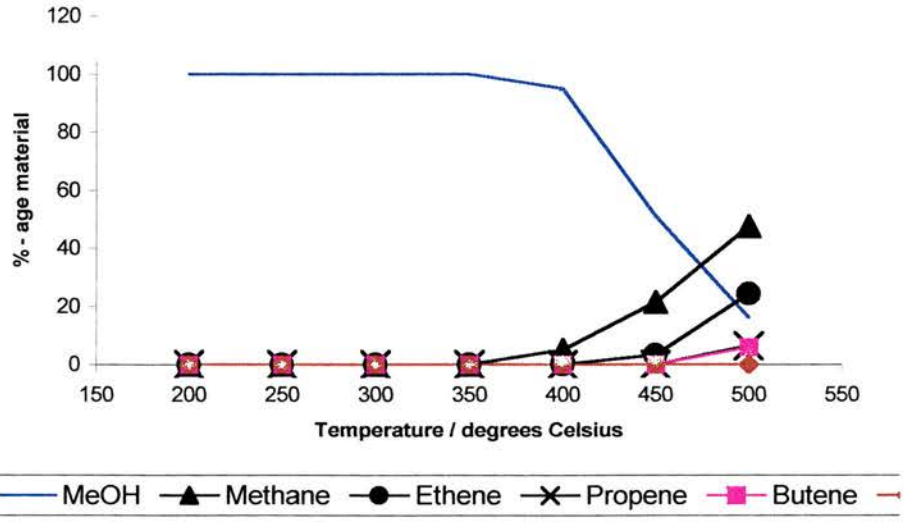

Figure 25 Summary of acid catalysis results for 15% AcP substituted sample of AlMePO-α.

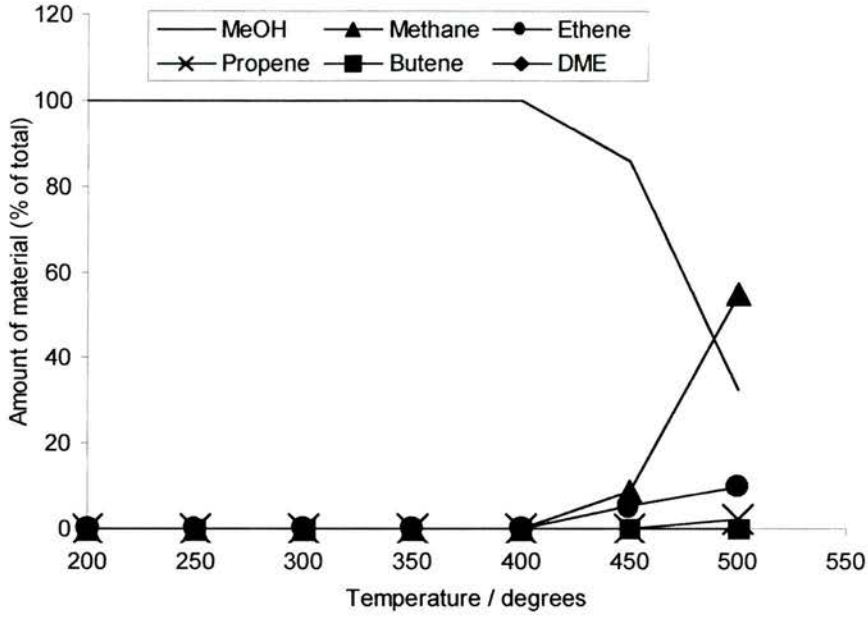

Figure 26 Results of thecatalysis of methanol conversion using AlMePO-β as a control.

As can be seen clearly, there is almost negligible difference between the results for the control experiment (Figure 26) and for that utilising the 15% acetophosphonate substituted sample (Figure 27). Certainly, within experimental error, the 15% AcP material is only as active as AlMePO-β (this is slightly more active than an empty tube but this is presumably due to a much larger available surface area, rather than significant solid acid activity.

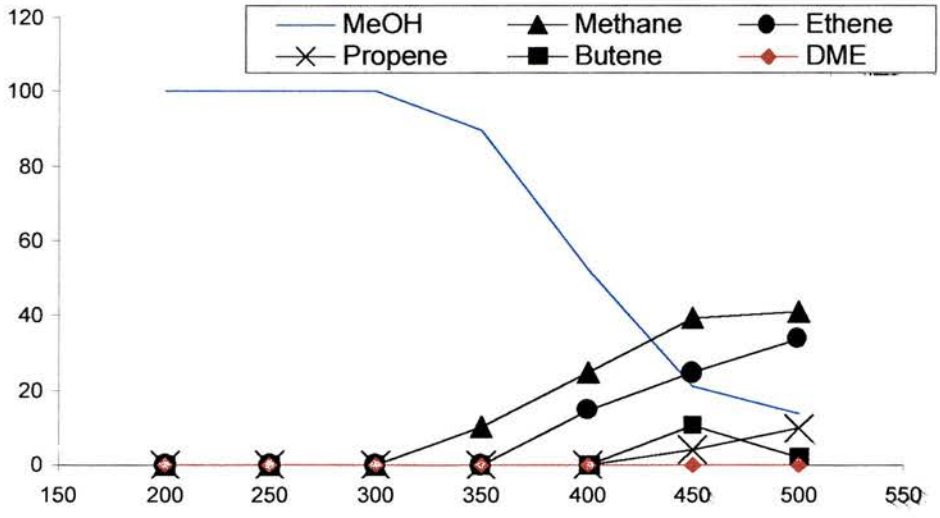

Figure 27 Results of the catalysis of MeOH to light alkenes using the 15% AcP sample. Note, there is no DME production, the normal product of acid catalysis. Compare with Figure 26, the control experiment.

In contrast, the 10% H_3PO_4 sample shows more activity than the AlMePO-β sample, or the 15% AcP sample. The catalysis starts at a lower temperature and rises to a larger proportion of methanol conversion. This indicates that the phosphoric acid substitution attempt has resulted in more acid sites in the material.

Conclusion

Phosphonate substitution within AlMePO-β and AlMePO-α is not achieved readily. Whilst there is some evidence for the presence of different phosphonates within the structure, there is always a large margin of uncertainty. It is clear that large scale (>15%) substitution is not taking place. Despite this lack of definite success in producing AlMePO-β, or AlMePO-α, with modified internal environments through mixed phosphonate groups, a new phase was produced which did seem to have this quality. Not only was it clear that the Al[33-75H]MePO samples contained a novel solid of high purity, it also appeared that the material was capable of taking up a varying amount of phosphite during its synthesis. Although there is, as yet, no direct, structural evidence that the material is microporous, the data are not inconsistent with this. In addition, this material gives a very low 2θ peak in its XRD pattern, increasing the likelihood that it is either layered or a molecular sieve.

Both the phosphonoacetate and phosphate substitutions appear to have been successful to some extent for the preparations with gel concentrations of up to 20%. The degree of replacement also increased in proportion to the gel concentration. Particularly the phosphoric acid substituted sample showed increased acid catalysis activity, strongly supporting this conclusion. The intermediate range of concentrations, at which the novel compound was formed for the phosphite materials, gave mainly amorphous products in both cases. The upper concentrations (> 75% for HP, >50% for AcP and >75% for H_3PO_4) gave materials containing solely the replacement phosphorus group.

In general, it seems that it is possible to gain some control over the character of the phosphorus groups within phosphonate materials using a hydrothermal synthesis technique of replacement. However, this approach is subject to the effects of replacement on the framework stability and vulnerable to crystallisation of the phosphonates in separate materials if suitable structures exist. This appears to have happened in the case of the attempted phosphite substitution of AlMePO-β in which impurity phases were observed in every sample.

Finally, it is worth noting the complex nature of the crystallisation processes taking place. The production of AlMePO-α rather than AlMePO-β from some samples indicates the extent to which the phase system is unknown. A further investigation of the effects of pH and other conditions on the crystallisation route / product would be a logical extension to this work, particularly in view of the known greater thermodynamic stability of the less commonly produced phase, AlMePO-α.

References

1 K. Maeda, J. Akimoto, Y. Kiyozumi and F .Mizukami, *Angewandte Chemie International Edition English*, 1994, **33**, 2335.

2 K. Maeda, J. Akimoto, Y. Kiyozumi and F. Mizukami, *Journal of the Chemical Society, Chemical Communications,* 1995, 1033.

3 K. Maeda, J. Akimoto, Y. Kiyozumi and F. Mizukami, *Angewandte Chemie International Edition English.*, 1995, **34**, 1199.

4 M. H. ZahadiNiaki, P. N. Joshi, S. Kaliaguine, *Studies in Surface Science and Catalysis*, 1997, **105**, Pt A-C, 1013-1020.

5 G. Hix and K. Harris, *Journal of the Chemical Society, Dalton Transactions*, submitted.

6 G. Alberti, E. Giontella, S. MurciaMascaros, *Inorganic Chemistry*, 1997, **36**, 2844-49.

7 L. Benes, K. Melanova, V. Zima, J. Kalousova and J. Votinsky, *Journal of Inclusion Phenomena and Molecular Recognition in Chemistry*, 1998, 31(3), 275-286

8 T. Nakato, Y. Furumi and T. Okuhara, *Chemistry Letters*, 1998, 611-612

9 R. E. Morris, M. P. Attfield and A. K. Cheetham, *Acta Crystallographica Section C – Crystal Structure Communications*, 1994, **50**(4), 473-476.

10 G. Hix, V. J. Carter, P. A. Wright, R. E. Morris, *Journal of Materials Chemistry*, 1998, in press.

11 G. Hix, R. Morris, P. A. Wright, *Journal of the Chemical Society, Dalton Transactions*, 1998, in press.

12 *Chemical Applications of Infrared Spectroscopy*, C. N. R. Rao, 1963, Academic Press (London), a) pp. 291-296, b) p. 337.

13 *Instrumental Methods of Analysis*, 7th Edition, H. Willard, L. Merritt, Jr., J. Dean and F. Settle, Jr., 1988, Wadsworth Publishing Company (Belmont, California), p. 291.

14 *CRC Handbook of Chemistry and Physics*, 73rd Edition 1992-1993, D. R. Lide (Editor-in-Chief), Pub. 1992 Chemical Rubber Company Publishing (USA), p **9**-8.

15 L.-J. Sawers, V. J. Carter, A. R. Armstrong, P. G. Bruce, P. A. Wright and B. E. Gore, *Journal of the Chemical Society, Dalton Transactions*, 1996, 3159.

16 V. J. Carter, P. A. Wright, J. D. Gale, R. E. Morris, E. Sastre and J. Perez-Pariente, *Journal of Materials Chemistry*, 1997, **7**, 2287.

17 J. Chen, P. A. Wright, S. Natarajan, J. M. Thomas, *Studies in Surface Science and Catalysis*, 1994, **84**, Pt A-C, 1731-1736.

Chapter 7

Attempted Incorporation of Transition Metals into Aluminium Phosphonates

Introduction

Molecular sieves have received much interest since the coining of the phrase in 1932 by McBain.[1] They are of interest to chemists because of the potential of a solid of a structure whose scale of interaction with sorbates is comparable to that of molecular processes. Solids containing pores of similar dimensions to small organic molecules have many potential applications, in areas such as adsorption and catalysis, in which use can be made of size and shape selectivity. Zeolites and, in general, zeotypes are particularly interesting since their crystalline nature ensures that the pore size distribution is very narrow allowing great discrimination in the adsorption of different molecules.

For the purpose of catalysis, either acidic or oxidation, wholly siliceous zeolites are relatively inert since their frameworks are neutral and silicon does not have notable redox properties. This is also the case for aluminium phosphate materials. In these compounds, neutral frameworks are formed because the tetrahedrally coordinated framework atoms, Si(IV) in siliceous zeolites, are replaced in equal numbers by Al(III) and P(V). Whilst the change from a siliceous to an aluminium phosphate (AlPO) framework causes greater hydrophilicity, the materials remain inert.

Two approaches are used in order to introduce catalytic activity into these materials, depending upon whether an oxidation or bond rearrangement / formation reaction is required. Oxidation is achieved by introducing a redox active species into the structure, either residing within the micropores or isomorphously replacing some of the framework atoms. Reactions requiring acid catalysis utilise materials in which charge imbalances have been caused through the substitution of framework atoms for those of different valency, e.g. the modification of siliceous zeolites through the insertion of aluminium into the structure. The replacement of Si(IV) by Al(III) causes a net negative charge on the framework which is counteracted by the presence of additional protons thus resulting in Brønsted acid sites[1,2] (these materials are known as solid acids). In a similar manner, it is possible to create solid acids from AlPOs through the insertion of silicon (for phosphorus) or divalent metal ions (for aluminium). Some of the most successful systems produced from AlPOs are MAPOs, magnesium substituted sieves, e.g. DAF-1 and MAPO-3 which have been shown to catalyse the isomerisation of 1-butene to 2-methylpropene.[3,4]

Microporous oxidation catalysts utilise a wide variety of transition metals substituted into the framework of various molecular sieves. One of the most effective microporous oxidation catalysts to date has been titanium silicate-1 (TS-1), a material isostructural with silicalite in which some silicon has been replaced with titanium. This compound is known to catalyse the mild oxidation of numerous alkanes,[5] alkenes[6] and alcohols[7] to epoxides. TS-1 is a neutral material since the framework is composed of tetrahedral silicon (IV) and titanium (IV) atoms. It is possible to create a molecular sieve in which both acid sites and oxidation activity occur through the substitution of the framework with a redox metal of different charge to the atom which it replaces. However, this results in a complex combination of both types of catalytic site in one material, often resulting in a lack of selectivity and unpredictable behaviour.[8,9] Despite this, much work has been done on the insertion of titanium into aluminium substituted zeolites[10,11] and silicon substituted AlPOs (SAPOs).[12] Aluminium substituted zeolites and SAPOs are strong solid acids and, therefore, the resulting materials do combine acid sites with a material having redox activity. The production of side products through the action of the acid sites can be mitigated by replacing the protons in these materials with sodium counterions, reducing the acid properties of the sieve.[13] Also, although, in many cases, aluminium is necessary to the effective synthesis of mainly siliceous zeolitic materials there has been some effort to produce samples free of aluminium[14] and, hence, of acid sites.

In addition to the work on silicon derived materials, there has been considerable interest in creating redox molecular sieves from AlPOs. The presence of CrAPO-5 (the chromium substituted AlPO-5 material) was shown to catalyse the oxidation of secondary alcohols, alkylbenzenes and cyclohexane.[15,16] It has been possible to synthesise VAPO-5[17] also, and CoAPO-5,[18] both of which have been shown to enhance the rate of several oxidation reactions. However, despite the great interest in MeAlPOs (Me = redox metal) as promising catalysts, recently it has been shown that they suffer from problems of leaching of the redox metal into solution. It is this leached material that is responsible for the catalytic effects observed and not a true heterogeneous process within the pores.[19] Sheldon *et al*[19] also noted that, even assuming no leaching from the framework, transition metal substituted AlPOs are unlikely to be good catalysts for oxidation since the pores are hydrophilic (oxidation processes generally have at least one hydrophobic reactant and products of greater hydrophilicity – the pores are expected to fill with products and exclude most of the reactants).

The recent discovery of microporous aluminium methylphosphonates[20-22] brings the possibility of a new class of catalytic materials to replace the AlPOs. In contrast to the purely inorganic frameworks of the AlPOs, the unidimensional pores of these new

materials, AlMePO-β and AlMePO-α, are hydrophobic in character due to the layer of methyl groups that partially covers the internal surface. Isomorphous replacement of some of the aluminium atoms with redox metals could introduce catalytic activity to AlMePO-β. A similar modification with divalent metal ions would lead to materials containing acid sites for hydrocarbon transformation reactions. This chapter reports attempts to create catalysts from microporous aluminium phosphonate materials by substituting heteroatoms into the structure by direct hydrothermal synthesis. This methodology mimics the techniques used to modify AlPOs[17,23] to give substituted frameworks in which a small proportion of the metal salt is added to a synthesis gel which has an aluminium content reduced by a similar amount. The metals used to give redox properties are : chromium, titanium, iron, cobalt and vanadium; to give acid properties: magnesium, manganese and zinc. Some success is obtained for zinc, titanium, vanadium and chromium. These samples are subjected to preliminary catalytic testing as a further method characterisation. The zinc sample is tested for the presence of Brønsted acid sites with the conversion of methanol to light hydrocarbons as for SAPO-18 and -34.[24] The three relatively successful redox examples are tested for oxidation activity using a variety of substrates by H_2O_2 in refluxing CH_3CN.

Experimental

Samples were prepared using a procedure modified from that of Maeda *et al*[21] in which gels were prepared containing aluminium hydroxide hydrate mixed with a source of the replacement metal in a range of proportions. The components of the gel were $Al(OH)_3$: replacement metal source : $CH_3P(O)(OH)_2$: H_2O : 1,4-dioxane where the molar ratio was 1-x : x : 1.5 : 40 : 0.5 respectively (x ranged from 0 to 0.3 at most, or a value at which the product was amorphous if that was less) and the metal sources were, chromium acetate, magnesium acetate, manganese acetate, vanadyl acetylacetonate, cobalt acetate, titanium (IV) butoxide, iron (II) acetate and zinc acetate. Gels were stirred until homogeneous and reacted in PTFE-lined stainless steel autoclaves of 24 ml volume at 160 °C for 48 hrs, except for chromium for which three durations were used, 24 hrs, 48 hrs and 144 hrs. Immediately before heating the gels had a pH of 3.5 which varied negligibly with the amount of substituting metal ion. Products were filtered, washed with 40-60 cm^3 distilled water and dried in air at 60°C. The materials were characterised by powder X-ray crystallography (XRD), ultra-violet and visible spectroscopy (UV-vis), and scanning electron microscopy (SEM) with selected area elemental analysis by energy dispersive analysis of electron stimulated X-ray emission (EDX) analysis. It is necessary to select a particular area to analyse so that one can be sure in which part of the sample, in which particles, the elements giving rise to the X-rays that are detected actually reside.

Powder x-ray diffraction was performed on a STOE STADIP diffractometer with a linear position sensitive detector covering 6° in 2θ and employing Ge monochromated Cu-$K\alpha_1$ radiation (λ=1.54056 Å). Samples were prepared by mounting in a glass capillary or between two sheets of milar as rotating discs in the X-ray beam. SEM and EDX were performed on a JEOL JSM-35CF microscope with an accelerating voltage of 10kV fitted with a LINK AN 10000 EDX system.

Materials for testing for catalytic oxidation activity were heated for 8 hrs at 410 °C in a silica glass tube under dry nitrogen before use. Oxidation experiments were performed in reflux apparatus using mixtures containing 3.87 g (38.5 mmol) cyclohexanol, 4.87 g (38.5 mmol) of 30 wt% aqueous H_2O_2, 30 cm^3 CH_3CN and the catalyst (varying amounts were used and are reported in the Results section) which was added last. A small (2 cm^3) sample of the reaction mixture was taken before adding the catalyst and after the reaction on cooling and filtering the solution. Both samples were analysed immediately by gas chromatography (GC) on a CE Instruments GC 8000 TOP equipped

with a Supelcowax©-10 column, 30 m in length with a 0.53 mm i.d., and a Fisons DP700 electronic integrator.

Acid catalysis was performed in an upright silica glass tube, heated in a tube furnace, in which the sample rested on a sinter. A flow of dried nitrogen was maintained to which methanol could be added for the period of reaction. Samples were prepared by lightly crushing them to break up larger particles. Before adding methanol to the nitrogen flow, samples were heated for several hours at 410 °C to ensure the removal of 1,4-dioxane from the channels. The weight hourly space velocity (WHSV), g reactant (g catalyst)$^{-1}$ hr^{-1} was 0.38 hr^{-1} and the nitrogen flow 30 cm^3 min^{-1}. Samples were taken using a gas sampling valve of volume 0.25 cm^3, and analysed using a CE Instruments GC 8000 TOP equipped with a Chrompak Poraplot-U© column, 25 m in length with a 0.53 mm i.d., and a Fisons DP700 electronic integrator.

Results and Discussion

Attempts were made to prepare samples of AlMePO-β in which some of the aluminium, or phosphorus, framework atoms had been replaced by a different metal. A range of replacement metals was attempted, chosen for their potential as catalytically active sites within the framework. These metals were; potential acid catalysts : Zn, Mg and Mn; potential oxidation : Co, Fe, V, Cr and Ti. The work on heteroatom replacement in AlMePO-β is reported in two sections. The first deals with the success of producing crystalline phases of AlMePO-β, or AlMePO-α in which the particular metal had been inserted. The second reports the investigation into the catalytic properties of those materials in which there was reason to believe heteroatoms had been inserted.

Isomorphous heteroatom substitution in AlMePO-β

Magnesium (II)

The attempt to prepare MgAlMePO-β using a gel in which 5% of the aluminium was replaced with $Mg(Ac)_2$ produced phase pure AlMePO-β (Figure 1). However, the EDX spectrum of this material in bulk showed no magnesium peak indicating that no substitution had taken place (see Table 1). The scanning electron micrograph (Figure 2) reveals a very pure sample of needle-like crystals of 50-200 μm in length and 1-5 μm in diameter.

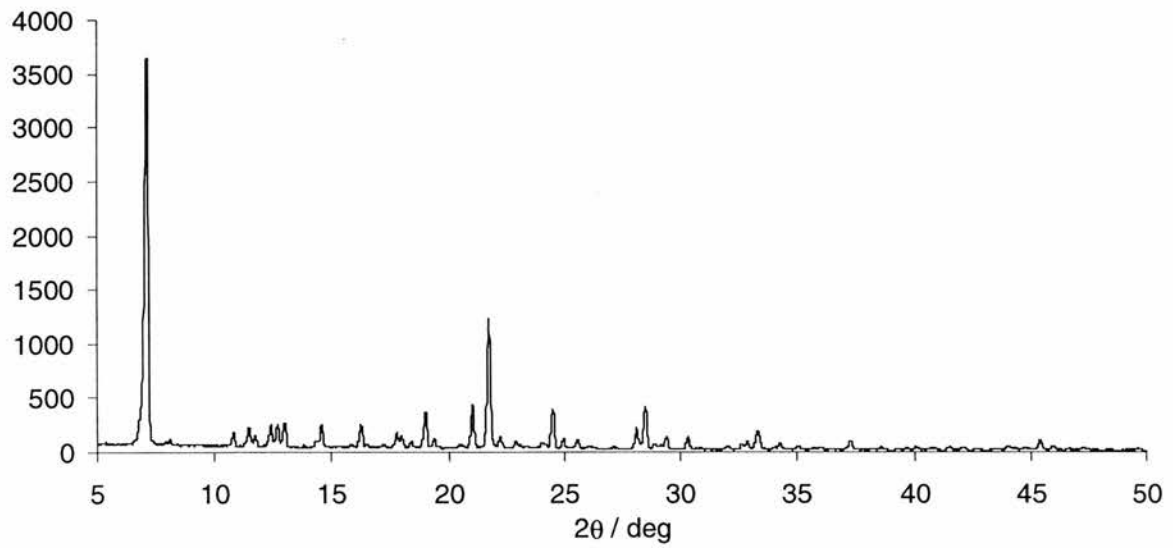

Figure 1 XRD of the 5% Mg sample

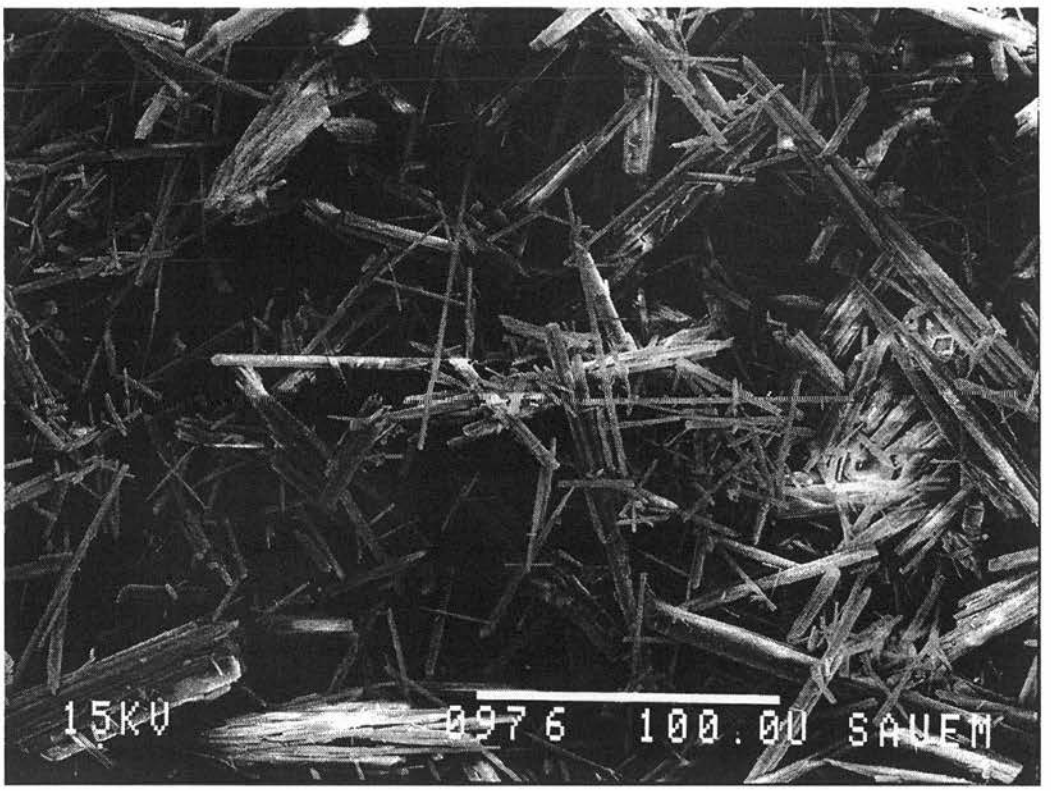

Figure 2 Electron micrograph of the 5% Mg AlMePO-β preparation.

Manganese (II)

As with the material formed in the presence of magnesium, the manganese sample also produced phase pure AlMePO-β (Figure 3). The electron micrograph (Figure 4) shows the needle-like crystals, 60-150 μm in length and 2-5 μm in diameter, typical of AlMePO-β. EDX results (Table 1) indicated no manganese in the sample. The attempt to replace aluminium with manganese was unsuccessful.

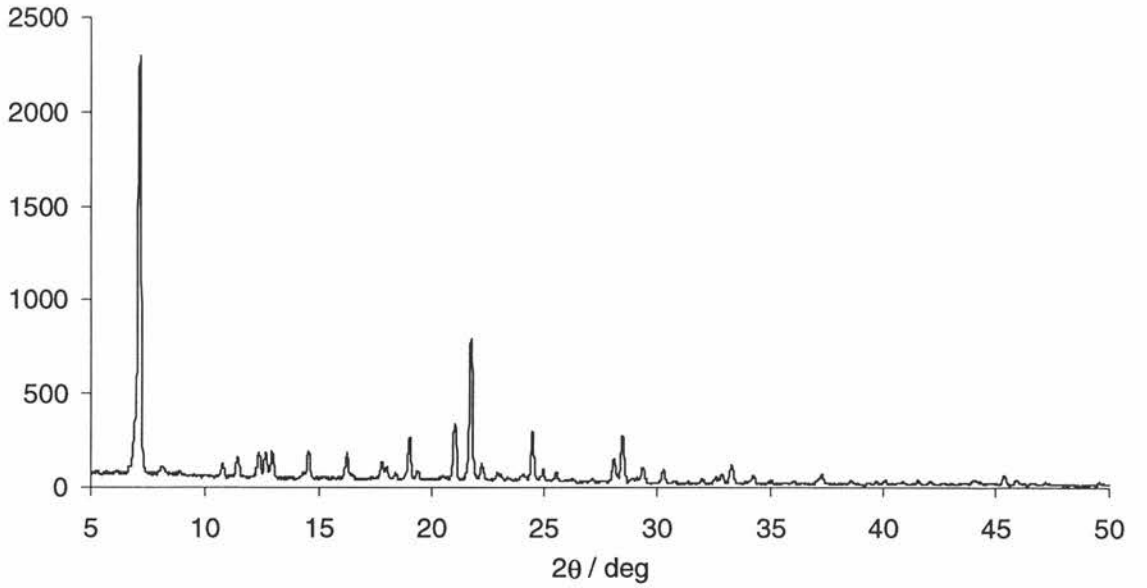

Figure 3 XRD of the 5% Mn sample

Figure 4 Electron micrograph of the 5% Mn AlMePO-β preparation.

Zinc (II)

A comparison of the XRDs (Figure 5) for samples from gels containing various amounts of zinc acetate shows the formation of phase-pure AlMePO-β at loadings of 5-10%. Greater concentrations of zinc in the gel cause the production of two other materials, one of which is AlMePO-1 and the other unknown. The EDX results (Table 1) indicate no zinc incorporation in the 5% sample. The 10% sample, however, has considerable zinc present. This is evidenced not only by the zinc peak but also by the relative reduction of the aluminium peak when compared to the constant phosphorus peak, i.e. the Al:P ratio increases. This fact may be misleading however, as it seems unlikely that the zinc resides in framework sites in this material. 31P MASNMR of the 10% revealed no change from the unmodified AlMePO-β material. If Zn were in place in the framework, satellite peaks would form in the NMR spectrum. It is possible that these would manifest only as broadening but there is nothing the sort in evidence. The 20% sample is not phase-pure so it is not possible to determine the location of the zinc in this sample.

Table 1 Comparison of the ratio of EDX peaks for the divalent metal preparations

Sample	Ratio Al:P:M (M is Mg, Mn or Zn)
5% Mg	1:1.61:0
5% Mn	1:1.64:0
5% Zn	1:1.63:0
10% Zn	1:1.80:0.18
20% Zn	1:2.07:0.20

Scanning electron microscopy of the 5% sample (Figure 1) shows a combination of small (~40 μm in length and ~4 μm in diameter) needle-like crystals and large (200-400 μm by 40-100 μm) bundles of crystallites apparently of the same individual morphology. The 10% sample (Figure 7) contains large aggregated particles whose make-up is hard to ascertain although, from the top left region of the micrograph, it appears that bundles of the needle-like crystals normally associated with AlMePO-β are the major component of this sample. The impure 20% sample (Figure 8) has similar particles, presumably containing the AlMePO-β component of the mixture, as well as flatter, more plate-like formations of a type similar to the preferred morphology of crystals of AlMePO-1.

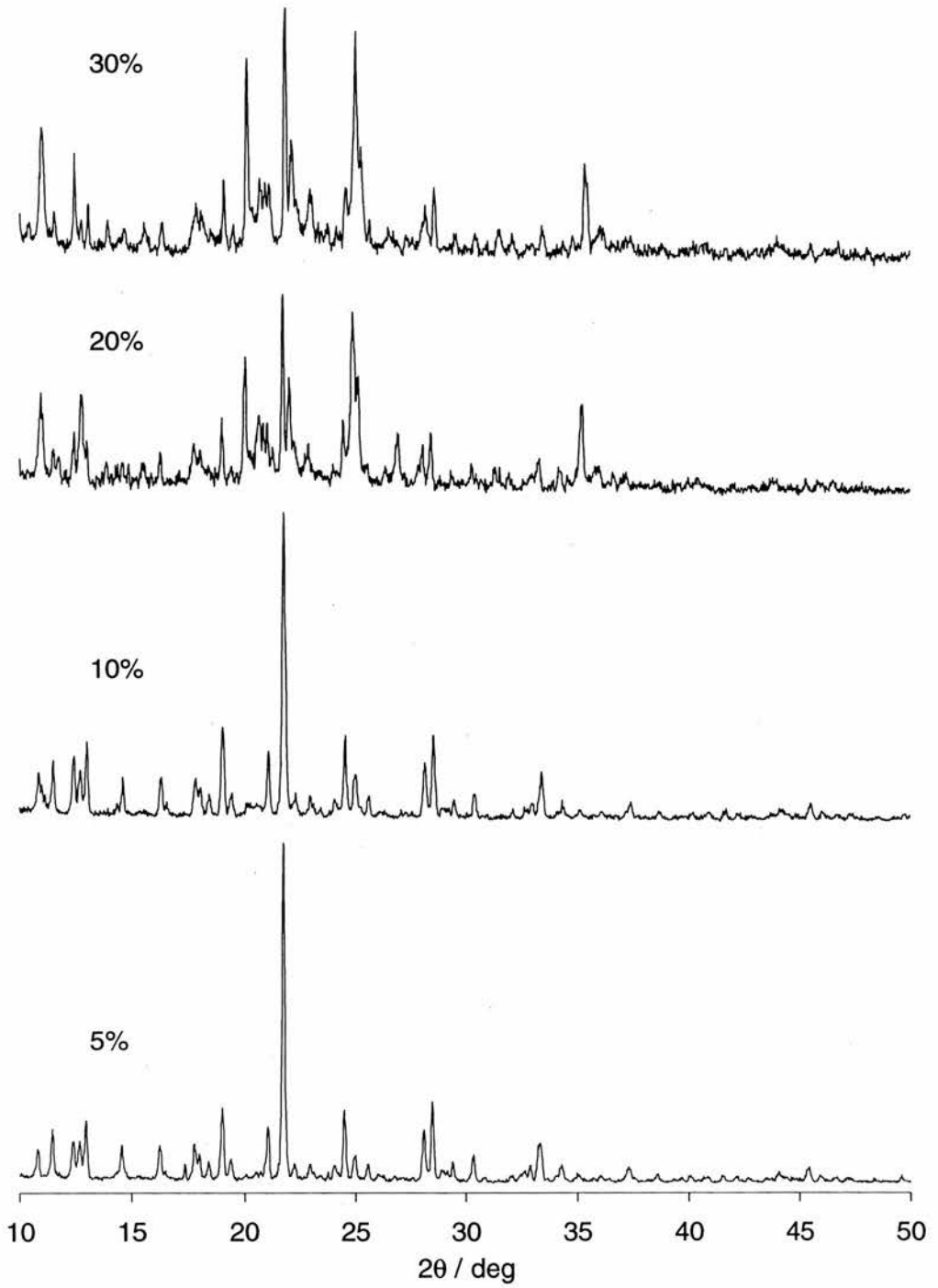

Figure 5 Comparison of the XRD patterns for gels with various different amounts of Zn

Figure 6 5% Zn AlMePO-β

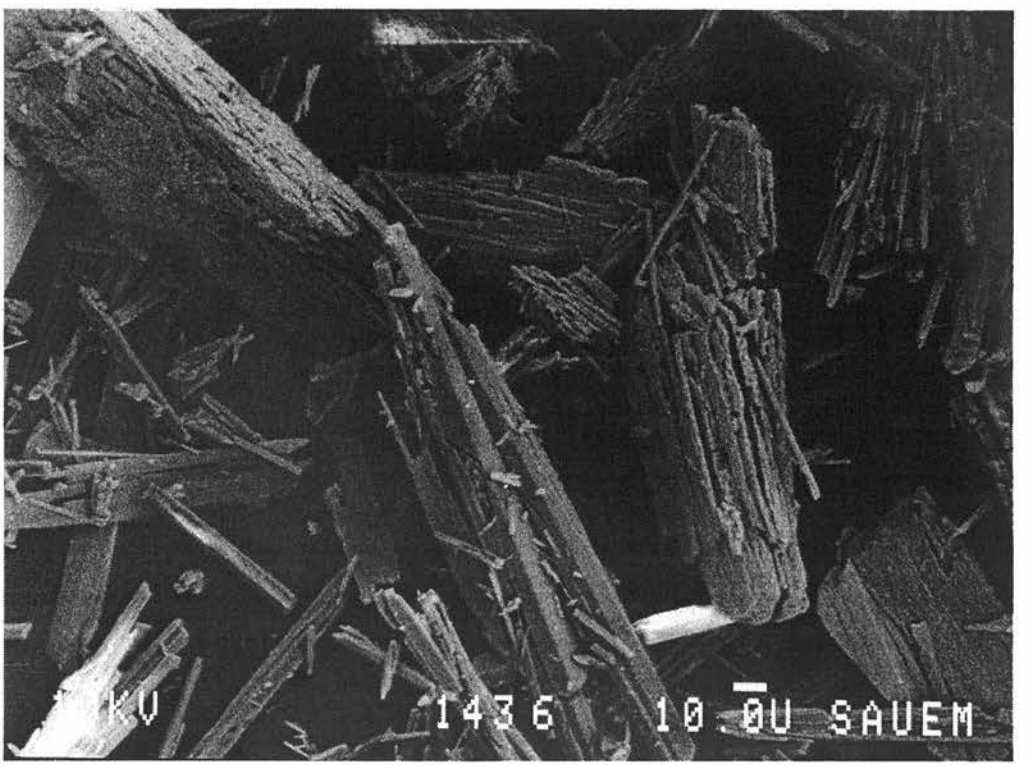

Figure 7 10% Zn AlMePO-β

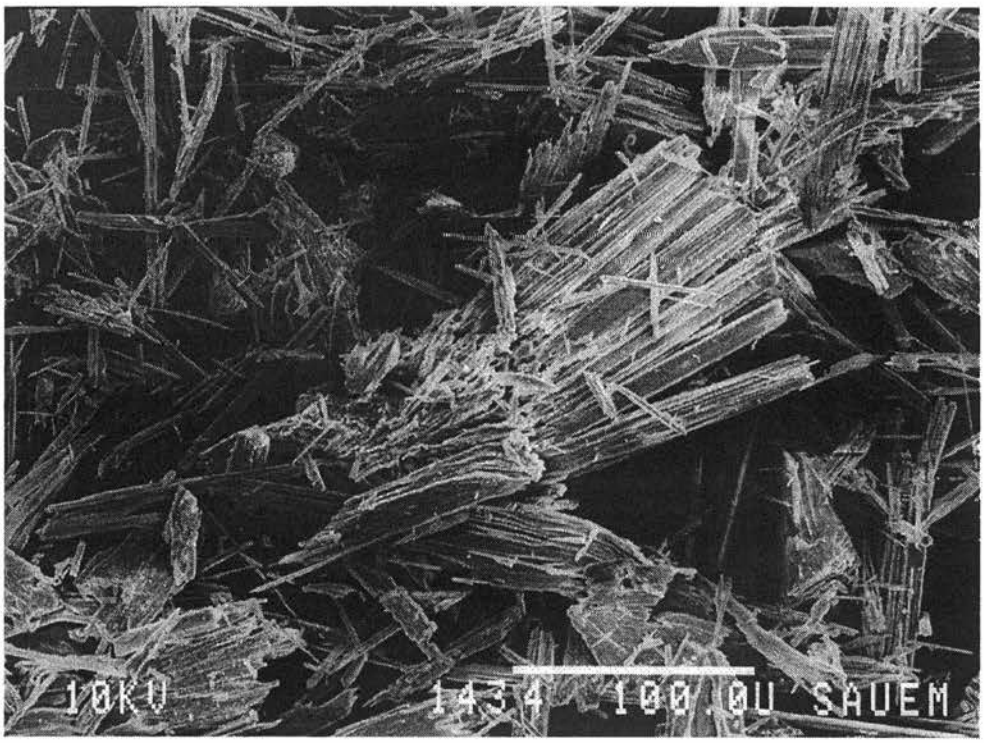

Figure 8 20% Zn AlMePO-β

Redox metals

Co

Attempts were made to substitute AlMePO-β with Co^{III} by using cobalt acetate tetrahydrate in the synthesis gel. However, it was not possible either to produce phase-pure AlMePO-β in this way or to cause any substitution of the aluminium in the AlMePO-1 that was produced. Instead, white crystalline powders being a mixture of AlMePO-1 and AlMePO-β were produced along with small, intensely pink particles of a substance thought to be a cobalt phosphonate.

Fe

The attempts to produce iron substituted AlMePO-β resulted in samples that were all amorphous except in the case of the 5% loading (Figure 9) which produced pure AlMePO-β. EDX results (Table 2) show that substitution with iron has not been successful in the 5% sample. Although the samples from higher gel loadings do show the presence of iron, these samples are not crystalline. Scanning electron microscopy shows typical needle-like AlMePO-β crystals for the 5% sample (Figure 10) with some other bodies of unknown identity (see left central region of the micrograph). The micrographs for the 10% (Figure 11) and the 20% (Figure 12) samples confirm the amorphous nature of these solids showing no signs of crystalline formations.

Table 2 EDX results for attempted substitution of AlMePO-β with iron (II) ions.

Sample Loading	Ratio (Al:P:Fe)
5%	1:1.74:0
10%	1:1.97:0.06
20%	1:2.07:0.07

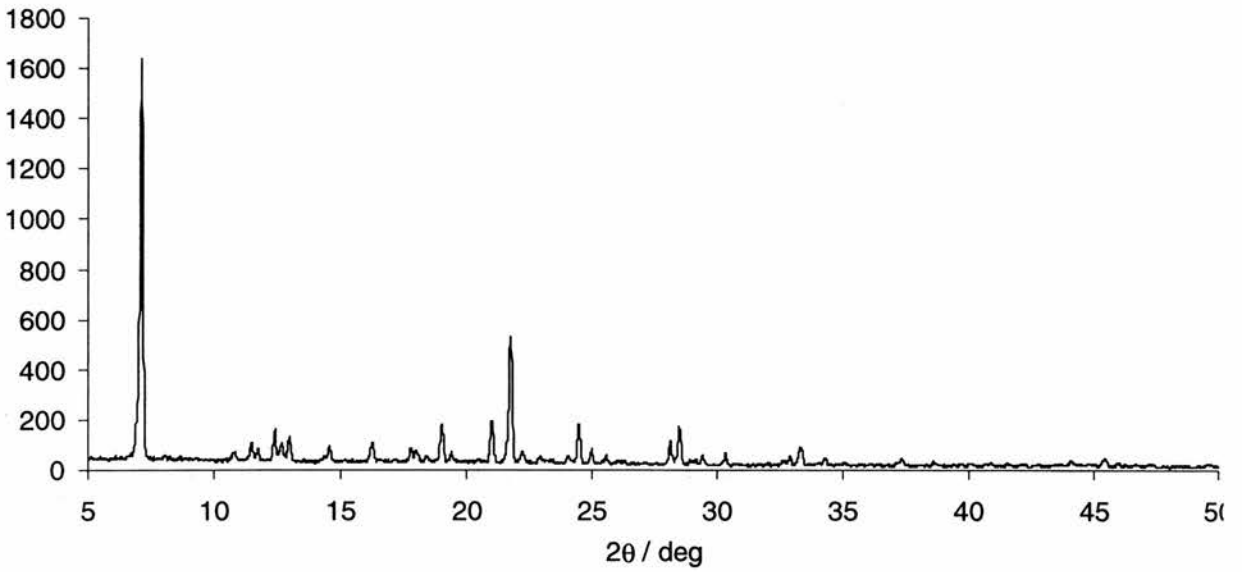

Figure 9 XRD of 5% Fe AlMePO-β

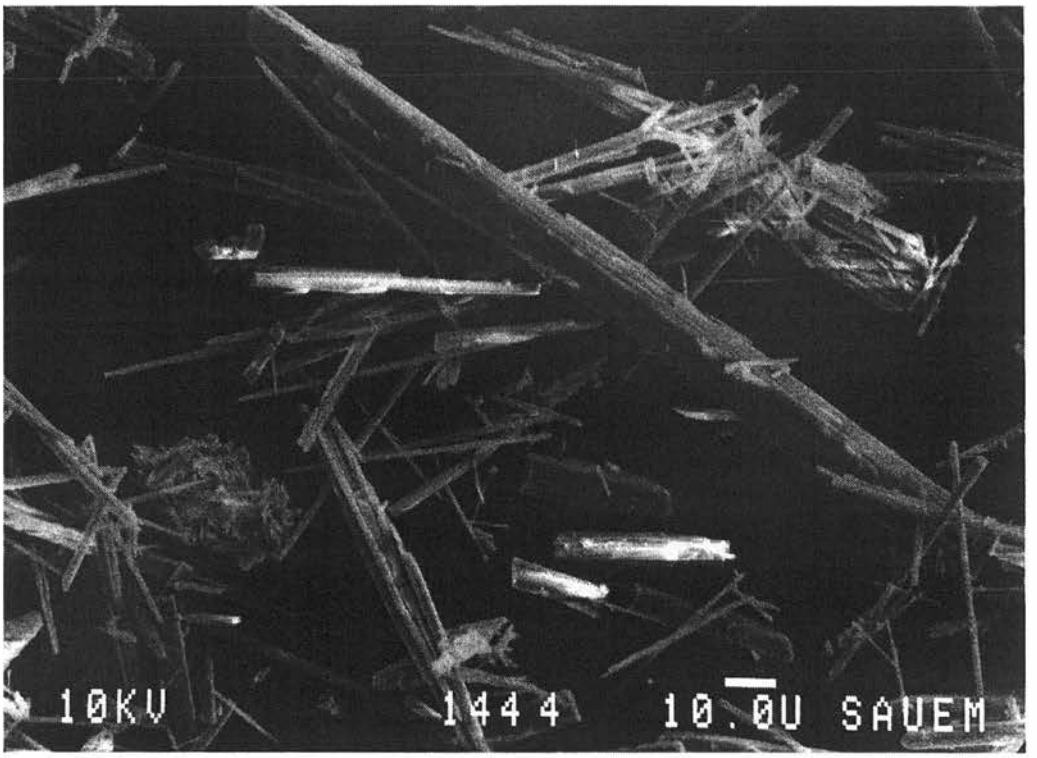

Figure 10 5% Fe AlMePO-β

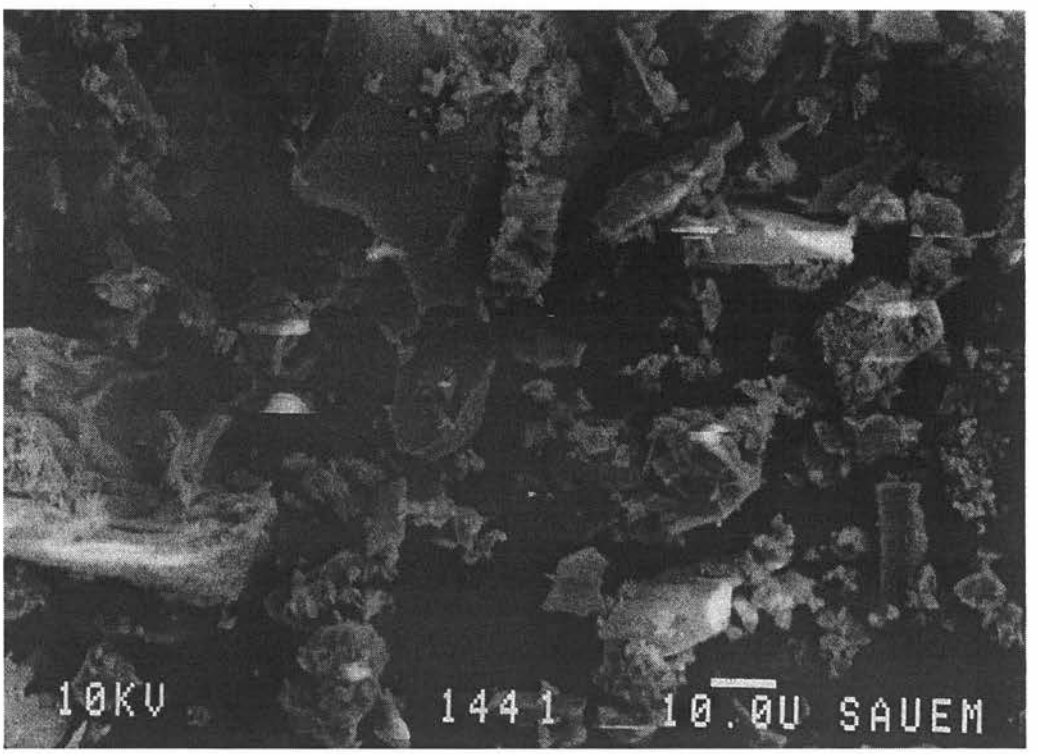

Figure 11 10% Fe AlMePO

Figure 12 20% Fe AlMePO

V

X-ray diffraction results (Figure 13) show the formation of AlMePO-β for the 5% and 10% samples together with a small amount of impurity (XRD peak at 10.56°). Both of these samples contain substantial amounts of vanadium (Table 3). The 20% loading gave several mixed phases, each with different Al:V ratios as measured by EDX with a tightly focused electron beam. Although identification of the material was not possible from XRD it appears that one of the compounds produced in this sample was a vanadium phosphonate containing no aluminium. Other areas of the sample examined also contained vanadium but the identity and crystallinity of this material was not known.

The low level of impurity in the 5% and 10% samples measured by XRD is reflected in the very 'clean' samples viewed by scanning electron microscopy (Figure 14 and Figure 15). The crystals in both samples are shorter (~40 μm rather than 100 μm) and wider (~10 μm rather than ~5 μm) than were observed in other samples of AlMePO-β (notice that the micrographs are at 10 times the magnification of the others in this chapter). It is also noticeable that the needle-like particles are not the only morphology present. The other particles must be due to the impurity phase and, perhaps, some amorphous material. The 20% sample (Figure 16) shows several types of material, the large structure in the bottom left of the picture being representative of the conglomerated particle which had a very high vanadium content as measured by EDX.

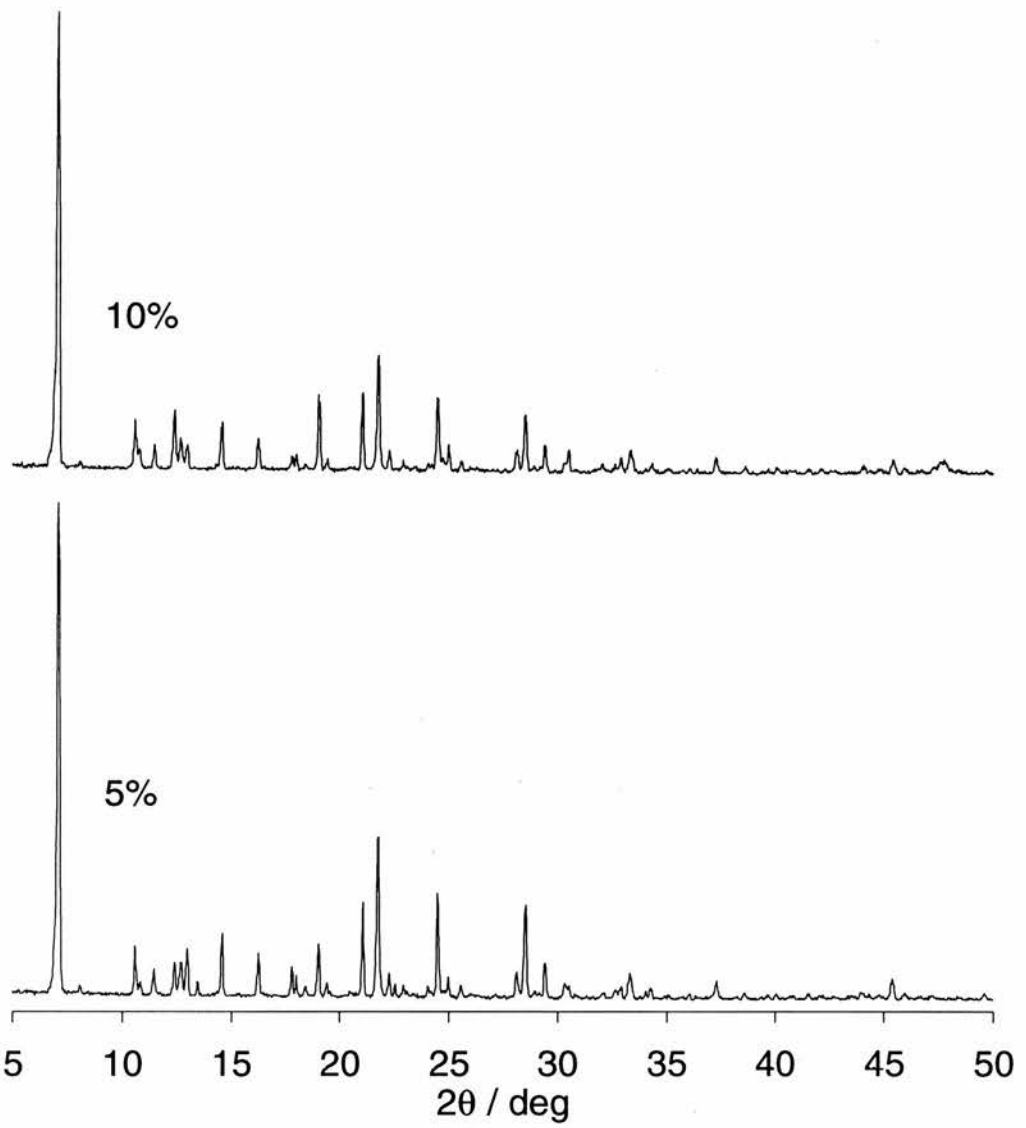

Figure 13 Comparison of the XRD patterns for samples containing 5 and 10% V. Samples containing more vanadium were poorly crystalline.

Table 3 EDX results of the attempts to substitute with vanadium

Sample	Al:P:V
5%	1:1.78:0.07
10%	1:2.69:0.38 (needle-like crystals)
20% (bulk)	1:?:0.07
20% (large crystal)	0.04:1:0.80
20% (conglomerated particle)	1:4.82:1

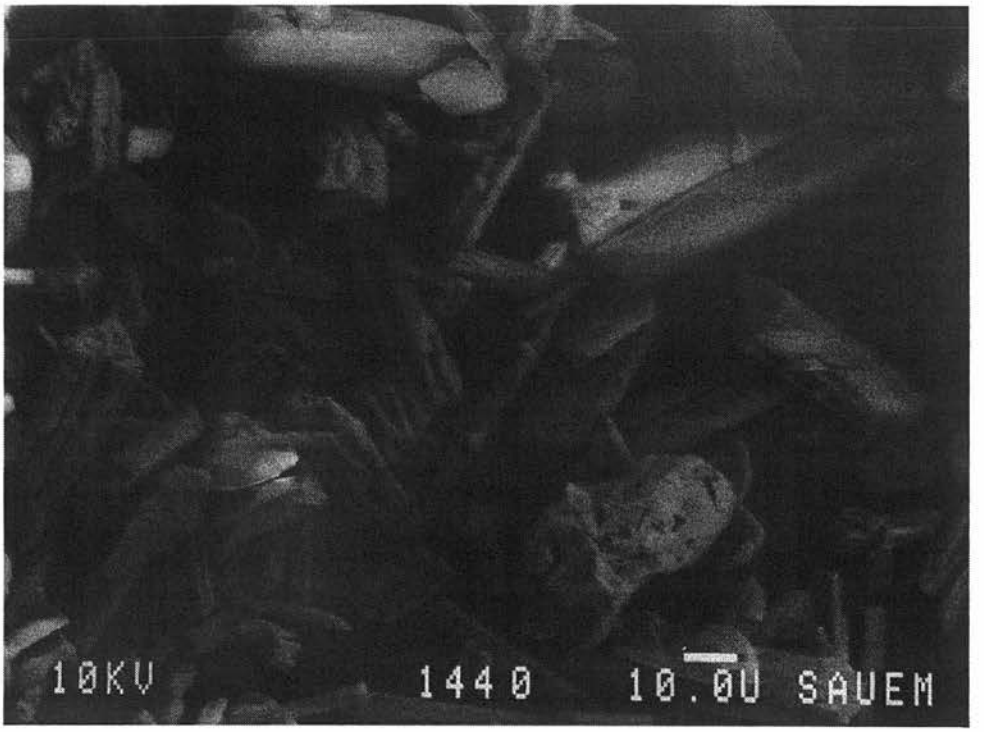

Figure 14 5% V AlMePO-β

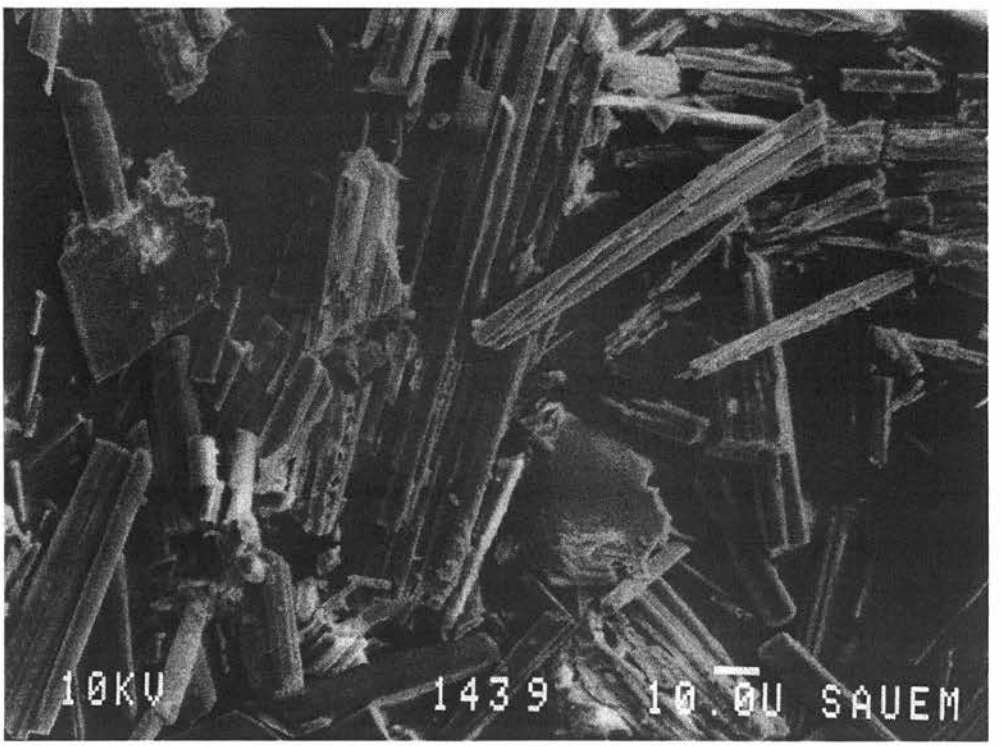

Figure 15 10% V AlMePO

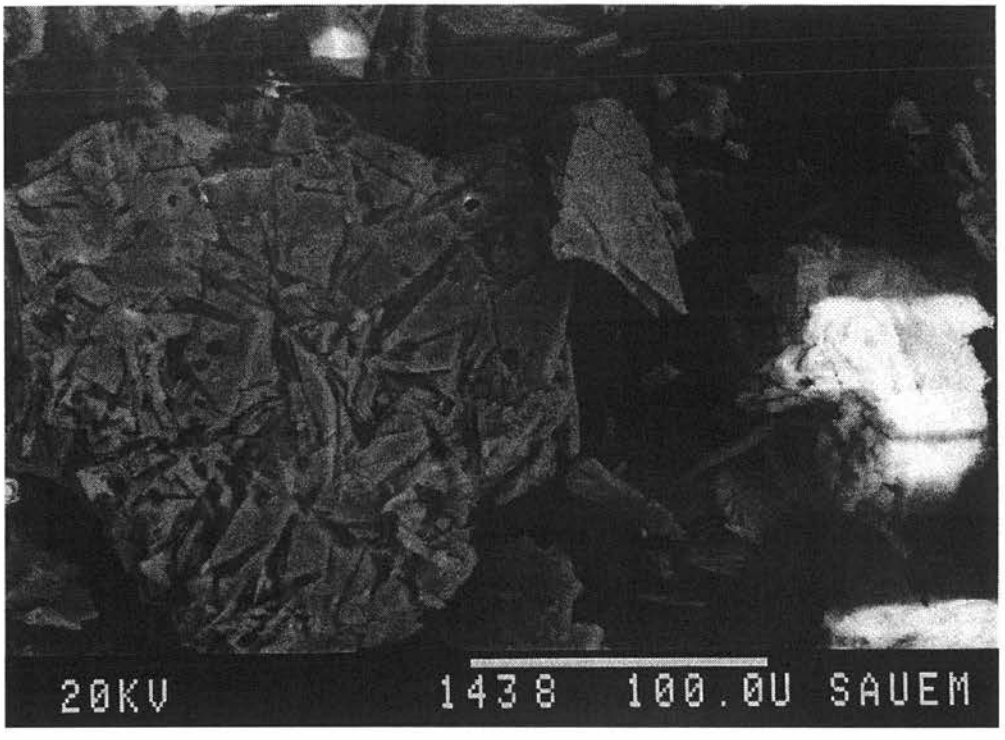

Figure 16 20% V AlMePO

Cr

Several variations were made to the synthesis procedure in an attempt to cause the incorporation of the chromium into the framework of AlMePO-β. Although the composition of the gels was kept constant, apart from variations in the amount of chromium added, three durations of heating were used, 1, 2 and 7 days. The normal period of heating, 2 days, gave pure samples of AlMePO-β (Figure 17) in some preparations, but others were of varying purity. The 1 day preparation gave a sample of very pure AlMePO-α from XRD. The EDX results are consistent with the incorporation of chromium into the structure. The electron micrograph (Figure 19), however, shows a sample that is not entirely 'clean' in the sense that there appears to be excess material that could be amorphous impurities. In such a case the exact location of the chromium detected is uncertain. The 6 day heated samples consistently gave almost phase-pure AlMePO-β (Figure 18) of a uniform green colour at low loadings (5%), the only impurity being a small amount of AlMePO-1 (peak at 11.76°). Thus, it was this procedure that was adopted for the preparation of future samples of CrAlMePO-β for further characterisation. As with other methods of preparation loadings > 5% gave samples of mixed phases and at 20% inhibited crystallisation to such an extent that the sample was almost entirely amorphous.

Table 4 EDX results for various samples substituted with chromium

Sample	Ratio (Al:P:Cr)
5% 6 day	1:1.85:0.05
5% 1 day (bulk)	1:1.52:0.02
5% 1 day (single crystal)	1:-:0.03

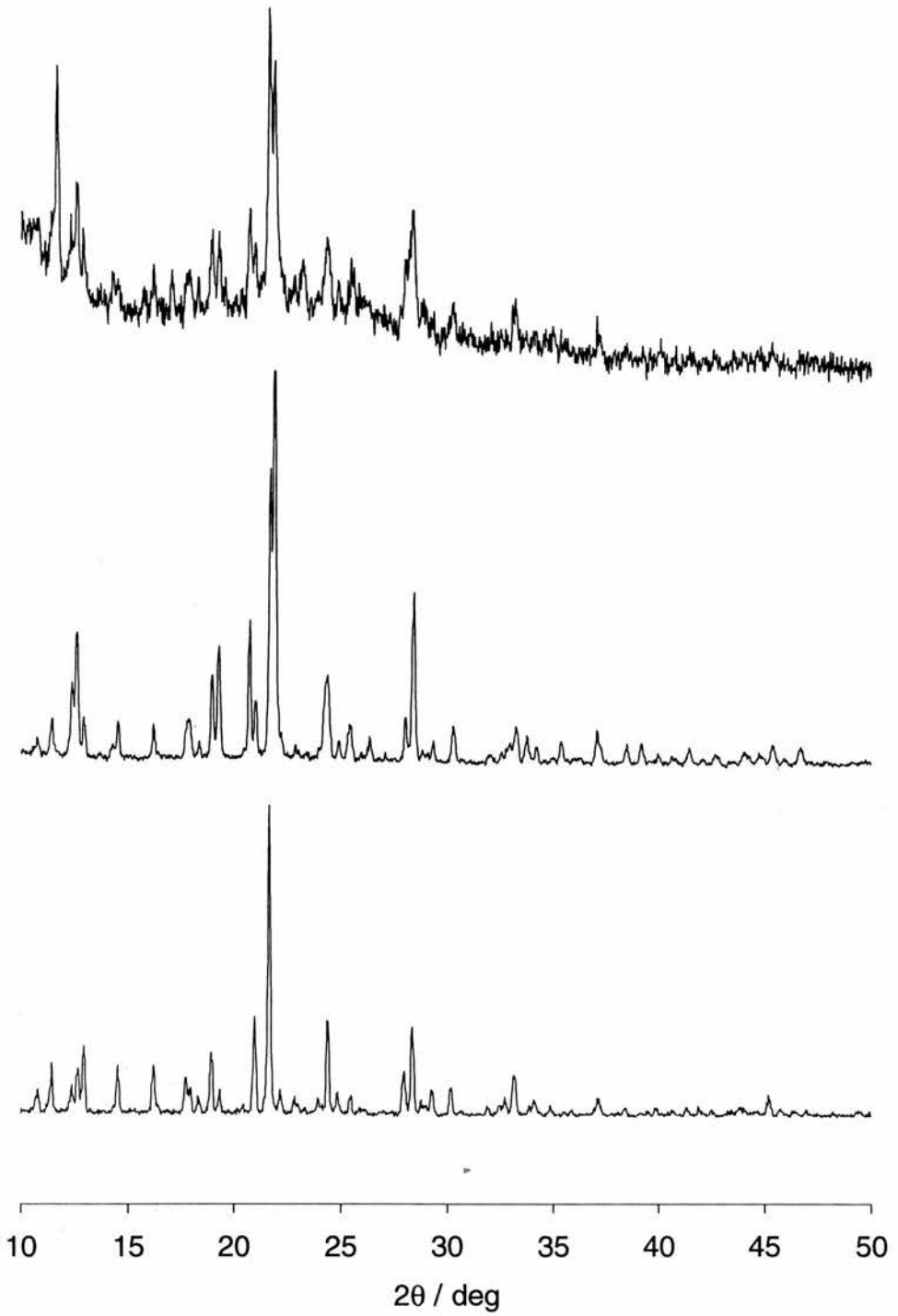

Figure 17 Comparison of XRDs for samples heated for 2 days with that of a sample of phase-pure unsubstituted AlMePO-β

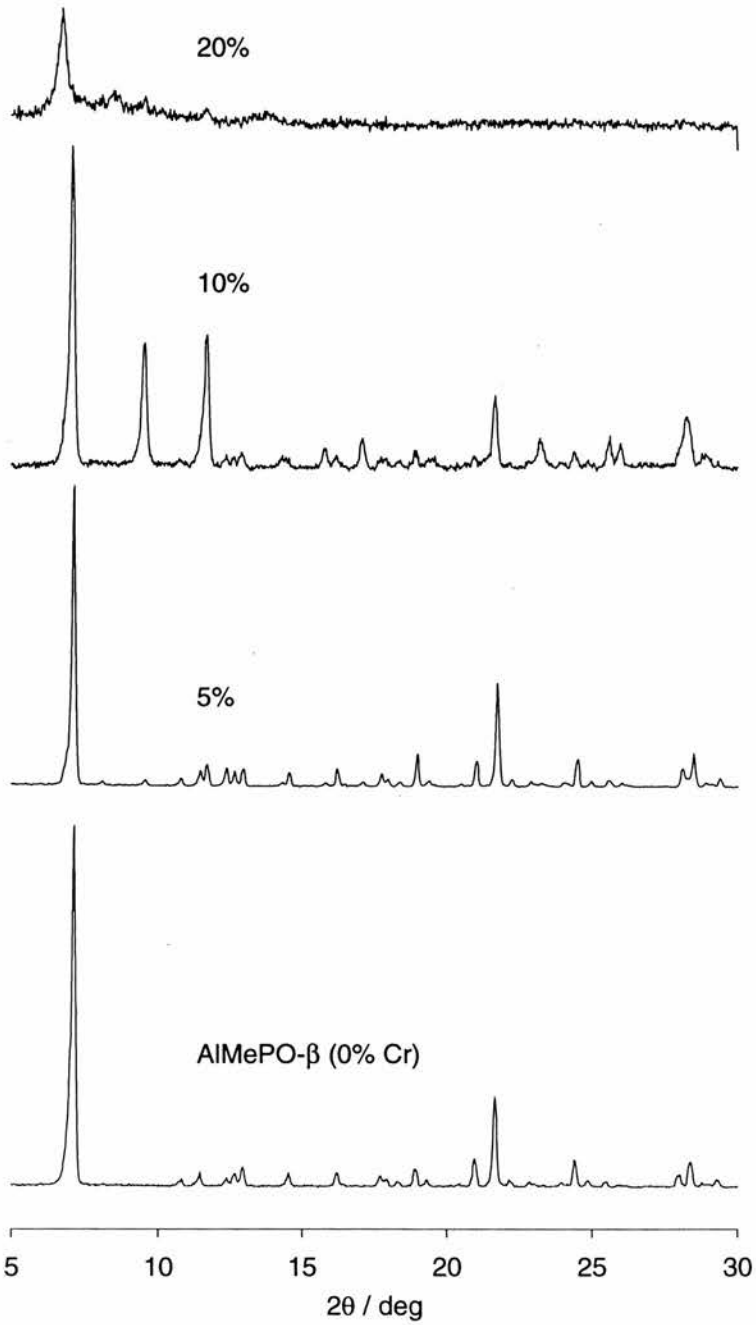

Figure 18 Comparison of XRDs for different Cr compositions heated for 6 days

Scanning electron microscopy of the 5% sample (6 days) reveals small crystals (~10-20 Å in length) whose morphology is indefinite but little resembling needles. If one looks extremely closely however, it is possible to see structures that appear to be the ends of bundles of needles.

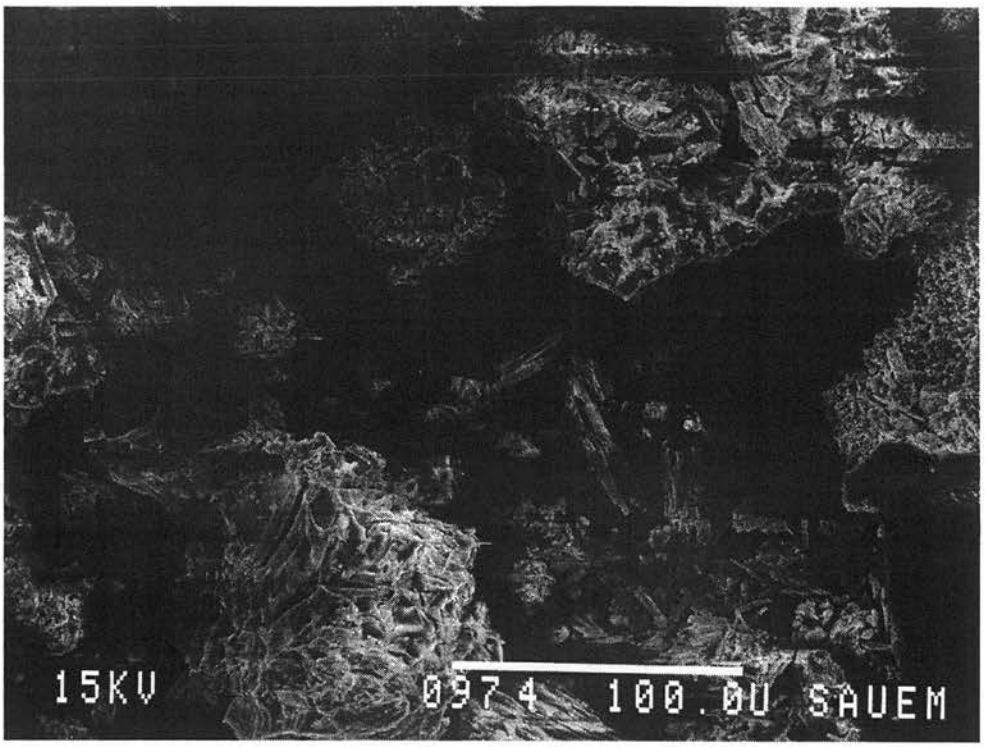

Figure 19 5% Cr AlMePO-α (1 day)

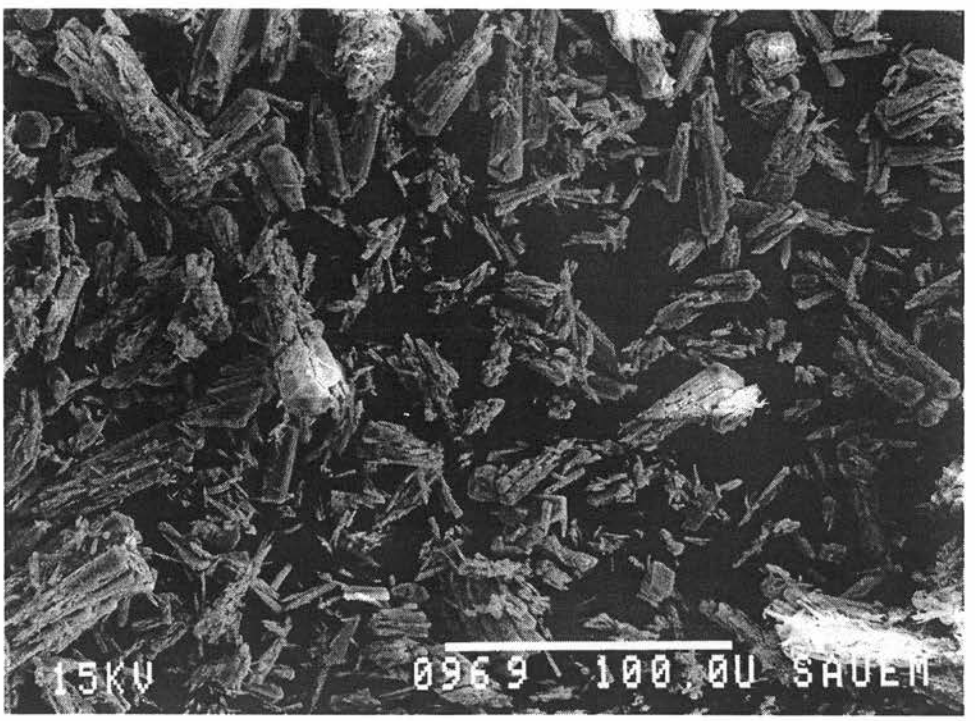

Figure 20 5% Cr AlMePO-β (6 days)

Ti

At 5% loading of the synthesis gel with titanium ions, XRD (Figure 21) shows almost phase-pure AlMePO-β except for a small amount of AlMePO-1 (peak at $2\theta = 11.74°$).

In the 10% sample the impurity peak has increased in size. The 20% sample shows a loss of crystallinity and the impurity is no longer visible. The EDX of the samples indicated no titanium incorporation into the 5% sample but substantial amounts in the 10% sample. Although the latter solid was not phase-pure, the EDX measurement was made upon the larger, striated particles within the sample (Figure 23). It is likely that these particles are made up of many needle-like AlMePO-β crystals grown together, causing the striation effect. The other particles observed in the micrograph are numerous enough to account for all the impurity material. The lack of a well defined shape for this latter phase is inconsistent with them being AlMePO-β which infrequently crystallises in other than a needle-like morphology.

Although the impurity content of the sample increases with increasing titanium loading of the gel, the 5% sample, which shows no Ti by EDX, shows a considerable amount of this material. This would lead to the conclusion that the titanium is not located in the impurity. However, it should be noted that after catalysis experiments a yellow colour was observed on the 5% sample and in the reaction mixture. The yellow colour is due to the complex formed of titanium and peroxo- compounds indicating the presence of at least a small amount of the metal. This result shows not only that titanium was definitely present in the 5% sample but also that the EDX lower limit of detection is not at a negligible level. In addition, the issue is clouded further by the realisation that, if the impurity was a compound involving titanium, it is likely that it would appear in the 20% sample since much more of the metal is available. In view of this evidence it is uncertain whether the observed Ti was incorporated into the AlMePO-β part of the sample or the impurity.

Table 5 EDX results for various loadings of the sample with Ti^{IV}.

Sample	Ratio (Al:P:Ti)
5%	1:1.51:0
10%	1:1.69:0.11

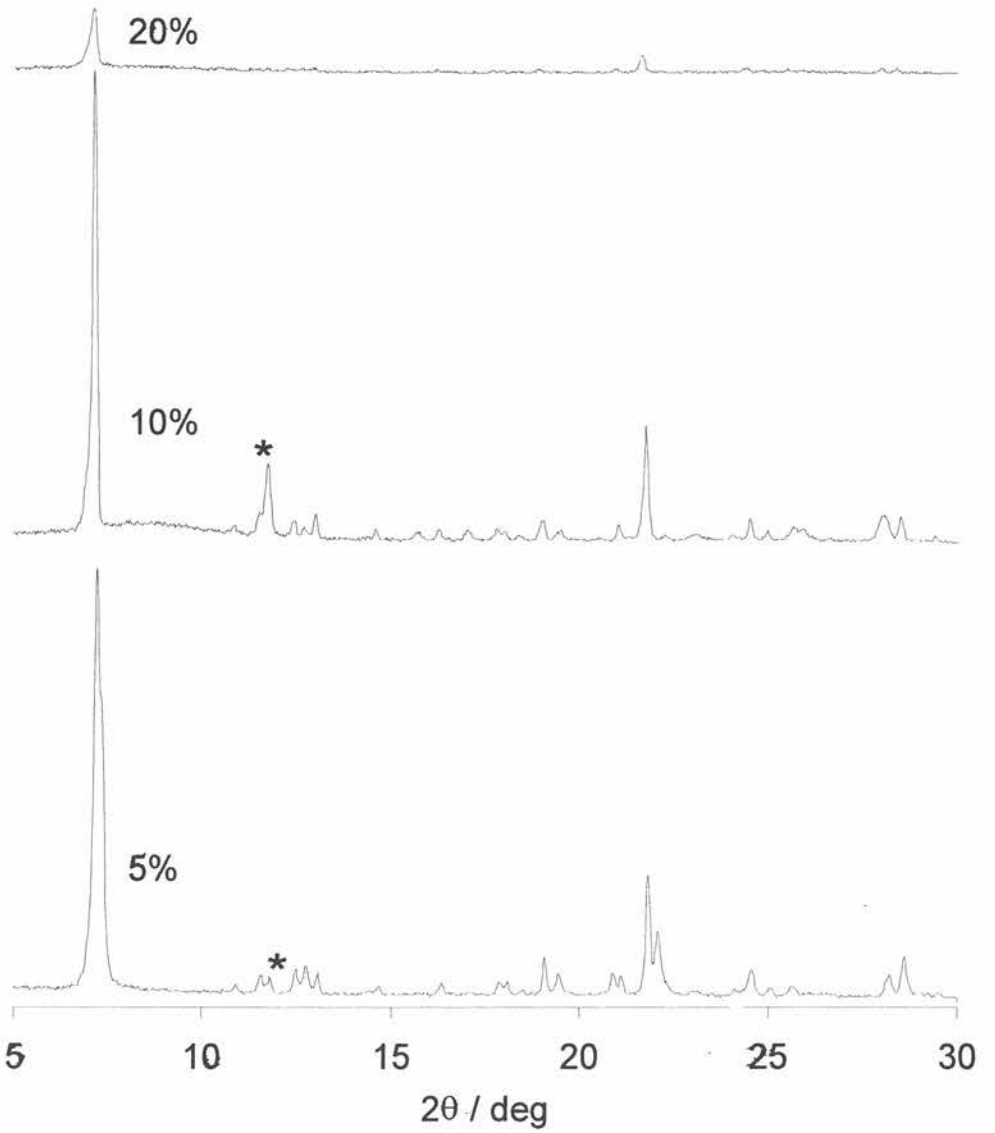

Figure 21 Comparison of XRDs for different Ti content of the synthesis gels. The asterisk marks an impurity peak.

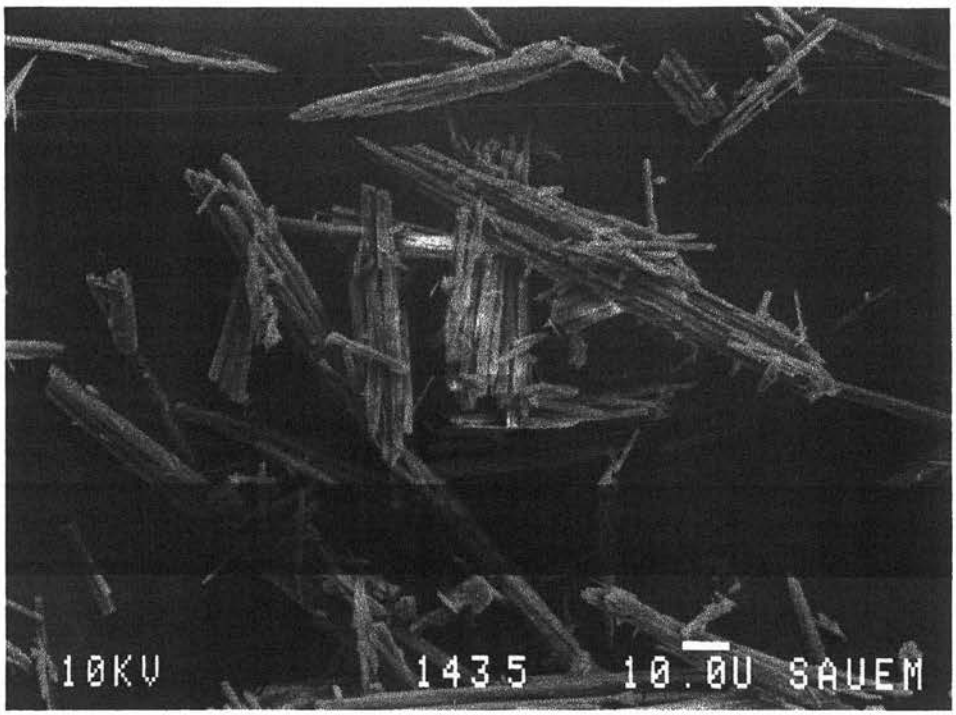

Figure 22 5% Ti AlMePO-β

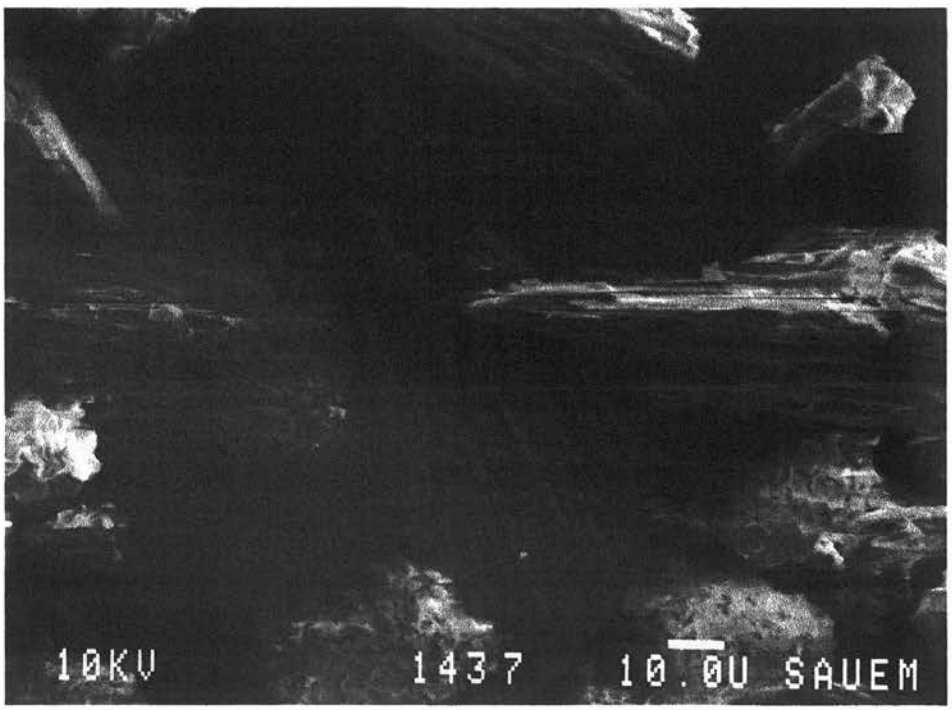

Figure 23 10% TiAlMePO-β

Catalysis

Although there is some doubt as to which metals may or may not have been substituted into the framework successfully, it was decided to perform some work investigating the catalytic activity of the samples. The aim of the work was not to produce a very detailed and accurate study of the behaviour and mechanisms of the catalysis but to answer the question as to whether the materials containing heteroatoms have any potential as catalytic materials at all. To this end, two types of experiments were performed, a liquid /solid reaction designed to test the activity in oxidation catalysis, and a heterogeneous gas/solid reaction investigating acidic properties of the materials.

Oxidation Catalysis

Many different substrates have been utilised in the study of heterogeneous oxidation catalysts and it was decided as a first step to use several with the TiAlMePO-β samples, considered to be the most likely to have activity. The substrates used were cyclohexene, cyclohexanol, 1-hexanol, 2-hexanol and 1-hexene. Samples of AlMePO-β without transition metal substitution were tested also as a control. A very small amount of activity was noted, likely to be due to the uncatalysed oxidation which is perceptible under the conditions used. This baseline activity was taken into account when calculating and reporting the conversions and standard conversions (Table 6).

It was found that there was no activity in oxidising alkenes and, of the alcohols, the cyclohexanol was the most easily transformed. Further experiments were performed with cyclohexanol as the substrate in which the reaction time and amount of catalyst sample were varied. Also, the other samples containing transition metals were tested using cyclohexanol only, not with the full range of substrates to which the titanium samples were subjected.

It is important to realise the approximate nature of the numbers reported in Table 6. No external standards were used to relate the areas of the peaks to the amounts of material causing them. The areas of the GC peaks for cyclohexanol and cyclohexanone were used without further processing to approximate the amounts of those compounds present in the reaction mixture (the GC was equipped with a flame ionisation detector (FID) whose response depends on the number and type of carbon atoms in the compound of interest – for the purpose of the FID response, cyclohexanol and cyclohexanone are almost identical). Whilst this is a valid approximation thus far, the calculation for the amount of conversion needs a measure of the total cyclohexanol present originally. This information is available only in absolute units, e.g. moles or grams, not in the relative units of peak area used in the GC analysis. Thus to approximate the total amount of cyclohexanol originally present, the total area of both the alcohol and ketone peaks are summed. This approximation has the inherent assumption that the material that has been present as cyclohexanol was not converted into any other material than the ketone. In some cases, particularly those of reused chromium and vanadium samples, the above assumption is not true as many other, albeit small, product peaks were detected.

Table 6 Summary of the oxidation catalysis test results; for each sample the molar percentage of the replacement metal in the synthesis gel and the mass of the material used in the reaction is reported.

Sample	Amount of Metal / %	Mass of sample /g	Conversion to ketone / %	Reaction time / hr	Std conversion % / g hr
Ti not finely ground	5	0.10	6.8	20	3.4
Ti finely ground	5	0.10	2.8	24	1.2
Ti finely ground	5	0.10	8.6	70	1.2
Ti finely ground	10	0.10	5.5	16	3.4
Cr	5	0.10	3.4	6.75	5.0
Cr	5	0.20	3.2	6	2.7
Cr recovered	5	0.09	27	17	17.6
V	5	0.11	17	24	6.4
V	10	0.10	8	6.75	11.9
V	10	0.15	6	6.75	6.0
V recovered	10	0.11	17	10.5	14.7

The results of the testing indicate that all of the samples do have activity in catalysing the oxidation of cyclohexanol to cyclohexanone. The amount of activity is small but definite. Strangely, there seems to be a marked increase in activity for the reused samples. However, this could be due to an artefact of the analysis. As explained above, not all the original material is converted to the ketone or remains as the alcohol – any material not represented by those GC peaks is left out of the calculation thus increasing the apparent degree of conversion observed. The reused samples usually gave product mixtures containing more compounds than the fresh catalysts.

The amount of the apparent increase in activity is so large though, that it is difficult to ascribe it all to an artefact. It is also possible that the reused samples are more active than they were at first. It was noted in the cases of chromium and vanadium that all the reaction solutions were heavily contaminated with the colour of the catalyst testing. As mentioned above, the titanium samples also caused gave a yellow solution after reaction. This leads to the conclusion that some of the metal has leached from the solid into the liquid. If leaching did take place, as seems to be the case, it is the hydrogen peroxide that is likely to be involved in removing the metal from the framework.[19] Hence, the higher activity of the reused samples could be a result of the leaching process having been started previously, making further transport from the solid to the active liquid metal species more rapid.

Acid catalysis of methanol conversion to light alkenes and dimethylether (DME)

The attempts to substitute AlMePO-β with divalent metals were motivated by the desire to produce materials containing Brønsted acid sites. As with aluminium phosphates (AlPOs), aluminium phosphonate structures such as AlMePO-β are neutral. Introducing divalent heteroatoms into the structure by replacing some of the Al^{III} species causes a charge imbalance that must be recovered through the addition of protons to Al-O-P bridging oxygens. Such additional protons act as Brønsted acids.

Although the evidence indicates that attempts to substitute magnesium and manganese into the AlMePO-β framework were unsuccessful, it does appear that zinc has been included in the structure. Such a material should have greater acidity than AlMePO-β allowing it to catalyse several types of alkene production and rearrangement reactions. Experiments were conducted to test the activity of the 10% ZnAlMePO-β sample in catalysing such a transformation. The results are compared also with those for STA-2, a MAPO with a small pore system expected to have considerable acidity due to magnesium within the structure. The reaction chosen to be the test for the catalytic

activity of the samples was the conversion of methanol to light alkenes and dimethyl ether (DME).

Table 7 Summary of the catalytic testing results for STA-2

Temperature / °C	MeOH / %	Methane / %	Ethene / %	Propene / %	Butene / %	DME / %
250	50.5	0.7	0	0.2	0	48.6
300	35.1	1.5	3.2	18.6	3.7	37.9
350	28.1	2.1	12.2	45.4	3.2	9.1
400	26.2	5.0	26.4	36.8	3.6	3
450	25.7	10.9	35.8	27.7	0	0
500	20.1	17.5	37.2	25.3	0	0

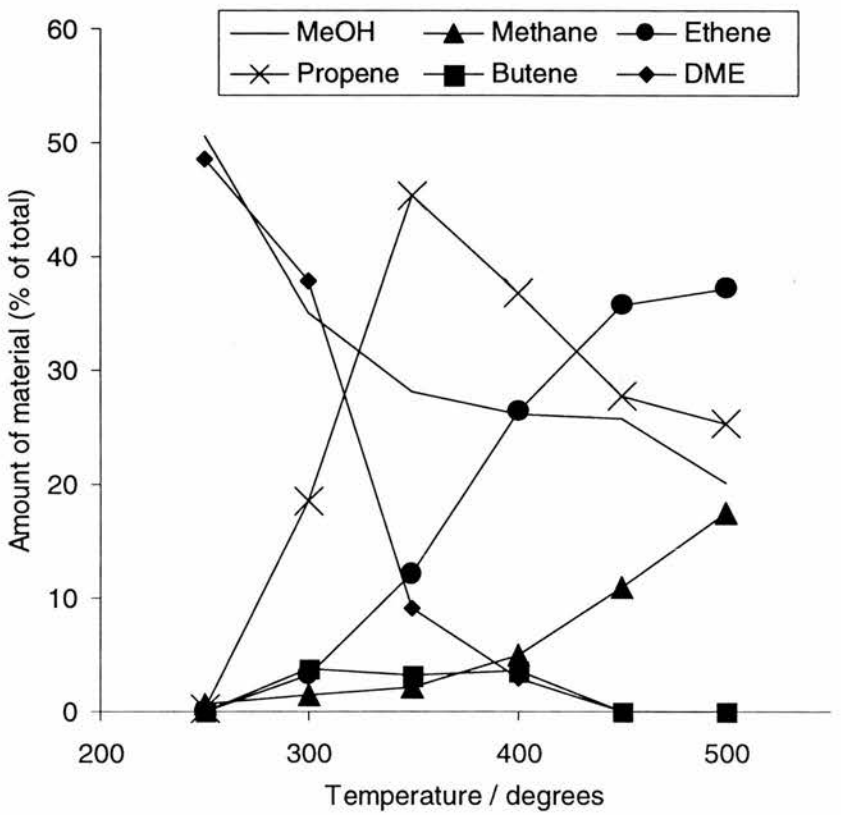

Figure 24 Plot of the catalysis results for STA-2

Table 8 Summary of the results of the catalytic testing of 10% ZnAlMePO-β

Temperature / °C	MeOH / %	Methane / %	Ethene / %	Propene / %	Butene / %	DME / %
200	100	0	0	0	0	0
250	100	0	0	0	0	0
300	100	0	0	0	0	0
350	100	0	0	0	0	0

400	100	0	0	0	0	0
450	94.6	5.4	0	0	0	0
500	58.3	17.6	15.1	9	0	0

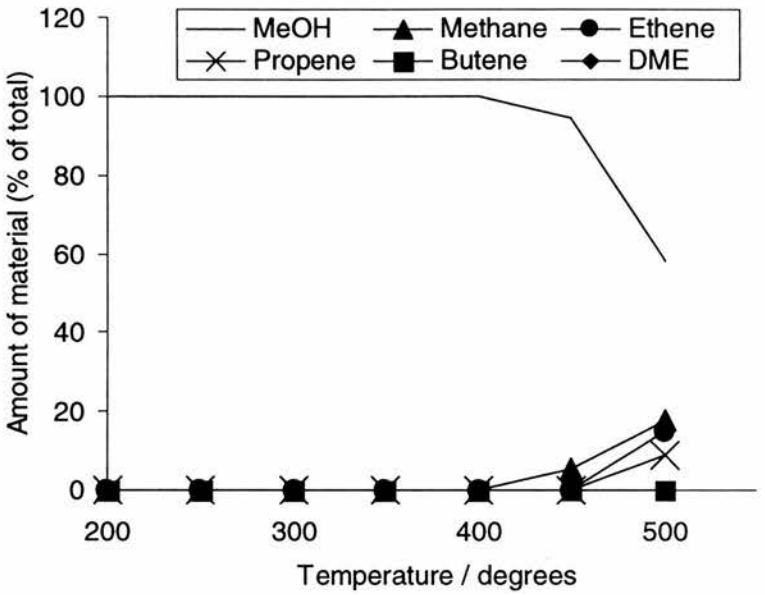

Figure 25 Plot of the catalysis results for 10% ZnAlMePO-β

The two materials, STA-2 and ZnAlMePO-β, display markedly different behaviour as catalysts. STA-2 is expected to have many Brønsted acid sites which allow it to catalyse the conversion of methanol to DME at quite low temperatures. As the results show (Figure 24), DME is the major product of the reaction in the presence of STA-2 at temperatures below 320°C. After this, the material is quite selective for propene at 350°C, the production of which drops off with temperature thereafter in favour of ethene which becomes the dominant product at 450°C. There is also an increase in methane formation at higher temperatures but this does not attain the same level as the propene.

In contrast to STA-2, the 10% ZnAlMePO-β sample catalyses no conversion to DME and the little production of light alkenes that does occur takes place at a much higher temperature. In essence, the zinc material is much less active as an acid catalyst than STA-2. Indeed, when compared with AlMePO-β containing no heteroatoms (Table 9 and Figure 26), it is clear that ZnAlMePO-β shows negligible, if any, more activity than the unmodified material. The activity of unmodified AlMePO-β is due to hydroxyl groups, the presence of which has been detected by FTIR,[25] presumably located within flaws in the structure. The very low activity noted for ZnAlMePO-β indicates that even the acid sites resulting from structural flaws are in low abundance. It follows from this that the zinc detected within AlMePO-β crystallites must be in extra-framework sites

where it causes no charge imbalance. Also, the low abundance of hydroxyl sites, indicates that the AlMePO-β which forms in the presence of Zn(II) ions is more crystalline than that normally produced.

Table 9 Results of the catalysis of methanol conversion by AlMePO-β

Temperature / °C	MeOH / %	Methane / %	Ethene / %	Propene / %	Butene / %	DME / %
200	100	0	0	0	0	0
250	100	0	0	0	0	0
300	100	0	0	0	0	0
350	100	0	0	0	0	0
400	100	0	0	0	0	0
450	86	8.8	5.3	0	0	0
500	32.7	55	10	2.3	0	0

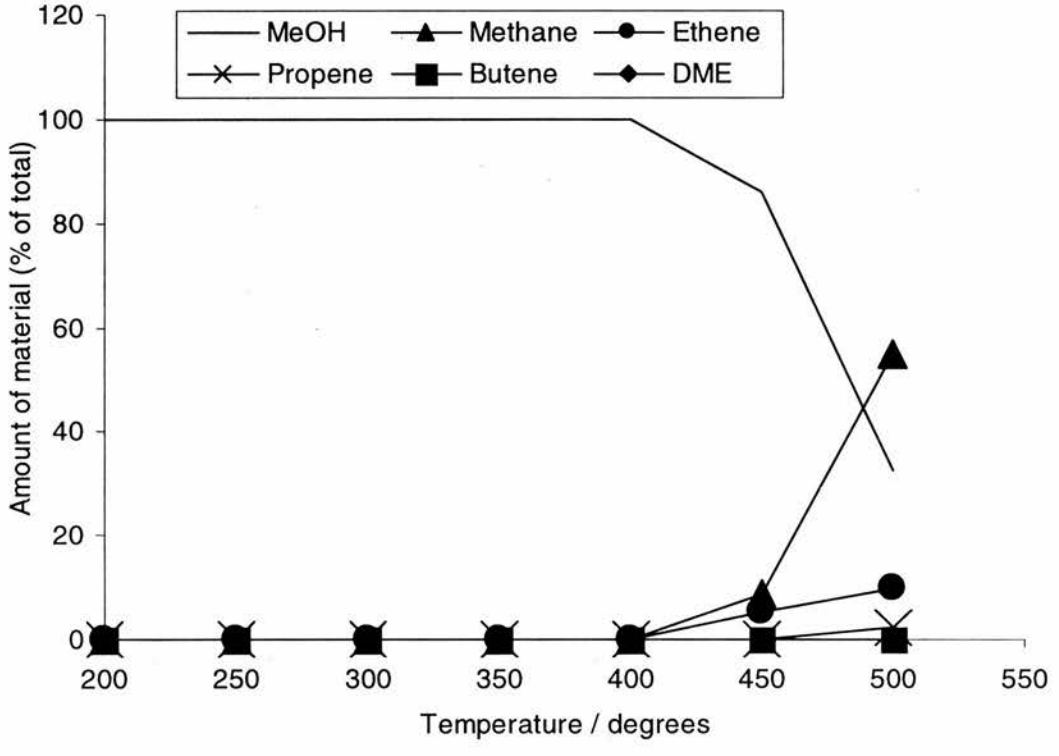

Figure 26 Results of the catalysis of methanol conversion by AlMePO-β

Summary and Conclusion

Attempts were made to prepare aluminium phosphonate molecular sieves modified by heteroatom replacement of a portion of the framework aluminium to have acid or oxidation catalytic properties. The metals used as potential replacements were Ti^{IV}, Cr^{III}, V^{IV}, Fe^{II}, Co^{II}, Zn^{II}, Mn^{II} and Mg^{II}. Preparations were performed with varying amounts of replacement metals in the synthesis gels. The lowest level of replacement always gave either AlMePO-β or AlMePO-β as the major phase. However, only the 5% Zn, 5% Mg and 5% Mn samples were free of impurities although the 5% Cr 6 day preparation, 5% Ti, 5% V and 5% Fe were only slightly contaminated. Of the 5% Zn, Mg and Mn samples, intended as possible acid catalysts, none contained any detectable level of the replacement metal. The 10% Zn sample was very slightly impure (less so than the 5% samples of the Cr, Ti, V and Fe samples) but did show the presence of the metal. Of the slightly impure 5% samples of Fe, V, Cr and Ti, only V and Cr revealed the presence of those metals. In all cases except that of the Zn mentioned the 10% samples were significantly contaminated or amorphous. The iron samples were particularly poorly crystalline at > 5% loading. As a result, even the 5% Fe sample was omitted from the catalytic testing since it was both colourless and deemed less likely to have any successful substitution in view of the effect of the metal on the synthesis.

The effect of the metal ions on the final product of crystallisation is also interesting. Generally, preparations containing 1,4-dioxane were directed strongly towards the AlMePO-β phase. However, in some cases, additions of metal ions caused the crystallisation of AlMePO-α. Particularly surprising is the case of Cr, mentioned above. Two portions of the same gel containing 5% Cr, can be made to crystallise both as the alpha and as the beta material. A heating duration of 1 day gives the alpha and of 6 days, the beta phase. Given the known great stability of alpha compared to beta, this seems strange. Despite having attempted to form a consistent hypothesis to explain these observations, there appears to be no way in which to fit them together coherently.

Preliminary testing for catalytic oxidation activity was carried out on the 5% Ti , Cr, V, and on the 10% Cr and V samples. Of the potential acid catalysts only the 10% Zn sample was tested. In the catalysis tests, the zinc sample appeared to have less activity than unmodified AlMePO-β itself. All the materials tested for oxidation activity showed a small but definite effect above that of the blank. However, in every case, these was discolouring of the reaction solution indicating the leaching of the active, replacement metal from the solid.

In conclusion, it was not possible to create magnesium or manganese substituted AlMePO-β. It appeared that it was possible to prepare a sample containing zinc but the lack of catalytic activity points to an extra framework location for the heteroatom. Indeed, the activity is so low as to indicate a more highly crystalline sample than that given by the standard synthesis. The attempted iron substitution does not seem to have worked and the crystallisation of AlMePO-β appears particularly sensitive to the presence of this ion. It was possible to produce materials containing, respectively, Ti, V, and Cr, although one cannot be certain whether the heteroatoms were located in the framework or distributed throughout the pores or on the surface. This is particularly true since, under catalysis conditions, the metals were leached from the structure into the reaction mixture. However, as it is known that transition metals are susceptible to removal from aluminium phosphate frameworks by the action of peroxide compounds, the leaching is inconclusive evidence of location.

References

1 I. Arends, R. Sheldon, M. Wallau and U. Schuchardt, *Angewandte Chemie International Edition English*, 1997, **36,** 1144-1163.

2 J. Thomas, R. Bell, P. A. Wright, *Bulletin Societe Chimique Francais*, 1994, **131**, 463-485.

3 S. Natarajan, P. A. Wright, J. Thomas, *Journal of the Chemical Society, Chemical Communications*, 1993, 1861-1863.

4 P. A. Wright, R. Jones, S. Natarajan, R. Bell, J. Chen, M. Hursthouse and J. Thomas, *ibid*, 1993, 633-635.

5 Ulf Schudardt, Heloise Pastore, Estevam Spinacé, *Studies in Surface Science and Catalysis,* 1994, **84**, 1877.

6 Carlos Cativiela, José García, José Mayoral, *Journal of Molecular Catalysis A: Chemical*, 1996, **112**, 259-267.

7 Pradeep Kumar, Rajiv Kumar, Bipin Pandey, *Synlett*, 1995, 289.

8 G. Hutchings and D. Lee, *Journal of the Chemical Society, Chemical Communications*, 1994, 1095-1096.

9 P. Wu, T. Komatsu, T. Yashima, *Journal of Physical Chemistry*, 1996, **100**, 10316-10322.

10 G. J. Kim, B. R. Cho and J. H. Kim, *Catalysis Letters*, 1993, **22**, 259-270.

11 J. Klaas, G. Schultz-Ekloff and N. Jaeger, *Journal of Physical Chemistry B*, 1997, **101**, 1305-1311.

12 H.-X. Li, M. Davis, *Journal of Physical Chemistry*, 1992, **96**, 331-334.

13 Z. Tvaruzkova and N. Zilkova, *Applied Catalysis A : General*, 1993, **103**, L1-L4.

14 T. Blasco, M. Camblor, A. Corma, P. Esteve, A. Martinez, C. Prieto and S. Valencia, *Journal of the Chemical Society, Chemical Communications*, 1996, 2367-2368.

15 R. Sheldon, J. Chen, J. Dakka and E. Neeleman, *Studies in Surface Science and Catalysis*, 1994, **83**, 407-416.

16 J. Chen, M. Haanepen, J. van Hooff, R. Sheldon, *Studies in Surface Science and Catalysis*, 1994, **84**, 973-981.

17 C. Montes, M. Davis, B. Murray, M. Narayana, *Journal of Physical Chemistry*, 1990, **94**, 6431-6435

18 D. Akolekar, *Journal of the Chemical Society, Faraday Transactions*, 1994, **90**(7), 1041-1046.18

19 H. Lempers and R. Sheldon, *6th International Symposium on the Activation of Dioxygen and Homogeneous Catalytic Oxidation, 1996, Noordwijkerhout, The Netherlands*, 244-245.

20 K. Maeda, J. Akimoto, Y. Kiyozumi and F .Mizukami, *Angewandte Chemie International Edition English*, 1994, **33**, 2335.

21 K. Maeda, J. Akimoto, Y. Kiyozumi and F. Mizukami, *Journal of the Chemical Society, Chemical Communications*, 1995, 1033.

22 K. Maeda, J. Akimoto, Y. Kiyozumi and F. Mizukami, *Angewandte Chemie International Edition English*, 1995, **34**, 1199.

23 N. Ulagappan and V. Krishnasamy, *Journal of the Chemical Society, Chemical Communications*, 1995, 373-374.

24 J. Chen, J. Thomas, P. A. Wright and R. Townsend, *Catalysis Letters*, 1994, **28**, 241-248.

25 K. Maeda, Y. Kiyozumi and F. Mizukami, *Journal of Physical Chemistry B.*, 1997, **101**, 4402-4412.

Chapter 8

Conclusions

MQMASNMR

The huge increase in resolution provided by MQMASNMR over conventional single quantum NMR techniques for quadrupolar nuclei has been made very apparent by its application to a range of aluminium phosphates and phosphonates. Three aluminium phosphate materials were investigated providing a range of challenges in obtaining resolved spectra. As prepared AlPO-31 contained seven different Al environments, many in a very narrow band of chemical shift, yet all were resolved in the 5Q spectrum. Further evidence of the advantages of this technique was given on running STA-1 and STA-2, which were magnesium doped aluminium phosphate materials. The presence of the disordered magnesium in the structure hugely broadens the resonances for phosphorus spectra which normally are used to complement the aluminium NMR in AlPOs and allow the extrapolation of the number of Al sites. Despite this, it was possible to obtain good data on the chemical shifts and other parameters of all the sites in these two materials by using MQMASNMR. Further use of this technique on a range of aluminium phosphonates continued to prove its remarkable efficacy in resolving inequivalent sites in very similar environments. Also, it was noted that the quadrupolar data also obtained from the technique were not being used to their full potential to give structural information useful to chemists. An attempt was made to correlate empirically the data obtained in this study with known structural parameters to allow future extrapolation on unknown materials. It quickly became apparent, however, that there were insufficient data for the number of variables involved. Although this is a valid and useful aim, much more data will be needed before it will be possible.

Novel Materials

Three pure new materials were synthesised during this study and attempts were made to solve their structures. *Ab initio* solution was performed very successfully on AlMePO-1 yielding a very convincing model of a layered structure. A similar process applied to AlMePO-2 gave good results but there was still doubt as to its validity, most particularly because the MQMASNMR results contradicted the presence of tetrahedral aluminium, an integral part of the model obtained. AlMePO-3 received an enormous amount of attention in an attempt to find a method of solving its structure. The direct methods approach which had yielded good results for the other two materials failed to give a good starting model for the refinement of the structure. Various other methods were used including simulated annealing and model building but to no avail. Further attempts to solve the last two

materials should concentrate on preparing crystals of good quality and of a large enough size to be used for microcrystalline diffraction at a synchotron facility.

Solid State Transformation

The solid state transformation of AlMePO-β into AlMePO-α at elevated temperatures and humidity was characterised very successfully by a combination of thermogravimetric, NMR and computer modelling techniques. It was possible to pinpoint the change taking place in the structure during the transformation and to postulate a mechanism for the process. A future step towards greater understanding of this area would be a high flux neutron diffraction study of the transformation *in situ*. Such work should enable the confirmation, modification or denial of the postulated mechanism. The original conclusion that the transformation might be a good route to AlMePO-α has been tempered by the observation that different preparations of AlMePO-β transform at different temperatures to different extents.

Neutron Diffraction Study

Very high quality data was recorded on a deuterated sample of AlMePO-β at the HRPD station at ISIS, Rutherford. The synthesis of a deuterated sample of AlMePO-β *via* the Arbutzov reaction was successful confirming this route as the preferred method to prepare alkyl phosphonic acids. Refinement of the neutron data allowed the fixing in space of the position of the methyl groups, including the deuterium atoms, for the first time. Deuterium NMR data suggested that although undergoing rapid rotation at room temperature, the methyl groups were stationary at 4.6 K, the temperature at which the diffraction data were recorded. The diffraction data supported this conclusion. Extrapolation of the shape of the cones occupied by the spinning groups revealed that there was still a substantial space over one of the aluminium atoms which was free from organic covering. This confirmed the potential of these materials to act as hosts for dispersed transition metal centres to form oxidation catalysts.

Modification of Phosphonate groups

Attempts were made to substitute the methylphosphonate groups with varying amounts of other phosphorus groups, these being, acetophosphonate, phosphonate (otherwise known as phosphite) and phosphate. In general, the microporous phases AlMePO-β and AlMePO-α were not formed at intermediate levels ($20\% < x < 66\%$) of the substituting acid in the gel.

In the case of acetophosphonate and phosphate, amorphous materials were formed from those compositions. Phosphonic acid formed a new material which appears to contain mixed phosphonates and to be able to accommodate varying ratios of these. It has not been possible to characterise this phase although attempts continue. Some success was achieved in substituting small amounts of the new phosphorus group into the microporous materials at low (<20%) loadings. However, the data that this conclusion is based upon are not totally without ambiguity.

Incorporation of Transition Metals into AlMePO-β / AlMePO-α

Attempts to incorporate divalent metals such as Mg, Mn and Zn into the structure of the above materials were unsuccessful. Although zinc did appear to have been taken into the crystalline particle, there was no evidence of it being part of the framework. Not only did the phosphorus NMR show no sign of its presence but the material had a lower catalytic activity than unmodified AlMePO-β itself. Cr, Ti and V all appeared to have isomorphously substituted for atoms within the framework but this conclusion was not totally unambiguous. Although these materials showed some oxidation activity above that expected of the pure aluminium material, it appeared that dissolved material due to leaching from the framework was the cause of this effect. As with the aluminium phosphates that Sheldon *et al*[1] decided were acting more as homogeneous than heterogeneous catalysts, so with the aluminium phosphonates. It seems that if transition metals make bonds to the oxygens attached to phosphorus, they are readily extracted in the presence of the co-oxidant material, e.g. H_2O_2, causing leaching from the framework.

Summary

The primary aim of this thesis was to work towards new catalysts for mild oxidation and solid acid activity. It appears that the aluminium phosphonates are unsuitable for a role as oxidation materials due to leaching of the active metal from the structure in the presence of the oxidant. No evidence was found that any of the attempts to introduce acid catalysis by the isomorphous replacement of aluminium was successful. There was some success in introducing organic acids into the structure in the form of phosphonates. Perhaps this area will prove more fruitful in the future in preparing solid acids from these materials. However, although it appears that catalysis is not a suitable application for aluminium phosphonates, they have all the qualities required for use in adsorption. The materials are

quite stable in non-oxidising atmospheres, particularly considering their organic component, and it is possible to control, on a small scale at least, the type of groups that line the micropores. A potential challenge confronting anyone trying to use the aluminium phosphonates in this way is the need to produce very small particles. Although, it has not been reported above, attempts were made to form small particles of AlMePO-β, all without notable success.

The work on furthering the applicability and power of the characterisation techniques available for use on microcrystalline powders was more successful than that applied towards novel catalysts. The *ab initio* technique was applied successfully on one, perhaps two, occasions (it would be interesting to measure the degree of success on AlMePO-2 with a structure obtained by more routine crystallographic methods). The MQMASNMR technique has been proven to be incredibly versatile and powerful in elucidating the state of previously inaccessible quadrupolar nuclei. As the field matures and the amount of data increases, the usefulness of this technique can only increase also. The potential for work in this area is enormous, particularly for chemists who have not, thus far, been overly involved in what is regarded still as a somewhat esoteric technique for physicists.

---

1 R. A. Sheldon and H E. B. Lempers, *The stability of chromium in chromium molecular sieves under the conditions of liquid phase oxidations with* tert-*butyl hydroperoxide*, *6th International Symposium on the Activation of Dioxygen and Homogeneous Catalytic Oxidation,* April, 1996, Noordigkerhout, The Netherlands.

Appendix I

This Appendix contains extra data from Chapter 3.

AlMePO-1

Lattice parameters

The unit cell is monoclinic with dimensions a =9.474 Å, b =7.07Å,c =7.865Å and β = 106.6°. Space group is $P2_1/a$.

Table 1 Original coordinates derived from SIRPOW run using the 2θ range 10-75°.

Atom	x	y	z
Al1	0.909	0.383	0.260
P2	0.765	0.605	0.512
O1	0.726	0.362	0.565
O2	0.836	0.355	0.050
O3	0.630	0.719	0.607

Profile parameters : U = 234(11); V = -103(7); W = 42(1)

Table 2 Final refined atomic coordinates and isotropic thermal parameters for AlMePO-1.

Atom	x	y	z	U_{iso}
Al1	0.7600(4)	0.6228(16)	0.5145(5)	0.011(1)
P1	0.9048(3)	0.3717(7)	0.2680(3)	0.010(1)
C1	0.822(1)	0.380(2)	0.031(1)	0.003(3)
O1	0.6458(7)	0.6830(10)	0.6643(9)	0.016(3)
O2	0.5641(7)	0.5990(2)	0.3138(7)	0.0060(20)
O3	0.7659(6)	0.8670(10)	0.4263(6)	0.0030(20)
O4	0.8559(6)	0.5490(10)	0.3450(8)	0.0080(30)
O5	0.9299(6)	0.6350(20)	0.7034(6)	0.0090(20)
H1	0.712(3)	0.410(15)	0.032(8)	0.025
H2	0.488(4)	0.705(5)	0.329(6)	0.025
H3	0.833(8)	0.242(4)	-0.019(8)	0.025
H4	0.868(4)	0.488(6)	-0.032(11)	0.025
H5	0.531(12)	0.495(10)	0.395(11)	0.025

AlMePO-2

Lattice parameters

The unit cell is orthorhombic with dimensions : a=19.733 Å, b = 10.154 Å, c = 5.148 Å, volume = 1031 $Å^3$. Space group is *Pmnb*.

Table 3 First five most intense peaks output from SIRPOW using the 10-80° range of data for AlMePO-2

Atom	x	y	z
Al1	0.679	0.403	0.718
P2	0.618	0.525	1.236
O3	0.75	0.637	1.563
O4	0.622	0.435	1.016
O5	0.680	0.621	1.297

Table 4 Final atom parameters for AlMePO-2.

Atom	x	y	z	Frac	UISO
Al1	0.6796(2)	0.3960(1)	0.7355(1)	1	0.015(1)
Al2	0.2500(0)	-0.1644(10)	0.4581(18)	1	0.044(1)
P1	0.6241(2)	0.5325(5)	1.2234(11)	1	0.021(1)
O1	0.6226(5)	0.4329(10)	0.9907(21)	1	0.016(3)
O2	0.2500(0)	0.1656(21)	0.5691(30)	0.72	0.010(3)
O3	0.6218(5)	0.4528(10)	1.4796(20)	1	0.008(3)
O4	0.2500(0)	0.0021(13)	0.3358(27)	1	0.009(2)
O5	0.8187(4)	0.2179(8)	0.7645(24)	1	0.007(3)
O6	0.6867(4)	0.1270(9)	0.2762(24)	1	0.014(2)
C1	0.5433(6)	0.6066(14)	1.2130(4)	1	0.058(3)
H1	0.506(6)	0.403(5)	0.700(11)	1	0.025
H2	0.461(7)	0.353(15)	0.978(13)	1	0.025
H3	0.425(9)	0.332(4)	0.669(20)	1	0.025

AlMePO-3

Lattice parameters

The unit cell is triclinic with dimensions, a = 9.644 Å, b = 12.374 Å, c = 5.063 Å, α = 91.14°, β = 90.36°, γ = 92.13°, volume = 604 Å^3. The space group is $P\bar{1}$.

Direct Methods

Table 5 The six most intense peaks obtained from repeated cycling of EXPO until the most chemically sensible model was obtained.

Atom	Height	x	y	z
P1	1633	0.344	0.406	-0.021
P2	1573	0.236	0.093	0.512
P3	1432	0.492	0.300	0.433
Al4	1110	0.429	0.164	0.432
Al5	914	0.190	0.344	0.012
O1	906	0.249	0.074	0.829

Simulated Annealing

Table 6 Atom coordinates for the model obtained from the first Simulated Annealing attempt.

Atom	x	y	z
Al1	0.52820	0.48460	0.72800
Al2	0.28140	0.37220	0.00400
P3	0.81260	0.43870	0.66000
O4	0.85640	0.57170	0.55800
C5	0.89300	0.35700	0.49200
O6	0.65560	0.41600	0.62200
O7	0.85150	0.42720	0.95300
P8	0.61190	0.82330	0.42500
O9	0.63800	0.68860	0.31900
C10	0.75100	0.88900	0.42100
O11	0.55400	0.82300	0.70800
O12	0.50800	0.87490	0.23900
P13	0.32660	0.86960	0.08600
O14	0.47100	0.93040	-0.07700
C15	0.22000	0.95600	0.14900
O16	0.37540	0.81930	0.34400
O17	0.25900	0.78070	-0.09500

Table 7 Atom coordinates for the model obtained from the second Simulated Annealing attempt.

Atom	x	y	z
Al1	0.14770	0.22490	0.62120
Al2	0.58060	0.15300	0.99900
P1	0.70460	0.47020	0.65660
O1	0.60160	0.51110	0.90600
O2	0.72550	0.34760	0.64860
O3	0.84660	0.53110	0.65110
C1	0.63120	0.49620	0.37570
P2	0.60470	0.69140	0.49620
O4	0.76850	0.76080	0.26870
O5	0.50760	0.75140	0.06780
O6	0.54150	0.68700	0.53090
C2	0.62250	0.57560	0.14510
P3	0.25740	0.99930	0.31500
O7	0.08840	1.02660	0.20270
O8	0.33580	1.10600	0.38850
O9	0.33580	0.94030	0.09450
C3	0.24756	0.92740	0.55960

Modelling Approach

Table 8 Original atom coordinates from the model structure stacking along the *b* axis

Atom	x	y	z
Al4	0.34000	0.83000	0.00000
Al5	0.90000	0.72220	0.50000
P1	0.65000	0.77778	0.00000
O1	0.75700	0.77778	0.25000
O2	0.75700	0.77778	0.75000
O3	0.49600	0.80600	0.00000
C1	0.70000	0.89000	0.00000
P2	0.05000	0.61110	0.00000
O4	0.97500	0.66667	0.75000
O5	0.97500	0.66667	0.25000
O6	0.19500	0.72222	0.00000
C2	0.10000	0.55000	0.00000
P3	0.10000	0.88889	0.50000
O7	0.22000	0.86100	0.75000
O8	0.22000	0.86100	0.75000
O9	0.00000	0.80600	0.50000
C3	0.12000	0.98000	0.50000

Table 9 Fully refined without constraints atom coordinates from the model structure stacking along the *b* axis

Atom	x	y	z
Al4	0.32360	0.81910	0.03300
Al5	0.99170	0.74400	0.49600
P1	0.67160	0.79510	-0.01100
O1	0.87000	0.84190	0.18100
O2	0.72000	0.63790	0.72700
O3	0.49700	0.82120	-0.10500
C1	0.89900	0.92500	-0.09800
P2	0.16940	0.53260	-0.04700
O4	1.03700	0.64890	0.55000
O5	1.09000	0.58800	0.08600
O6	0.19500	0.63600	0.02400
C2	0.20200	0.47700	0.15500
P3	0.17100	0.85420	0.55700
O7	0.38600	0.94550	0.69400
O8	0.30800	0.90850	0.34500
O9	-0.02800	0.84610	0.63100
C3	0.25200	0.97300	0.56400

Table 10 Original atom coordinates for polymorph a.

Atom	x	y	z
Al4	0.55000	0.41000	0.26300
Al5	0.56600	0.12000	0.74400
P1	0.72500	0.01000	0.26300
O1	0.65000	0.05500	0.50000
O2	0.65000	0.05500	0.00000
O3	0.58000	-0.06500	0.25900
C1	0.89500	0.01000	0.26300
P2	0.40000	0.20600	0.26300
O4	0.48300	0.16300	0.50000
O5	0.48300	0.16300	0.00000
O6	0.47500	0.30800	0.26300
C2	0.23000	0.20600	0.26300
P3	0.30200	0.54600	0.26300
O7	0.42600	0.47800	0.26300
O8	0.37600	0.56800	0.50000
O9	0.37600	0.56800	0.00000
C3	0.13000	0.54600	0.26300

Table 11 Fully refined atom coordinates for polymorph a.

Atom	x	y	z
Al4	0.44078	0.34110	0.16460
Al5	0.57100	0.17032	0.73410
P1	0.73275	0.02808	0.23390
O1	0.87748	0.13672	0.34872
O2	0.63023	0.07247	-0.25346
O3	0.52437	-0.11068	0.33986
C1	0.95725	0.06351	0.35401
P2	0.17994	0.17720	0.34130
O4	0.46316	0.23720	0.42700
O5	0.46050	0.20970	0.10170
O6	0.24620	0.21350	0.16000
C2	0.04511	0.14530	0.39930
P3	0.34580	0.56910	0.21337
O7	0.39290	0.43578	0.40960
O8	0.31860	0.54190	0.60910
O9	0.44440	0.52600	-0.22160
C3	0.01761	0.62760	0.10000

Table 12 Original atom coordinates for polymorph b.

Atom	x	y	z
Al4	0.41000	0.41000	0.26300
Al5	0.56600	0.12000	0.74400
P1	0.72500	0.01000	0.26300
O1	0.65000	0.05500	0.50000
O2	0.65000	0.05500	0.00000
O3	0.58000	-0.06500	0.25900
C1	0.89500	0.01000	0.26300
P2	0.40000	0.20600	0.26300
O4	0.48300	0.16300	0.50000
O5	0.48300	0.16300	0.00000
O6	0.40000	0.30800	0.26300
C2	0.23000	0.20600	0.26300
P3	0.35100	0.49100	0.74400
O7	0.38100	0.45100	0.50000
O8	0.38100	0.45100	0.00000
O9	0.47100	0.54100	0.74100
C3	0.18000	0.49100	0.74400

Table 13 Fully refined atoms coordinates for polymorph b

Atom	x	y	z
Al4	0.32180	0.28440	0.23190
Al5	0.47220	0.10900	0.55960
P1	0.83650	0.11070	0.34440
O1	0.86860	-0.01770	0.09250
O2	0.45800	0.04430	-0.21680
O3	0.86520	-0.03500	0.37860
C1	1.09400	0.29970	0.67910
P2	0.36680	0.20210	0.18510
O4	0.64380	0.20630	0.60080
O5	0.37030	0.15560	-0.20860
O6	0.54560	0.19970	0.34610
C2	0.09880	0.24170	0.18860
P3	0.30300	0.48710	0.68020
O7	0.53950	0.36170	0.23320
O8	0.53800	0.47410	-0.28340
O9	0.42820	0.51730	0.90760
C3	0.12490	0.48440	0.75100

Table 14 Original atom coordinates from polymorph c

Atom	x	y	z
Al4	0.64000	0.40000	0.73900
Al5	0.74100	0.06500	0.26100
P1	0.35400	0.06500	0.26100
O1	0.54900	0.06500	0.26100
O2	0.30650	0.00000	0.50000
O3	0.30650	0.00000	0.00000
C1	0.27000	0.20000	0.26100
P2	0.80200	0.16200	0.73900
O4	0.73600	0.28100	0.73900
O5	0.77200	0.11350	0.50000
O6	0.77200	0.11350	0.00000
C2	0.97200	0.16200	0.73900
P3	0.29700	0.50000	0.73900
O7	0.48000	0.45000	0.73900
O8	0.31400	0.55000	0.00000
O9	0.31400	0.55000	0.50000
C3	0.20000	0.40000	0.73900

Table 15 Fully refined coordinates from polymorph c.

Atom	x	y	z
Al4	0.85270	0.39070	1.02800
Al5	0.66500	0.16510	0.47400
P1	0.40740	0.16890	0.06500
O1	0.44200	0.08640	-0.15600
O2	0.49800	-0.07590	0.55600
O3	0.20450	0.01680	-0.21900
C1	0.29300	0.28500	0.32100
P2	0.77610	0.12890	0.51700
O4	0.66800	0.17500	0.78100
O5	0.57200	-0.16250	0.64600
O6	0.77650	0.30310	-0.37700
C2	1.05800	0.01600	0.43400
P3	0.36940	0.48060	0.52660
O7	0.62490	0.35510	1.03700
O8	0.17240	0.50330	0.19900
O9	0.50700	0.58000	0.99300
C3	0.19600	0.25100	0.33300

Table 16 Original atom coordinates for polymorph d. It was not possible to refine this structure.

Atom	x	y	z
Al4	0.51000	0.33200	0.73900
Al5	0.74100	0.06500	0.26100
P1	0.35400	0.06500	0.26100
O1	0.54900	0.06500	0.26100
O2	0.30650	0.00000	0.50000
O3	0.30650	0.00000	0.00000
C1	0.27000	0.20000	0.26100
P2	0.80200	0.16200	0.73900
O4	0.77200	0.11350	0.00000
O5	0.77200	0.11350	0.50000
O6	0.65600	0.24700	0.73900
C2	0.97200	0.16200	0.73900
P3	0.35800	0.42000	0.26100
O7	0.43400	0.37600	0.50000
O8	0.43400	0.37600	0.00000
O9	0.42400	0.54400	0.26100
C3	0.20000	0.40000	0.26100

Appendix II

This Apppendix contains supplementary material for Chapter 4.

Matrices for the transformation of P31c description of AlMePO-α to the R3c description.

$$\begin{pmatrix} a' \\ b' \\ c' \end{pmatrix} = \begin{pmatrix} 1 & \bar{1} & 0 \\ 1 & 2 & 0 \\ 0 & 0 & 3 \end{pmatrix} \cdot \begin{pmatrix} a \\ b \\ c \end{pmatrix}$$

$$\begin{pmatrix} x' \\ y' \\ z' \end{pmatrix} = \begin{pmatrix} 2/3 & -1/3 & 0 \\ 1/3 & 1/3 & 0 \\ 0 & 0 & 1/3 \end{pmatrix} \cdot \begin{pmatrix} x \\ y \\ z \end{pmatrix}$$

Table 1 Atomic Coordinates for AlMePO-β

Atom	x	y	z
Al1	0.33660	0.33850	0.47050
Al2	0.47740	0.42860	0.33690
Al3	0.24380	0.37220	0.32600
Al4	0.42230	0.48220	0.60440
P1	0.40580	0.29830	0.38470
P2	0.20490	0.26540	0.40690
P3	0.37220	0.45000	0.38750
P4	0.29360	0.40660	0.55550
P5	0.47120	0.40940	0.53170
P6	0.27580	0.21140	0.53810
O1	0.35550	0.30970	0.40680
O2	0.25360	0.30510	0.44610
O3	0.35660	0.41590	0.43890
O4	0.31100	0.36150	0.53310
O5	0.42070	0.37550	0.49260
O6	0.31790	0.26370	0.50290
O7	0.46330	0.36000	0.36660
O8	0.43130	0.45730	0.36220
O9	0.24880	0.37730	0.60260
O10	0.26020	0.14950	0.51490
O11	0.21020	0.29840	0.35550
O12	0.31920	0.42190	0.34860
O13	0.53270	0.45920	0.50520
O14	0.30640	0.21710	0.59240
O15	0.38050	0.25360	0.33690
O16	0.13930	0.24390	0.43090
O17	0.35150	0.46650	0.57480
O18	0.45440	0.44210	0.57510
C1	0.43130	0.26140	0.43030
C2	0.20670	0.19660	0.39220
C3	0.39080	0.52930	0.40150
C4	0.25430	0.42750	0.50870
C5	0.48930	0.35730	0.56530
C6	0.20390	0.20920	0.55050

Table 2 Atomic coordinates of AlMePO-α (Unconventional Description R3c)

Atom	x	y	z
Al1	0.333367	0.333333	0.163267
Al2	0.297300	0.197300	0.019600
Al3	0.566667	0.036033	0.019600
Al4	0.233333	0.369367	0.019600
P1	0.220050	0.250380	0.077133
P2	0.363663	0.446617	0.077133
P3	0.416287	0.303003	0.077133
P4	0.127810	0.389910	0.066567
P5	0.461143	0.056577	0.066567
P6	0.276757	0.071233	0.066567
O1	0.262367	0.278633	0.122933
O2	0.349600	0.404300	0.122933
O3	0.388033	0.317067	0.122933
O4	0.068667	0.346633	0.039067
O5	0.402000	0.013300	0.039067
O6	0.320033	0.055367	0.039067
O7	0.244567	0.221633	0.038033
O8	0.371067	0.241633	0.047900
O9	0.128967	0.361533	0.120233
O10	0.266500	0.118600	0.035933
O11	0.425033	0.462767	0.047900
O12	0.185433	0.400167	0.035933
O13	0.518767	0.066833	0.035933
O14	0.305133	0.100767	0.120233
O15	0.203900	0.295600	0.047900
O16	0.310400	0.422100	0.038033
O17	0.643733	0.088767	0.038033
O18	0.462300	0.028200	0.120233
C1	0.468967	0.132633	0.076833
C11	0.135633	0.465967	0.076833
C31	0.200700	0.003000	0.076833
C2	0.377867	0.521733	0.099967
C12	0.144933	0.189467	0.099967
C22	0.477200	0.288800	0.099967

Table 3 Atomic Coordinates for AlMePO-a, conventional (P31c) description

Atom	x	y	z
Al1	0.66670	0.33330	0.48980
Al2	0.60270	0.50540	0.5880
P1	0.65201	0.51772	0.69970
P2	0.81028	0.52957	0.23140
O1	0.62460	0.41530	0.61720
O2	0.61490	0.58560	0.60780
O3	0.59410	0.49050	0.86070
O4	0.75390	0.45900	0.36880
O5	0.88780	0.50050	0.14370
O6	0.73250	0.53380	0.11410
C1	0.79630	0.60160	0.73050
C2	0.89960	0.66560	0.29990

Table 4 **Approximate shifts of Aluminium and Phosphorus atoms on transformation from AlMePO-β to AlMePO-α.**

Atom	Shift / Å
Al1	0.00
Al2	0.39
Al3	0.23
Al4	2.47
P1	0.22
P2	0.88
P3	0.21
P4	0.78
P5	0.29
P6	0.16

Appendix III

This Appendix contains supplementary data from Chapter 5.

Raw neutron diffraction data from the HRPD station at ISIS, the Rutherford Appleton Laboratory, on a sample of deuterated, dried AlMePO-β, at 4.62 K.

There follow the four diffraction patterns collected from Rutherford with reflection markers for the cell. The data were collected from two time windows, 30-130 ms and 100-200 ms, with two banks of detectors, one at 90° and the other at 168° of 2θ.

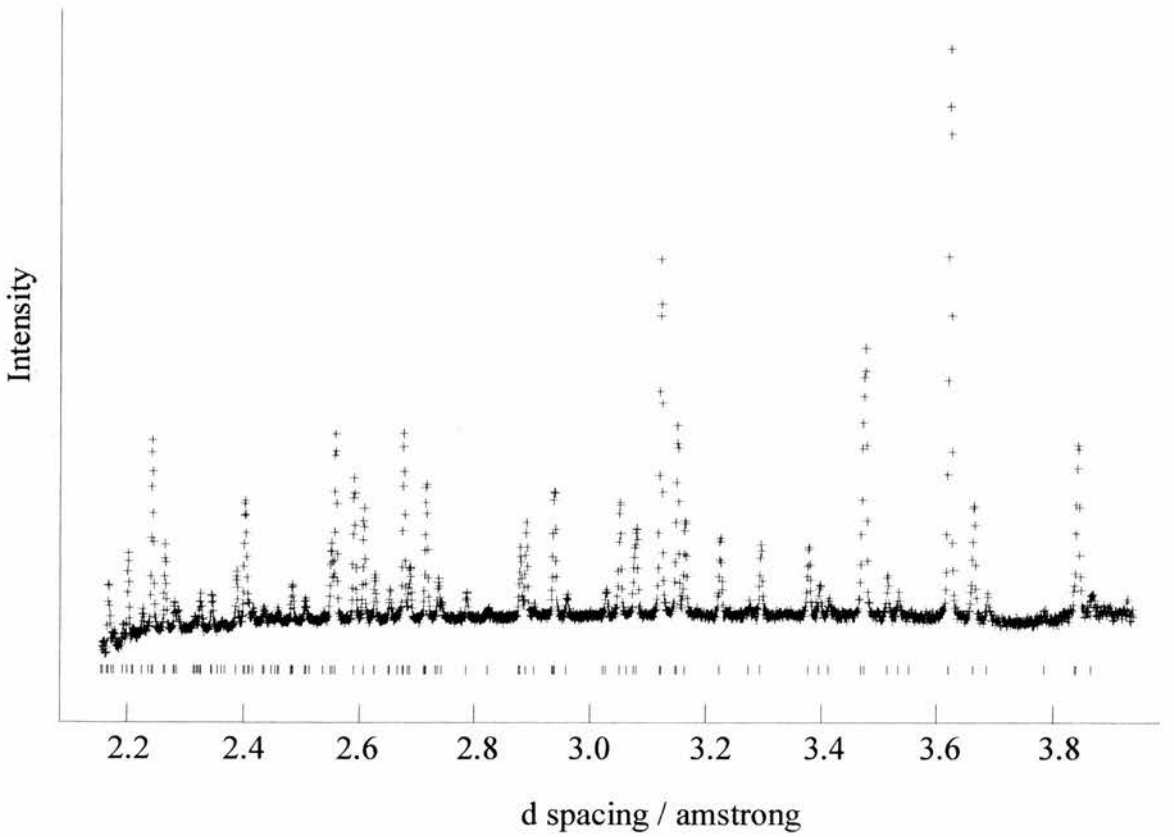

Figure 1 The 30-130 ms data set from the 168° detector bank.

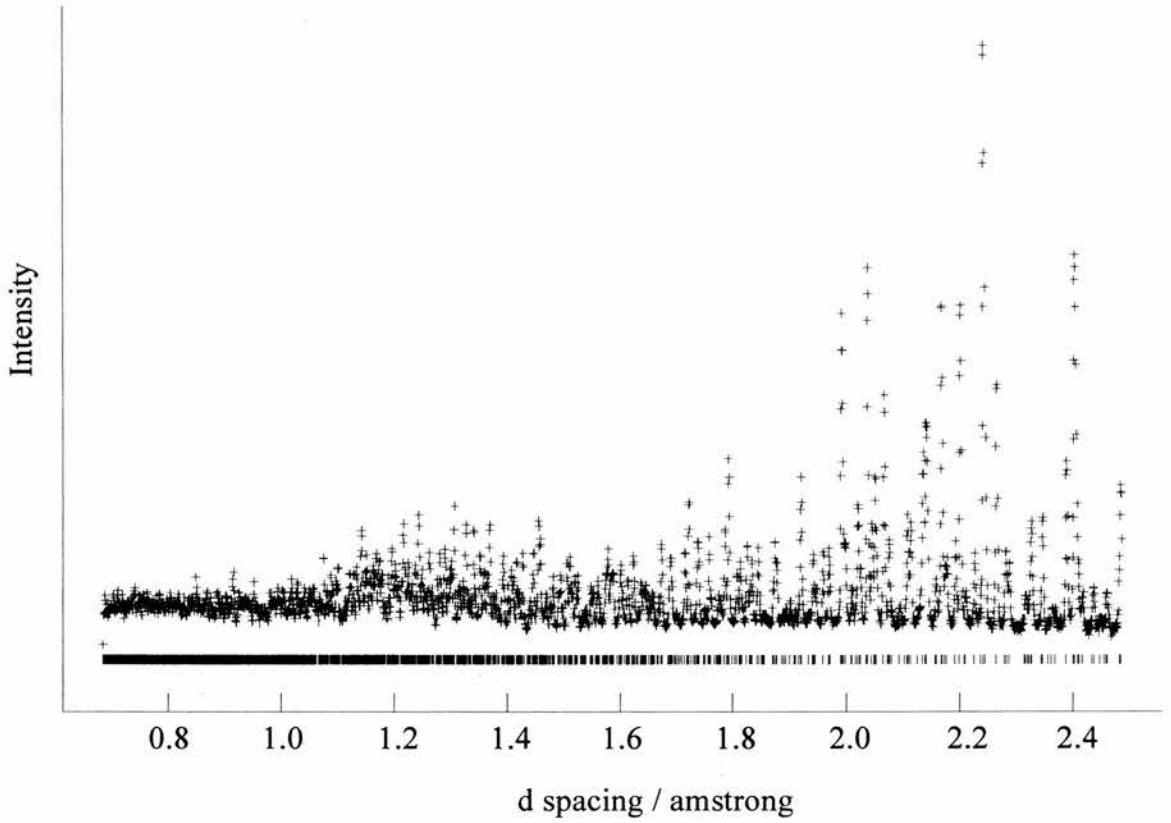

Figure 2 100-200 ms data set from the 168° detector bank.

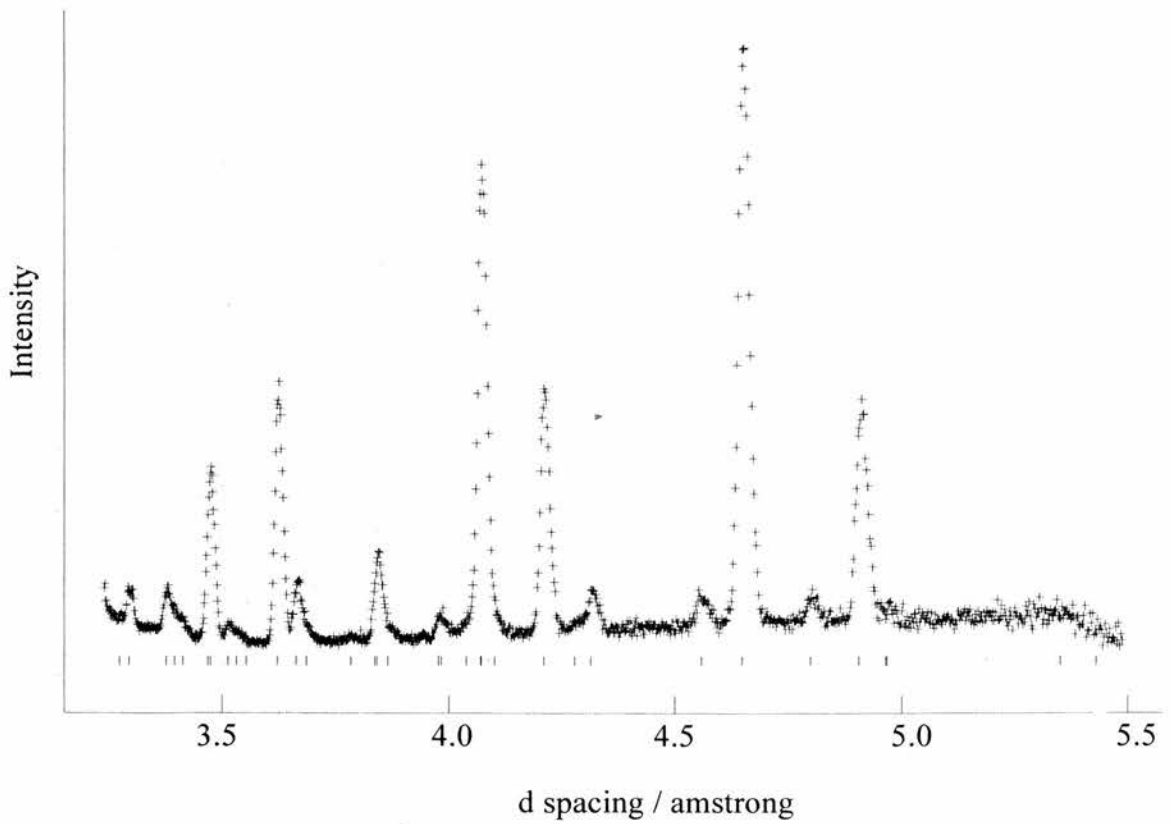

Figure 3 30-130 ms data set from the 90° detector bank.

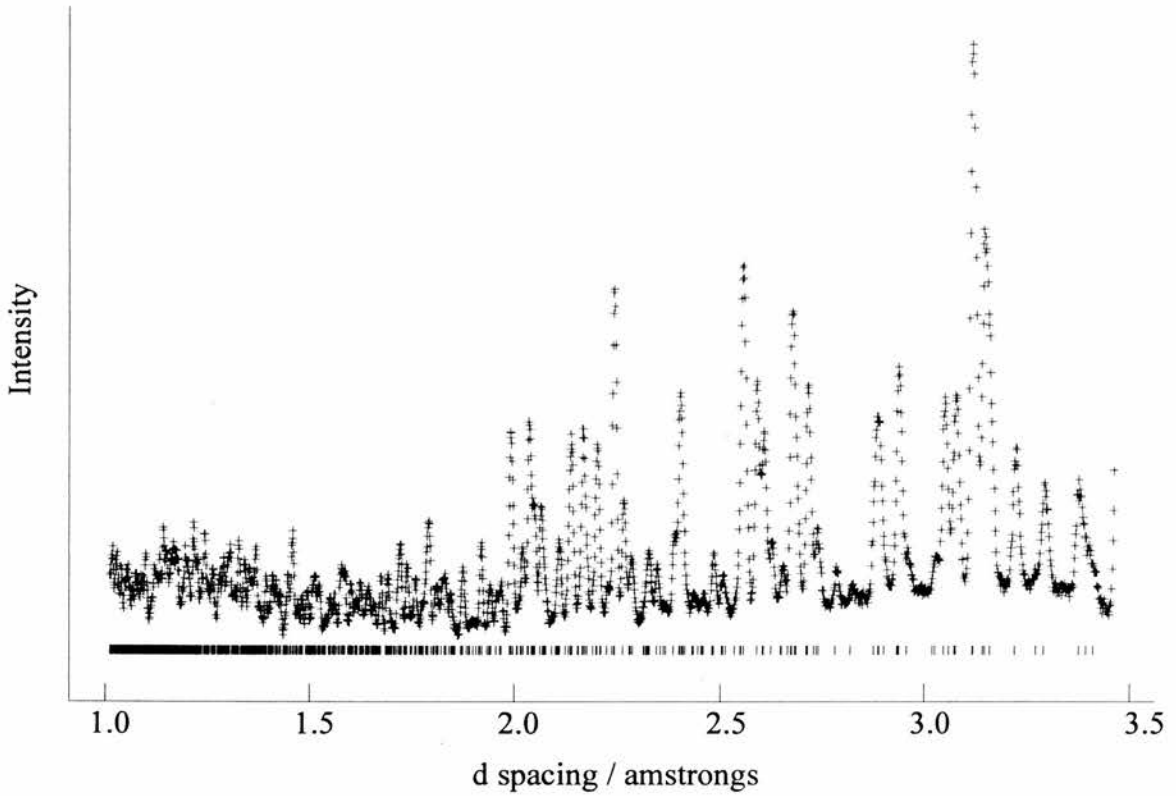

Figure 4 100-200 ms data set from the 90° detector bank.

Data for the starting model used for the refinement

Table 1 Lattice constants for the starting model taken from single crystal data[1] at room temperature. Space group is *R3c*.

a / Å	b / Å	c / Å	α / °	β / °	γ / °
24.650	24.650	25.299	90	90	120

Table 2 Coordinates from the published single crystal data for AlMePO-β[1] at room temperature used as the starting model for refinement of the neutron diffraction data. Default isotropic temperature factors of 0.025 were used as the starting point for all atoms.

Atom	x	y	z
Al1	0.3366	0.3385	0.4705
Al2	0.4774	0.4286	0.3369
Al3	0.2438	0.3722	0.3260
Al4	0.4223	0.4822	0.6044
P5	0.4058	0.2983	0.3847
P6	0.2049	0.2654	0.4069
P7	0.3722	0.4500	0.3875
P8	0.2936	0.4066	0.5555
P9	0.4712	0.4094	0.5317
P10	0.2758	0.2114	0.5381
O11	0.3555	0.3097	0.4068
O13	0.2536	0.3051	0.4461
O14	0.3566	0.4159	0.4389
O15	0.3110	0.3615	0.5331
O16	0.4207	0.3755	0.4926
O17	0.3179	0.2637	0.5029
O18	0.4633	0.3600	0.3666
O19	0.4313	0.4573	0.3622
O20	0.2488	0.3773	0.6026
O21	0.2602	0.1495	0.5149
O22	0.2102	0.2984	0.3555
O23	0.3192	0.4219	0.3486
O24	0.5327	0.4592	0.5052
O25	0.3064	0.2171	0.5924
O26	0.3805	0.2536	0.3369
O27	0.1393	0.2439	0.4309
O28	0.3515	0.4665	0.5748
O29	0.4544	0.4421	0.5751
C30	0.4313	0.2614	0.4303
C31	0.4609	0.2526	0.4135
H32	0.3960	0.2231	0.4423
H33	0.4508	0.2887	0.4599
C34	0.2067	0.1966	0.3922
H35	0.1712	0.1697	0.3706
H36	0.2052	0.1754	0.4244
H37	0.2445	0.2071	0.3734
C38	0.3908	0.5293	0.4015
H39	0.4219	0.5456	0.4288
H40	0.3537	0.5294	0.4130
H41	0.4066	0.5543	0.3701
C42	0.2543	0.4275	0.5087
H43	0.2484	0.4604	0.5228
H44	0.2143	0.3918	0.5008
H45	0.2788	0.4419	0.4769
C46	0.4893	0.3573	0.5653
H47	0.5166	0.3787	0.5945
H48	0.5097	0.3430	0.5415
H49	0.4514	0.3221	0.5782
C50	0.2039	0.2092	0.5505
H51	0.2121	0.2476	0.5672
H52	0.1784	0.1746	0.5733
H53	0.1824	0.2044	0.5177

Final results for the unconstrained refinement using anisotropic temperature factors for the deuterium atoms

Table 3 Final profile fit results for Model 2 using anisotropic temperature factors for the deuterium atoms.

	WRp / %	Rp / %	Reduced χ^2
Histogram 1	5.11	4.31	-
Histogram 2	4.21	3.98	-
Total	4.46	4.10	3.20

Table 4 Lattice constants for the fully refined model using anisotropic temperature factors for the deuterium atoms. Space group is *R3c*.

a / Å	b / Å	c / Å	α / °	β / °	γ / °
24.62053(6)	24.62062(6)	25.27337(11)	90	90	120

Table 5 Background coefficient values for a cosine fourier series function with 6 terms, for the fully refined model using anisotropic temperature factors for the deuterium atoms.

Coefficient	1	2	3	4	5	6
Histogram 1	3.991	-38.43	3.643	-20.35	1.190	-4.587
Sigmas	0.098	0.0	0.146	0.284	0.461	0.352
Histogram 2	12.26	-19.05	12.40	-5.43	1.23	0.0975
Sigmas	0.191	0.0	0.646	0.839	0.503	0.141

Table 6 Histogram 1's peak profile coefficients for an exponential pseudovoigt convolution Von Dreele, 1990 (unpublished), for the fully refined model using anisotropic temperature factors for the deuterium atoms.

Coefficient	Value	Coefficient	Value	Coefficient	Value
alp	0.1185	bet-0	0.0249	bet-1	0.0074
sig-0	0.0	sig-1	488.6	sig-2	-2.6
gam-0	0.0	gam-1	23.49	gam-2	0.7
gsf	0.0	g1ec	0.0	g2ec	0.0
rstr	0.0	rsta	0.0	rsca	0.0
L11	0.0	L22	0.0	L33	0.0
L12	0.0	L13	0.0	L23	0.0

Table 7 Histogram 2's peak profile coefficients for an exponential pseudovoigt convolution Von Dreele, 1990 (unpublished), for the fully refined model using anisotropic temperature factors for the deuterium atoms.

Coefficient	Value	Coefficient	Value	Coefficient	Value
alp	0.1185	bet-0	0.0249	bet-1	0.0074
sig-0	0.0	sig-1	449.1	sig-2	4.0
gam-0	0.0	gam-1	23.07	gam-2	0.57
gsf	0.0	g1ec	0.0	g2ec	0.0
rstr	0.0	rsta	0.0	rsca	0.0
L11	0.0	L22	0.0	L33	0.0
L12	0.0	L13	0.0	L23	0.0

Table 8 Atomic coordinates from the unconstrained fully refined structure, utilising anisotropic temperature factors for the deuterium atoms.

Atom	x	y	z
Al1	0.3384(7)	0.3374(6)	0.4715(9)
Al2	0.4800(8)	0.4291(8)	0.3415(7)
Al3	0.2436(6)	0.3680(6)	0.3285(4)
Al4	0.4216(7)	0.4788(7)	0.6065(5)
P5	0.4060(4)	0.2988(4)	0.38584(34)
P6	0.2041(4)	0.2652(4)	0.4092(4)
P7	0.3712(4)	0.4498(4)	0.38669(30)
P8	0.2933(5)	0.4056(5)	0.5594(4)
P9	0.4704(4)	0.4106(4)	0.53246(30)
P10	0.2764(4)	0.2123(4)	0.53901(35)
O11	0.35514(35)	0.3123(4)	0.40597(32)
O12	0.2541(4)	0.3059(4)	0.44621(34)
O13	0.3549(4)	0.4184(4)	0.43921(32)
O14	0.3121(4)	0.3609(4)	0.53329(34)
O15	0.4188(4)	0.3772(4)	0.49263(31)
O16	0.32113(34)	0.2652(4)	0.50141(30)
O17	0.4629(4)	0.3577(4)	0.36671(29)
O18	0.4329(4)	0.4615(4)	0.36481(31)
O19	0.2465(4)	0.3729(4)	0.60412(32)
O20	0.2594(4)	0.1503(4)	0.51321(32)
O21	0.2107(4)	0.2989(4)	0.35695(30)
O22	0.3200(4)	0.4201(4)	0.34619(32)
O23	0.5335(4)	0.4595(4)	0.50608(31)
O24	0.3088(4)	0.2174(4)	0.5913(4)
O25	0.3796(4)	0.25330(34)	0.33563(34)
O26	0.1384(4)	0.2415(4)	0.43211(31)
O27	0.3472(4)	0.4658(4)	0.57752(32)
O28	0.4551(4)	0.4435(4)	0.57455(33)
C29	0.4294(4)	0.2596(4)	0.4303(4)
H30	0.4722(5)	0.2614(6)	0.4190(4)
H31	0.3850(6)	0.2139(6)	0.4411(4)
H32	0.4420(5)	0.2871(6)	0.4677(4)
C33	0.2071(4)	0.1982(4)	0.39188(31)
H34	0.1678(5)	0.1653(4)	0.3664(4)
H35	0.2047(7)	0.1710(5)	0.4260(4)
H36	0.2495(6)	0.2098(6)	0.3743(4)
C37	0.3855(4)	0.5267(4)	0.39655(29)
H38	0.4224(5)	0.5522(4)	0.4309(4)
H39	0.3434(5)	0.5271(4)	0.4113(4)
H40	0.4006(7)	0.5538(5)	0.3612(4)
C41	0.2558(4)	0.4270(4)	0.50916(33)
H42	0.2441(4)	0.4581(5)	0.52561(32)
H43	0.2101(6)	0.3882(5)	0.50290(34)
H44	0.2805(6)	0.4457(8)	0.4733(5)
C45	0.4861(4)	0.35838(33)	0.56440(30)
H46	0.5201(5)	0.3796(5)	0.59855(31)
H47	0.5054(5)	0.3355(6)	0.5409(4)
H48	0.4450(5)	0.3193(5)	0.58163(31)
C49	0.2075(4)	0.2129(5)	0.5521(4)
H50	0.2138(4)	0.2557(5)	0.5672(4)
H51	0.1765(4)	0.1741(5)	0.57889(35)
H52	0.1806(6)	0.2081(6)	0.5164(4)

Table 9 Isotropic temperature factors for the non-deuterium atoms from the fully refined Model 2 which uses anistropic temperature factors for the deuterium atoms.

Atom	Uiso
Al1	0.02098
Al2	0.02598
Al3	0.00120
Al4	0.00511
P5	0.00782
P6	0.00602
P7	0.00705
P8	0.02480
P9	0.00036
P10	0.00254
O11	0.00194
O12	0.01074
O13	0.00923
O14	0.00949
O15	0.00848
O16	0.00509
O17	0.01051
O18	0.00989
O19	0.01212
O20	0.01049
O21	0.00476
O22	0.01125
O23	0.01467
O24	0.01348
O25	0.00466
O26	0.00666
O27	0.01419
O28	0.00353
C29	0.01622
C33	0.00785
C37	0.01763
C41	0.01019
C45	0.01433
C49	0.02675

Table 10 Anisotropic temperature factors for the deuterium atoms from the fully refined Model 2 structure.

Atom	U_{11}	U_{22}	U_{33}	U_{12}	U_{13}	U_{23}
D30	0.07564	0.13970	0.01000	0.08439	0.03290	0.03965
D31	0.06246	0.05336	0.02903	0.01877	0.00951	-0.02740
D32	0.06254	0.12630	0.01000	0.07221	0.01141	-0.00870
D34	0.04907	0.03063	0.03343	0.01362	0.01593	0.003406
D35	0.17400	0.02259	0.01922	0.03655	-0.00169	0.02446
D36	0.06206	0.09082	0.02586	0.05472	-0.03246	0.00212
D38	0.09825	0.02597	0.03249	0.02420	0.00624	0.00766
D39	0.06719	0.01751	0.06603	0.01715	0.05715	0.02460
D40	0.10683	0.04463	0.05914	0.02638	0.04787	0.04777
D42	0.01730	0.04419	0.01331	0.02171	0.01916	0.03478
D43	0.09632	0.06243	0.00074	0.05935	-0.03382	0.00315
D44	0.05531	0.17041	0.07592	0.05501	0.06974	0.11616
D46	0.04854	0.09691	0.01065	0.03047	0.00753	0.009298
D47	0.07628	0.09793	0.02600	0.08429	0.00856	0.01405
D48	0.06971	0.05030	0.02102	0.02814	0.00896	0.02758
D50	0.01657	0.03866	0.04739	0.00931	0.02220	-0.00624
D51	0.04870	0.07115	0.01015	0.02080	0.04052	0.00663
D52	0.07365	0.06326	0.03499	0.04441	-0.00341	-0.02693

Final results for the unconstrained refinement using isotropic temperature factors for the deuterium atoms

Table 11 Final profile fit results

	WRp / %	Rp / %	Reduced χ^2
Histogram 1	5.26	4.41	-
Histogram 2	5.09	4.63	-
Total	5.13	4.55	4.35

Table 12 Background coefficient values for a cosine fourier series function with 6 terms.

Coefficient	1	2	3	4	5	6
Histogram 1	3.90	-38.2	3.52	-20.2	1.16	-4.55
Sigmas	0.479	2.50	0.668	1.34	0.192	0.312
Histogram 2	11.3	-19.1	15.9	-9.90	4.00	0.689
Sigmas	0.248	0.000	0.838	1.09	0.654	0.183

Table 13 Background coefficient values for a cosine fourier series function with 6 terms.

Histogram	1	2
Scale Factor	4.193	27.33
Sigmas	0.025	0.075

Table 14 Lattice constants for the fully refined model with isotropic temperature factors. Space group is *R3c*.

a / Å	b / Å	c / Å	α / °	β / °	γ / °
24.62064(7)	24.62072(7)	25.27347(14)	90	90	120

Table 15 Peak profile coefficients, for Histogram 1, for exponential pseudovoigt convolution Von Dreele, 1990 (unpublished)

Coefficient	Value	Coefficient	Value	Coefficient	Value
alp	0.1185	bet-0	0.0249	bet-1	0.0074
sig-0	0.0	sig-1	440.1	sig-2	-2.6
gam-0	0.0	gam-1	23.49	gam-2	0.7
gsf	0.0	g1ec	0.0	g2ec	0.0
rstr	0.0	rsta	0.0	rsca	0.0
L11	0.0	L22	0.0	L33	0.0
L12	0.0	L13	0.0	L23	0.0

Table 16 Peak profile coefficients, for Histogram 2, for exponential pseudovoigt convolution Von Dreele, 1990 (unpublished)

Coefficient	Value	Coefficient	Value	Coefficient	Value
alp	0.1185	bet-0	0.0249	bet-1	0.0074
sig-0	0.0	sig-1	440.1	sig-2	4.0
gam-0	0.0	gam-1	23.69	gam-2	0.57
gsf	0.0	g1ec	0.0	g2ec	0.0
rstr	0.0	rsta	0.0	rsca	0.0
L11	0.0	L22	0.0	L33	0.0
L12	0.0	L13	0.0	L23	0.0

See Chapter 7 for the atomic coordinates for this structure.

Comparison of Structures

Table 17 Bond length comparison of the final structure refined with anisotropic temperature factors for the deuterium atoms with the starting model from the original single crystal data collected at room temperature.

Final structure refined using anistropic temperature factors for the deuterium atoms				**Starting structure, taken from single crystal data recorded at room temperature**			
Bond	**Bond length / Å**	**Mean length / Å**	**Range (std dev) / Å**	**Bond**	**Bond length / Å**	**Mean length / Å**	**Range (std dev) / Å**
Al1_P6	3.27	3.24	0.051	Al1_P5	3.21	3.23	0.024
Al1_P7	3.27			Al1_P6	3.24		
Al1_P8	3.29			Al1_P7	3.21		
Al1_P9	3.21			Al1_P8	3.22		
Al1_P10	3.17			Al1_P9	3.27		
				Al1_P10	3.21		
Al1_O11	1.88	1.88	0.083	Al1_O11	1.91	1.89	0.019
Al1_O13	1.93			Al1_O13	1.89		
Al1_O14	2.00			Al1_O14	1.89		
Al1_O15	1.89			Al1_O15	1.89		
Al1_O16	1.79			Al1_O16	1.88		
Al1_O17	1.78			Al1_O17	1.85		
Al2_P5	3.00	3.10	0.086	Al2_P5	3.04	3.09	0.050
Al2_P7	3.18			Al2_P8	3.14		
Al2_P8	3.16			Al2_P10	3.10		
Al2_O18	1.71	1.76	0.068	Al2_O18	1.72	1.73	0.011
Al2_O19	1.80			Al2_O19	1.73		
Al2_O20	1.84			Al2_O20	1.74		
Al2_O21	1.70			Al2_O21	1.74		
Al3_P6	3.01	3.10	0.067	Al3_P6	3.08	3.10	0.017
Al3_P7	3.13			Al3_P9	3.10		
Al3_P9	3.13			Al3_P10	3.12		
Al3_P10	3.16						
Al3_O22	1.64	1.74	0.072	Al3_O22	1.75	1.73	0.012
Al3_O23	1.73			Al3_O23	1.73		
Al3_O24	1.79			Al3_O24	1.72		
Al3_O25	1.80			Al3_O25	1.72		
Al4_P5	3.08	3.07	0.058	Al4_P5	3.12	3.07	0.046
Al4_P6	3.09			Al4_P6	3.06		
Al4_P8	2.99			Al4_P8	3.03		
Al4_P9	3.13						
Al4_O26	1.63	1.74	0.107	Al4_O26	1.73	1.73	0.017
Al4_O27	1.83			Al4_O27	1.73		
Al4_O28	1.84			Al4_O28	1.76		
Al4_O29	1.68			Al4_O29	1.71		
P5_O11	1.54	1.55	0.049	P5_O11	1.51	1.53	0.019
P5_O18	1.51			P5_O18	1.54		
P5_O26	1.60			P5_O26	1.54		
P5_C30	1.76			P5_C30	1.77		
P6_O13	1.47	1.51	0.035	P6_O13	1.49	1.51	0.034
P6_O22	1.52			P6_O22	1.50		

Bond	Bond length / Å	Mean length / Å	Range (std dev) / Å	Bond	Bond length / Å	Mean length / Å	Range (std dev) / Å
P6_O27	1.53			P6_O27	1.55		
P6_C34	1.74			P6_C34	1.76		
P7_O14	1.49	1.50	0.010	P7_O14	1.49	1.50	0.014
P7_O19	1.51			P7_O19	1.52		
P7_O23	1.50			P7_O23	1.50		
P7_C38	1.76			P7_C38	1.81		
P8_O15	1.54	1.52	0.030	P8_O15	1.49	1.52	0.026
P8_O20	1.53			P8_O20	1.54		
P8_O28	1.48			P8_O28	1.53		
P8_C42	1.80			P8_C42	1.76		
P9_O16	1.50	1.52	0.036	P9_O16	1.48	1.52	0.037
P9_O24	1.56			P9_O24	1.55		
P9_O29	1.49			P9_O29	1.54		
P9_C46	1.72			P9_C46	1.77		
P10_O17	1.54	1.52	0.016	P10_O17	1.48	1.51	0.030
P10_O21	1.51			P10_O21	1.49		
P10_O25	1.52			P10_O25	1.54		
P10_C50	1.74			P10_C50	1.77		
C30_P5	1.76	1.75	0.027	C30_P5	1.77	1.77	0.017
C34_P6	1.74			C34_P6	1.76		
C38_P7	1.76			C38_P7	1.81		
C42_P8	1.80			C42_P8	1.76		
C46_P9	1.72			C46_P9	1.77		
C50_P10	1.74			C50_P10	1.77		
C30_D31	1.07	1.09	0.039	C30_D31	0.96	0.96	0.001
C30_D32	1.14			C30_D32	0.96		
C30_D33	1.11			C30_D33	0.96		
C34_D35	1.11			C34 D35	0.96		
C34_D36	1.08			C34_D36	0.96		
C34_D37	1.03			C34_D37	0.96		
C38_D39	1.18			C38_D39	0.96		
C38_D40	1.11			C38_D40	0.96		
C38_D41	1.06			C38_D41	0.96		
C42_D43	1.03			C42_D43	0.96		
C42_D44	1.06			C42_D44	0.96		
C42_D45	1.06			C42_D45	0.96		
C46_D47	1.13			C46_D47	0.96		
C46_D48	1.08			C46_D48	0.96		
C46_D49	1.08			C46_D49	0.96		
C50_D51	1.06			C50_D51	0.96		
C50_D52	1.11			C50_D52	0.96		
C50_D53	1.09			C50_D53	0.96		
D31_D32	1.94	1.76	0.121	D31_D32	1.57	1.57	0.002
D31_D33	1.71			D31_D33	1.57		
D32_D31	1.94			D32_D31	1.57		
D32_D33	1.77			D32_D33	1.57		
D33_D31	1.71			D33_D31	1.57		
D33_D32	1.77			D33_D32	1.57		

Bond	Bond length / Å	Mean length / Å	Range (std dev) / Å	Bond	Bond length / Å	Mean length / Å	Range (std dev) / Å
D35_D36	1.73			D35_D36	1.57		
D35_D37	1.76			D35_D37	1.57		
D36_D35	1.73			D36_D35	1.57		
D36_D37	1.67			D36_D37	1.57		
D37_D35	1.76			D37_D35	1.57		
D37_D36	1.67			D37_D36	1.57		
D39_D40	1.79			D39_D40	1.57		
D39_D41	1.85			D39_D41	1.57		
D40_D39	1.79			D40_D39	1.57		
D40_D41	1.76			D40_D41	1.57		
D41_D39	1.85			D41_D39	1.57		
D41_D40	1.76			D41_D40	1.57		
D43_D44	1.60			D43_D44	1.57		
D43_D45	1.71			D43_D45	1.57		
D44_D43	1.60			D44_D43	1.57		
D44_D45	1.77			D44_D45	1.57		
D45_D43	1.71			D45_D43	1.57		
D45_D44	1.77			D45_D44	1.57		
D47_D48	1.74			D47_D48	1.57		
D47_D49	1.75			D47_D49	1.57		
D48_D47	1.74			D48_D47	1.57		
D48_D49	1.68			D48_D49	1.57		
D49_D47	1.75			D49_D47	1.57		
D49_D48	1.68			D49_D48	1.57		
D51_D52	1.77			D51_D52	1.57		
D51_D53	1.65			D51_D53	1.57		
D52_D51	1.77			D52_D51	1.57		
D52_D53	1.77			D52_D53	1.57		
D53_D51	1.65			D53_D51	1.57		
D53_D52	1.77			D53_D52	1.57		

Table 18 Bond angle comparison of the final structure refined with anisotropic temperature factors for the deuterium atoms with the starting model from the original single crystal, room temperature refinement. The deviation from perfect symmetry column measures the difference of the angle from the angle normally associated with geometry of the central atom, i.e. 90° between adjacent ligands of octahedral geometry and 109.5° between ligands of a tetrahedral geometry.

Final structure with anisotropic temperature factors					**Starting model from single crystal data collected at room temperature**				
	Angle / °	Deviation from perfect geometry / °	Mean deviation from symmetry / °	Standard Deviation of distortion / °		Angle / °	Deviation from perfect geometry / °	Mean deviation from symmetry / °	Standard Deviation of distortion / °
O13_Al1_O14	84.6	5.40	2.80	1.59	O13_Al1_O15	87.3	2.68	1.55	0.82
O13_Al1_O15	86.1	3.90			O14_Al1_O16	88.2	1.81		
O11_Al1_O13	86.8	3.20			O15_Al1_O17	88.5	1.51		
O14_Al1_O16	87.7	2.30			O11_Al1_O13	88.5	1.46		
O14_Al1_O15	87.8	2.20			O13_Al1_O14	88.9	1.10		
O11_Al1_O14	89.9	0.10			O11_Al1_O17	89.4	0.63		
O15_Al1_O17	90.5	0.50			O14_Al1_O15	90.5	0.53		
O11_Al1_O17	91.6	1.60			O11_Al1_O16	90.9	0.94		
O15_Al1_O16	92.3	2.30			O16_Al1_O17	90.9	0.94		
O13_Al1_O17	93.8	3.80			O11_Al1_O14	91.7	1.68		
O16_Al1_O17	93.8	3.80			O13_Al1_O17	92.0	1.98		
O11_Al1_O16	94.5	4.50			O15_Al1_O16	93.3	3.30		
O13_Al1_O16	172.2	174.23	3.10		O11_Al1_O15	175.3	176.98	1.69	
O11_Al1_O15	172.7				O13_Al1_O16	177.0			
O14_Al1_O17	177.8				O14_Al1_O17	178.7			
O18_Al2_O19	116.7	7.20	3.87	3.74	O18_Al2_O19	112.9	3.36	2.05	1.26
O18_Al2_O20	109.0	0.50			O18_Al2_O20	111.0	1.50		
O18_Al2_O21	112.7	3.20			O18_Al2_O21	106.5	3.04		
O19_Al2_O20	99.9	9.60			O19_Al2_O20	106.5	2.96		
O19_Al2_O21	110.0	0.50			O19_Al2_O21	109.3	0.21		
O20_Al2_O21	107.3	2.20			O20_Al2_O21	110.7	1.22		
O22_Al3_O23	116.5	7.00	3.37	2.31	O22_Al3_O23	112.2	2.71	1.63	1.00
O22_Al3_O24	112.1	2.60			O22_Al3_O24	110.5	1.00		
O22_Al3_O25	109.0	0.50			O22_Al3_O25	106.5	3.04		
O23_Al3_O24	106.4	3.10			O23_Al3_O24	108.2	1.33		
O23_Al3_O25	107.5	2.00			O23_Al3_O25	110.6	1.09		
O24_Al3_O25	104.5	5.00			O24_Al3_O25	108.9	0.62		
O26_Al4_O27	110.4	0.90	2.90	3.06	O26_Al4_O27	111.0	1.53	2.58	1.46
O26_Al4_O28	111.4	1.90			O26_Al4_O28	112.4	2.89		
O26_Al4_O29	109.7	0.20			O26_Al4_O29	105.2	4.29		
O27_Al4_O28	101.6	7.90			O27_Al4_O28	106.0	3.47		
O27_Al4_O29	108.4	1.10			O27_Al4_O29	109.7	0.22		
O28_Al4_O29	114.9	5.40			O28_Al4_O29	112.5	3.04		
O11_P5_O18	111.4	1.90	2.85	2.44	O11_P5_O18	111.2	1.73	2.08	1.39
O11_P5_O26	109.0	0.50			O11_P5_O26	110.3	0.81		
O11_P5_C30	115.7	6.20			O11_P5_C30	113.0	3.50		
O18_P5_O26	106.0	3.50			O18_P5_O26	108.4	1.09		
O18_P5_C30	109.4	0.10			O18_P5_C30	108.3	1.23		
O26_P5_C30	104.6	4.90			O26_P5_C30	105.4	4.14		
O13_P6_O22	110.9	1.40	2.80	1.63	O13_P6_O22	113.4	3.93	2.22	1.31

	Angle / °	Deviation from perfect geometry / °	Mean deviation from symmetry / °	Standard Deviation of distortion / °		Angle / °	Deviation from perfect geometry / °	Mean deviation from symmetry / °	Standard Deviation of distortion / °
O13_P6_O27	112.5	3.00			O13_P6_O27	108.9	0.56		
O13_P6_C34	112.8	3.30			O13_P6_C34	112.0	2.51		
O22_P6_O27	109.9	0.40			O22_P6_O27	108.5	1.03		
O22_P6_C34	104.7	4.80			O22_P6_C34	107.5	1.96		
O27_P6_C34	105.6	3.90			O27_P6_C34	106.1	3.36		
O14_P7_O19	114.3	4.80	4.12	2.11	O14_P7_O19	113.4	109.39	3.54	
O14_P7_O23	114.5	5.00			O14_P7_O23	113.1			
O19_P7_O23	111.4	1.90			O19_P7_O23	109.9			
O19_P7_C38	101.9	7.60			O19_P7_C38	104.2			
O23_P7_C38	106.8	2.70			O23_P7_C38	108.6			
O14_P7_C38	106.8	2.70			O14_P7_C38	107.1			
O15_P8_O20	110.9	1.40	2.63	1.49	O15_P8_O20	110.6	1.08	1.72	0.66
O15_P8_O28	114.0	4.50			O15_P8_O28	111.3	1.81		
O20_P8_O28	111.2	1.70			O20_P8_O28	108.1	1.45		
O20_P8_C42	108.3	1.20			O20_P8_C42	106.7	2.80		
O28_P8_C42	105.1	4.40			O28_P8_C42	108.4	1.10		
O15_P8_C42	106.9	2.60			O15_P8_C42	111.6	2.11		
O16_P9_O24	112.3	2.80	2.73	1.34	O16_P9_O24	111.9	2.38	2.79	1.19
O16_P9_O29	113.7	4.20			O16_P9_O29	113.8	4.27		
O16_P9_C46	110.4	0.90			O16_P9_C46	110.9	1.42		
O24_P9_O29	108.1	1.40			O24_P9_O29	107.9	1.58		
O24_P9_C46	105.5	4.00			O24_P9_C46	106.3	3.19		
O29_P9_C46	106.4	3.10			O29_P9_C46	105.6	3.91		
O17_P10_O21	107.9	1.60	1.53	1.27	O17_P10_O21	111.3	1.79	2.28	0.79
O17_P10_O25	110.1	0.60			O17_P10_O25	111.0	1.54		
O21_P10_O25	109.2	0.30			O21_P10_O25	107.9	1.57		
O21_P10_C50	108.2	1.30			O21_P10_C50	107.2	2.33		
O25_P10_C50	108.0	1.50			O25_P10_C50	106.3	3.15		
O17_P10_C50	113.4	3.90			O17_P10_C50	112.8	3.30		
H31_C30_H32	122.7	13.20	19.49	4.16	H31_C30_H32	109.7	0.16	11.16	0.08
H31_C30_H33	103.3	6.20			H31_C30_H33	109.5	0.01		
H32_C30_H33	103.7	5.80			H32_C30_H33	109.5	0.04		
H35_C34_H36	104.8	4.70	14.55	2.49	H35_C34_H36	109.5	0.02	11.20	0.08
H35_C34_H37	110.1	0.60			H35_C34_H37	109.3	0.19		
H36_C34_H37	104.4	5.10			H36_C34_H37	109.6	0.13		
H39_C38_H40	102.8	6.70	14.05	3.24	H39_C38_H40	110.1	0.60	11.58	0.22
H39_C38_H41	110.4	0.90			H39_C38_H41	110.1	0.64		
H40_C38_H41	108.2	1.30			H40_C38_H41	109.3	0.24		
H43_C42_H44	99.5	10.00	15.49	5.08	H43_C42_H44	109.4	0.12	11.21	0.04
H43_C42_H45	109.6	0.10			H43_C42_H45	109.3	0.16		

	Angle / °	Deviation from perfect geometry / °	Mean deviation from symmetry / °	Standard Deviation of distortion / °		Angle / °	Deviation from perfect geometry / °	Mean deviation from symmetry / °	Standard Deviation of distortion / °
H44_C42_H45	112.6	3.10			H44_C42_H45	109.4	0.08		
H47_C46_H48	104.1	5.40	16.85	1.00	H47_C46_H48	109.5	0.03	11.12	0.02
H47_C46_H49	104.5	5.00			H47_C46_H49	109.5	0.05		
H48_C46_H49	102.6	6.90			H48_C46_H49	109.5	0.01		
H51_C50_H52	109.6	0.10	14.82	4.45	H51_C50_H52	109.5	0.04	11.14	0.01
H51_C50_H53	100.8	8.70			H51_C50_H53	109.4	0.06		
H52_C50_H53	107.1	2.40			H52_C50_H53	109.5	0.05		

Table 19 Bond length comparison of the final structure refined with anisotropic temperature factors for the deuterium atoms with final structure refined with isotropic temperature factors only.

Final structure refined using anistropic temperature factors for the deuterium atoms				**Final structure refined using isotropic temperature factors for the deuterium atoms**			
Bond	Bond length / Å	Mean length / Å	Range (std dev) / Å	Bond	Bond length / Å	Mean length / Å	Range (std dev) / Å
AL1_O11	1.88	1.88	0.083	Al1_O11	1.86	1.89	0.14
AL1_O13	1.93			Al1_O13	1.96		
AL1_O14	2.00			Al1_O14	2.10		
AL1_O15	1.89			Al1_O15	1.92		
AL1_O16	1.79			Al1_O16	1.79		
AL1_O17	1.78			Al1_O17	1.69		
AL2_O18	1.71	1.76	0.068	Al2_O18	1.70	1.76	0.05
AL2_O19	1.80			Al2_O19	1.80		
AL2_O20	1.84			Al2_O20	1.80		
AL2_O21	1.70			Al2_O21	1.72		
AL3_O22	1.64	1.74	0.072	Al3_O22	1.68	1.73	0.04
AL3_O23	1.73			Al3_O23	1.76		
AL3_O24	1.79			Al3_O24	1.73		
AL3_O25	1.80			Al3_O25	1.76		
AL4_O26	1.63	1.74	0.107	Al4_O26	1.63	1.75	0.12
AL4_O27	1.83			Al4_O27	1.84		
AL4_O28	1.84			Al4_O28	1.86		
AL4_O29	1.68			Al4_O29	1.66		
P5_O11	1.54	1.55	0.049	P5_O11	1.52	1.60	0.12
P5_O18	1.51			P5_O18	1.53		
P5_O26	1.60			P5_O26	1.56		
P5_C30	1.76			P5_C30	1.78		
P6_O13	1.47	1.51	0.035	P6_O13	1.43	1.57	0.17
P6_O22	1.52			P6_O22	1.53		
P6_O27	1.53			P6_O27	1.51		
P6_C34	1.74			P6_C34	1.81		
P7_O14	1.49	1.50	0.010	P7_O14	1.43	1.55	0.13
P7_O19	1.51			P7_O19	1.52		
P7_O23	1.50			P7_O23	1.52		
P7_C38	1.76			P7_C38	1.73		
P8_O15	1.54	1.52	0.030	P8_O15	1.53	1.58	0.12
P8_O20	1.53			P8_O20	1.51		
P8_O28	1.48			P8_O28	1.54		
P8_C42	1.80			P8_C42	1.76		
P9_O16	1.50	1.52	0.036	P9_O16	1.50	1.58	0.11
P9_O24	1.56			P9_O24	1.57		
P9_O29	1.49			P9_O29	1.50		
P9_C46	1.72			P9_C46	1.73		
P10_O17	1.54	1.52	0.016	P10_O17	1.55	1.57	0.08
P10_O21	1.51			P10_O21	1.54		
P10_O25	1.52			P10_O25	1.52		

Bond	Bond length / Å	Mean length / Å	Range (std dev) / Å	Bond	Bond length / Å	Mean length / Å	Range (std dev) / Å
P10_C50	1.74			P10_C50	1.70		
C30_D31	1.07	1.11	0.04	C30_D31	1.10	1.09	0.02
C30_D32	1.14			C30_D32	1.11		
C30_D33	1.11			C30_D33	1.07		
C34_D35	1.11	1.07	0.04	C34_D35	1.13	1.11	0.03
C34_D36	1.08			C34_D36	1.08		
C34_D37	1.03			C34_D37	1.11		
C38_D39	1.18	1.12	0.06	C38_D39	1.19	1.14	0.05
C38_D40	1.11			C38_D40	1.10		
C38_D41	1.06			C38_D41	1.13		
C42_D43	1.03	1.05	0.02	C42_D43	1.02	1.06	0.04
C42_D44	1.06			C42_D44	1.05		
C42_D45	1.06			C42_D45	1.10		
C46_D47	1.13	1.10	0.03	C46_D47	1.14	1.11	0.02
C46_D48	1.08			C46_D48	1.10		
C46_D49	1.08			C46_D49	1.10		
C50_D51	1.06	1.09	0.03	C50_D51	1.04	1.07	0.03
C50_D52	1.11			C50_D52	1.07		
C50_D53	1.09			C50_D53	1.09		

Table 20 Bond angle comparison of the final structure refined with anisotropic temperature factors for the deuterium atoms with the final structure refined with isotropic temperature factors alone. The deviation from perfect symmetry column measures the difference of the angle from the angle normally associated with geometry of the central atom, i.e. 90° between adjacent ligands of octahedral geometry and 109.5° between ligands of a tetrahedral geometry.

Final structure with anisotropic temperature factors					Final structure with isotropic temperature factors				
	Angle / °	Deviation from perfect geometry / °	Mean deviation from symmetry / °	Standard Deviation of distortion / °		Angle / °	Deviation from perfect geometry / °	Mean deviation from symmetry / °	Standard Deviation of distortion / °
O13_A11_O14	84.6	5.4	2.8	1.6	O13_A11_O14	81.2	8.8	4.9	2.0
O13_A11_O15	86.1	3.9			O14_A11_O15	84.1	5.9		
O11_A11_O13	86.8	3.2			O13_A11_O15	84.6	5.4		
O14_A11_O16	87.7	2.3			O11_A11_O13	85.2	4.8		
O14_A11_O15	87.8	2.2			O14_A11_O16	86.5	3.5		
O11_A11_O14	89.9	0.1			O11_A11_O14	87.7	2.3		
O15_A11_O17	90.5	0.5			O15_A11_O17	93.2	3.2		
O11_A11_O17	91.6	1.6			O15_A11_O16	93.4	3.4		
O15_A11_O16	92.3	2.3			O13_A11_O17	93.8	3.8		
O13_A11_O17	93.8	3.8			O11_A11_O17	94.3	4.3		
O16_A11_O17	93.8	3.8			O11_A11_O16	95.2	5.2		
O11_A11_O16	94.5	4.5			O16_A11_O17	98.5	8.5		
O13_A11_O16	172.2				O13_A11_O16	167.6			
O11_A11_O15	172.7				O11_A11_O15	167.7			
O14_A11_O17	177.8				O14_A11_O17	174.5			
O18_A12_O19	116.7	7.2	3.9	3.7	O18_A12_O19	117.0	7.5	3.4	3.4
O18_A12_O20	109.0	0.5			O18_A12_O20	111.7	2.2		
O18_A12_O21	112.7	3.2			O18_A12_O21	109.3	0.2		
O19_A12_O20	99.9	9.6			O19_A12_O20	101.7	7.8		
O19_A12_O21	110.0	0.5			O19_A12_O21	108.9	0.6		
O20_A12_O21	107.3	2.2			O20_A12_O21	107.6	1.9		
O22_A13_O23	116.5	7.0	3.4	2.3	O22_A13_O23	113.2	3.7	1.9	0.9

	Angle / °	Deviation from perfect geometry / °	Mean deviation from symmetry / °	Standard Deviation of distortion / °		Angle / °	Deviation from perfect geometry / °	Mean deviation from symmetry / °	Standard Deviation of distortion / °
O22_A13_O24	112.1	2.6			O22_A13_O24	111.3	1.8		
O22_A13_O25	109.0	0.5			O22_A13_O25	108.3	1.2		
O23_A13_O24	106.4	3.1			O23_A13_O24	108.4	1.1		
O23_A13_O25	107.5	2.0			O23_A13_O25	107.8	1.7		
O24_A13_O25	104.5	5.0			O24_A13_O25	107.7	1.8		
O26_A14_O27	110.4	0.9	2.9	3.1	O26_A14_O27	112.8	3.3	3.2	2.9
O26_A14_O28	111.4	1.9			O26_A14_O28	111.3	1.8		
O26_A14_O29	109.7	0.2			O26_A14_O29	112.3	2.8		
O27_A14_O28	101.6	7.9			O27_A14_O28	100.6	8.9		
O27_A14_O29	108.4	1.1			O27_A14_O29	108.4	1.1		
O28_A14_O29	114.9	5.4			O28_A14_O29	111.0	1.5		
O11_P5_O18	111.4	1.9	2.9	2.4	O11_P5_O18	113.4	3.9	3.5	2.3
O11_P5_O26	109.0	0.5			O11_P5_O26	109.9	0.4		
O11_P5_C30	115.7	6.2			O11_P5_C30	115.2	5.7		
O18_P5_O26	106.0	3.5			O18_P5_O26	105.5	4		
O18_P5_C30	109.4	0.1			O18_P5_C30	108.3	1.2		
O26_P5_C30	104.6	4.9			O26_P5_C30	103.7	5.8		
O13_P6_O22	110.9	1.4	2.8	1.6	O13_P6_O22	112.3	2.8	3.8	2.3
O13_P6_O27	112.5	3.0			O13_P6_O27	115.0	5.5		
O13_P6_C34	112.8	3.3			O13_P6_C34	109.9	0.4		
O22_P6_O27	109.9	0.4			O22_P6_O27	111.6	2.1		
O22_P6_C34	104.7	4.8			O22_P6_C34	103.5	6		
O27_P6_C34	105.6	3.9			O27_P6_C34	103.6	5.9		

	Angle / °	Deviation from perfect geometry / °	Mean deviation from symmetry / °	Standard Deviation of distortion / °		Angle / °	Deviation from perfect geometry / °	Mean deviation from symmetry / °	Standard Deviation of distortion / °
O14_P7_O19	114.3	4.8	4.1	2.1	O14_P7_O19	115.3	5.8	4.1	1.9
O14_P7_O23	114.5	5.0			O14_P7_O23	115.5	6		
O19_P7_O23	111.4	1.9			O14_P7_C38	108.5	1		
O19_P7_C38	101.9	7.6			O19_P7_O23	106.5	3		
O23_P7_C38	106.8	2.7			O19_P7_C38	104.5	5		
O14_P7_C38	106.8	2.7			O23_P7_C38	105.7	3.8		
O15_P8_O20	110.9	1.4	2.6	1.5	O15_P8_O20	112.5	3	2.1	1.4
O15_P8_O28	114.0	4.5			O15_P8_O28	109.5	0		
O20_P8_O28	111.2	1.7			O15_P8_C42	108.7	0.8		
O20_P8_C42	108.3	1.2			O20_P8_O28	112.4	2.9		
O28_P8_C42	105.1	4.4			O20_P8_C42	107.5	2		
O15_P8_C42	106.9	2.6			O28_P8_C42	105.9	3.6		
O16_P9_O24	112.3	2.8	2.7	1.3	O16_P9_O24	111.3	1.8	2.7	2.0
O16_P9_O29	113.7	4.2			O16_P9_O29	115.6	6.1		
O16_P9_C46	110.4	0.9			O16_P9_C46	109.3	0.2		
O24_P9_O29	108.1	1.4			O24_P9_O29	106.7	2.8		
O24_P9_C46	105.5	4.0			O24_P9_C46	105.9	3.6		
O29_P9_C46	106.4	3.1			O29_P9_C46	107.6	1.9		
O17_P10_O21	107.9	1.6	1.5	1.3	O17_P10_O21	108.0	1.5	2.0	0.9
O17_P10_O25	110.1	0.6			O17_P10_O25	112.0	2.5		
O21_P10_O25	109.2	0.3			O17_P10_C50	112.8	3.3		
O21_P10_C50	108.2	1.3			O21_P10_O25	107.9	1.6		
O25_P10_C50	108.0	1.5			O21_P10_C50	108.9	0.6		
O17_P10_C50	113.4	3.9			O25_P10_C50	107.1	2.4		
H31_C30_H32	122.7	13.2	19.5	4.2	H31_C30_H32	122.4	12.9	7.2	5.4

	Angle / °	Deviation from perfect geometry / °	Mean deviation from symmetry / °	Standard Deviation of distortion / °		Angle / °	Deviation from perfect geometry / °	Mean deviation from symmetry / °	Standard Deviation of distortion / °
H31_C30_H33	103.3	6.2			H31_C30_H33	107.3	2.2		
H32_C30_H33	103.7	5.8			H32_C30_H33	103.1	6.4		
H35_C34_H36	104.8	4.7	14.6	2.5	H35_C34_H36	101.0	8.5	4.4	3.9
H35_C34_H37	110.1	0.6			H35_C34_H37	108.8	0.7		
H36_C34_H37	104.4	5.1			H36_C34_H37	113.6	4.1		
H39_C38_H40	102.8	6.7	14.1	3.2	H39_C38_H40	105.8	3.7	3.7	0.6
H39_C38_H41	110.4	0.9			H39_C38_H41	105.2	4.3		
H40_C38_H41	108.2	1.3			H40_C38_H41	106.3	3.2		
H43_C42_H44	99.5	10.0	15.5	5.1	H43_C42_H44	103.5	6	2.5	3.1
H43_C42_H45	109.6	0.1			H43_C42_H45	108.0	1.5		
H44_C42_H45	112.6	3.1			H44_C42_H45	109.5	0		
H47_C46_H48	104.1	5.4	16.9	1.0	H47_C46_H48	106.1	3.4	5.0	2.2
H47_C46_H49	104.5	5.0			H47_C46_H49	105.4	4.1		
H48_C46_H49	102.6	6.9			H48_C46_H49	102.0	7.5		
H51_C50_H52	109.6	0.1	14.8	4.5	H51_C50_H52	109.82	0.3	7.6	6.8
H51_C50_H53	100.8	8.7			H51_C50_H53	95.69	13.8		
H52_C50_H53	107.1	2.4			H52_C50_H53	100.96	8.5		

Instrument parameter file for the HRPD station at ISIS supplied by Dr Kevin Knight, Rutherford Appleton laboratory.

```
12345678901234567890123456789012345678901234567890123456789012345678901234567890
INS   BANK   2
INS   FPATH1    95.0
INS   FPATH2    96.0
INS   HTYPE   PNTR
INS  1 ICONS  48234.50      2.77      8.00
INS  1BNKPAR    0.8918    168.33      0.00    .00000     .3000    1    1
INS  1I HEAD   HRPD cycle 975 #15986 NBS silicon - backscattering bank
INS  1I ITYP    0    1.000    300.000       2
INS  1PRCF      3   14   0.001000
INS  1PRCF 1   1.185100E-01   0.024859E+00   0.007427E+00   0.000000E+00
INS  1PRCF 2   2.226950E+02   0.000000E+00   0.000000E+00   0.595960E+01
INS  1PRCF 3   0.000000E+00   0.000000E+00   0.000000E+00   0.000000E+00
INS  1PRCF 4   0.000000E+00   0.000000E+00   0.000000E+00   0.000000E+00
INS  2 ICONS  34625.26     -5.03      8.00
INS  2BNKPAR    0.8660     90.00      0.00    .00000     .3000    1    1
INS  2I HEAD   HRPD cycle 975 #15986 NBS silicon - 90degree detectors
INS  2I ITYP    0    1.000    300.000       2
INS  2PRCF      3   14   0.001000
INS  2PRCF 1   1.185100E-01   0.024859E+00   0.007427E+00   0.000000E+00
INS  2PRCF 2   1.330600E+02   0.000000E+00   0.000000E+00   0.595960E+01
INS  2PRCF 3   0.000000E+00   0.000000E+00   0.000000E+00   0.000000E+00
INS  2PRCF 4   0.000000E+00   0.000000E+00   0.000000E+00   0.000000E+00
```

References

1 K. Maeda, J. Akimoto, Y. Kiyozumi and F. Mizukami, *J. Chem. Soc., Chem. Commun.*, 1995, 1033.